

INFLUENCES OF COMPOSITION, MELT VISCOSITY AND CRYSTALLIZATION  
ON THE COLOR STRENGTH AND STABILITY OF MULTI-OXIDE GLASS  
FRIT/ZIRCON-VANADIUM PIGMENT SYSTEMS FOR CERAMIC  
WHITEWARES COATINGS APPLICATIONS

By

DAVID A. EARL

A DISSERTATION PRESENTED TO THE GRADUATE SCHOOL  
OF THE UNIVERSITY OF FLORIDA IN PARTIAL FULFILLMENT  
OF THE REQUIREMENTS FOR THE DEGREE OF  
DOCTOR OF PHILOSOPHY

UNIVERSITY OF FLORIDA

1998

## ACKNOWLEDGMENTS

I am grateful for the guidance and inspiration provided by Dr. David E. Clark, chairman of my supervisory committee. My association with Dr. Clark has greatly enhanced my academic, professional and personal growth over the past five years.

I would like to thank Dr. Joseph Simmons, Dr. E. Dow Whitney, Dr. Jack Mecholsky and Dr. Dinesh Shah for participating on my supervisory committee. Thanks also go to Kristie Leiser, Mark Moore, Robert DiFiori, Diane Folz and Rebecca Schulz of Dr. Clark's research group for their advice.

In addition I would like to acknowledge the industrial support of this research. I would like to thank Florida Tile Industries; Bob Blonski, Klaus Meinssen, Bruno Burzacchini and Marzia Barrattini of Ferro Corporation; and Dan Swiler, Hong Chen and Pam Lucas of Ceredec Corporation.

Finally, and most importantly, I am grateful for the patience and encouragement of my wife, Jacquie. This

research effort would not have been possible without her support.

## TABLE OF CONTENTS

	<u>Page</u>
ACKNOWLEDGMENTS.....	ii
LIST OF TABLES.....	viii
LIST OF FIGURES.....	x
ABSTRACT.....	xix
CHAPTERS	
1. INTRODUCTION.....	1
1.1 Color in the Ceramics Industry.....	1
1.2 Glaze Colorants.....	5
1.3 Potential Influence of Frit.....	7
1.4 Overview of Dissertation Goals.....	12
1.5 Guide for Using This Dissertation.....	16
2. BACKGROUND.....	21
2.1 Color Theory.....	21
2.1.1 Light and the Visible Spectrum.....	22
2.1.2 Materials Interactions with Light.....	29
2.1.2a Refraction.....	30
2.1.2b Surface Reflection and Gloss.....	36
2.1.2c Opacity and Translucency.....	42
2.1.2d Absorption, Transmission and Color.....	51
2.1.3 Color Perception by the Human Eye.....	60
2.1.4 Color Measurement.....	65
2.1.4a Spectrophotometry.....	65
2.1.4b Basis for Color Quantification....	72
2.1.4c CIE L*a*b* Measurement Scale.....	78



2.2	Color in Ceramic Glazes.....	86
2.2.1	Silicate Glass Structures and Properties.....	87
2.2.2	Glaze Base Materials and Formulas.....	99
2.2.3	Fast-Fire Whiteware Glazes and Frits...	105
2.2.4	Ceramic Colorants.....	113
2.2.4a	Zircon Triaxial Pigments.....	115
2.2.4b	Kubelka-Munk Analysis of Colorant Layers.....	127
2.2.5	Frit Influence on Color Development....	132
2.2.5a	Crystallization Mechanisms.....	132
2.2.5b	Zircon Crystallization and Dissolution.....	145
2.2.5c	Liquid-Liquid Phase Separation....	152
2.2.5d	Viscosity Relationships.....	155
3.	EXPERIMENTAL PROCEDURES.....	161
3.1	Materials and Methods.....	161
3.1.1	Glass Frits and Zr-V Pigment.....	161
3.1.2	Coatings Preparation and Application...	165
3.1.3	Firing Curves.....	167
3.2	Materials Characterization and Analytical Techniques.....	169
3.2.1	AAS and XRF.....	169
3.2.2	Frit Density Determination.....	169
3.2.3	Laser Diffraction Particle Size Analysis.....	170
3.2.4	Spectrophotometry and Color Calculations.....	170
3.2.5	Gloss Measurements.....	172
3.2.6	Heating Microscopy.....	173
3.2.7	Dilatometry.....	174
3.2.8	X-Ray Diffraction (XRD).....	174
3.2.9	Scanning Electron Microscopy (SEM) and Energy Dispersive X-Ray Spectroscopy (EDS)..	176
3.3	Statistical Methods for Deriving Equations....	177
4.	RESULTS.....	180
4.1	Frit and Pigment Properties.....	180
4.2	Color of Fired Coatings.....	181
4.2.1	Spectral Reflectance Curves.....	182
4.2.2	Pigment Absorption Factors (K/S).....	188

4.2.3	Color in L*, a* and b* Values.....	193
4.2.4	Color Stability.....	206
4.2.5	Specular Gloss.....	208
4.3	Viscosity of Coatings During Heating.....	210
4.3.1	Heating Microscope Images.....	210
4.3.2	Dilatometric T <sub>g</sub> and T <sub>2</sub> .....	213
4.3.3	Viscosity vs. Temperature.....	216
4.4	Derived Statistical Models.....	219
4.4.1	K/S vs. Coating Composition and Temperature.....	220
4.4.2	ΔE* vs. Coating Composition.....	235
4.4.3	Log Viscosity vs. Coating Composition and Temperature.....	244
4.5	Evolved Crystalline Species.....	246
4.5.1	XRD, SEM and EDS Evaluations.....	246
4.5.1a	Frits with ZrO <sub>2</sub> .....	246
4.5.1b	Frits without ZrO <sub>2</sub> .....	260
4.5.2	Zircon Quantitative Analysis.....	277
4.5.2a	Frits with ZrO <sub>2</sub> and ZnO.....	280
4.5.2b	Frits with ZrO <sub>2</sub> and SrO.....	280
4.5.2c	Frits without ZrO <sub>2</sub> .....	281
5.	DISCUSSION.....	282
5.1	Color Strength and Stability Dependency.....	282
5.1.1	Coating Composition.....	284
5.1.1a	Zr-V Loading.....	284
5.1.1b	ZrO <sub>2</sub> .....	286
5.1.1c	SrO vs. ZnO.....	290
5.1.1d	Al <sub>2</sub> O <sub>3</sub> /Alkalis .....	293
5.1.2	Crystalline Species.....	296
5.1.2a	Zircon.....	296
5.1.2b	Diopside.....	305
5.1.2c	Hardystonite.....	307
5.1.2d	Strontium Calcium Silicate.....	308
5.2	Melt Viscosity.....	312
5.2.1	Influence on Crystallization and Zr-V Dissolution.....	312
5.2.2	Value as a Predictor of K/S and ΔE*....	315

6.	SUMMARY AND CONCLUSIONS.....	320
6.1	Zr-V Pigment and Color Values.....	324
6.2	Frit Oxide Composition.....	326
6.3	Viscosity, Crystallization and Zr-V Dissolution.....	328
7.	FUTURE WORK.....	333
APPENDICES		
A	UNITS FOR DESCRIBING LIGHT AND COLOR.....	337
B	THE 15 CAUSES OF COLOR.....	339
C	DENSITY, PARTICLE SIZE AND APPLICATION WEIGHT DATA.	341
D	DATA FROM COATINGS BATCHED WITH FRIT, 2.5% BENTONITE AND Zr-V PIGMENT, AND FIRED USING A 45-MINUTE CERAMIC TILE CYCLE.....	343
E	FRIT SPECTRAL REFLECTANCE DATA AND CURVES AT EACH TEMPERATURE AND PIGMENT LOADING.....	347
	REFERENCES.....	359
	BIOGRAPHICAL SKETCH.....	367

## LIST OF TABLES

<u>Table</u>	<u>Page</u>
1.1 Example of Ceramic Coatings Applications on a Decorated Floor Tile .....	8
1.2 Variables That Influence Ceramic Glaze Color.....	9
2.1 Index of Refraction of Selected Materials at 589 nm Wavelength in Air .....	32
2.2 Properties of Materials Used for Opacifying Ceramic Glazes .....	45
2.3 Transition Elements and Their Properties.....	58
2.4 Factors for Uniform Color Scales for Normalizing to a Standard Reference White .....	81
2.5 Glass Formers, Intermediates and Modifiers Materials Commonly Employed in Whiteware Glazes.....	92
2.6 Properties Associated with the Presence of Various Oxides in Glass .....	98
2.7 Common Ceramic Tile Glaze Base Materials.....	100
2.8 Examples of Compositions (Weight %) of Commercial Glazes .....	101
2.9 Summary of Important Glaze Properties and Characteristics .....	102
2.10 Seger's Formula for Classifying Glazes.....	103
2.11 Typical Empirical Formulas, in Molar Equivalents, for Fast-Fire Gloss and Matte Glazes .....	111

2.12	Glaze Pigments and Their Requirements.....	117
3.1	Frits Investigated.....	162
E.1	Engobe and Frits A and B Reflectance Data.....	347
E.2	Frits C and D Reflectance Data.....	348
E.3	Frits E and F Reflectance Data.....	349
E.4	Frits G and H Reflectance Data.....	350

## LIST OF FIGURES

<u>Figure</u>	<u>Page</u>
1.1 Flow chart summary of main research variables.....	17
2.1 Electromagnetic spectrum.....	25
2.2 Wavelength vs. energy distribution of daylight....	26
2.3 Refractive index vs. wavelength of incident light for three glasses.....	34
2.4 Reflection and transmission of light by a glassy material containing suspended particles.....	37
2.5 Fresnel reflection for a) an air/glass boundary and b) total reflectivity for different index of refraction.....	40
2.6 Reflectance vs. wavelength of light for a $\text{TiO}_2$ opacified white glaze fired to $1000^\circ\text{C}$ , at various glaze application weights in $\text{g/ft}^2$ .....	50
2.7 The 5 d orbitals.....	57
2.8 Human optical system.....	61
2.9 Luminosity functions of the rods (nighttime scotopic vision) and cones (daytime photopic vision) of the human eye.....	63
2.10 Reflectance versus wavelength for opaque coatings colored with pigments that absorb a portion of incident light.....	67
2.11 Basic components of spectrophotometers.....	69

2.12	Schematic of the Hardy spectrophotometer.....	70
2.13	Weighting functions used for the standard observer at a 2° field of view.....	74
2.14	Luminosity or lightness (Y) and chromaticity (x, y) MacAdam limits for colors viewed in daylight.....	79
2.15	Schematic of L*a*b* color space.....	83
2.16	Comparison of structures and XRD patterns of crystalline and vitreous silica.....	90
2.17	Two-dimensional representation of modifiers (a) Na <sup>+</sup> and (b) Ca <sup>2+</sup> in the silicate glass structure.....	95
2.18	Inorganic pigment family.....	114
2.19	CIE a* and b* chroma of ceramic pigments.....	116
2.20	Typical forms of zircon crystals. (a-c): a{100}, m{110}, p{101}, x{211}; and zircon lattice structure (d,e).....	120
2.21	Splitting of the d orbital in V <sup>4+</sup> by tetrahedral (T <sub>d</sub> ) and tetragonal (D <sub>2d</sub> ) crystal fields.....	124
2.22	Schematic of basis for Kubelka-Munk analysis of colorant layers.....	128
2.23	Relationship between viscosity and temperature favoring nucleation and growth in glazes.....	137
2.24	Crystal growth rate as a function of temperature in Na <sub>2</sub> O-CaO-Al <sub>2</sub> O <sub>3</sub> -SiO <sub>2</sub> glass.....	144
2.25	Binary phase diagram of ZrO <sub>2</sub> and SiO <sub>2</sub> system.....	149
2.26	Viscosities of some commercial silicate glasses...	157

3.1	Time-temperature profiles used to fire the tiles..	168
4.1	Spectral reflectance of unfired raw materials and the engobe substrate backing.....	183
4.2	Spectral reflectance of coatings batched with frit C, fired to 1000°C.....	186
4.3	Spectral reflectance of coatings batched with frit H, fired to 1100°C.....	187
4.4	Spectral reflectance of coatings batched with 2.0% Zr-V, fired to 1000°C.....	189
4.5	Spectral reflectance of coatings batched with 2.0% Zr-V, fired to 1050°C.....	190
4.6	Spectral reflectance of coatings batched with 2.0% Zr-V, fired to 1100°C.....	191
4.7	Pigment absorption factors versus weight percent Zr-V batched in coatings fired to 1000°C, 1050°C and 1100°C peak temperature.....	192
4.8	Color values of coatings batched with frits (A-H) and Zr-V pigment, and fired to 1050°C.....	194
4.9	Color values of coatings batched with frits (A-H) and Zr-V pigment, and fired to 1100°C.....	195
4.10	Color values of coatings batched with frits (A-H) and no Zr-V, and fired to 1000°C, 1050°C or 1100°C.....	198
4.11	Color values of coatings batched with frits (A-H) and 0.5% Zr-V, and fired to 1000°C, 1050°C or 1100°C.....	199
4.12	Color values of coatings batched with frits (A-H) and 2.0% Zr-V and fired to 1000°C, 1050°C or 1100°C.....	200



4.13	Color values of coatings batched with frits (A-H) and 5.0% Zr-V, and fired to 1000°C, 1050°C or 1100°C.....	201
4.14	Relationship between lightness ( $L^*$ ) and blueness ( $-b^*$ ) of coatings batched with Zr-V pigment and fired to 1000°C, 1050°C and 1100°C peak temperature.....	203
4.15	Zr-V pigment absorption factor relationships with $L^*$ , $a^*$ and $b^*$ color values of fired coatings.....	205
4.16	Color changes ( $\Delta E^*$ ) due to a variation in peak firing temperature from 1050°C to 1100°C for coatings batched with frits (A-H) and Zr-V pigment.....	207
4.17	Specular gloss of fired coatings at a 60° angle of incidence.....	209
4.18	Heating microscope images of coatings batched with frits (A-H) and 2.0% Zr-V, at 900°C, 1000°C and 1100°C.....	211
4.19	Heating microscope images of characteristic stages of flow of coatings batched with frits (A-H) and 2.0% Zr-V.....	212
4.20	Thermal dilatometric analyses of coatings A-D batched with 2.0% Zr-V.....	214
4.21	Thermal dilatometric analyses of coatings E-H batched with 2.0% Zr-V.....	215
4.22	Log $\eta$ versus temperature of coatings batched with 2.0% Zr-V. Frits A-D incorporate 8% $ZrO_2$ .....	217
4.23	Log $\eta$ versus temperature of coatings batched with 2.0% Zr-V. Frits E-H contain no $ZrO_2$ .....	218

4.24	Pigment absorption factor actual and equation (4.2) predicted results for fired coatings batched with 2.0% Zr-V.....	224
4.25	Individual effects of frit oxides on K/S based on statistical model (4.2) for 2.0% Zr-V and a peak firing temperature of 1050°C.....	225
4.26	Variables weight of influence on K/S, based on statistical models 4.1 (0.5% Zr-V), 4.2 (2% Zr-V) and 4.3 (5% Zr-V).....	228
4.27	Pigment absorption factor trends with frit Al <sub>2</sub> O <sub>3</sub> :alkalis ratio of coatings batched with 2.0% Zr-V and fired to 1000°C, 1050°C or 1100°C.	229
4.28	Pigment absorption factor versus frit ZnO and SrO molar equivalents of fired coatings batched with 2.0% Zr-V and fired to 1000°C, 1050°C or 1100°C peak temperature.....	230
4.29	Influence of frit ZrO <sub>2</sub> , in the presence of SrO or ZnO, on K/S of fired coatings batched with 2.0% Zr-V and fired to 1000°C, 1050°C or 1100°C.....	231
4.30	Variations in pigment absorption factor (K/S) due to changes in peak firing temperature, for coatings batched with 2.0% Zr-V and frits containing 8% ZrO <sub>2</sub> versus 0% ZrO <sub>2</sub> .....	232
4.31	Delta E* actual and equation (4.7) predicted results for fired coatings batched with 2.0% Zr-V.....	239
4.32	Individual effects of frit oxides on Delta E*, based on statistical model 4.7 for 2.0% Zr-V....	240
4.33	Variables weight of influence on Delta E*, based on statistical models 4.6 (0.5% Zr-V), 4.7 (2.0% Zr-V) and 4.8 (5.0% Zr-V).....	242

4.34	Color changes due to variations in peak firing temperature and frit $\text{Al}_2\text{O}_3$ :alkali ratio of coatings batched with 2.0% Zr-V.....	243
4.35	XRD patterns from coatings batched with frit A and 2.0% Zr-V, and fired to 1000°C, 1050°C and 1100°C. Frit A includes 8% $\text{ZrO}_2$ , 12% $\text{ZnO}$ , 0% $\text{SrO}$ , 5% alkalis.....	247
4.36	SEM micrographs of a coating batched with frit A and 2.0% Zr-V, and fired to 1100°C. Magnification is (a) X 1,000 and (b) X 6,000. Shown are large Zr-V particles surrounded by fine zircon precipitates.....	248
4.37	XRD patterns from coatings batched with frit B and 2.0% Zr-V, and fired to 1000°C, 1050°C and 1100°C. Frit B includes 8% $\text{ZrO}_2$ , 12% $\text{ZnO}$ , 0% $\text{SrO}$ , 10% alkalis.....	249
4.38	SEM micrographs of a coating batched with frit B and 2.0% Zr-V, and fired to 1100°C. Magnification is (a) X 1,000 and (b) X 6,000. Shown are large Zr-V particles, fine zircon precipitates and large zircon fibers.....	250
4.39	XRD patterns from coatings batched with frit C and 2.0% Zr-V, and fired to 1000°C, 1050°C and 1100°C. Frit C includes 8% $\text{ZrO}_2$ , 0% $\text{ZnO}$ , 12% $\text{SrO}$ , 5% alkalis.....	251
4.40	XRD patterns from coatings batched with frit D and 2.0% Zr-V, and fired to 1000°C, 1050°C and 1100°C. Frit D includes 8% $\text{ZrO}_2$ , 0% $\text{ZnO}$ , 12% $\text{SrO}$ , 10% alkalis.....	252
4.41	SEM micrographs of coatings batched with 2.0% Zr-V, (a) frit C and (b) frit D, and fired to 1100°C. (magnification X 1,000). Particles shown are Zr-V pigment.....	253
4.42	X-ray diffraction profile for zircon, $\text{ZrSiO}_4$ .....	255

4.43	SEM micrograph of zircon-vanadium (Zr-V) pigment, Ceredec 41715A, X 1,000 magnification.....	256
4.44	XRD patterns from coatings batched with frit E and 2.0% Zr-V, and fired to 1000°C, 1050°C and 1100°C. Frit E includes 0% ZrO <sub>2</sub> , 12% ZnO, 0% SrO and 5% alkalis.....	261
4.45	SEM micrograph of a coating batched with frit E and 2.0% Zr-V, and fired to 1050°C. Magnification is X 1,000. Shown are large Zr-V particles surrounded by dispersed diopside.	262
4.46	XRD patterns from coatings batched with frit F and 2.0% Zr-V, and fired to 1000°C, 1050°C and 1100°C. Frit F includes 0% ZrO <sub>2</sub> , 12% ZnO, 0% SrO and 10% alkalis.....	263
4.47	SEM micrographs of a coating batched with frit F and 2.0% Zr-V, and fired to 1100°C. Magnification is (a) X 1,000 and (b) 6,000. All particles shown are hardystonite.....	264
4.48	XRD patterns from coatings batched with frit G and 2.0% Zr-V, and fired to 1000°C, 1050°C and 1100°C. Frit G includes 0% ZrO <sub>2</sub> , 0% ZnO, 12% SrO and 5% alkalis.....	265
4.49	SEM micrograph of a coating batched with frit G and 2.0% Zr-V, fired to 1100°C (magnification X 1,000). Shown is crystallized SrCa <sub>2</sub> Si <sub>3</sub> O <sub>9</sub> .....	266
4.50	XRD patterns from coatings batched with frit H and 2.0% Zr-V, and fired to 1000°C, 1050°C and 1100°C. Frit H includes 0% ZrO <sub>2</sub> , 0% ZnO, 12% SrO and 10% alkalis.....	267
4.51	SEM micrographs of a coating batched with frit H and 2.0% Zr-V, and fired to 1100°C. Magnification is (a) X 1,000 and (b) X 6,000. Shown is crystallized SrCa <sub>2</sub> Si <sub>3</sub> O <sub>9</sub> .....	268

4.52	Relationship between XRD [312] integrated intensity and weight percent zircon in unfired coatings.....	278
4.53	Weight percent zircon in fired coatings batched with 2.0% Zr-V.....	279
5.1	Changes in reflectance distributions at 400 nm and 640 nm wavelengths due to increases in peak firing temperature for coatings batched with 0.5%, 2.0% and 5.0% Zr-V.....	285
5.2	Influence of frit density on the color stability of coatings batched with 2.0% Zr-V pigment.....	289
5.3	Pigment absorption factors (K/S) for coatings batched with Zr-V pigment and frits containing 8% ZrO <sub>2</sub> , and fired to 1000°C, 1050°C or 1100°C peak temperature.....	291
5.4	Visual lightness (L*), greenness (-a*) and blueness (-b*) as a function of weight percent zircon in the fired coatings batched with 2.0% Zr-V.....	299
5.5	Pigment absorption factor (K/S) as a function of Zr-V pigment and zircon contents in coatings batched with 2.0% Zr-V.....	302
5.6	Changes in color stability denoted by K/S and Delta E*, as a function of weight percent zircon in coatings batched with 2.0% Zr-V.....	304
5.7	Color lightness (L*) and blueness (-b*) progression with diopside crystallization and pigment dissolution in coatings batched with frit E and 2.0% Zr-V.....	306
5.8	Color lightness (L*) and blueness (-b*) progression with hardystonite crystallization and pigment dissolution in coatings batched with frit F and 2.0% Zr-V.....	309

5.9	Color lightness ( $L^*$ ) and blueness ( $-b^*$ ) progression with $\text{SrCa}_2\text{Si}_3\text{O}_9$ crystallization and pigment dissolution in coatings batched with 2.0% Zr-V.....	311
5.10	Integrated log viscosity from 700°C to 1100°C versus fired color strength (K/S) and stability ( $\Delta E^*$ ) in coatings batched with 2.0% Zr-V...	316
5.11	Slope in the log viscosity versus temperature near the softening point versus fired color strength (K/S) and stability ( $\Delta E^*$ ) in coatings batched with 2.0% Zr-V.....	318
E.1	Frit A spectral reflectance curves.....	351
E.2	Frit B spectral reflectance curves.....	352
E.3	Frit C spectral reflectance curves.....	353
E.4	Frit D spectral reflectance curves.....	354
E.5	Frit E spectral reflectance curves.....	355
E.6	Frit F spectral reflectance curves.....	356
E.7	Frit G spectral reflectance curves.....	357
E.8	Frit H spectral reflectance curves.....	358

Abstract of Dissertation Presented to the Graduate School  
of the University of Florida in Partial Fulfillment of the  
Requirements for the Degree of Doctor of Philosophy

INFLUENCES OF COMPOSITION, MELT VISCOSITY AND CRYSTALLIZATION  
ON THE COLOR STRENGTH AND STABILITY OF MULTI-OXIDE GLASS  
FRIT/ZIRCON-VANADIUM PIGMENT SYSTEMS FOR CERAMIC  
WHITEWARES COATINGS APPLICATIONS

By

David A. Earl

December 1998

Chairman: David E. Clark

Major Department: Materials Science and Engineering

Color control is becoming increasingly important in the industrial processing of ceramics coatings. Multi-oxide glass frits are the predominant materials in ceramic whitewares coatings, and zircon doped pigments are the most commonly used colorants.

The primary objective of this research was to determine if glass frits could be formulated to improve the fired color strength and high-temperature stability of ceramic coatings colored with zircon-vanadium (Zr-V) blue pigments. The results would also be applicable to other ceramic pigments that utilize the same zircon structure to incorporate

colorant metal ions. A secondary goal was to relate the frit oxide composition, pigment content, firing temperature, melt viscosity and microstructural development to the fired color. A ceramic tile process was applied to fabricate sample coatings for the study. A coating's color was quantified and related to human perception with CIE  $L^*$ ,  $a^*$  and  $b^*$  values and pigment absorption factors (K/S), calculated based on spectral reflectance data.

The research was successful in quantifying the influence of individual glass frit oxides on the fired color strength and high-temperature stability of the coatings. Opaque and transparent glossy frit compositions which yield excellent color strength and stability were formulated. Mathematical models for predicting a coating's color strength and stability given the frit oxide composition, Zr-V pigment loading and peak firing temperature were derived. Frit oxides of  $ZrO_2$ ,  $SrO$ ,  $ZnO$ ,  $Al_2O_3$ ,  $Na_2O$  and  $K_2O$  were found to have a significant influence on crystallization, pigment dissolution and color development. The properties, sizes, morphologies and quantities of crystalline phases that precipitated in the coatings during firing were related to the color. A technique for producing uniquely light yet high



chroma colors through control of zircon precipitate particle size was demonstrated.

In addition, a statistical model was developed for calculating the coating melt viscosity as a function of the frit oxide composition and temperature. Melt viscosity versus temperature curves were applied to predict a frit's potential for producing strong and stable color.

## CHAPTER 1 INTRODUCTION

### 1.1 Color in the Ceramics Industry

The color of a product often determines its aesthetic and monetary value. Selling prices of ceramics such as tile, brick, artware, dinnerware, cookware, porcelain enamel, concrete, bathroom fixtures and decorative glass are directly related to their appearance.

Customers often select ceramic products based on viewing sample chips or prototypes at stores or retail distributors. Sometimes buyers wish to color coordinate with the fixtures, appliances or paint of an existing building. Occasionally, customers purchase more of the same product in the future, for example, adding the same color floor tile to an enlarged room. In all of these cases, it is imperative that manufacturers strictly conform to tight color tolerances, year after year, in order for goods to comply visually with customer expectations.

Inconsistencies in manufactured colors lead to significant increases in industrial costs. Noticeable color

variations in fired coatings due to normal fluctuations in manufacturing processing conditions result in nonstandard, scrap products and lower productivity. For example, a major portion of the \$120 million worth of products scrapped in 1997 by U.S. ceramic tile manufacturers resulted from out-of-tolerance colors. Since the U.S. ceramic tile market only comprises about 0.6% of the world ceramic whitewares sector, problems with color variations result in significant industrial waste worldwide [Sez98]. In addition, product inventory levels must be increased in order to accommodate multiple color shades per item.

Color consistency in manufacturing has become increasingly difficult due to the rapid evolution of processing technology to improve productivity and profitability. Often during the transition, accessories for the same product line must match in color but are made with two different processes. For example, in the ceramic tile industry, flat "field" tile is predominately manufactured with completely automated fast-fire roller kiln technology, while difficult to handle trim and angle shapes are constrained to high-labor slow-fire tunnel kiln processes. Firing differences between the processes (30-minute fast-fire vs. 14-hour slow-fire cycles) complicate the formation of

matching glaze colors, but customers demand no noticeable difference between coordinating trim and field glazes. Color incompatibility between these products is currently the largest customer complaint in the ceramic tile industry. Other whitewares companies, including some manufacturers of sanitaryware and dinnerware, are planning to convert to the same fast-fire roller kiln technology and will encounter similar problems with color variations.

Undesirable color differences between coatings batched with the same formula occur even in facilities that utilize the same type of firing technology throughout the factory. Firing variations result from different kiln models, sizes and shapes, the debugging of new kiln equipment, kiln fan and burner wear over time, and changes in ambient conditions which cause the kiln intake air density, humidity and temperature to vary. Gaps in the product load entering a kiln, normally due to breakdowns in machines upstream in the production line, also cause firing temperature versus time profiles to fluctuate. Shifts in firing conditions result in variations in crystallization and pigment dissolution in ceramic coatings, which alter their fired gloss, opacity and color. This burdens industry with low yields, customer complaints and potential loss of business.

Another source of color variation can be attributed to the continued effort to reformulate ceramic coatings in order to lower raw material costs. Unfortunately, some of the cheaper systems have also yielded lower color strength and stability during high-temperature processing. Due to increasing foreign competition, domestic companies have been compelled to lower manufacturing costs to enable selling price reductions and gain a competitive edge. For example, in the ceramic tile industry, import market share rose from about 20% in the mid-1970s to over 60% in the 1990s [ Ear94] . Glaze raw material costs comprise roughly 10% of all tile manufacturing expenses or approximately \$100 million per year [ Fer96, Sez98] . In order to stay in business, it is crucial for whitewares companies to optimize color consistency while minimizing glaze costs.

There is an increasing interest in the ceramics industry to develop low cost color systems which are reproducible over a range of processing conditions. High-temperature interactions between multi-oxide glass frits and pigments in ceramic glazes greatly affect the fired color. The influence of frit is most significant since it is a relatively expensive, carefully manufactured material usually added at the highest weight percent of ingredients in fast-fire glaze

batches. Compared to other glaze components, frit normally has the lowest melting temperature and is the most corrosive to ceramic colorants. Most frit in the U.S. is used by ceramic tile manufacturers, but frit consumption by other whitewares industries will increase as they convert to fast-fire roller kiln technology. Zircon doped pigments are the most commonly used colorants for whitewares coatings because they have the best high-temperature stability.

The overall objective of this research was to determine the influence of various oxides in glass frits on color development with zircon doped pigments during firing. The results could be used to improve the color strength and stability of industrial ceramic glaze systems.

This chapter very briefly introduces the reader to color in ceramic glazes, the potential influence of frit on color and an overview of the dissertation goals. More detailed discussions are included in succeeding chapters.

## 1.2 Glaze Colorants

Ceramic glazes provide an impervious glassy decorative coating for whitewares. Colors are produced with selective scattering or absorption of incident light by colloidal-sized particles suspended in the glassy matrix.

Solution colorants are sometimes introduced into the glaze batch as oxides, then dissolved and precipitated as metal ions during the firing process. Oxides such as  $\text{Cr}_2\text{O}_3$  (green),  $\text{CoO}$  (blue),  $\text{CuO}$  (green to red),  $\text{Fe}_2\text{O}_3$  (yellow to brown) and  $\text{MnO}_2$  (purple to brown) were common sources of metal ion solution colorants.

They are now rarely used in high volume whitewares processes such as ceramic tile manufacturing because their solubility and reprecipitation, and thus the color produced, are extremely sensitive to the glaze composition, particle size distribution, firing time and kiln atmosphere.

More typically, manufactured inert pigment particles are added to glazes to obtain color. The most widely used for industrial glazes are zircon crystal lattices doped with metal ions. They provide a lower chroma than other pigments, but the zircon structure is less soluble at high temperature. Besides, most of the demand in the whitewares market is for relatively weak, light colors.

The most common zircon-based pigments are zircon-vanadium blue, zircon-iron coral and zircon-praseodymium yellow. They are referred to as the triaxial pigments and can be blended to achieve most glaze colors desired by customers. Even though zircon crystals are more stable at

high temperature than other colorants, color variations still occur. During firing, zircon may remain stable and protect the metal ions, partially dissolve with that portion reprecipitating or remaining in solution, or totally dissolve.

Color control is further complicated because most decorated ceramic whitewares contain multiple layers of coatings. For example, a typical "stone look" floor tile produced by Florida Tile Industries requires nine different coatings over the pressed body (Table 1.1). Some applications overlap, while others are distinctly separate on the surface to create a more natural appearance and depth of design. Both physical and chemical interactions between layers influence pigment dissolution and the nucleation and growth of new phases which affect opacity, gloss and color.

### 1.3 Potential Influence of Frit

Many variables influence color development in ceramic glazes, as outlined in Table 1.2. The strength and high temperature stability of ceramic pigments are highly dependent upon the base glaze composition. Limited preliminary studies [Dec93, Byr94, Blo93] indicate that



Table 1.1. Example of Ceramic Coatings Applications on a Decorated Floor Tile.

Glaze Coating	Color/Opacity	Application Method	Application Weight (g/cm <sup>2</sup> )
Engobe (primer coat)	White/Opaque	Rotating disk	0.05
Fume	Taupe/Opaque	Spray gun	0.007
---	---	Brushing machine	---
Middle coat	Off-white/ Translucent	Rotating disk	0.09
Fume	Grey/Opaque	Spray gun	0.003
Ink 1	Light Grey/ Opaque	Screen printer	<0.001
Ink 2	Gold/Opaque	Screen printer	<0.001
Ink 3	Light Beige/ Opaque	Screen printer	<0.001
Ink 4	White/Opaque	Screen printer	0.001
Topcoat	Transparent	Spray gun	0.02

Table 1.2. Variables That Influence Ceramic Glaze Color.

---

I. Batch Composition

- a. Base ingredients (oxide composition and phases present)
- b. Pigments (composition, structure and loading)
- c. Chemical additives (influence application drying rate and smoothness)

II. Glaze Preparation with Ball Milling

- a. Particle size distribution (influences melting point)

III. Application

- a. Thickness (hiding power)
- b. Drying rate (can affect composition gradient caused by differences in particle settling rates)
- c. Smoothness (influences gloss or degree of specular reflectance)

IV Firing

- a. Time vs. temperature (phase dissolution and precipitation)
  - b. Kiln atmosphere (oxidation/reduction reactions, sulfur "scumming," etc.)
-

improved slow-fire glaze compositions may reduce color changes resulting from variations in glaze preparation, application and firing conditions. However, there is no published comprehensive or quantitative research on the subject. There is also a great lack of research on fast-fire glaze systems.

Frits are ceramic compositions that have been fused, quenched to form a glass and granulated [Dod94]. They are the primary ingredients in fast-fire ceramic glazes and in most cases are the most reactive and corrosive part of the formula.

Frits for whitewares coatings are classified as either opaque (opacified; containing  $\text{ZrO}_2$ ) or transparent (unopacified; no  $\text{ZrO}_2$ ), and glossy or matte. Besides  $\text{ZrO}_2$ , frits also normally employ  $\text{SiO}_2$  as the primary glass former, alkalis ( $\text{K}_2\text{O}$  and  $\text{Na}_2\text{O}$ ),  $\text{B}_2\text{O}_3$  and  $\text{ZnO}$  or  $\text{SrO}$  as the main fluxes, and other oxides such as  $\text{CaO}$ ,  $\text{Al}_2\text{O}_3$  and  $\text{MgO}$ . These oxides are cost effective, environmentally safe and provide the desired glaze properties. Compositions with  $\text{BaO}$  or  $\text{PbO}$  are avoided because these elements are deemed hazardous by the EPA. There is also an increasing interest in replacing  $\text{ZnO}$  with  $\text{SrO}$  because  $\text{ZnO}$  is classified as a regulated chemical by EPA. Sections 2.2.1-2.2.3 and 2.2.5 detail the

theoretical effects of individual frit oxides on the properties of glasses and ceramic glazes.

High temperature properties of frits influence crystal growth and dissolution rates in glazes. It was observed [Jam85, Dor94] that dissolution and crystallization velocities in multi-oxide glasses are diffusion transport related and inversely proportional to the glass melt viscosity, although no accurate models have been developed. Glass viscosity, in turn, varies with composition and overall has an Arrhenius-type inverse exponential relationship to temperature. Phase changes in the glass resulting from these phenomena alter the optical properties and color.

During fast-fire ceramic processing, a glaze is typically in the molten stage at the peak temperature for only 3 to 5 minutes. The rapid changes in heating and cooling rates create a complex thermodynamic system where phases are often not brought to equilibrium at high temperature. Frit compositions which reduce the sensitivity of crystallization and pigment dissolution to processing variations would be beneficial for color control. The "ideal" frit would preserve the pigment and precipitate the same quantity and morphology of desired crystalline phases over a wide range of firing conditions. The frit should also

produce a coating with enough opacity to hide the substrate without significantly concealing the pigment and achieve the desired surface gloss without defects. Currently, it is not known if zircon pigments dissolve during fast-fire cycles, and there is uncertainty regarding what phases precipitate.

#### 1.4 Overview of Dissertation Goals

The main goals of this investigation were to

1. Determine if glass frit oxide compositions could be formulated to improve the fired color strength and high-temperature stability of industrial whitewares coatings colored with zircon pigments.
2. Relate the optical properties resulting from zircon-vanadium pigment in a glass matrix to the color perceived.
3. Quantify the influence of individual frit oxides, pigment loading and peak firing temperature on a coating's color.
4. Correlate the evolution of the coating's structure and properties to the original frit oxide composition and the fired color.

5. Ascertain whether frit melt viscosity data can be applied as an industrial quality control tool for predicting a frits potential for producing strong and/or stable color with zircon pigments.

"Fast-fire" ceramic tile manufacturing constitutes a major portion of the whitewares industry and consumes most of the frit produced in the U.S. This was the chosen processing method for preparing and firing coating samples. Materials selected for the study were eight laboratory-smelted frits and a zircon-vanadium (Zr-V) blue pigment. Oxide compositions of the frits were designed to provide cost effective, environmentally safe formulas and comply with Seger's rules (Section 2.2.2) for ensuring insolubility of the frit and fired coating, and ready fusion at high temperature. The range of oxide contents tested encompassed and exceeded the range normally employed for glossy ceramic tile glazes. Special emphasis was placed on comparing frit compositions with  $ZrO_2$  (opacified) versus no  $ZrO_2$  (unopacified),  $SrO$  versus  $ZnO$  as the secondary flux, and alkali/silica ratios. The  $B_2O_3$  contents were kept low in order to avoid liquid-liquid phase separation. The Zr-V pigment tested was the blue colorant most commonly used in the ceramic tile industry. The results will also be

applicable to other ceramic pigments which utilize the same zircon structure to incorporate colorant metal ions.

Research goals were achieved by performing the following tasks:

1. Each of the eight experimental frits were loaded with four different pigment concentrations of 0%, 0.5%, 2.0% and 5.0% by weight. They were blended with water and a suspending agent to produce 32 different glaze coatings.
2. Coatings were applied to opaque 2"x6" wall tile body substrates using a wet spray method. Samples of each formula were fired to 1000°C, 1050°C and 1100°C peak temperatures using a standard "fast-fire" ceramic tile industrial heating profile. A total of 96 different fired coatings were produced.
3. The spectral reflectance versus wavelength and the gloss of each fired coating were measured. The CIE  $L^*$   $a^*$   $b^*$  color values, pigment absorption factors (K/S), and color differences between tiles fired to 1050°C and 1100°C ( $\Delta E^*$ ) were calculated. Relationships between light absorption by the pigment and color values based on human perception were quantified.

4. Dilatometry and heating microscopy methods were employed to measure the  $T_g$ ,  $T_s$  and melt viscosity versus temperature of coatings batched with 2.0% Zr-V.
5. In coatings batched with 2.0% Zr-V, phase changes and resulting microstructures that formed during firing were identified using x-ray diffraction, scanning electron microscopy and energy dispersive x-ray spectroscopy techniques. Fired coatings were quantitatively analyzed for contents of Zr-V pigment and zircon which precipitated from  $ZrO_2$  and  $SiO_2$  in the frit.
6. Statistical models were derived to predict K/S and  $\Delta E^*$  given the original frit oxide composition, pigment loading and peak firing temperature. An equation was also developed for calculating  $\log \eta$  of the frit with 2.0% Zr-V given the frit oxide composition and temperature.
7. Color strength and stability were correlated to melt viscosity, crystallization and Zr-V pigment dissolution.
8. The mathematical models and experimental observations were related to current scientific literature in order to collate hypotheses which explain the results.



The foundation of materials science and engineering research is to gain a better understanding of relationships between processing, structure and properties of materials. Figure 1.1 summarizes critical steps taken during this research to define the processing-structure-properties relationships of interest. This investigation focused mainly on variables that influence a ceramic coating's color strength and stability.

### 1.5 Guide for Using This Dissertation

The present document is greater in length than most dissertations. The primary objective was not only to unveil valuable information for basic science interests but also to compile a text that could be used as a reference by engineers working in industry. Thus, some sections may be bypassed if only very specific information is desired.

In the Background chapter, Section 2.1 overviews current scientific principles behind (a) materials interactions with light with a focus on ceramics, (b) color perception by the human eye and (c) the most common industrial method for quantifying color and correlating it to human vision. Section 2.2 summarizes current knowledge of the materials, processing, structures and properties of ceramic whitewares

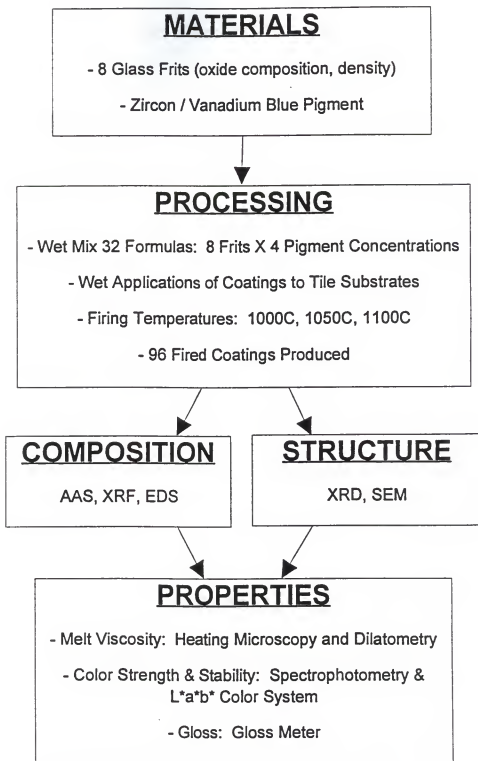


Figure 1.1. Flow chart summary of main research variables.

coatings and their influences on color. A special emphasis is placed on ceramic tile glazes. A review of common frit compositions, ceramic colorants, crystallization, phase separation and melt viscosity relationships is given.

Throughout the Procedure, Results and Discussion chapters, references are made to specific principles and equations outlined in Chapter 2.

Chapter 3 details the experimental procedures applied for the research. This includes descriptions of typical industrial "fast-fire" ceramic glaze frit compositions, wet coating application methods and firing profiles. The two main categories of frits investigated were with and without  $ZrO_2$ . Materials characterization and analytical techniques and procedures typically applied by industry to evaluate whitewares coatings are also reviewed.

Chapter 4 shows the results of the research performed for this dissertation. The particle size distributions, densities and chemical analyses of the starting frits and Zr-V blue pigment are given in Section 4.1. Section 4.2 details the optical properties of each of the 96 fired coatings samples, as indicated by spectral reflectance curves, gloss measurements and calculated color values of  $L^*$ ,  $a^*$ ,  $b^*$ ,  $K/S$  and  $\Delta E^*_{1050-1100^\circ C}$ . Section 4.3 reveals the

viscosity versus temperature profiles, heating microscope images and dilatometric data for coatings loaded with 2.0% Zr-V. Statistical models for predicting color strength (K/S), color stability ( $\Delta E^*_{1050-1100^\circ\text{C}}$ ) and melt viscosity as a function of the frit oxide composition and firing temperature are given in Section 4.4. These equations provide a method for engineers in the whitewares industry to estimate the potential color strength, color stability and melt viscosity resulting from various frit compositions when utilizing a typical "fast-fire" heating profile. If the reader is only interested in specifying frit compositions to obtain certain color or viscosity results but is not concerned with the crystallization or pigment dissolution processes responsible for the optical properties, then it is not necessary to read Sections 4.5 and 5.1.

Section 4.5 details the structures, compositions and morphologies of crystalline species that precipitated in the coatings during firing. An analysis for zircon present in the coatings quantifies the amount of zircon precipitation from fritted  $\text{SiO}_2$  and  $\text{ZrO}_2$ , and Zr-V pigment dissolution that occurred during firing. Results from XRD, SEM and EDS analyses are shown.

In Chapter 5, the Discussion, relationships are established between color strength and stability, specific oxides in the glass frit, Zr-V loading, crystallization, Zr-V dissolution and melt viscosity. Scientific explanations for observed phenomena are proposed. The Discussion focuses on basic science interests, although Section 5.2.2 is also noteworthy for engineers in industry. It correlates important characteristics of a coating's  $\log \eta$  versus temperature plot to the color strength and stability.

## CHAPTER 2 BACKGROUND

### 2.1 Color Theory

The color of an object is its most apparent attribute. Other properties such as gloss and opacity also contribute to appearance.

Color is a term that can be used to describe the reflection or transmission of light in visible wavelengths, the properties of an object and the perception of the eye.

As one pioneer of color science, Dean B. Judd, stated [Nas83],

Color is that aspect of the appearance of objects and lights which depends upon the spectral composition of the radiant energy reaching the retina of the eye and upon its temporal and spatial distribution thereon. (p. 3)

Thus, in order to understand color, we must consider the three elements involved with the production of color: the light source, the physical modifications of light by matter and the human eye as a color sensor. Various units typically applied to quantify light and color are listed in Appendix A along with essential conversion factors.

### 2.1.1 Light and the Visible Spectrum

Light is the visible radiant energy which interacts with matter to produce what our eyes detect as color. It is an electromagnetic wave that propagates as electric and magnetic fields. Maxwell's theory [Hal86] predicted the existence of a spectrum of electromagnetic waves differing only in wavelength and traveling through space in a vacuum with a speed of  $c = 3 \times 10^8$  m/s. Electromagnetic waves other than light include radio waves, microwaves and x-rays.

The energy of a light wave is quantized into small bundles called photons. According to Einstein, the energy (E) of a photon is [Tip80]

$$E = hf = h \frac{c}{\lambda} \quad (2.1)$$

where  $h = 6.63 \times 10^{-34}$  J-sec is Planck's constant,  $f$  is its frequency and  $\lambda$  the wavelength.

Other photonic relationships frequently applied are [Hum93]

$$E = mc^2 = \frac{p^2}{2m} \quad (2.2)$$

$$p = mc \quad (2.3)$$

$$\lambda p = h \quad (2.4)$$

where  $m$  is the mass of a particle and  $p$  is its momentum.

These equations allow us to contemplate a photon or light as

either a particle of energy  $E$  or a wave with a characteristic frequency and wavelength.

The wave-particle duality of light can be described mathematically by considering two harmonic waves with slightly different frequencies which contain time and space dependent components [Hum93]:

$$\Psi_1 = \sin [kx - \omega t] \quad (2.5)$$

and

$$\Psi_2 = \sin [(k + \Delta k)x - (\omega + \Delta \omega)t] \quad (2.6)$$

$$\text{where } k = \frac{2\pi}{\lambda} = \text{the wave number} \quad (2.7)$$

$$\omega = 2\pi f = \text{angular frequency} \quad (2.8)$$

Superposition of  $\Psi_1$  and  $\Psi_2$  and considering  $\sin \alpha + \sin \beta = 2 \cos \frac{1}{2}(\alpha - \beta) \cdot \sin(\alpha + \beta)$  yield a new wave [Hum93]:

$$\begin{aligned} \Psi &= \Psi_1 + \Psi_2 = \\ 2 \cos \left( \frac{\Delta \omega}{2} t - \frac{\Delta k}{2} x \right) &\cdot \sin \left[ \left( k + \frac{\Delta k}{2} \right) x - \left( \omega + \frac{\Delta \omega}{2} \right) t \right] \end{aligned} \quad (2.9)$$

In (2.9), if  $\Delta \omega = 0$  and  $\Delta k = 0$ , a monochromatic wave results of the form

$$\Psi = 2 \sin (kx - \omega t) \quad (2.10)$$

Equation (2.10) illustrates the wave characteristics of photons.



If  $\Delta\omega$  and  $\Delta k$  are very large, the cosine part of (2.9) modulates the amplitude of the wave, resulting in a string of wave packets. If many waves are considered with frequencies ranging between  $\omega$  and  $\Delta\omega$ , one wave packet results and the photon can be depicted as a particle. A better intuitive understanding of materials interactions with light can be achieved by noting light's wave and particle characteristics.

The color of light is related to its energy and thus its frequency or wavelength. As shown on the electromagnetic spectrum in Figure 2.1 [Hun87], visible light falls in a range of 380 nm to 760 nm in wavelength. White light is comprised of all the visible wavelengths.

Light can be produced by heating objects to incandescence, or by exciting atoms or molecules with other forms of energy.

Incandescent sources are applied to produce light with a wavelength energy distribution similar to daylight (Figure 2.2) [Bil67]. When a material is heated to incandescence, the increased vibration of its atoms results in kinetic energy that is sufficient to excite electrons to higher energy levels. Photons are released when the electrons drop back to their normal energy levels. As atom vibrations become more energetic, the frequency and energy of emitted

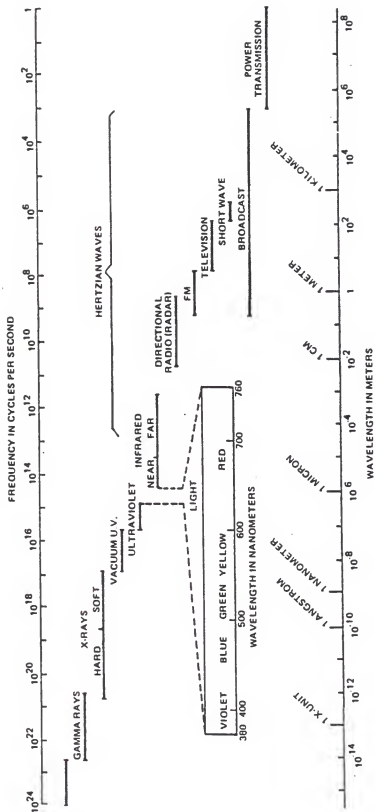


Figure 2.1. Electromagnetic spectrum. [Adapted from Hun87]

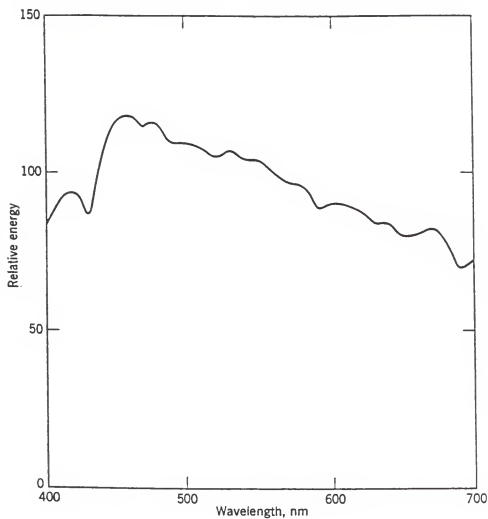


Figure 2.2. Wavelength vs. energy distribution of daylight. [Adapted from Bil67] (Note: Relative energy distribution plots set the energy at 555 nm equal to 100, and the rest of the curve is relative to the distribution radiated from the source.)

light increases. The color of light produced changes from red at low temperatures to nearly white at higher temperatures.

The correlated color temperature of an incandescent source is defined by the temperature at which a black body would operate to produce a visual color match with the incandescent source [Hun87]. The color of a real black body depends only on its temperature, not its composition. According to Wien's displacement law [Wea79], the product of the absolute temperature of a radiating black body and the wavelength corresponding to the maximum energy is a constant:

$$\lambda_{\max} T = W \quad (2.11)$$

where  $W$  = Wien's displacement constant.

A common incandescent light source which operates at a high enough temperature to emit a spectrum close to daylight involves heating a tungsten filament enclosed in an evacuated fused silica bulb. Tungsten filaments are close approximations to black bodies. Some tungsten filament lamps used for light sources in color measurement devices incorporate glass filters to provide a more accurate match to the daylight spectral energy distribution.

Light can also be generated from luminescence or outer electron shell interactions in fluorescent and phosphorescent

materials [Ask94]. In luminescence, kinetic heat energy is not essential for the mechanism of excitation. Luminescence occurs when light has sufficient energy to excite valence band electrons through the energy gap and into the conduction band. When the electrons eventually fall back to the valence band, photons are emitted. If the photon energy corresponds to wavelengths between 380 nm-760 nm, visible light is produced. In fluorescent materials, photon wavelengths can be calculated with

$$\lambda = \frac{hc}{E_g} \quad (2.12)$$

where  $E_g$  is the energy gap. Fluorescent lamps are electrically excited to produce light. Normally with such light, the spectral energy distribution is not as continuous as with incandescent sources. Spectral lines are typically narrow at specific wavelengths. In order to broaden the spectral curve, sometimes more than one source is used in combination. For example, in common household fluorescent lamps, a spectrum from mercury vapor, electrically stimulated inside the bulb, interacts with fluorescent powder on the inside of the glass tube to generate a "cool white" light. It is common to use from one to several light sources acting

in combination as illuminates in color measurement devices such as spectrophotometers [ Bil67] .

### 2.1.2 Materials Interactions with Light

Properties of a material that influence its appearance include index of refraction, gloss, translucency, reflectivity, transparency, absorption and color. These properties result primarily from the interaction between light and a material's electronic structure and microstructure. When photons interact with a material, they are either attenuated (reflected or absorbed) or transmitted. As photons enter a material, their speed will also change, resulting in refraction. Light may be partially reflected, absorbed, or transmitted as related to the incoming beam intensity [  $I_o$  ] by [ Ask94]

$$I_o = I_r + I_a + I_t \quad (2.13)$$

where  $I_r$ ,  $I_a$  and  $I_t$  are portions of the incident beam that is reflected, absorbed and transmitted, respectively. The combination of wavelengths of light reflected from an opaque material or reflected and/or transmitted from a nonopaque material produce its color.

### 2.1.2a Refraction

The refraction of light by a material is estimated by Snell's law [Che83]:

$$\frac{\sin \theta_i}{\sin \theta_t} = \frac{n_t}{n_i} = n_{21} \quad (2.14)$$

where

$\theta_i$  = angle of incidence from the line normal to the irradiated surface.

$\theta_t$  = angle of transmission from the same plane.

$n_t$  = index of refraction of material.

$n_i$  = index of refraction of medium.

$n_{21}$  = relative index of refraction of material to medium.

Normally,  $n$  is used as the notation for index of refraction if the medium is air or a vacuum. Snell's law can be derived from Fermat's principle [Tip80]:

The path taken by light in traveling from one point to another is such that the time of travel is a minimum compared with nearby paths. (p. 612)

When light passes from air into a denser material, its velocity decreases. Following Fermat's principle, light will minimize its travel time by increasing its optical path length in air relative to the path length in the denser material. This results in a change in  $\theta_i$ ,  $\theta_t$  and  $n$ . Thus,  $n$

is related to the velocity and wavelength of light, which is given by

$$n = \frac{c}{v} = \frac{\lambda_{\text{air}}}{\lambda_{\text{material}}} \quad (2.15)$$

where  $v$  and  $\lambda_{\text{material}}$  are the velocity and wavelength of light passing through a material and  $\lambda_{\text{air}}$  is the wavelength of incident light in air.

At a constant wavelength of incoming light,  $n$  tends to increase for denser materials. When comparing values for ceramic vs. polymeric (teflon and polystyrene) materials in Table 2.1 [Wea79], it becomes evident that the structure of a material also influences  $n$ .

If a material is easily polarized, there are increased interactions of its electronic structure with incident photons. In dielectrics such as ceramics, the index of refraction is related to the relative dielectric constant ( $K'$ ) by [Kin76]

$$n = \sqrt{K' + K_1^2} \quad (2.16)$$

where  $K_1$  is the index of absorption.

Polarization ( $P$ ) of the electron cloud around an atomic nucleus is proportional to the electric field strength ( $E$ ) of the incoming light:

$$P = N \alpha E \quad (2.17)$$



Table 2.1. Index of Refraction of Selected Materials  
at 589 nm Wavelength in Air [Wea79] .

Material	Density (g/cm <sup>3</sup> )	Mean Refractive Index (n)
Water	1.0	1.33
Polystyrene	1.06	1.60
SiO <sub>2</sub> (glass)	1.41-1.46	1.46
Teflon	2.17	1.35
Silicon	2.33	3.49
SiO <sub>2</sub> (quartz)	2.64-2.66	1.55
CaCO <sub>3</sub>	2.93	1.60
Diamond	3.51	2.41
$\alpha$ Al <sub>2</sub> O <sub>3</sub>	3.97	1.77
Fe <sub>2</sub> O <sub>3</sub> (hematite)	5.24	2.95

where  $\alpha$  is the average dipole moment per unit field strength or the polarizability and  $N$  is the number of material particles per unit volume.

By the Lorentz-Lorentz equation, electronic polarization is linked to the refractive index of a monatomic gas:

$$\alpha = \frac{3 \epsilon_0}{N_0} n_{\infty}^2 \quad (2.18)$$

where  $\epsilon_0$  is the dielectric constant in a vacuum,  $N_0$  is avagadro's number, and  $n_{\infty}$  is the molar refractivity. The molar refractivity  $n_{\infty}$  is determined by measuring  $n$  at various wavelengths of light as shown in Figure 2.3 and then extrapolating to infinite wavelength.

Since the electron density is uniform within an atomic radius ( $r_0$ ), polarizability is also related to the atomic volume of a material:

$$\alpha \approx r_0^3 \quad (2.19)$$

Equation (2.19) shows that larger atoms, which contain more electrons, exhibit greater polarizability and thus tend to have a higher refractive index.

Ionic charge also plays an important role in influencing the index of refraction. As the ionic charge becomes increasingly negative, outer electrons are more loosely bound and can increase polarizability. In addition, the refractive index is dependent upon crystal structure symmetry, except in

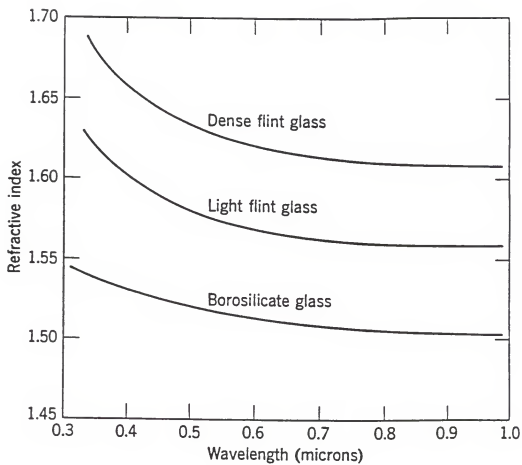


Figure 2.3. Refractive index vs. wavelength of incident light for three glasses. [Adapted from Kin76]

glasses and cubic crystals which are isotropic. Crystals have a higher index of refraction in denser, close-packed directions. For anisotropic substances, the mean index of refraction is estimated as [ Par73]

$$n = \frac{\alpha + \beta + \gamma}{3} \quad (2.20)$$

where  $\alpha$ ,  $\beta$  and  $\gamma$  are refractive indices of the principle crystallographic directions.

Multiphase crystalline and glassy substances have specific refractive energies that are the sum of the refractive energies of their components [ Par73] :

$$\frac{n-1}{\rho} = K_r \quad (2.21)$$

and

$$K_r = k_1 \frac{p_1}{100} + k_2 \frac{p_2}{100} + \dots \quad (2.22)$$

where

$K_r$  = specific refractive energy of a substance.

$n$  = mean index of refraction of a substance.

$\rho$  = density of a substance.

$k_1, k_2 \dots$  = specific refractive energies of the components.

$p_1, p_2 \dots$  = weight percentages of the components.

Reference values for specific refractive energies of oxides can be used to estimate the refractive indices of glasses, glazes and crystalline species.

#### 2.1.2b Surface Reflection and Gloss

When a beam of light strikes a material, a portion of the photons may be reflected. The light reflected at an angle equal to the incident angle is referred to as *specular* reflection (Figure 2.4). This "mirror-like" scattering occurs at one angle from the point of reflection on a smooth, nonmetallic surface. If the surface has some roughness, some light may be scattered at all angles from the point of reflection. This *diffuse* reflection is common in ceramics where surfaces are not normally perfectly smooth. The total reflectivity is the fraction of incident light specularly and diffusely reflected. The *gloss* of a surface is related to the relative amounts of specular and diffuse reflections. It can be defined as the degree of approach to a mirror surface. A perfect mirror surface has a maximum gloss and reflects all visible light. This surface itself is invisible and has no apparent microstructure.

Within the visible spectrum, the reflectivity ( $R$ ) from a perfectly smooth surface in an air medium is the fraction of

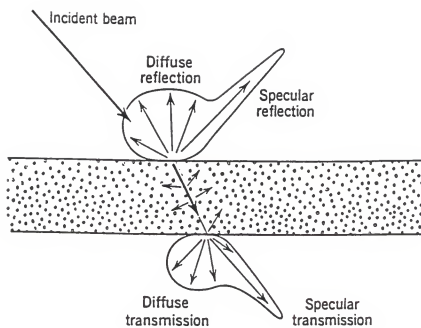


Figure 2.4. Reflection and transmission of light by a glassy material containing suspended particles. [Adapted from Kin76]

incident light reflected at an angle equal to the incident angle. This fraction of specular reflectance from normal incidence ( $\theta_i=0$ ) is calculated for the optical region of the spectrum with Fresnel's formula [Kin76]:

$$R = \left( \frac{n-1}{n+1} \right)^2 \quad (2.23)$$

Equation (2.22) shows that materials with a high index of refraction have a high reflectivity. Since the index of refraction varies with the wavelength of light, so does  $R$ .

From Fresnel's law, equations can be written to compare the reflectivity of plane polarized light so oriented to a plane mirror surface that its reflection (ratio of reflected to incident flux) is most facilitated ( $R_{\parallel}$ ) or most hindered ( $R_{\perp}$ ) in an air medium [Jud65]:

$$R_{\parallel} = \left( \frac{\cos \theta_i - \sqrt{n^2 - \sin^2 \theta_i}}{\cos \theta_i + \sqrt{n^2 - \sin^2 \theta_i}} \right)^2 \quad (2.24)$$

and

$$R_{\perp} = \left( \frac{n^2 \cos \theta_i - \sqrt{n^2 - \sin^2 \theta_i}}{n^2 \cos \theta_i + \sqrt{n^2 - \sin^2 \theta_i}} \right)^2 \quad (2.25)$$

where  $\theta_i$  is the angle of incidence.

For unpolarized incident light, the total reflectivity ( $R_T$ ) is the average of  $R_{\parallel}$  and  $R_{\perp}$ :

$$R_T = (R_i + R_\perp) / 2 \quad (2.26)$$

Thus, the reflectivity,  $R_T$ , for unpolarized light is the average of reflectivities for plane polarized light in ( $R$ ) and perpendicular to ( $R_\perp$ ) the plane of the incident beam. If  $\theta_i = 0^\circ$ , the incident beam is perpendicular to the surface and perfect mirror specular reflection results. In this case, equations (2.24) and (2.25) reduce to equation (2.23) ( $R_T = R$ ). If  $\theta_i = 90^\circ$ , only grazing incidence occurs and  $R = R_\perp = R_T = 1$ . Between perpendicular and grazing incidence,  $R_i$ ,  $R_\perp$  and  $R_T$  vary.

For a perfect mirror surface  $R_i = R_\perp = R_T = 1.0$  regardless of  $\theta_i$ . For real colorant layers with a glossy medium, mirror reflectance approaches unity with grazing incidence as  $\theta_i \rightarrow 90^\circ$ . In this case, the incident beam contacts only that part of the colorant layer which is just below the surface. This is the high-gloss transparent medium carrying suspended pigment particles.

Figure 2.5(a) shows the relationship between  $R_i$ ,  $R_\perp$  and  $R_T$  for  $\theta_i$  from  $5^\circ$  to  $90^\circ$  for an air/glass boundary where the refractive index of the glass is 1.5. Figure 2.5(b) plots total reflectivity as a function of  $\theta_i$  and index of refraction. Figure 2.5 can be used to estimate the gloss or



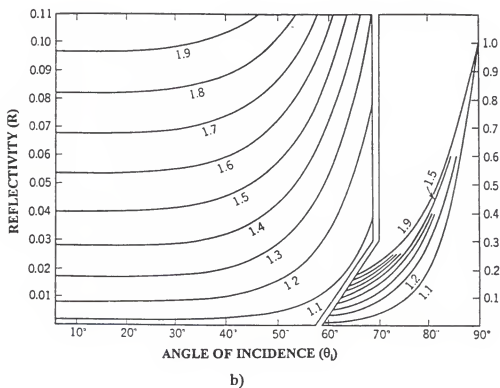
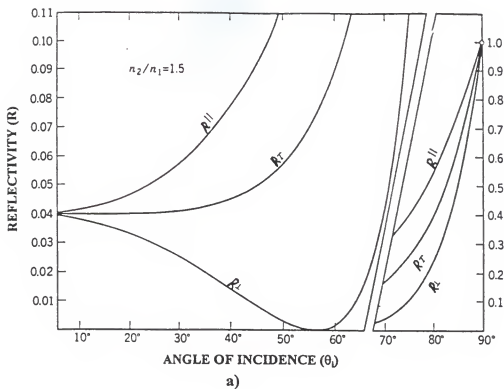


Figure 2.5. Fresnel reflection for a) an air/glass boundary and b) total reflectivity for different index of refraction glasses.

degree of approach to a mirror surface for mediums such as plastics, glass, textile fibers and paint vehicles [Jud65].

Note in Figure 2.5(a) that for a smooth glass with  $n = 1.5$ ,  $R_{\perp} \rightarrow 0$  at  $\theta_i = 56^\circ$ . This follows Brewster's law, which states that mirror reflectance is most facilitated ( $R_{\perp} = 0$ ) when [Jud65]

$$\tan \theta_i = n \quad (2.27)$$

Thus, for a glass of  $n = 1.5$  at incident and viewing angles of approximately  $56^\circ$ , there is a lack of polarized diffusely reflected light. Parallel polarized light in the reflected beam is the only component present from the unpolarized incident light. This principle has been applied to measure gloss through the use of a polarizing element which subtracts the specular component at Brewster's angle where  $R_{\perp} = 0$ .

Brewster's law is also employed to measure the index of refraction of smooth glass [Fle93]. A light polarizer and detector are used to measure the polarization effectiveness of light reflecting from the glass surface. The angle of incidence ( $\theta_i$ ) where reflected polarization is most efficient is applied to calculate  $n$  with equation (2.27).

As the surface roughness of an opaque coating or a glass matrix with suspended colorant particles increases, a greater portion of the reflection becomes diffuse. This broadening

of the reflection band and lowering of the specular intensity tends to lower the gloss. Gloss is greater for smoother, higher index of refraction surfaces. Surface roughness in ceramic glazes caused by crystal structures, defects, interfaces, or a uneven application usually lowers the gloss by increasing the amount of diffuse reflection.

The relative amounts of specular and diffuse reflection, and the gloss of the material, have an effect on the color revealed. For example, glossy paint will appear to lose its color in daylight glare, but "flat" paint will look nearly the same. Most color measurement devices take reflection and gloss into account when generating values for color.

#### 2.1.2c Opacity and Translucency

Subsurface reflections can occur in materials that are not completely opaque. The reflectivity of opaque metals is typically 0.9 to 0.95, where most clear glasses are closer to 0.05 [Ask94].

Optical characteristics of ceramic glazes, glasses and enamels can be developed by modifying their internal reflective and light-scattering properties. Characteristics such as the portion of light specularly reflected (gloss), the portion of light diffusely reflected (opacity), and the

portions of light directly and diffusely transmitted are important (Figure 2.4). These attributes are influenced by the light-scattering properties of phases or small opacifying particles suspended in the glassy matrix. Good opacification is obtained with the high light scattering and reflectivity this mechanism provides.

Common opacifiers used in ceramics coatings include zircon ( $\text{ZrO}_2 \cdot \text{SiO}_2$ ), zirconia ( $\text{ZrO}_2$ ),  $\text{SnO}_2$ ,  $\text{TiO}_2$  and  $\text{Al}_2\text{O}_3$ . They are selected based on their optical properties, the desired coating composition, processing limitations and properties that affect compatibility with the matrix phase such as thermal expansion, solubility, hardness and melting temperature.

Opacifiers can be inert with respect to the host matrix phase, formed during melting, or crystallized from the glass melt. Very fine particles can be obtained from materials such as  $\text{TiO}_2$ , or at higher firing temperatures  $\text{ZrO}_2$ , which can be melted, nucleated and re-crystallized during the heating cycle.

The degree of opacity of ceramics which contain particles suspended in a glassy matrix depends on five main factors [ Par73] :

1. The difference in refractive index between the matrix and dispersed particles. This effect is described by Kerstan:

$$I_r = I_o \frac{(n_2 - n_1)^2}{(n_2 + n_1)^2} \quad (2.28)$$

where

$I_r$  = intensity of diffuse reflected light or intensity of opacification.

$I_o$  = incident beam intensity.

$n_1$  = index of refraction of the glassy matrix.

$n_2$  = index of refraction of the opacifier.

In ceramic coatings, this mechanism provides the greatest influence on opacity. As the difference between the refractive indices of the matrix and particle phases increases, more light scattering and higher opacification is achieved. Generally, glazes and enamels have refractive indices ranging from 1.50 to 1.70 while opacifiers range from 2.0 to 2.8 (Table 2.2) [Ree83].

2. The size of dispersed particles which scatter light.

The light-scattering ability of an optically heterogeneous material can be estimated with the scattering or turbidity coefficient (S). This coefficient is a

Table 2.2. Properties of Materials Used for Opacifying Ceramic Glazes [ Par73] .

Opacifier Material	Mean Index of Refraction (n)	Difference in n: Opacifier-Glaze	Melting Temp. (C)	Coefficient of Expansion $\times 10^7 / ^\circ\text{C}$
$\text{TiO}_2$	2.50	0.95	1,830	88
$\text{ZrO}_2$	2.40	0.85	2,715	70
$\text{ZrO}_2 \cdot \text{SiO}_2$	2.05	0.50	2,430	41
$\text{SnO}_2$	2.04	0.49	1,625	41
Air	1.00	0.55	---	---
Glaze	1.50- 1.70	0	---	---

measurement of the attenuation due to scattering of light as it traverses a medium containing scattering particles

[Kin76]:

$$S = \frac{3}{4} S_f V_p r^{-1} \quad (2.29)$$

and

$$\frac{I_s}{I_o} = \exp \left( -3S_f V_p \frac{x}{4r} \right) = \exp(-Sx) \quad (2.30)$$

where

$S_f$  = scattering factor that varies between 0 and 4.

$V_p$  = volume fraction of scattering particles.

$r$  = radius of the scattering particle.

$I_s/I_o$  = ratio of light intensity scattered/initial intensity.

$x$  = optical path length.

Equation (2.29) shows that scattering, and thus opacity, tends to increase up to a point with decreasing particle size. The scattering constant ( $S_f$ ) increases with particle size ( $r$ ) and is inversely proportional to the fourth power of wavelength for particle sizes much smaller than the wavelength of incident light. When the particle size is approximately equal to the wavelength of light,  $S_f$  reaches its maximum value, then decreases with increasing particle size. Thus, maximum scattering occurs when the opacifier has a

particle size similar to the wavelength of light used, which is in the range of 0.38 to 0.76 microns in diameter for visible light.

3. The number of reflecting particles per unit volume.

Equations (2.29) and (2.30) indicate that opacity increases with the number of particles. As the concentration of opacifier increases, the rate of increase of opacity decreases. Glazes and enamels typically utilize a maximum of 17% zircon by weight for opacification. Approximately 3% to 4% becomes an intermediate part of the amorphous glass structure, while the rest serves as light-scattering particles.

4. Higher opacification is obtained when there is a distinct boundary and steep concentration gradient between the matrix and particle phases.

Diffusion and the consequent reduction in concentration gradient between the matrix and particles results in lower opacification. Opacifier/glass systems with relatively low diffusion coefficients at the required processing temperatures are most effective. Crystals precipitated in a



glass during the heating or cooling cycle tend to have sharp interface boundaries.

5. The thickness of a coating applied to a substrate.

Coating thickness effects on covering power can be related with the Kubelka and Munk equations [Kin76]:

$$R_p = \frac{(1/R_\infty)(R' - R_\infty) - R_\infty \left(R' - \frac{1}{R_\infty}\right) \exp \left[ Sx \left( \frac{1}{R_\infty} - R_\infty \right) \right]}{(R' - R_\infty) - \left(R' - \frac{1}{R_\infty}\right) \exp \left[ Sx \left( \frac{1}{R_\infty} - R_\infty \right) \right]} \quad (2.31)$$

and

$$R_\infty = 1 + \frac{K}{S} - \left( \frac{K^2}{S^2} + \frac{2K}{S} \right)^{1/2} \quad (2.32)$$

where

$R_R$  = coating reflectance.

$R'$  = substrate reflectance.

$R_\infty$  = total reflectivity of a colorant layer so thick that further increases in layer thickness do not change the reflectivity.

$S$  = scattering coefficient

$K$  = absorption coefficient.

$x$  = coating thickness.

Equation (2.31) shows that coating reflectance increases up to a point with thicker applications and higher reflection substrates. Figure 2.6 demonstrates the increase in reflectance with application thickness of a typical  $\text{TiO}_2$  opacified white glaze fired to  $1000^\circ\text{C}$ . The main disadvantages of a thicker coating is the increased material requirements and cost.

Equations (2.31) and (2.32) indicate that opacifiers with a high scattering coefficient ( $S$ ) and low absorption coefficient ( $K$ ) are most powerful. The quantity  $S_x$  is often applied to estimate the scattering power of a coating. Another method gauges opacity with the ratio of reflectance obtained from a coating over a black ( $R' = 0$ ) versus a white ( $R' = 0.89$ ) backing. This is the Tappi Opacity Method for determining the contrast ratio  $C_{0.89} = R'_0/R'_{0.89}$ .

Liquid-liquid phase separation during glass formation is another method by which glaze opacification can occur. For example, the  $\text{Li}_2\text{O} - \text{SiO}_2 - \text{TiO}_2$  system separates at high temperature into a low refractive index silicate glass and a high index titania rich glass [Kim59]. One disadvantage of this mechanism is that it is very sensitive to processing temperature. Therefore, in current manufacturing settings where heating variations during firing are common, the

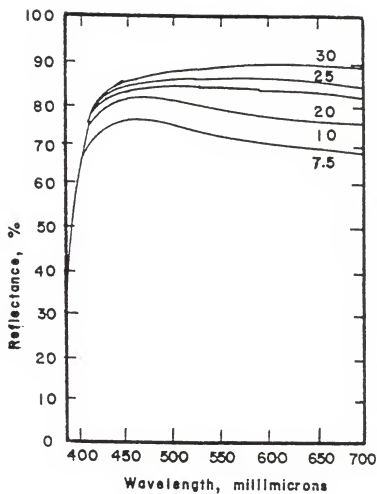


Figure 2.6. Reflectance vs. wavelength of light for a  $\text{TiO}_2$  opacified white glaze fired to  $1000^\circ\text{C}$ , at various glaze application weights in  $\text{g/ft}^2$ . [Adapted from Par73]

relative proportions of glassy phases and opacification would be inconsistent and cause product appearance variations.

If translucent rather than opacified appearances are desired, particles in the glassy phase must create diffuse transmission. Translucency is important for products such as opal glass, where opaque substrates are not utilized. It is most common to achieve translucency by dispersing a particulate phase with a *slightly* different index of refraction than the glassy matrix. Translucency is also often controlled with porosity, where lower pore concentrations (higher material density) or higher pore size at a given concentration increase translucency.

#### 2.1.2d Absorption, Transmission and Color

Light that is not reflected or transmitted by a material is absorbed. The linear absorption coefficient (K) indicates the portion of normally incident radiant energy absorbed through a unit distance (x) in a single phase material by [Wea79]

$$T = \frac{I_t}{I_i} = \exp(-Kx) \quad (2.33)$$

where

T = fraction of light transmitted as it passes through a material.

$I_t/I_i$  = transmitted intensity of light/initial intensity  
of beam after reflection.

In the *Raleigh* scattering mechanism of absorption, photons are deflected from electrons orbiting an atom without any change in energy. This mechanism is more common for high atomic number atoms and low photon energies [Ask94]. If an electron is ejected from an atom, consuming some of the photon energy, this is referred to as *Compton* scattering. *Resonance* occurs when the frequency of material oscillations is close to the frequency of incident radiation, which results in the absorption of radiation.

If incident light stimulates electrons to change their energy level, the photons are absorbed and the material is opaque to this particular wavelength of light. Because there is no energy gap in metals, electron movement into higher energy levels occurs at almost any photon energy. Therefore, metals have a high absorption coefficient and are opaque to most wavelengths of electromagnetic radiation.

The energy gap in semiconductors is greater than metals and smaller than insulators. Semiconductors with small band gaps can transmit photons with energies below the energy gap  $E_g$  or become opaque and absorb photons of higher energy. For

example, at 300 K, Si has a gap energy of 1.12 eV, while diamond has a gap energy of 5.47 eV [Hum93]. Therefore, silicon requires less energy for electron transitions and appears opaque in daylight, while pure diamond is transparent. In the visible spectrum,  $E_g \geq 3.1$  eV materials do not absorb any photons, where  $E_g \leq 1.8$  eV materials absorb all visible light [Ask94]. For intermediate energy gaps, a fraction of the incident visible light is absorbed.

In ionic ceramics, filled shells of tightly bound electrons do not have energy levels available for electron movement [Ric92], and most single crystals are transparent. Covalent ceramics, however, vary in the level of absorption. For example, diamond and graphite both have covalently bonded carbon atoms, but their optical properties are significantly different. Diamond is transparent while graphite appears black. Although there is a strong covalent bonding within the graphite hexagonal network, weak Vander Waal's bonding between the layers allows for electron movement. This results in electron transitions and absorption of visible light. Good insulators with a large  $E_g$  such as diamond tend to transmit light.

Absorption due to electron transitions and resonance is intrinsic, while extrinsic effects in ceramics can also cause

absorption and color. Extrinsic effects include grain boundaries, pores, inclusions, anisotropy and atom vacancies.

In ceramics, the absorption coefficient ( $K$ ) is related to the index of absorption ( $k_i$ ) (also referred to as the attenuation index or extinction coefficient) by [Kin76]

$$K = 4\pi k_i / \lambda \quad (2.34)$$

From equations (2.15), (2.16) and (2.34),  $K$  increases with  $k_i$  and the index of refraction of a ceramic material and decreases with higher wavelengths of incident light.

The overall fraction of light transmitted ( $T'$ ) after both reflectance and absorption losses is

$$T' = \frac{I_t}{I_o} = (1-R)^2 \exp(-Kx) \quad (2.35)$$

where  $R$  is the reflectivity and  $I_t/I_o$  is the ratio of transmitted to incident light intensities. By equations (2.13), (2.23), (2.28) and (2.35), all of the incoming light can be accounted for by reflection, absorption and transmission.

Total light interaction with a material can thus be written [Ask94]

$$I_{rf} = I_o R \quad (2.36)$$

$$I_a = (I_o - I_{rf}) - [I_o (1-R) \exp(-Kx)] \quad (2.37)$$

$$I_{tb} = I_o R (1-R) \exp(-Kx) \quad (2.38)$$

$$I_t = I_o (1-R)^{-1} \exp(-Kx) \quad (2.39)$$

$$I_o = I_{rf} + I_a + I_{rb} + I_t \quad (2.40)$$

where

$I_{rf}$  = intensity of light reflected at the incident surface.

$I_a$  = intensity of light absorbed by the material.

$I_{rb}$  = intensity of light reflected at the back face.

Color is produced in many materials through selective scattering and absorption of incident light. This selectivity often results from variations in the absorption coefficient with wavelength. Four electron transitions concurrent with this type of absorption are common causes of color [Ric92]:

1. Internal transitions with rare-earth or transition metals or other ions with incomplete inner electron shells.
2. Charge transfer, where electrons are transferred from one ion to another.
3. Electronic transition caused by crystal imperfections.
4. Bad gap transitions found in many semiconducting compounds, as discussed earlier in this section.



Transitions (1), (2) and (3) usually are caused by impurities or defects in a material, while (4) is a bulk property. Often, particles are suspended in a matrix such as a glass to create electronic transitions and color. The absorption coefficient is proportional to the concentration of absorbing ion ( $c$ ), according to Beer's law [Ree83]:

$$T = \exp (-\epsilon cx) \quad (2.41)$$

and

$$K = \epsilon c \quad (2.42)$$

where  $\epsilon$  is the extinction coefficient observed per unit concentration. This is the fundamental law of simple subtractive colorant mixing.

The most commonly used colorant ions are from transition metal compounds or impurities such as V, Cr, Mn, Fe, Co, Ni and Cu shown in Table 2.3 [Ree83]. They provide color in many ceramic bodies, glazes, glasses, minerals, gems, pigments and paints.

Crystal or ligand field theories describe how these elements produce color [Pet72]. Transition metals have unfilled inner orbitals available for the creation of split energy levels for electronic transitions. In "free" ions, orbitals have equal energies but different spatial orientations, as shown in Figure 2.7 for the five d orbitals. But the coordination of negatively charged anions about the

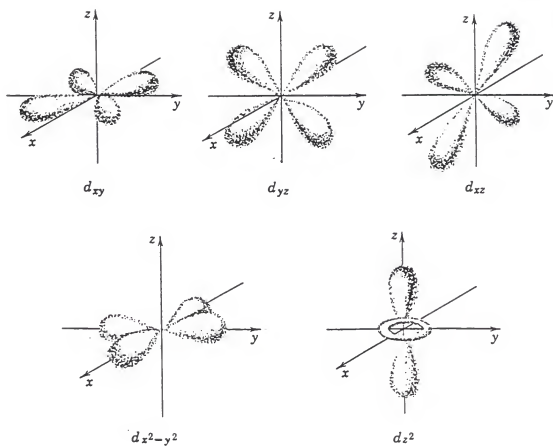


Figure 2.7. The 5 d orbitals. [Adapted from Kin76]

Table 2.3. Transition Elements and Their Properties [Pet72].

	V	Cr	Mn	Fe	Co	Ni	Cu
Atomic number	23	24	25	26	27	28	29
Atomic Radius, Angstroms	1.31	1.25	1.37	1.24	1.25	1.25	1.28
Electronic configuration <sup>1</sup>	3d <sup>3</sup> 4s <sup>2</sup>	3d <sup>5</sup> 4s <sup>1</sup>	3d <sup>5</sup> 4s <sup>2</sup>	3d <sup>6</sup> 4s <sup>2</sup>	3d <sup>7</sup> 4s <sup>2</sup>	3d <sup>8</sup> 4s <sup>2</sup>	3d <sup>10</sup> 4s <sup>1</sup>
Ionization energies <sup>2</sup>							
First	155	156	171	182	181	176	
Second	338	334	361	373	393	418	
Third	676	713	777	706	772	810	
Oxidation potential <sup>3</sup>	+1.2	+0.91	+1.18	+0.44	+0.28	+0.25	-0.34
Oxidation States <sup>4</sup>	2, 3, 4, 5	2, 3, 6	2, 3, 4, 7	2, 3	2, 3	2	1, 2
Melting point, °C	1710	1930	1220	1535	1495	1455	1083
Density, g/cc	5.96	7.20	7.20	7.86	8.9	8.90	8.92
Hardness <sup>5</sup>	---	9.0	5.0	4.5	---	---	2.5-3.0
Electrical conductivity <sup>6</sup>	---	62	32	16	17	24	96

<sup>1</sup>Each atom has an argon inner core configuration.<sup>2</sup>Values are in kcal/mole.<sup>3</sup>For the oxidation process:  $M(s) = M^{2+}(aq) + 2e^{-}$ .<sup>4</sup>Common oxidation states; the most stable one is italic.<sup>5</sup>Hardness values are on the Mohs scale.<sup>6</sup>Compared to an arbitrarily assigned value of 100 for silver.

metal cation produces an electrostatic field that raises inner orbital energies nonuniformly. This electrostatic interaction between anions and metal ion's electron clouds splits inner d or f orbitals into different energy levels. The energy and corresponding wavelength of light absorbed by the metal which produces color is equal to the difference in the split energy levels.

For example, in a tetrahedral structure surrounding a metal ion with unfilled d orbitals, the  $d_{xy}$ ,  $d_{xz}$  and  $d_{yz}$  orbitals have more energy than the  $d_{x^2-y^2}$  and  $d_{z^2}$  orbitals. Color-producing transitions are allowed between these two split groups, and the wavelengths of light absorbed depend upon the magnitude of the splitting. Thus, only a limited range of colors can be produced by any given ion.

The oxidation state of the metal also has an influence on the magnitude of splitting and resulting spectral properties. For example,  $\text{Cu}^+$  is colorless in solution while  $\text{Cu}^{+2}$  has a strong blue color [Pot67]. When the valence of a given element increases (e.g., smaller d occupancy), so does the strength of the ligand field.

This section reviewed the most common causes of color in materials and the method by which color will be derived during the subsequent research involved with this

dissertation. A comprehensive list of all of the possible causes of color are listed in Appendix B.

### 2.1.3 Color Perception by the Human Eye

The eye is the human optical system (Figure 2.8) [Tip80] that allows us to perceive the color, gloss, opacity and dimensions of an object. The eye is sensitive to light between wavelengths of 400 and 700 nanometers.

Light enters the eye through the pupil and is focused by the cornea-lens system on the retina. As the distance of an object from the eye varies, the ciliary muscle changes the lens shape to improve focus of the image on the retina.

The photosensitive parts of the eye are the rods and cones of the retina. These tiny structures receive images and transmit information along the optic nerve to the brain. The size of an image on the retina increases with the number of rods and cones activated, which is proportional to the apparent size of the object being viewed.

Rods respond to very small amounts of radiant energy and, thus, serve for night vision. Rods do not detect hue or chromatic colors but only perceive neutral colors such as white, gray and black.

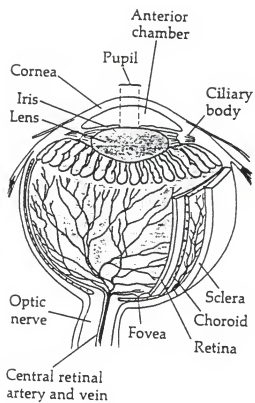


Figure 2.8. Human optical system. [Adapted from Tip80]

On the other hand, cones sense chromatic as well as neutral colors. Cones, which are responsible for day vision, can detect a much higher density of radiant flux than rods but are less sensitive at very low levels of light. Rods respond to minute quantities of light as low as  $10^{-6}$  candelas per square meter ( $\text{cd/m}^2$ ), while cones require at least  $10^{-3}$   $\text{cd/m}^2$  [Jud65].

At illumination commonly referred to as twilight, both rods and cones are active. The approximate range of luminances which correspond to twilight or the mesopic region is from  $10^{-3}$   $\text{cd/m}^2$  to  $10$   $\text{cd/m}^2$  [Jud65]. In this range, color judgments are extremely unreliable because the relative degree of rod and cone vision continually changes. Therefore, color inspections in manufacturing should not be carried out in this condition, although many factories and industrial inspection areas are dimly lit. Luminance at approximately  $10^6$   $\text{cd/m}^2$  is the maximum level where the human eye can perceive color with cone vision.

The eye is not equally sensitive to all wavelengths of light. It has been demonstrated that 555 nm light is viewed more easily than other wavelengths. Figure 2.9 graphically shows the sensitivity or relative response of the human eye at daytime (cone or photopic curve) and nighttime (rod or

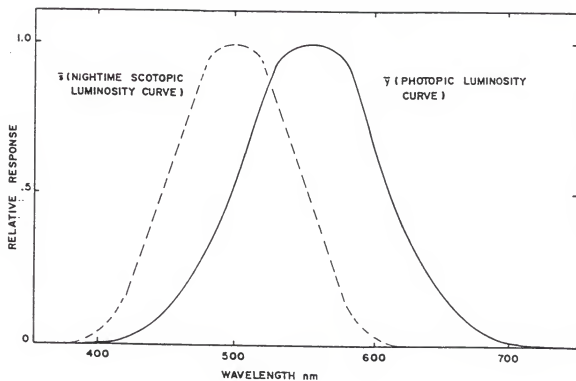


Figure 2.9. Luminosity functions of the rods (nighttime scotopic vision) and cones (daytime photopic vision) of the human eye. [Adapted from Hun87]



scotopic curve) for the same amount of energy at different wavelengths of light in the visible spectrum. The curves were developed from experiments where 52 human observers adjusted the intensity of light at different wavelengths until they appeared equally luminous or bright [Hun87]. The property of light by which we define how easily we can see it is referred to as luminosity.

Both the Young-Helmholtz and Hering experiments of the mid-1800s confirmed that human observers see colors with three spectrally unique receptors which detect black-white, red-green and yellow-blue. Subsequent numeric scales developed for quantifying color contain three values; one for each opponent-color pair.

Color sensory responses of the eye are not linear with the amount of stimulus. For example, there is a logarithmic relationship between the actual light level reflected from an object and its perceived lightness. Color perception is also a function of the light source and directions of illumination and view. For these reasons standardized observation conditions are required for industrial inspection. Even so, differences between individuals are great enough to affect visual color quality control. Most often, human observations are coupled with color measurements performed by machines

such as spectrophotometers in order to make final determinations.

#### 2.1.4 Color Measurement

Color measurement, like human eye perception, depends on the light source, the sample being viewed and the observing apparatus. Properly operated color measurement equipment, however, can provide more repeatable results than subjective human perception. Through a series of calculations, measured colorimetric data can be converted into values that better relate to human vision.

##### 2.1.4a Spectrophotometry

The spectral characteristics of an object determine its perceived color. Spectral characteristics are defined by the reflectance or transmittance of light from a material as a function of its wavelength. Spectrophotometers are used to measure reflectance or transmittance from a sample as a percentage of incident light at each wavelength in the visible spectrum, normally in 0.5 nm increments [Mac91a]. Typically, reflectance is measured for opaque materials and transmittance for transparent materials where the color of light after it passes through a material is important.

Figure 2.10 reveals reflectance curves for opaque coatings colored with pigments which absorb a portion of the incident light [Hun87]. The white coating reflects a high portion of the incident light across the whole visible spectrum while the black coating absorbs most of the light flux over the wavelength range. Colors of blue, green, yellow and red are created through selective absorption and reflection of different light wavelengths by the pigment. For example, the blue coating is shown to absorb primarily yellow to red light (550-700 nm) while reflecting blue (450-550 nm). The color of a ceramic whiteware glaze coating results from this mechanism. Glazes are applied over an opaque white substrate, and the reflectance curve produced is the sum of reflectances from the pigment particles, other crystalline species present, and the white substrate minus specific wavelengths of light absorbed by the pigment colorant. Normally, the background substrate and undoped pigment crystal strongly reflect all visible wavelengths and appear white or light yellow without the light absorbing metal ion incorporated in the pigment. In contrast, the color of light *transmitted* through a nonopaque glass results from the incident beam *minus* both light absorbed by the structure and reflected from the irradiated side.

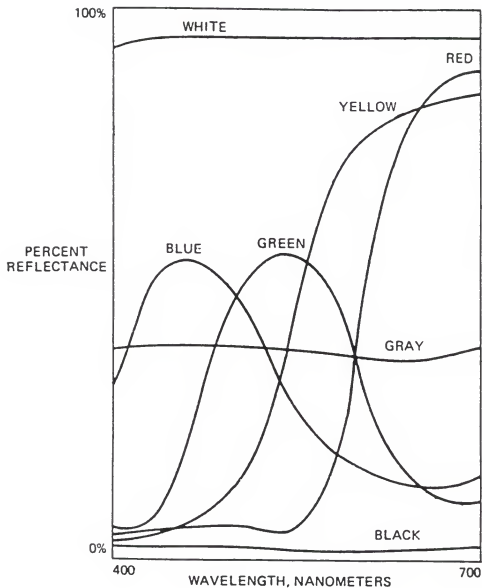


Figure 2.10. Reflectance versus wavelength for opaque coatings colored with pigments that absorb a portion of incident light. [Adapted from Hun87].

The basic components of spectrophotometers are outlined in Figure 2.11. Reflectance factors are measured one wavelength at a time, normally at 0.5 nm increments, by isolating wavelengths with gratings, prisms or interference filters and slits. This is the monochromator device in Figure 2.11 [Hun87]. Current spectrophotometers are similar to original mechanism developed by A. C. Hardy in 1928, shown in Figure 2.12. The position of mirror slit #2 is adjusted for wavelength isolation.

Typical light sources include a tungsten filament lamp or a pulsed xenon bulb, which, in conjunction with a prism, produce white light. Illumination is normally near  $10^3$  cd/m<sup>2</sup> where only cone vision occurs. For accurate color comparisons, the relative energy versus wavelength distribution from the source must exactly match the desired standard, but the total energy or illuminance from the source can range from 10 cd/m<sup>2</sup> to  $10^6$  cd/m<sup>2</sup> where the rods are inactive.

Real light sources are difficult to standardize, and it is often useful to compare the color of objects viewed under various wavelength energy distributions. Normally reflectance values from the real light source are

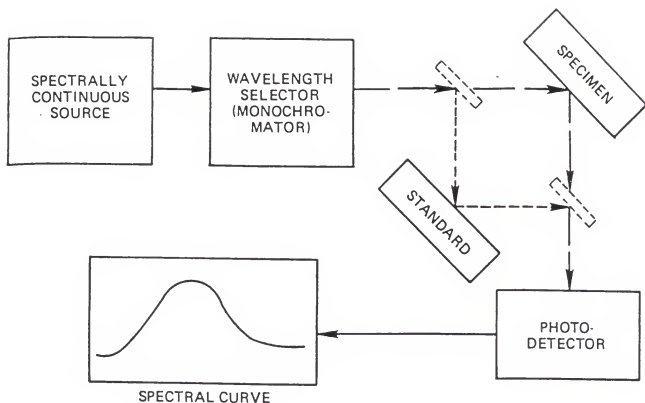


Figure 2.11. Basic components of spectrophotometers.  
[Adapted from Hun87]

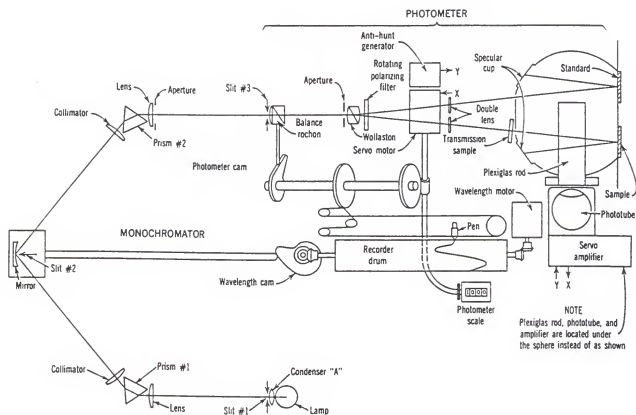


Figure 2.12. Schematic of the Hardy spectrophotometer.  
[Adapted from Bil67]

mathematically converted to represent theoretical sources or illuminants before color values are derived. Outputs from spectrophotometric measurements include color values derived from relative energy distributions of standard light sources such as D65 (average noon daylight from the total sky), illuminant A (incandescent lamp), illuminant B (near sunlight) and illuminant C (average daylight from the total sky).

The standard full visual field of view utilized to detect light reflecting from an object is  $2^\circ$  angular subtense. Occasionally, a  $10^\circ$  observer is used to provide a larger field of view.

Light flux reflected from a sample is collected for measurement by a white-lined integrating sphere. Elimination of surface gloss from the color measurement provides results which better correlate to visual inspection. This can be accomplished by replacing the white plug on the sphere's specular cup with a black plug. Since the specular cup is offset to be illuminated at an angle of reflection equal to the angle of the incident beam, the black plug absorbs primarily specularly reflected light. Diffusely reflected flux is diverted up the sphere to the photodetector. The collected photon energy distribution is converted into an



electrical signal and sent to a computer. The computer program converts measured spectral data into numbers that can be more easily interpreted and correlated to the response of the human eye.

Measurements of gloss can be performed separately with goniophotometers or gloss meters, which measure the spectral reflectance or quantity of light emitted in directions related to the surface characteristics of the object. The gloss of ceramic coatings is normally measured at a  $60^\circ$  angle of incidence, where mirror reflectance is most facilitated, according to Brewster's law (equation 2.27).

#### 2.1.4b Basis for Color Quantification

The average sensitivity of the human eye to each wavelength of light has been determined through extensive experimentation [Bil67, Hun87, Jud65, MacA35, MacA42]. Human observers were asked to visually match the colors of light from individual wavelengths by mixing together lights from three colored primaries. Three primaries were applied because the eye contains three spectrally unique receptors for detecting colors. The amounts of energy of each of the three lights required to match single wavelength colors were used to develop standard observer functions for the basis of

all color measurement. These weighting functions are applied to transform spectrophotometric data into numbers that better correlate to the way the human eye perceives colors.

The weighting functions ( $\bar{x}$ ,  $\bar{y}$  and  $\bar{z}$ ) are plotted in Figure 2.13. Mathematical functions for describing colors obtained by mixing different sets of primary colors have been shown to always be related by a set of linear transformations [Hun87]. Therefore, there was some flexibility for selecting the three standard primaries which provide  $\bar{x}$ ,  $\bar{y}$  and  $\bar{z}$  the most user-friendly set of weighting functions. The curves in Figure 2.13 were derived with the following useful properties:

1. One of the functions, the  $\bar{y}$  curve, was made to equal the photopic plot shown previously in Figure 2.9, which indicates the eye's response to luminosity or color brightness.
2. The areas underneath the three curves were made equal for light of equal energy at all wavelengths.
3. One function was selected to be as near to zero as possible for as much of the spectrum as possible.

In this form  $\bar{x}$ ,  $\bar{y}$  and  $\bar{z}$  do not represent any real colored primaries but can be converted to values that are

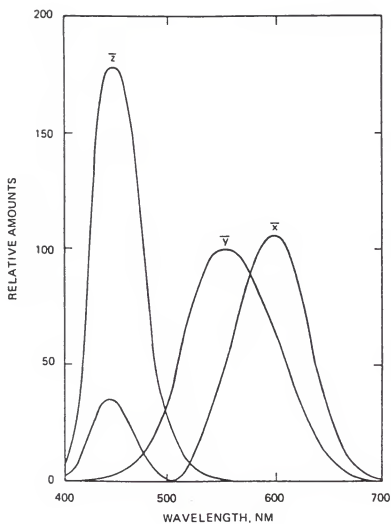


Figure 2.13. Weighting functions used for the standard observer at a 2° field of view. [Adapted from Bil67]

easier to apply. The weighting functions are used to transform spectral reflectance curves into three numbers referred to as tristimulus values, X, Y and Z. These values specify color in terms of the mixture of red (X), green (Y) and blue (Z) primary light that would produce the same color. The Y value also still includes brightness detected. If two materials are found to have the same measured X, Y and Z, they will appear to have the same color under that specific viewing condition.

At any one wavelength,  $X = \bar{x}$ ,  $Y = \bar{y}$  and  $Z = \bar{z}$ . For example, at a wavelength of 450 nm in Figure 2.13, the light detected would consist of proportions 32 : 5 : 175 of red ( $\bar{x}$  or X) : green ( $\bar{y}$  or Y) : blue ( $\bar{z}$  or Z) light. For all wavelengths in the visible spectrum, the contribution of each tristimulus value can be calculated with [Hun87]

$$X = S_{\lambda_1} \bar{x}_{\lambda_1} + S_{\lambda_2} \bar{x}_{\lambda_2} + S_{\lambda_3} \bar{x}_{\lambda_3} + \dots + S_{\lambda_n} \bar{x}_{\lambda_n} \quad (2.43)$$

or

$$X = \int_{400}^{700} S_{\lambda} \bar{x}_{\lambda} d\lambda \quad (2.44)$$

where

$\bar{x}_{\lambda}$  = weighting function ( $\bar{x}$ ) value at  $\lambda$  wavelength.

$S_{\lambda}$  = spectral energy at  $\lambda$  wavelength.

Y ( $\bar{y}$ ) and Z ( $\bar{z}$ ) can be calculated in the same manner as X ( $\bar{x}$ ) with (2.43) and 2.44). The spectral energy, in turn, is a function of the properties of the light source for an illuminate or aperture color ( $S_{\lambda\text{source}}$ ) or the reflectance from a reflecting object ( $S_{\lambda\text{material}}$ ):

$$S_{\lambda\text{source}} = E_{\lambda} \quad (2.45)$$

and

$$S_{\lambda\text{material}} = E_{\lambda} R_{\lambda} \quad (2.46)$$

where

$E_{\lambda}$  = energy of the light source at  $\lambda$  wavelength.

$R_{\lambda}$  = percent reflectance of light of  $\lambda$  wavelength from the material.

Since objects are viewed in relation to their surroundings, X, Y and Z are normally expressed relative to the luminosity of a perfect white opaque material where  $R = 100$ , as

$$X = 100 \frac{\int E_{\lambda} R_{\lambda} \bar{x}_{\lambda} d\lambda}{\int E_{\lambda} \bar{y}_{\lambda} d\lambda} \quad (2.47)$$

$$Y = 100 \frac{\int E_{\lambda} R_{\lambda} \bar{y}_{\lambda} d\lambda}{\int E_{\lambda} \bar{y}_{\lambda} d\lambda} \quad (2.48)$$

$$Z = 100 \frac{\int E_{\lambda} R_{\lambda} \bar{z}_{\lambda} d\lambda}{\int E_{\lambda} \bar{y}_{\lambda} d\lambda} \quad (2.49)$$

Thus, for a perfectly white material, Y is 100 and X and Z vary depending upon the light source.

Trichromatic coefficients (x, y, z) are often calculated from tristimulus values:

$$x = \frac{X}{X + Y + Z} \quad (2.50)$$

$$y = \frac{Y}{X + Y + Z} \quad (2.51)$$

$$z = \frac{Z}{X + Y + Z} \quad (2.52)$$

where  $x + y + z = 1.0$ . The x and y are coefficients used to indicate chromaticity or color, while tristimulus Y is normally kept to represent luminosity. MacAdam in 1935 [MacA35] proposed the first color measurement space with Y, x, y cartesian coordinates.

Most current color measurement systems apply tristimulus values rather than trichromatic coefficients. Tristimulus values are further converted to allow for easier interpretation of color in three-dimensional black-white, red-green and yellow-blue space. Since the tristimulus system was sanctioned by the International Commission on Illumination or CIE in 1931, there have been over 30 three-dimensional color spaces developed through transformations of X, Y and Z values. The best scales provide an approximately

uniform color space where equal distances within the space represent nearly equal visual color differences. The current most commonly used color space in the world is the CIE  $L^*a^*b^*$  scale which was developed in 1976 (Mac96).

#### 2.1.4c CIE $L^*a^*b^*$ Color Measurement Scale

Tristimulus data are converted into scales which, based on visual discrimination experiments, correlate to perceived color differences. Approximately uniform scales have been developed where differences between measured colors throughout the color space are proportional to visual distinction.

Human eye sensitivity for detecting color differences varies across the visible spectrum of wavelengths observed. Visual color discrimination is greatest near 485 nm and 590 nm and least around 425 nm and 650 nm. This is represented in the MacAdam color limits (Y, x, y) diagram in Figure 2.14). The greater the distance between two wavelengths on the perimeter of the plot, the greater the range of colors that can be perceived in the interval. The third dimension indicated in the graph is the Y-value from 0 through 95. Note as the Y-value or lightness increases, the potential

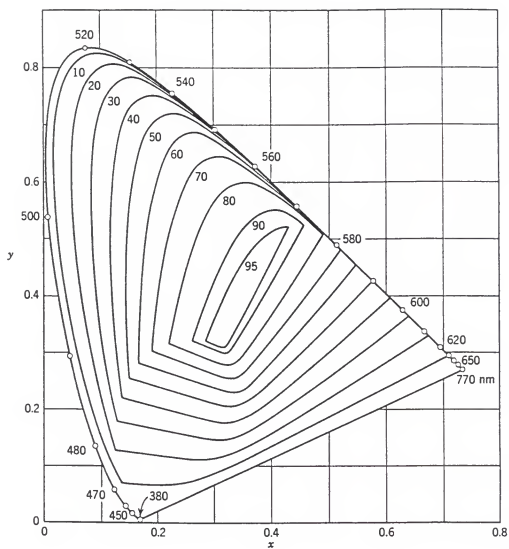


Figure 2.14. Luminosity or lightness ( $Y$ ) and chromaticity ( $x, y$ ) MacAdam limits for colors viewed in daylight.  
 [Adapted from Bil67]



range of colors that can be perceived decreases. This horseshoe-shaped plot exhibits nonuniform color space.

The CIE  $L^*a^*b^*$  scale provides for more equivalent visual distances and easier interpretation than the  $(Y, x, y)$  scale [Jud65, Hun87]. In this uniform system, cartesian coordinates are employed to represent three-dimensional color space as the eye sees color with three spectrally unique receptors. The space is defined by a set of equations which incorporate tristimulus values from equations 2.47, 2.48 and 2.49 [Hun87]:

$$L^* = 116 \left( Y/Y_n \right)^{1/3} - 16 \quad (2.53)$$

$$a^* = 500 \left[ \left( X/X_n \right)^{1/3} - \left( Y/Y_n \right)^{1/3} \right] \quad (2.54)$$

$$b^* = 200 \left[ \left( Y/Y_n \right)^{1/3} - \left( Z/Z_n \right)^{1/3} \right] \quad (2.55)$$

(with constraints of  $Z/X_n, Y/Y_n, Z/Z_n > 0.01$ )

where

$L^*$  = Lightness dimension (0:black to 100:white).

$a^*$  = redness (positive  $a^*$ ) or greenness (negative  $a^*$ ).

$b^*$  = yellowness (positive  $b^*$ ) or blueness (negative  $b^*$ ).

$X_n, Y_n$  and  $Z_n$  = Tristimulus values of a standard reference white object.

The  $X_n$  and  $Z_n$  values vary depending on the illuminant and observer angle, as shown in Table 2.4. Cubed root functions

Table 2.4. Factors for Uniform Color Scales for Normalizing to a Standard Reference White.

Illuminants	2° Observer		10° Observer	
	$X_n$	$Z_n$	$X_n$	$Z_n$
D65	95.021	108.849	94.825	107.399
Cool white fluorescent bulb	98.166	68.073	102.158	69.623
Westinghouse Ultralume	108.354	34.352	111.350	35.352

$Y_n = 100.00$  in all cases for standard white.

in equations (2.53) through (2.55) were found to best equate the logarithmic relationship between actual object lightness (Y) and human perception [San57] as discussed in Section 2.1.3.

Figure 2.15 demonstrates L\*a\*b\* color coordinates. Values for a\* and b\* approach zero for neutral colors such as whites, grays and blacks. The higher the a\* and b\* values, the more saturated the color. For example in ceramic glazes, L\*a\*b\* values can be applied to specify colors such as

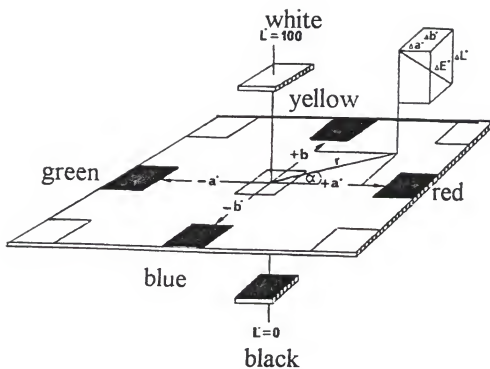
<u>Glaze Color</u>	<u>L*</u>	<u>a*</u>	<u>b*</u>
Light Gray	83.7	-0.5	0.5
Dark Gray	57.0	0.0	0.5
Cr-Sn Red	29.9	22.9	4.8
Co-Cr Green	44.1	-18.0	-9.8
Zr-Pr Yellow	86.9	-8.5	21.5
Co-Si Blue	52.5	6.2	-28.1

The measurement of color difference between two objects using CIE L\*a\*b\* uniform color space is calculated from

$$\Delta E^* = \left[ (L_1^* - L_2^*)^2 + (a_1^* - a_2^*)^2 + (b_1^* - b_2^*)^2 \right]^{1/2} \quad (2.56)$$

where

$\Delta E^*$  = color difference as defined by the magnitude of the position vector between two points in color space, expressed in Judds units.



$$L^* = 116 \cdot (Y/Y_0)^{1/3} - 16$$

$$a^* = 500 \cdot [(X/X_0)^{1/3} - (Y/Y_0)^{1/3}]$$

$$b^* = 200 \cdot [(Y/Y_0)^{1/3} - (Z/Z_0)^{1/3}]$$

Figure 2.15. Schematic of  $L^*a^*b^*$  color space. [Adapted from Mor96]

$L^*_1, L^*_2$  = lightness units of objects 1 and 2.

$a^*_1, a^*_2$  = red-green units of objects 1 and 2.

$b^*_1, b^*_2$  = yellow-blue units of objects 1 and 2.

Experiments by MacAdam [MacA42] with human observers ascertained that a  $\Delta E^*$  of  $\geq 1.0$  Judds represents a noticeable color difference, regardless of the color in question. Since  $\Delta E^*$  represents the magnitude but not the direction of color difference, industry often compares individual values of  $\Delta L^*$ ,  $\Delta a^*$  and  $\Delta b^*$  between two colors. This helps to uncover the best approach for adjusting material formulations to modify colors. Normally  $\Delta E^*$  calculations are confirmed with a visual assessment.

It is customary to specify the color of whiteware glazes using CIE  $L^*a^*b^*$  values [Epp96]. Ceramic tile manufacturers follow American National Standard Institute (ANSI) A137.1 specifications, which stipulate American Standard Test Method (ASTM) C609-90 for measuring small color differences between ceramic tiles [Mur89, Aza97]. ANSI specifies a tolerable color difference of 3.0 Judds for compatible glaze appearances, even though the difference is noticeable by human observers.

Good results of color specification and comparison are achieved from the  $L^*a^*b^*$  system in part because the standard

observer weighting functions and response curves are approximately linear over a short segment.

On the other hand, the  $L^*a^*b^*$  system can provide anomalous results when relating green and red colors to pigment concentration [Epp96]. The  $a^*$  is a function of both  $X(\bar{x})$  and  $Y(\bar{y})$  tristimulus values and corresponding weighting functions (equation 2.54). These curves overlap significantly (Figure 2.13), especially in red (650-680 nm) and green (530-550 nm) wavelength regions. There is also nonlinear correlation between  $X(\bar{x})$  and  $Y(\bar{y})$ , and  $a^*$  is heavily weighed by *both* functions, especially in the red wavelength region. Thus, red and green color is a complex function of both  $L^*$  and  $a^*$ . Cases result where as red or green pigment concentration is increased, the  $L^*$ -value drops but the  $a^*$ -value does not change. This can be misleading when evaluating color strength due to the pigment. The Kubelka-Munk absorption function, described in Section 2.2.4b, is often used to provide a better quantitative correspondence for evaluating red or green colorants. The absorption factor ( $K/S$ ) normally has a linear dependency on pigment concentration.

Conversely, the  $b^*$  value is effective for evaluating blue or yellow color intensity as a function of pigment

concentration. There is very little overlapping of  $\bar{y}$  and  $\bar{z}$  weighting functions (Figure 2.13) in the blue (450-500 nm) and yellow (550-600 nm) light regions. In the small overlapped area, there is a strong inverse negative correlation and  $b^*$  is weighed heavily by either  $\bar{z}$  or  $\bar{y}$ , but not both. Thus, the relative influence of blue and yellow pigments on color intensity in terms of  $b^*$  and lightness  $L^*$  can be easily separated and correlated to visual interpretation.

## 2.2 Color in Ceramic Glazes

Glazes are thin glassy layers formed on the surface of ceramic products by firing an applied coating. They are utilized mainly to improve strength and chemical durability and provide a readily cleanable decorative surface for many products including tile, sanitary ware, dinnerware and electrical porcelain. Glazes are formulated to achieve desired mechanical and optical properties of the final product through careful control of processing parameters. Since ceramic whitewares glazes are normally applied over an opaque white substrate, the color produced is a function of the reflectance of the incoming beam from the pigment and other crystalline species in the glass matrix, plus any

reflectance from the substrate, minus absorption from the metal ion on the doped pigment structure. Ceramic glazes are usually opaque; therefore, reflection by the substrate is insignificant.

The glaze composition and behavior during processing determines the color developed by dissolved metallic atoms or suspended inert pigments. Glass is the major phase present in glazes; therefore, glazes are classified as amorphous or glassy in their physical and chemical nature. Thus, current glass science theories should apply in defining the mechanisms involved with their color development.

The research of this dissertation focuses on the pigment system most widely used in the ceramic tile industry, the doped zircon structure.

### 2.2.1 Silicate Glass Structures and Properties

A glass is an amorphous solid, where no long range order of molecular constituents is observed [Dor94]. Glass is usually formed by rapidly cooling a melt and solidifying materials from the supercooled liquid. The cooling rate must be high enough to avoid the nucleation and growth of crystals. Nucleation and crystallization rates are dependent upon glass composition, viscosity, number of heterogeneous



nucleation sites and temperature. These variables will be further discussed in Section 2.2.5.

Silica is the predominant glass former used in industry. Knowledge of the properties of silicate glasses is essential for formulating glazes and enamels. The silicon-oxygen tetrahedron is the basic structural unit in all silicate glasses. The tetrahedra are linked to each other at the corners to form a three-dimensional random network. This structure has no long-range symmetry or periodicity beyond a few tetrahedra [Ban86]. Directional covalent and ionic bonding in accordance with Pauling's rules promotes the formation of  $(\text{SiO}_4)^{-4}$  structural units [Chi97].

Short range order is identical in crystalline and glassy  $\text{SiO}_2$ , where 4-fold coordination and a O-Si-O bond angle of  $109.5^\circ$  with each tetrahedral unit is present. But connectivity is maintained without crystalline long term order.

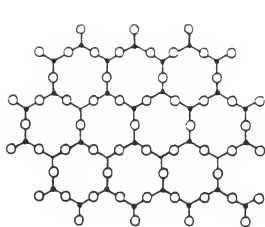
Differences in the medium range order of crystalline and amorphous  $\text{SiO}_2$  include Si-O-Si bond angles and rotational angles between tetrahedra, and the number of Si-O bonds that complete each of the rings. These parameters vary throughout

the glass but are fixed with crystalline  $\text{SiO}_2$ . Figure 2.16 compares crystalline and amorphous phases.

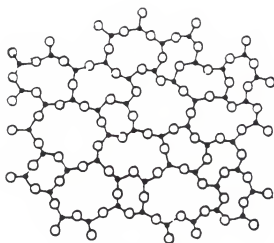
Silicate glasses follow Zachariasen's four rules for the formation of oxide glasses based on a random network [Kin76]:

1. Each oxygen ion should be linked to two or less cations.
2. The coordination number of oxygen ions about the central cation is not more than four.
3. Oxygen polyhedra share corners only.
4. For each polyhedron, at least three corners should be shared.

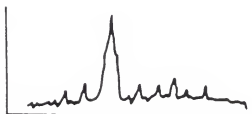
Cations which tend to form oxygen in polyhedra of triangles or tetrahedra are *glass formers*. In multi-oxide silicate glasses, other constituent ions refill the voids left by silicon and oxygen. These network *modifiers*, such as the alkalis, provide additional oxygen and occupy random positions to furnish local charge neutrality. Modifiers tend to break up the network structure and often cause the glass to crystallize or devitrify. *Intermediates* are cations of higher valence and lower coordination number than modifiers. They do not form a glass by themselves but may be incorporated in part into the network structure.



CRYSTAL STRUCTURE



VITREOUS STRUCTURE



SPECTRUM OF A CRYSTALLIZED BODY



SPECTRUM OF AN AMORPHOUS BODY

Figure 2.16. Comparison of structures and XRD patterns of crystalline and vitreous silica. [Sac86]

Table 2.5 lists glass formers, intermediates and modifiers. Most glass formers tend to have a high ionic potential ( $>7.0$ ) which is indicative of a strong bond with oxygen, while modifiers have a low ionic potential. In multi-oxide glasses, substitutions of cations with higher ionic potentials (e.g., alkaline earths for alkalis) tends to increase strength, durability, melting temperature, and viscosity. Ions such as Al, Zn, Zr and Pb are listed in more than one category in Table 2.5. Diezel [Sac86] hypothesized that a cation's capacity for forming, modifying or acting as an intermediate depends on its single-bond strength with oxygen relative to the other cations in the structure. Thus, as the coordinative force towards bonding with oxygen changes, the role of the cation transforms. Glass formers have the highest bond strength with oxygen while modifiers have the lowest.

Another convenient way to describe the network character of silicate glasses is with  $R$  [Kin76]

$$R = \frac{(\text{sum of oxygen atoms})}{(\text{sum of network forming ions})} \quad (2.57)$$

For example, given a formula of 80 g-atom %  $\text{SiO}_2$ , 10 g-atom %  $\text{Na}_2\text{O}$  and 10 g-atom %  $\text{CaO}$ ,

Table 2.5. Glass Formers, Intermediates and Modifiers Commonly Employed in Whiteware Glazes [Sha92, Chi97].

M in MO <sub>x</sub>	Valence	Ionic Potential*	Coordination Number	Dissociation Energy per MO <sub>x</sub> (kcal/mole)	Single Bond Strength (kcal/mole)
<u>Glass Formers</u>					
Si	4	10.3	4	424	106
B	3	15.0	3	356	119
B	3	15.0	4	356	89
V	5	12.5	4	449	90-112
Al	3	5.3	4	317-402	108
Zr	4	4.6	6	485	81
<u>Intermediates</u>					
Ti	4	6.3	6	435	73
Al	3	5.3	6	317-402	53-67
Zr	4	4.6	8	485	61
Zn	2	2.4	2	144	72
Pb	2	1.5	2	145	73
<u>Modifiers</u>					
Mg	2	2.6	6	222	37
Zn	2	2.4	4	144	36
Ca	2	1.9	8	257	32
Sr	2	1.6	8	256	32
Ba	2	1.5	8	260	33
Li	1	1.3	4	144	36
Na	1	1.0	6	120	20
K	1	0.8	9	115	13
Pb	4	4.3	6	232	39
Pb	2	1.5	4	145	36

\*Ionic Potential = valence/radius (Å)

The ionic potential indicates the importance of charge and space relationships.

$$R = \frac{(80 \times 2) + 10 + 10}{80} = 2.25$$

Glazes and enamels normally are in the range of  $R = 2.25$  to 2.75. As  $R$  increases, a greater number of oxygen are single-bonded which weakens the glass structure and lowers the melting temperature and viscosity.

For glasses with only one type of glass forming ion,

$$X + Y = Z \quad (2.58)$$

and

$$X + 0.5 Y = R \quad (2.59)$$

where  $Z$  is the number of oxygens surrounding the cation,  $X$  is the number of nonbridging oxygens (singly bonded) per polyhedron and  $Y$  is the number of bridging oxygens per polyhedron. Corresponding rules that apply for silicate glasses are

1. The  $\text{SiO}_4$  tetrahedra dictates that  $Z = 4.0$ .
2. The minimum requirement for a three-dimensional network is  $Y \geq 2.0$ .
3. When alkali or alkaline earths are present with  $\text{Al}_2\text{O}_3$ , the  $\text{Al}^{+3}$  occupies the centers of  $\text{AlO}_4$  tetrahedra which converts nonbridging to bridging oxygen. Hence, when  $\text{Al}^{+3}$  is a network forming ion, the  $\text{Al}_2\text{O}_3$  contribution is  $R = 1.5$ .

When comparing the most common industrial glass formers,  $\text{Si}^{+4}$  and  $\text{B}^{+3}$ , boron forms equilateral triangle 3-fold coordination with the  $\text{B}^{+3}$  ion placed at the center. Since silicon accommodates four oxygen bonds to boron's 3, boron's oxygen dissociation energy and corresponding viscosity and melting temperature are lower.

The most common modifiers employed in ceramic glazes are  $\text{Na}^{+1}$  and  $\text{Ca}^{+2}$ . Increasing the number of modifier ions causes more breaks in the silicon-oxygen tetrahedron and lowers the glass viscosity. This increases the freedom of the tetrahedrons to assume a crystalline structure and can consequently lead to devitrification. Higher valence modifiers such as  $\text{Ca}^{+2}$  are more tightly bound to the lattice and tend to strengthen the glass structure when replacing  $\text{Na}^{+1}$ . Figure 2.17 demonstrates that  $\text{Na}^{+}$ , like other monovalent modifiers, causes the formation of two non-bridging oxygen and a loss of connectivity. One  $\text{Na}^{+}$  joins an unsatisfied oxygen bond on one side, while the remaining  $\text{NaO}^{-}$  group occupies the vacancy at the corner of the tetrahedra and breaks the structure. When monovalent modifiers are replaced with divalent ions such as  $\text{Ca}^{+2}$ , the bridge across the gap is completed. This results in

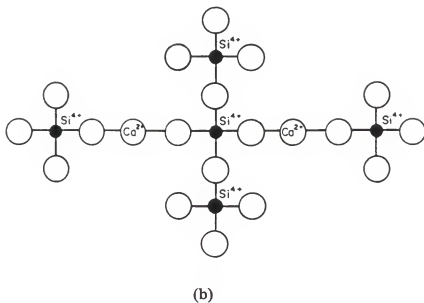
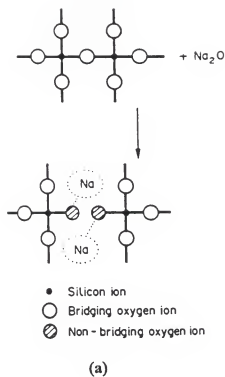


Figure 2.17. Two-dimensional representation of modifiers (a)  $\text{Na}^{+1}$  and (b)  $\text{Ca}^{+2}$  in the silicate glass structure. [Adapted from Tay86]



1. An increase in density.
2. An increase in refractive index.
3. A decrease in cation mobility and electrical conductivity.
4. An increase in  $T_g$  and melting temperature.
5. An increase in viscosity.

Aluminum is the most common intermediate incorporated in glaze formulations. By itself  $Al^{+3}$  cannot form a glass structure, but it can replace some silicon ions in the tetrahedrons. The result is a higher lattice bonding strength which increases viscosity, chemical resistance and hardness.

The role of  $Al^{+3}$  depends largely on the concentration of alkali ions. If an adjacent alkali ion is present and achieves charge neutrality,  $Al^{+3}$  can substitute for  $Si^{+4}$ . In  $SiO_2-Al_2O_3-Na_2O$  glasses, if the ratio of moles of  $Al/Na < 1.0$ ,  $Al^{+3}+Na^{+1}$  can substitute for  $Si^{+4}$ , and excess  $Na^{+}$  acts in its normal modifier role. As  $Al/Na$  approaches 1.0, glass strength and viscosity increase. At  $Al/Na = 1.0$ , or the equivalency point, aluminum is tetrahedrally coordinated ( $AlO_4$ ) and the glass strength is maximum. For  $Al/Na > 1.0$ , excess  $Al^{+3}$  acts as a modifier. Substitutions of small

amounts of  $\text{Al}^{+3}$  for  $\text{Na}^+$  or  $\text{Ca}^{+2}$  raises the strength because of the high bond strength trivalency provides. Large substitutions for silicon weakens the glass structure due to the lower ionic potential of  $\text{Al}^{+3}$  [Chi97].

Table 2.6 summarizes properties associated with the presence of oxides commonly employed in ceramic glaze and glass formulations. Computer programs have been developed [Din96, Din96a, Mal96] to use the additive rule for estimating glass linear properties as a function of the oxide composition:

$$P = c_1x_1 + c_2x_2 + c_3x_3 + \dots + c_nx_n \quad (2.60)$$

where  $P$  is the property,  $c$  is the weight percentage of an oxide component and  $x_1, x_2, x_3$  and  $x_n$  are appropriate factors. Linear properties such as coefficient of thermal expansion, surface tension and cost can be assessed, although results can vary considerably with processing parameters. Results are even less accurate for multiphase glass-ceramics such as glazes.

Algorithms for accurately calculating more useful properties and characteristics such as gloss, color and viscosity which has an exponential temperature dependence, have not been developed.

Table 2.6. Properties Associated with the Presence of Various Oxides in Glass [Mue83, Lac97, Vic97].

<b>SiO<sub>2</sub></b>	High melting point. High viscosity. High chemical resistance. Low expansion. Increases gloss.
<b>B<sub>2</sub>O<sub>3</sub></b>	Low melting point. Low viscosity. High setting rate. High surface hardness. Very low expansion up to a certain limit. Low surface tension. High chemical resistance.
<b>Na<sub>2</sub>O</b>	Low melting point. Low viscosity. Slow setting. Low chemical resistance. High expansion. Low mechanical strength. Excess causes devitrification.
<b>K<sub>2</sub>O</b>	Similar to Na <sub>2</sub> O but slightly higher viscosity.
<b>PbO</b>	Low melting point. Slow setting. High density. High refractive index. Low surface tension. High elasticity.
<b>BaO</b>	Assists melting. Some fluxing action. Can replace lead oxide.
<b>CaO</b>	Fluxing action at high temperatures. Very quick setting. Excess causes divitrification. Increases viscosity and strength when replacing Na <sub>2</sub> O.
<b>TiO<sub>2</sub></b>	Fluxing action when replacing silica. Good chemical resistance. Reduces viscosity. Slow setting.
<b>ZnO</b>	Generally has a fluxing action. High viscosity. Decreases chemical resistance. Low expansion.
<b>MgO</b>	Refractory. High viscosity. Slow setting. Low expansion. High mechanical strength. High elasticity. High chemical resistance. Can matten and opacify in large amounts.
<b>Al<sub>2</sub>O<sub>3</sub></b>	Refractory. Very high viscosity. Slow setting. Prevents devitrification. High chemical resistance. Low expansion. High mechanical strength. Can lower gloss.
<b> SrO</b>	High expansion. High surface tension. Low durability. Relatively high melting point and low viscosity compared to other fluxes. Can increase gloss.
<b>Li<sub>2</sub>O</b>	Low expansion. High chemical durability. High hardness. Low viscosity. High surface tension. Can increase gloss.
<b>ZrO<sub>2</sub></b>	High opacification and whiteness. Increases melting point, viscosity and surface tension. High mechanical strength. Low expansion.

### 2.2.2 Glaze Base Materials and Formulas

Materials for glazes include processed and beneficiated minerals, specially formulated glass frits and industrial grade chemicals [Tay86, Wor82, Mei97]. They are selected based on their cost, safety to the environment and ability to yield desired glaze properties. Table 2.7 lists materials used for batching ceramic tile glazes, and Table 2.8 shows oxide compositions of some commercial glazes bases. Table 2.9 outlines important properties and characteristics to consider when formulating glazes. Most whitewares glazes appear to be glossy (gloss  $\geq 60.0$  at  $60^\circ$  incidence) and incorporate materials that provide oxides of  $\text{SiO}_2$  (primary glass former),  $\text{Al}_2\text{O}_3$ ,  $\text{CaO}$ ,  $\text{MgO}$ ,  $\text{Na}_2\text{O}$ ,  $\text{K}_2\text{O}$ ,  $\text{B}_2\text{O}_3$ ,  $\text{SrO}$ ,  $\text{ZnO}$  and  $\text{ZrO}_2$ .

Batch ingredients are often multicomponent and multiphase compounds, making it difficult to predict fired properties from these components. Glaze or frit batch compositions are normally converted into an empirical formula or molar equivalents using Seger's formula in order to better classify the system [Epp97b]. To derive an empirical formula, materials are expressed in terms of moles of individual oxides present, then divided by the sum of the moles of RO group oxides, as shown in Table 2.10 [Sac86]. Thus, the

Table 2.7. Common Ceramic Tile Glaze Base Materials [Bra86, Epp97b, She97].

Minerals	Common Trade Names	Major Functions
Clay; $\text{Al}_2\text{O}_3 \cdot 2\text{SiO}_2 \cdot 2\text{H}_2\text{O}$	Glaze #1, EPK, OM-4	Suspension, film strength, rheology control
Frit; glass composition	PK493, 3336 CC261, P930	Introduces oxides such as $\text{SrO}$ and $\text{B}_2\text{O}_3$ ; affects overall glaze properties, color development, gloss, firing range, thermal expansion ( $\alpha$ ), etc; expensive.
Silica; $\text{SiO}_2$	Sil-Co-Sil	Primary glass former; increases gloss, m.p. and melt viscosity; lowers $\alpha$ .
Alumina; $\text{Al}_2\text{O}_3$	A-2, C-31	Increases hardness, durability, m.p., melt viscosity and firing stability; lowers gloss and $\alpha$ .
Feldspar; $\text{Na}_2\text{O} \cdot \text{Al}_2\text{O}_3 \cdot 6\text{SiO}_2$	NC-4, F-4	Inexpensive source of oxides; $\text{Na}_2\text{O}$ lowers m.p., melt viscosity, firing stability and durability; increases $\alpha$ .
Zinc Oxide; $\text{ZnO}$	Denzox, Zochem	Increases firing range and durability; improves glaze texture and elasticity to avoid crazing; expensive
Whiting; $\text{CaCO}_3$	#10	Increases durability; can matten and create "orange peel" texture.
Wollastonite; $\text{CaSiO}_3$	Vansil W-20	Intermediate properties between whiting and silica; mattens without "orange peel" texture (no volatiles).
Opacifier; $\text{ZrSiO}_4$	Ultrox, Superpax	Adds whiteness; improves color stability and glaze hardness; expensive.
Chemicals		
Deflocculant; Sodium Hexameta- phosphate	Quadrofos, Vitrofos	Lowers viscosity; can aid in suspension.
Binder; Sodium carboxymethyl- cellulose	CMC-7L2	Binds glaze to body; increases film strength; slows drying; aids in suspension.

Table 2.8. Examples of Compositions (Weight %) of Commercial Glazes [Par73, Tay86, Tey95].

Oxide	Fast-Fire Matte Wall Tile	Fast-Fire Gloss Opaque Wall Tile	Electrical Porcelain	Dinnerware	Sanitary Ware
SiO <sub>2</sub>	44.5	47.3	70.0	55.9	59.7
Al <sub>2</sub> O <sub>3</sub>	16.7	8.5	14.3	9.6	18.6
B <sub>2</sub> O <sub>3</sub>	3.0	1.6		6.0	
ZrO <sub>2</sub>	13.7	13.2			
Li <sub>2</sub> O					
Na <sub>2</sub> O	3.4	2.6		3.1	2.1
K <sub>2</sub> O	1.8	2.9	5.0	1.7	3.0
MgO	1.6				
CaO	11.3	9.5	10.7	7.7	11.2
ZnO	4.0	8.7			5.4
SrO		5.7			
BaO					
PbO*				16.0	

\*PbO is still used in dinnerware glazes but is rarely incorporated in other whitewares coatings due to its potential hazards to the environment.

Table 2.9. Summary of Important Glaze Properties and Characteristics [Ree95].

Glaze State	Property/ Characteristics	Main Influences
Wet suspension	Rheology	Application smoothness and defects.
	Density	Application smoothness and defects.
	Particle Size	Rheology and melting behavior.
	Particle surface chemistry	Dispersion stability and rheology.
Green on substrate	Thickness applied	Color, gloss, defects and cost.
	Adhesion to substrate	Defects such as "crawls."
	% Volatiles	Defects such as "pinholes."
During firing	Thermal expansion	Fired strength, warpage and crazing defects.
	Melting temperature	All fired properties/characteristics.
	Firing range	All fired properties/characteristics.
	Viscosity	All fired properties/characteristics.
	Surface tension	All fired properties/characteristics.
	Stability from reacting with kiln gases	All fired properties/characteristics.
Fired	Strength	
	Physical durability	
	Elasticity	(for avoiding crazing defects)
	Chemical resistance	
	Color	
	Gloss	
	Opacity	
	Surface smoothness	(influences gloss)
	Defects	
	Cost	

Table 2.10. Seger's Formula for Classifying Glazes [ Par73, Sac86] .

RO group (basic)	R <sub>2</sub> O <sub>3</sub> (neutral or amphoteric)	RO <sub>2</sub> (acidic)
Na <sub>2</sub> O, K <sub>2</sub> O, Li <sub>2</sub> O,	Al <sub>2</sub> O <sub>3</sub> , B <sub>2</sub> O <sub>3</sub> ,	SiO <sub>2</sub> , ZrO <sub>2</sub>
MgO, CaO, BaO,	Fe <sub>2</sub> O <sub>3</sub> , Cr <sub>2</sub> O <sub>3</sub> ,	SnO <sub>2</sub> , TiO <sub>2</sub>
SrO, ZnO, MnO,	Bi <sub>2</sub> O <sub>3</sub>	CeO <sub>2</sub> , ThO <sub>2</sub>
PbO, FeO, BeO,		
CdO, CuO, NiO,		
CoO		

## Sample Calculations:

(1)	(2)	(3)	(4)	(5)
Chemical	Oxide		Segger's Empirical	
Analysis	Molecular		Formula or Molar	Formula
<u>Oxide</u>	<u>Wt%</u>	<u>Weight</u>	<u>Equivalents</u>	<u>Weight*</u>
		(1)+(2)	(3)+Sum RO Moles	(4)x(2)

$$(\sum \text{RO molar equivalents} = 1.0)$$

$$*\text{Oxide formula weight}(5)+\text{total formula weight}(\sum 5) = \text{wt \% (1)}$$



summation of molar equivalents of RO or alkalis and alkaline earth oxides is always brought to unity and equals 1.0. This provides a standard system for organizing, representing and predicting fired properties associated with the presence of specific oxides in the glass structure (Table 2.6).

For simplicity, glazes and frits are further classified by ranges of molar equivalents in the amphoteric and acidic categories. For example, ceramic tile glazes total amphoterics are typically in the range of 0.1-0.3 and acidics of 2.0-4.0, while porcelain glazes contain 0.5-1.2 amphoterics and 6.0-12.0 acidics.

Certain empirical rules have been derived to ensure correct proportioning of batch ingredients [Par73]:

1. The  $RO:RO_2$  ratio should fall between 1:1 and 1:3.
2. The ratio of the alkalis to the other oxides in the RO group should be  $\leq 1:1$ .
3. The  $B_2O_3:SiO_2$  ratio should be  $\leq 1:2$ .
4. The  $Al_2O_3$  content should be  $\leq 0.2$ .

Rule 1 achieves proper fusion of the materials. The RO group or basic ingredients are the primary fluxes, with an order of decreasing effectiveness of  $Li_2O$ ,  $Na_2O$ ,  $K_2O$ ,  $BaO$ ,  $CaO$ ,  $SrO$ ,  $MgO$  and  $ZnO$ . The  $RO_2$  of interest for rule 1 is  $SiO_2$ , the primary glass former.

The second and third rules ensure that the fired glaze or frit is insoluble. High alkali content results in a solubility approaching that of sodium silicate, while high boric oxide can render a stability similar to boric acid.

The fourth rule is also intended to ensure ready fusion. High  $\text{Al}_2\text{O}_3$  content tends to increase the glass melting temperature and viscosity and thus inhibits fusion.

Most commonly, the glaze melting temperature is lowered by increasing alkali or  $\text{B}_2\text{O}_3$  content and reducing  $\text{SiO}_2$  and  $\text{Al}_2\text{O}_3$  while staying within the constraints of the four empirical rules. Other methods employed to lower the fusion point include

1. Milling the materials to a finer particle size to increase local curvature and capillarity effects [ DeH93, Rah95] .
2. Introducing oxides as frits rather than the raw state, because a glass lattice structure has a lower binding energy to overcome by heat than its corresponding crystalline phase.

### 2.2.3 Fast-Fire Whiteware Glazes and Frits

Fast-fire roller kiln processes are the most common employed to produce ceramic tile. Manufacturers of other

ceramic whitewares such as sanitaryware and dinnerware are also currently attempting to convert to these types of processes. They provide much greater productivity and lower energy costs than the slow-fire tunnel kiln technology that was predominant prior to 1990. Fast-fire tiles are heated utilizing 30 to 90 minute cycles at peak temperatures of 1050°C to 1200°C. These rapid schedules require precision in formulating glazes to achieve the desired optical and mechanical properties.

Shorter firing cycles have reduced the time available for

1. Evolution of gases from the body before the glaze fuses so that glaze bubbles are avoided.
2. Dissolution of glaze ingredients and reaching molten equilibrium at the peak temperature.
3. Crystallization of phases.

Thus, it is necessary to formulate glazes which

1. Afford the highest fusion temperature possible while rapidly maturing in a short period of time.
2. Incorporate as much of the final desired phases and properties in the starting materials as possible.
3. Allow for precise control of the formation of new phases during firing.

For these reasons, manufactured glass frits are the main batch ingredients in fast-fire glazes [Sac86, Toz86, Enr96]. Most frit in the U.S. is currently used by ceramic tile manufacturers, but frit consumption by other whitewares industries will increase as they convert to fast-fire roller kiln technology. Frits are prepared by melting a blend of crystalline raw materials at approximately 1500°C, and then fast quenching in water or with cooled stainless steel rolls to form a glass. There are hundreds of different compositions formulated to provide specific coatings properties, while using low cost and environmentally safe materials [Bar97]. Frit compositions can also influence wet glaze rheology through surface charge development and exchange of soluble ions with hydroxyl or hydronium ions [Yoo97, LaC97].

The main advantages of frits are

1. Fritted raw materials melt at a lower temperature and reach equilibrium in less time than their corresponding crystalline phases. This allows for compositions higher in  $\text{Al}_2\text{O}_3$  and  $\text{SiO}_2$ , which improve mechanical and high-temperature stability while increasing the fusion temperature. Vitreous silicates soften gradually through a range of relatively low temperatures when

compared to crystalline phases. This occurs because varying amounts of energy are required to detach network atoms which are structurally nonequivalently distributed [Chi97].

2. Ingredients are prereacted and thus require less time and temperature to achieve a homogeneous blend and the desired phases. Little or no decomposition gases are evolved.
3. Incorporation of  $\text{ZrO}_2$  in the frit rather than as a  $\text{ZrSiO}_4$  mineral causes nucleation and crystallization of a greater number of uniform, finely dispersed  $\text{ZrSiO}_4$  particles, which improves opacity and whiteness.
4. Suspensions obtained with raw materials varying in density and particle size are more prone to settling and segregation.
5. Solubility and potential toxicity of elements such as lead, barium, cadmium and zinc are reduced. Lower solubility of  $\text{Ca}^{+2}$ ,  $\text{B}^{+3}$ ,  $\text{F}^-$ , etc. results in more stable glaze rheology.

Fast-fire frits and glazes differ from traditional slow-fire formulas in that concentrations of alkalis (principally  $\text{Na}_2\text{O}$  and  $\text{K}_2\text{O}$ ) and  $\text{B}_2\text{O}_3$  are lower, while oxides such as  $\text{CaO}$ ,

ZnO and SrO are higher [Amo97, Teu95]. This aids in delaying the fusion temperature and thus keeps the coating permeable for a longer period of time and facilitates body outgasing without the creation of glaze bubbles.

Major categories of fast-fire frits tend to vary mainly in alkali/silica ratio, use of SrO versus ZnO for the secondary flux, and  $\text{ZrO}_2$  content. The  $\text{ZrO}_2$  normally ranges from 0% to 8% by weight, depending on the desired opacity. Frits which do not incorporate  $\text{ZrO}_2$  contain increased  $\text{Al}_2\text{O}_3$  and CaO in order to maintain sufficient glass strength.

There is an increasing interest in replacing ZnO with SrO, even though SrO increases the cost. ZnO is classified as a "313" regulated chemical by the EPA. Manufacturers must monitor and report spills of materials containing ZnO to federal and state governments, while no such regulations exist for SrO.

Fast-fire glazes are generally classified in four groups [Toz86]:

1. Opaque gloss
2. Transparent gloss
3. Matte
4. Special (satin, rustic, etc.)

Table 2.11 lists typical empirical formulas for fast-fire tile gloss and matte glazes.

The largest volume of whitewares sold worldwide is coated with opaque gloss glaze. Opacity arises mainly from zirconium crystalline phases (zirconia and zircon), added to the batch as a  $\text{ZrSiO}_4$  mineral or divitrified from the frit. The resulting micro-heterogeneities ( $<10\text{ }\mu\text{m}$ ) have a significantly different index of refraction (2.05-2.40) from the glassy matrix ( $\sim 1.50$ -1.70) and thus reflect and scatter light.

Transparent glazes and frits contain little or no  $\text{ZrO}_2$  and include more  $\text{CaO}$  and  $\text{Al}_2\text{O}_3$  to make up for the lost mechanical strength (i.e., Mohs hardness and abrasion resistance). Otherwise, their compositions are similar. High  $\text{CaO}$  and  $\text{ZnO}$  in these glazes can cause immiscible liquid/liquid phase separation and opalescent opacification that is not otherwise noticeable in zircon-opacified glazes. Phase separation varies with the firing cycle and can impart shade variations in colored glazes.

Matte glazes have many crystalline phases which create local discontinuities in refractive index. This yields high diffuse (opacity) and low specular (gloss) reflectances. The

Table 2.11 Typical Empirical Formulas, in Molar Equivalents, for Fast-Fire Ceramic Tile Gloss and Matte Glazes [Amo94, Apa94, Toz86].

	Opaque Gloss	Transparent Gloss	Calcium Matte	Alumina Matte
$\text{SiO}_2$	2.263	1.988	1.292	1.967
$\text{ZrO}_2^*$	0.293	0.054	0.070	0.277
$\text{B}_2\text{O}_3$	0.199	0.095	0.233	0.113
$\text{Al}_2\text{O}_3$	0.191	0.195	0.102	0.412
$\text{Na}_2\text{O}$	0.090	0.071	0.139	0.170
$\text{K}_2\text{O}$	0.088	0.094	0.092	0.056
$\text{CaO}$	0.346	0.434	0.769	0.515
$\text{MgO}$	0.069	0.110	0.000	0.130
$\text{SrO}$	0.134	0.128	0.000	0.000
$\text{ZnO}$	0.273	0.163	0.000	0.129

Notes:

- \*1) Frits normally contain  $\text{ZrO}_2$  in the range of 0.000 to 0.175. Additional  $\text{ZrO}_2$  is added to the glaze batch in the mineral form  $\text{ZrSiO}_4$ .
- 2) Clay is added to glazes as a suspending agent; therefore, gloss frits normally incorporate less  $\text{Al}_2\text{O}_3$  than listed above.



three types of matte glazes are produced with high  $\text{CaO}$ ,  $\text{ZnO}$  or  $\text{Al}_2\text{O}_3$  concentrations.

Calcium mattes derive  $\text{CaO}$  from the frit, whiting ( $\text{CaCO}_3$ ) or wollastonite ( $\text{CaSiO}_3$ ). The  $\text{Ca}^{+2}$  ion in glass has a high bond strength, and crystal formation is energetically favorable [Toz68]. If the concentration of ions ( $\sim \geq 15\%$  by weight  $\text{CaO}$ ) and cooling rate are sufficient, wollastonite and sometimes diopside ( $\text{CaO} \cdot \text{MgO} \cdot 2\text{SiO}_2$ ) crystals form [Esc96].

Zinc mattes are produced when lamellar hexagonal willemite ( $\text{Zn}_2\text{SiO}_4$ ) crystals form during the cooling cycle. Typically, at least 20% by weight of  $\text{ZnO}$  is necessary. Willemite nucleation and growth require a low melt viscosity and relatively long cooling cycle for sufficient ionic migration to create the species and is thus difficult to obtain with fast-fire cycles.

Alumina mattes are formulated with high mill additions of  $\text{Al}_2\text{O}_3$  particles, which cause the glaze to be somewhat underfired due to an increased melting temperature and viscosity. Underfired glazes appear matte but do not mature and develop the optimum amount of glassy phase during firing.

A more detailed description of the kinetics of dissolution, nucleation and growth in glass and their

potential influence on color development in fast-fire glazes is discussed in Section 2.2.5.

#### 2.2.4 Ceramic Colorants

Ceramic colorants are predominately inorganic mixed metal oxide pigments. This represents a small but very important part of the inorganic pigment family, listed in Figure 2.18. Inorganic mixed metal oxide pigments are the most chemically inert and heat resistant of all colorants [Dry82]. They are used not only for ceramics coatings but also for coloring paints and plastics when weather and heat resistance is necessary. These manufactured minerals are produced by reacting selected metal oxides at high temperature to induce ionic interdiffusion and form the desired crystalline matrix [Jac96].

A less common method for producing color in ceramics coatings is to utilize single metal oxide raw materials or additives. The oxides dissolve in the glass during heating and are reprecipitated as metal ions. The color developed is influenced by the metal ions valency state and nearby ions in the material structure that can alter the electronic energy levels of the metal ions [Tay86]. Metal oxides of transition metals such as Cr, Fe, Co, Mn, Ni, Cu, V and Ti

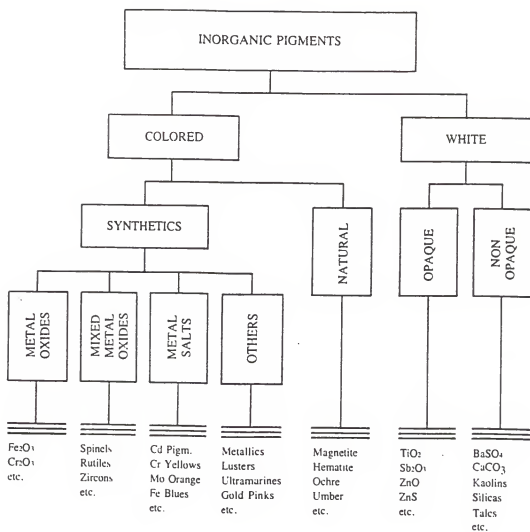


Figure 2.18. Inorganic pigment family. [Bur79]

and the lanthanide group's Pr and Ce are normally employed. Since development of their color is highly sensitive to processing conditions and interactions with other materials in the coating formulation, they are now rarely used in high volume whitewares processing where color control is essential.

Figure 2.19 diagrams the chroma of colorants commonly used in ceramics coatings. The distance from the origin indicates the purity of the pigment color. Table 2.12 lists glaze pigments, their maximum use temperature and glaze formulation requirements for optimum color.

The research of this dissertation focuses on the doped zircon structure pigment group of the mixed metal oxide family. It is the most widely used pigment system for ceramic whitewares coatings.

#### 2.2.4a Zircon Triaxial Pigments

Zircon ( $\text{ZrSiO}_4$ ) pigment systems have been used in the ceramics industry for over 30 years [Blo94a]. Zircon's tetragonal structure has the ability to accommodate a number of impurity ions substitutionally, and its high chemical and thermal stability make it ideal for use in ceramics coatings.

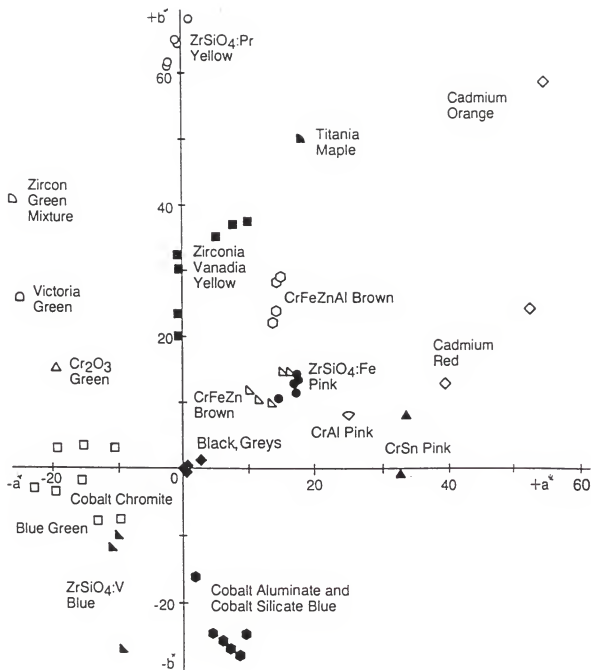


Figure 2.19. CIE  $a^*$  and  $b^*$  chroma of ceramic pigments.  
[Epp87]

Table 2.12. Glaze Pigments and Their Requirements [Tay86].

Color	Pigment	Maximum Firing Temperature (°C)	Glaze Base Characteristics for Optimum Color Strength and Stability
Blue, light	Zircon, vanadium*	1300	Suitable for use in all glazes
	Olivine, cobalt silicon	1400	Suitable for use in all glazes
	Spinel, cobalt zinc aluminium	1300	Suitable for use in all glazes
Green, light	Zircon, vanadium/praseodymium	1250	Suitable for use in all glazes
	Spinel, chromium cobalt (zinc)	1400	Suitable for use in most zinc-free glazes
	Garnet, calcium chromium silicon	1200	Zinc-free, high calcium compositions
Orange	Baddeleyite (indium, yttrium) vanadium	1400	Suitable for use in all glazes, especially those firing at high temperatures
	Pyrochlore, lead antimony	1050	High lead content glazes
	Rutile, titanium chromium	1100	Leadless glazes
Yellow	Zircon, praseodymium*	1250	Suitable for use in all glazes
	Cassiterite, vanadium	1300	Suitable for use in all glazes
	Cadmium sulphide	1050	Glaze must be specially designed to give temperature stability to the pigment
Red	Cadmium sulphoselenide	1050	Glaze must be specially designed to give temperature stability to the pigment.

Table 2.12--continued.

Color	Pigment	Maximum Firing Temperature (°C)	Glaze Base Characteristics for Optimum Color Strength and Stability
Pink	Zircon, iron*	1300	Suitable for use in all glazes
	Zircon, cadmium sulphoselenide	1300	Suitable for use in all glazes
	Spinel, chromium tin silicon	1200	Zinc-free, high calcium compositions
	Spinel, chromium aluminum zinc	1300	High zinc and aluminium glaze with low calcium content
Brown, dark	Spinel, iron chromium zinc	1300	Very suitable for use in zinc-containing glazes
	iron chromium (nickel)	1300	Very suitable for use in zinc-containing glazes
	iron aluminium chromium	1300	Very suitable for use in zinc-containing glazes
Black	zinc		
	Spinel, chromium cobalt iron nickel	1300	Zinc-free compositions
Grey	Cassiterite, antimony vanadium	1300	Suitable for use in all glazes

\*Vanadium, praseodymium and iron zircons are the most common triaxial pigments.

The triaxial system is based on blending zircon-vanadium blue, zircon-iron coral and zircon-praseodymium yellow structures to obtain a wide variety of colors. They can be either milled into the glaze batch or, more commonly, stirred into a prepared glaze base. Stir-in pigments require narrow particle size distributions and carefully controlled surfactants for good dispersion. Most calcined ceramic pigments are in the 1-12  $\mu\text{m}$  mean particle diameter range, with no particles greater than 44  $\mu\text{m}$ .

Zircon pigment concentrations in glazes range from 0.1% to 10% by weight, with most systems containing closer to 0.5% to 2.0%. Zircon-based pigments furnish a lower color strength than metal oxides but provide much more opacification and high temperature stability. They are insensitive to variations in kiln atmosphere, and their solubility varies with the melt composition.

Zircon is isomorphous with a tetragonal structure  $4/m\bar{2}/m\bar{2}/m$  (one fourfold and two twofold axes with perpendicular symmetry planes) as shown in Figure 2.20. It consists of a chain of alternating edge-sharing  $\text{SiO}_4$  tetrahedra and  $\text{ZrO}_8$  triangular dodecahedra extending parallel to the c-axis. The prismatic habit of zircon compounds results from edge-sharing



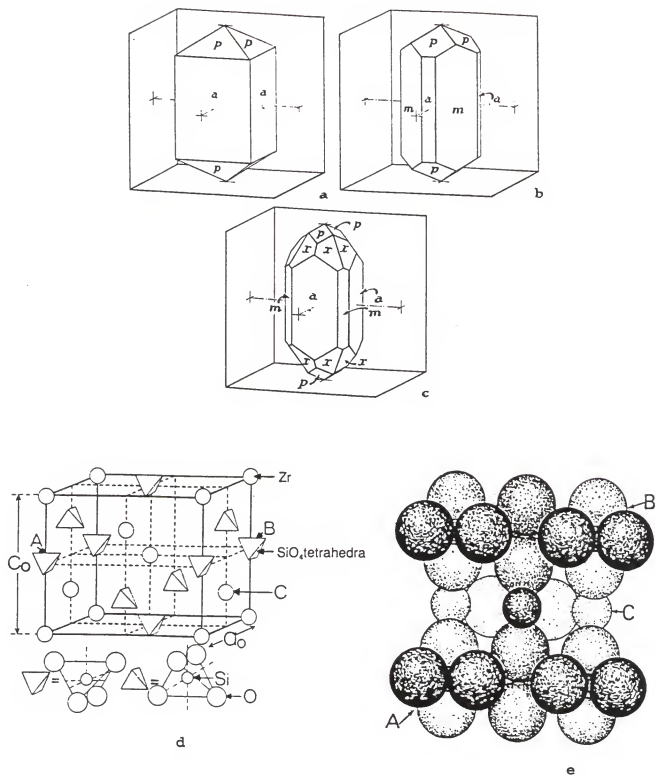


Figure 2.20. Typical forms of zircon crystals. (a-c):  $a\{100\}$ ,  $m\{110\}$ ,  $p\{101\}$ ,  $x\{211\}$ ; and zircon lattice structure (d,e). [Wyc65, Mas68]

dodecahedra, which join the chains. There are four molecules per unit cell [Gre82].

The  $\text{ZrO}_8$  polyhedra are two interlocked, tetragonally distorted tetrahedra. One tetrahedron is compressed, the other is stretched parallel to the c-axis. The  $\text{SiO}_4$  tetrahedra are elongated parallel to the c-axis. The two angles bisected by the c-axis are less than the  $109.4^\circ$  ideal tetrahedral angle and the remaining four are greater. Both tetrahedra  $\text{SiO}_4$  and dodecahedra  $\text{ZrO}_8$  site symmetry are  $D_{2d}$ , which is Schoenflies notation for a twofold principal axis and two twofold axes normal to it, with diagonal symmetry planes [Klu74].

Zircon-doped pigments are prepared by solid state reactions which approach equilibrium with difficulty [Epp87]. The research of this dissertation focuses on the zircon-vanadium blue pigment; therefore, its mechanisms for color production will be discussed in the most detail in this section. Phenomena involved with loss of color strength and stability of Zr-V pigments during processing also apply to the other two triaxials, which are based on the same zircon structure.

Zircon-vanadium blue is ordinarily formed from batches of 60-70%  $\text{ZrO}_2$ , 26-36%  $\text{SiO}_2$ , 3-5%  $\text{V}_2\text{O}_5$  or  $\text{NH}_4\text{VO}_3$  and 0.5-5.0%

NaF by weight. The materials are heated to 750-900°C for one to eight hours to complete the solid state reaction. It is then washed and leached to remove soluble  $V_2O_5$  because  $V^{+5}$  provides unwanted green color [Par73]. Without a mineralizer-catalyst such as NaF, the  $V^{+4}$  which provides the blue color does not form on the zircon lattice. NaF aids in the development of the solid state solution by lowering the required sintering temperature and increasing the mobility of  $Zr^{+4}$  and  $Si^{+4}$  for forming zircon. Without a catalyst, melting occurs for  $ZrO_2$  at 2700°C and  $SiO_2$  at 1713°C, while  $ZrSiO_4$  begins to decompose at 1720°C [Wea79, Sha92].

Some details regarding the origin of the blue color are still unexplained. A valency of  $V^{+4}$  is present, but the critical role of NaF and the exact location of  $V^{+4}$  in the lattice remain obscure. With an ionic radius of 0.61 Å,  $V^{+4}$  could theoretically occupy  $Si^{+4}$  (0.40 Å),  $Zr^{+4}$  (0.87 Å) or interstitial sites [Ric92, Sha92]. Demiray, Nath and Hummel surmised that  $V^{+4}$  is solely responsible for the blue color and occupies the dodecahedral  $Zr^{+4}$  site ( $ZrO_6$ ). They also stated that NaF increased the solubility and thermal stability of  $V^{+4}$  in zircon but did not affect coordination or valence [Par73]. Gregorio, Greenblatt, Pifer and Sturge published that the

optical spectra suggests that  $V^{+4}$  enters the tetrahedral  $Si^{+4}$  ( $SiO_4$ ) rather than dodecahedral site [Gre82].

Vanadium metal has an outer electronic structure of  $3d^3 4s^2$ . The cation  $V^{+4}$ , which produces a blue color, has a  $3d^1 4s^0$  configuration. When the coordination of anions about a single d electron is fourfold or eightfold, the electron's initial fivefold degeneracy (shown in Figure 2.7) is disrupted. This phenomenon is described with ligand field theory in Section 2.1.2d. The anion coordination about  $V^{+4}$  in the zircon structure results in the original d orbital electron energy level ground state ( $2_d$ ) splitting into a new doublet ground state ( $2_g$ ) and an excited triplet state ( $2_\tau$ ), as presented in Figure 2.21. The figure is based on a choice of axes where xz and yz planes contain the anion ligand atoms. When crystal site symmetry is reduced to tetragonal, the orbitals are further split into two ground and two excited states. The  $\sigma$  and  $\pi$  symbols shown in Figure 2.21 are differently polarized transitions due to orbital coupling. Mixing of split orbitals due to atomic vibrations can also occur. It has been suggested that this phenomena makes it difficult to evaluate the true d orbital energy levels in vanadium doped zircon [Gre82].

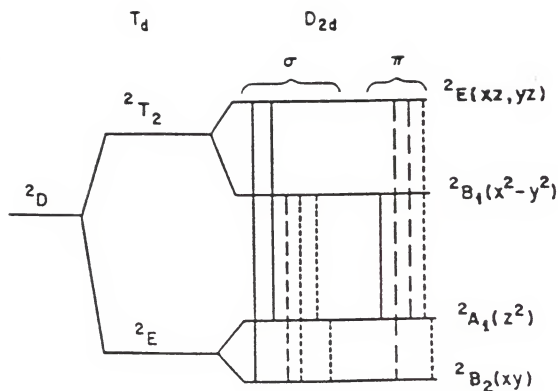


Figure 2.21. Splitting of the d orbital in  $V^{4+}$  by tetrahedral ( $T_d$ ) and tetragonal ( $D_{2d}$ ) crystal fields. (Possible electron transitions are shown with dotted and solid lines) [Adapted from Gre82]

The resulting  $V^{+4}$  electronic structure absorbs incident light in the range of approximately 600 nm-700 nm. These wavelengths correspond to the energy of light absorbed, which is equal to the difference in energy levels between the split orbitals which allow electron transitions from the ground to excited state. Vanadium is colorless when incorporated in a glass structure because its coordination does not allow for split orbitals and electronic transitions which correspond to the energy associated with the visible spectrum.

Zircon-iron coral is the high temperature reaction product of 50-75%  $ZrO_2$ , 15-50%  $SiO_2$ , 2-10% NaF and 0.25-25%  $Fe_2O_3$  by weight. The  $Fe^{+3}$  loses an electron and converts to  $Fe^{+4}$  ( $3d^4$ ) and substitutes for  $Zr^{+4}$  in zircon. This results in approximately 40%  $ZrSiO_4$  with 0.25%  $Fe^{+4}$  in the lattice. The wavelength of incident light absorbed by the structure falls in the range of 400 nm-570 nm [Par73].

Zircon-praseodymium yellow is manufactured by reacting 35-80%  $ZrO_2$ , 10-55%  $SiO_2$ , 0.25-3% NaF, 0.25-8% KNaO and 0.5-10%  $Pr_6O_{11}$  by weight. There is discord in theories regarding the solid state reactions that occur in forming the Zr-Pr structure. Decker [Dec90] suggested that  $Pr_6O_{11}$  is reduced to  $Pr_2O_3$  and then  $Pr^{+3}$  converts to  $Pr^{+4}$  by losing an electron. The  $Pr^{+4}$  substitutes for  $Zr^{+4}$  in zircon, and some unreacted

$\text{Pr}_6\text{O}_{11}$  is left dispersed in the material. Unfilled f orbitals ( $4f^1$ ) allow for split energy levels, and resulting selective absorption occurs in the range of approximately 400 nm-470 nm wavelength of light.

Light scattering from opacifiers such as zircon counters pigment absorption and thereby lowers color strength. It is difficult to overcome the whitening effect of unpigmented zircon except by adding large quantities of colorant. An optimum system would incorporate zircon pigments sized to scatter light in wavelength regions other than where its dopant transition metal absorbs light. In this way, increases in chroma through a decrease in reflectance in the pigment's absorbing wavelength area can be obtained [Blo94b]. For example, for zircon-vanadium blue pigments which absorb light in the 600 nm-700 nm range, a zircon particle size of 0.75  $\mu\text{m}$  or 750 nm would scatter light without affecting chroma. Current pigment manufacturing processes do not allow for such tight particle size control. In addition, extremely fine pigments can cause problems with agglomeration in the wet glaze base and increased solubility at high temperature. Optimizing color strength through improved particle size distributions is an area for future research.

Although zircon doped pigments are the most stable ceramic colorants up to approximately 1200°C, significant color variations can occur. Resulting color is a function of the stability of the zircon structure at high temperature and the optical properties of the coating matrix phases. The color of the substrate upon which the coating is applied is also important for translucent glossy coatings.

#### 2.2.4b Kubelka-Munk Analysis of Colorant Layers

Pigment particles produce almost perfect diffusion of light flux in every direction by Fresnel reflection or light scattering. Light proceeding parallel to the boundary of the colorant layer has just as much light diffused to the left as the right and thus may be canceled out for mathematical interpretations [Jud65]. Consider two diffuse light fluxes, one traveling downward ( $i$ ) and the other upward ( $j$ ), through an elementary colorant layer of  $dx$  which starts at zero from the unilluminated side, as shown in Figure 2.22. The thickness of  $dx$  is small compared to the total layer thickness ( $X$ ), but large compared to pigment particle diameters. The downward flux of light decreases due to absorption into pigments by  $Kidx$  and reverses direction through scattering by  $Sidx$ , where  $K$  is the absorption



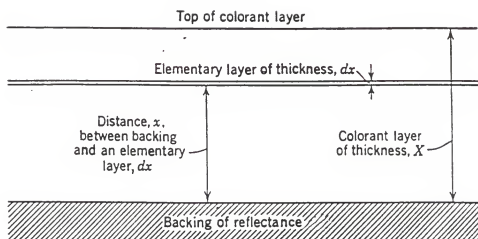


Figure 2.22. Schematic of basis for Kubelka-Munk analysis of colorant layers [Jud65].

coefficient and  $S$  is the scattering coefficient. Upward reflected light ( $j$ ) is also reduced by absorption and scattering. The changes in light flux caused by an elementary colorant layer can be written [Jud65]

$$dj = -(S+K)jdx + Sidx \quad (2.61)$$

$$-di = -(S+K)idx + Sjdx \quad (2.62)$$

where  $dj$  and  $-di$  are the total changes in upward and downward proceeding fluxes, respectively.

Exponential solutions to differential equations (2.61) and (2.62) in terms of reflectance were derived by Kubelka and Munk in 1931. They are equations (2.31) and (2.32) in Section 2.1.2c of this dissertation. From (2.32), the ratio of absorption to scattering coefficients is given by

$$K/S = (1-R_{\infty})^2 / 2 R_{\infty} \quad (2.63)$$

Important requirements of equations (2.31), (2.32) and (2.63) are 1) each colorant layer must be evaluated one wavelength unit at a time (normally in 0.5 nm increments), since  $K$  and  $S$  are a function of wavelength, and 2) complete hiding power or opacity of the substrate backing is assumed.

Beer's law (equation (2.41) in Section 2.1.2d) does not hold true for complex-subtractive colorant mixing and instead the Kubelka-Munk equations are applied. Absorption and scattering coefficients of materials are used to predict

colorant concentrations required to produce a color or to evaluate the hiding power of a coating. Equation (2.63) has been used by Selling [Sel47] for formulating dyes and by Duncan [Dun49] for paint formulations. Murdock, Wise, Eppler [Mur90] and Blonski [Blo93, Blo94b] evaluated ceramic pigments in glaze using Kubelka-Munk theory.

Application of equation (2.63) to pigment colored glazes presumes the composite system is the concentration of weighted sums of the individual components [Blo94b]. An absorption factor ( $K/S$ ) [Epp97a] can be used to measure the color strength of the coating, which is a function of the pigment concentration ( $C_{\text{pigment}}$ ):

$$K/S = \frac{(1-R)^2}{2R} = \frac{C_{\text{pigment}} K_{\text{pigment}} + K_{\text{glaze}}}{C_{\text{pigment}} S_{\text{pigment}} + S_{\text{glaze}}} \quad (2.64)$$

The requirements of (2.64) for evaluating pigmented ceramic coatings are

1. Spectrophotometric measurements of reflectance ( $R$ ) are substituted for reflectivity ( $R_w$ ) in (2.63) if an increase in coating thickness does not change the reflectance values.
2. Reflectance is diffuse; the specular component must be excluded.

In equation (2.64),  $(1-R)$  converts measured diffuse reflectance into absorption, since light that is not reflected by an opaque object must be absorbed. The factor  $2R$  allows that more than all of the incident light cannot be absorbed.

Since as  $C_{\text{pigment}} \rightarrow 0$ ;  $K/S \rightarrow \frac{K_{\text{glaze}}}{S_{\text{glaze}}}$ ,  $K/S$  calculated with the minimum reflectance ( $R_{\text{min}}$ ) value measured across the visible spectrum is where absorption of the glaze matrix is minimal and absorption due to the pigment is maximum. This provides the best indication of color strength due to pigment absorption. A higher  $K/S$  at the minimum reflectance indicates greater pigment strength.

Calculated absorption factors ( $K/S$ ) of various pigments and pigment/glaze systems are compared to weigh color strength. Plots of  $K/S$  versus pigment concentration are often collated and exhibit a linear relationship over most of the range [Epp97b]. The vertical distances between  $\log K/S$  versus wavelength curves are proportional to pigment concentration, or layer thickness if the coating does not completely hide the substrate.

### 2.2.5 Frit Influence on Color Development

The appearance of ceramic glazes is greatly affected by the structure and composition of the glassy matrix phase and dispersed crystalline or immiscible liquid phases which cause opacification and color. Light scattering in partially crystallized glasses can result in a range of optical properties from clear to completely opaque and white. Depending upon the starting frit composition and corresponding high-temperature properties, crystalline phases such as zircon, zirconia (monoclinic or tetragonal), wollastonite and willemite have been found to precipitate in slow-fire glazes during firing [Eld94, Esc96, Amo94, Gru78, Apa94]. Dissolution rates of zircon pigments are also a function of the glass composition and properties. In particular, nucleation, growth and dissolution of crystals is largely controlled by the glassy phase viscosity-time-temperature conditions during processing.

#### 2.2.5a Crystallization Mechanisms

In a glass melt at high temperature, unit lattices formed from attractive forces continually disintegrate due to the thermal motion of the atoms. Thermal agitation and the rate of rupture decrease as the melt is cooled. Atoms crowd

closer together, bonds are strengthened and crystal formation becomes more readily attainable. Crystallization at a sufficiently low temperature depends on three main factors: 1) number of nuclei formed, 2) crystal growth rate, 3) melt viscosity [ Par73] .

Nucleation begins when two atoms with sufficiently low velocities collide and come together at rest. If there is not sufficient energy to agitate the resulting mass, it becomes an easier target than a single atom. The pair is struck by other atoms and a nucleus begins to form. The free energy change ( $\Delta G$ ) required for homogeneous nucleation is (assuming spherical geometry) [ Sac96]

$$\Delta G = (4\pi r^2)\gamma + \left(\frac{4}{3}\pi r^3\right)\Delta G_v \quad (2.65)$$

The first term on the right side of (2.65) is the free energy required to form new interfaces, as a function of interfacial energy ( $\gamma$ ) and nucleus radius ( $r$ ). This term always has a positive value. The second term is the free energy for the bulk transition as a function of the free energy change per unit volume of the new phase formed ( $\Delta G_v$ ). This term can be positive or negative. Overall,  $\Delta G$  must be negative for nucleation to become thermodynamically favorable. The critical nuclei radius ( $r^*$ ) where  $\Delta G_v$  has a sufficiently

negative value to overcome the energy required to form new interfaces is determined from the  $\partial(\Delta G)/\partial r = 0$  maxima and is given by

$$r^* = \frac{-2\gamma}{\Delta G_v} \quad (2.66)$$

At embryo sizes greater than  $r^*$ , the chemical potential of the embryo is less than that of the bulk phase, and it becomes a growing crystalline nucleus. An approximate equation for  $\Delta G_v$  for condensed phases is [Dor94]

$$\Delta G_v = \Delta H_f (T - T_m) / VT_m \quad (2.67)$$

where  $\Delta H_f$  is the heat of fusion,  $T_m$  is the melting temperature and  $V$  is the molar volume of the matrix phase.

The activation energy required for nuclei formation ( $\Delta G^*$ ) is

$$\Delta G^* = \frac{16 \pi \gamma^3}{3 \Delta G_v^2} \quad (2.68)$$

The rate of nucleus formation ( $I$ ) is related to  $\Delta G^*$  by

$$I = K \exp\left(\frac{-\Delta G^*}{kT}\right) \text{ (no./cm}^3\text{/s)} \quad (2.69)$$

where  $k$  is Boltzmann's constant and  $K$  is a coefficient assumed independent of temperature. By combining (2.67), (2.68) and (2.69)

$$I = K \exp \frac{1}{kT} \left( \frac{-16\pi\gamma^3 V^2 T_m^2}{3\Delta H_f^2 (T - T_m)^2} \right) \quad (2.70)$$

Equation (2.70) indicates that because of the  $(T-T_m)^2$  factor, without a transport limitation there is a sharp increase in the nucleation rate at some critical temperature below  $T_m$ . The transport factor, or viscous flow, constrains the maximum nucleation rate possible with decreasing temperature. Thus,  $K$  is sometimes estimated as  $10^{30} \text{ cm}^{-3} \text{ sec}^{-1} \text{ poise}$  for oxide glass formers [Chi97].

The nucleation rate can be further related to the glass matrix viscosity ( $\eta$ ) by [Dor94]

$$\log \dot{n} = K_1/T(T-T_m)^2 \quad (2.71)$$

where  $K_1$  is a temperature independent factor. Equation (2.71) points out again that viscosity and nucleation rate are inversely proportional.

Glass systems are normally not completely pure, and thus heterogeneous rather than homogeneous nucleation occurs. The activation energy is lower for heterogeneous nucleation because the amount of required interfacial energy is reduced by the presence of nucleation catalysts. The catalysts can be surfaces, seed particles, contaminant particles, second phases, bubbles or defects. A higher nucleation rate results when interfacial energy is lowered due to the segregation of dissolved species at interfaces [Dor94].



In equations (2.65)-(2.71), heterogeneous nucleation can be accounted for by substituting an effective interfacial energy ( $\gamma_e$ ) for  $\gamma$  [Dor94]:

$$\gamma_e = \sum_i f_i \gamma \quad (2.72)$$

where  $f_i$  is a correction factor for nucleation catalysts of class  $i$ . In most cases, there is more than one catalyst present that speeds up nucleation at different undercoolings. Nuclei formed are typically  $5-10 \times 10^{-3}$  microns in diameter.

Figure 2.23 is a schematic of nucleation and crystallization in a glaze system as a function of undercooling temperature. Nucleation rates are low until the undercooling is sufficiently large, then rates increase rapidly with undercooling. Nucleation rates decrease at lower temperatures because the increase in viscosity slows diffusion transport.

The shapes of and spacing between nucleation and growth rate curves vary for different glass and glaze systems. The narrower the temperature range between peak nucleation and crystal growth rates, the higher the number and size of the crystals formed, providing that viscosity permits transport. Opposing factors for nucleation and growth occur where the curves overlap. In this region as temperature decreases, the

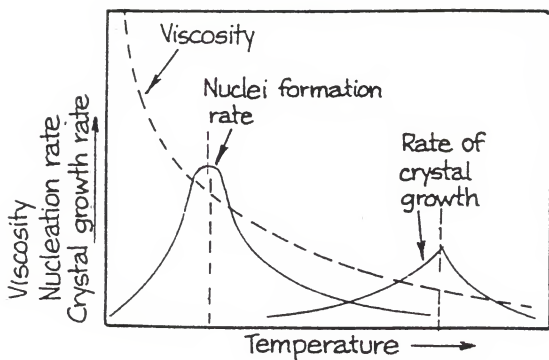


Figure 2.23. Relationship between viscosity and temperature favoring nucleation and growth in glazes. [Adapted from Par73]

driving force for nucleation increases, but the diffusion transport rate lowers enough to inhibit growth. Both processes also need time to occur. If cooling is too rapid, nucleation and crystallization may not result.

Crystallization from solution is a function of impurity and nuclei types and concentrations, the number of phases separating, time-temperature processing, matrix phase viscosity and diffusion coefficients ( $D$ ).

The rate of growth of a spherical particle of radius  $r$  is [Dor94]

$$\frac{dr}{dt} = \alpha \frac{D}{r} \quad (2.73)$$

where  $\alpha$  is a coefficient dependent only on concentrations. Thus, upon integrating separable equation (2.73), it becomes evident that the crystal radius grows proportional to the square roots of both time and the diffusion coefficient.

The diffusion coefficient is related to the gradient of concentration  $c$  in the  $x$  direction [Ban86]:

$$\frac{\partial c}{\partial t} = D \frac{\partial^2 c}{\partial x^2} \quad (2.74)$$

and has an Arrhenius type relationship to temperature:

$$D = D_0 \exp (-Q/RT) \quad (2.75)$$

where  $D_0$  is a material factor with the same units as  $D$ ,  $Q$  is the activation energy for the transport process and  $R$  is the gas constant.

When the matrix phase is near its equilibrium composition during the later stages of growth, the crystal radius is proportional to the cube root of time ( $t$ ):

$$r^3 - r_0^3 = \frac{8\gamma C_e D V_m t}{9RT} \quad (2.76)$$

where  $r_0$  is the mean crystal radius at  $t=0$ ,  $C_e$  is the crystal concentration and  $V_m$  is the molar volume of particles.

The thermodynamic driving force for crystallization is related to heat flow and rearrangement at the melt-crystal interface. It is measured as the difference in Gibbs free energy between the liquid and crystal. This is also referred to as the molar free energy of crystallization of an undercooled liquid [Chi97], ( $\Delta G_m$ ) given by

$$\Delta G_m = \Delta H_f (T - T_m) / T_m = \Delta H_f - T_m \Delta S_m \quad (2.77)$$

where  $\Delta H_f$  is the heat of fusion at the melting temperature  $T_m$ . At the melting point,  $\Delta G_m$  is zero. The high viscosities of glass melts and corresponding small growth rates enable the interface temperature ( $T$ ) to be taken as the glass bath or furnace temperature [Kin76], which are easier to measure. Equation (2.77) is useful for small undercoolings, but fails

at very large undercoolings since  $\Delta H_f$  and  $\Delta S_m$  are temperature dependent.

For large undercoolings, it has been presumed [Chi97] that the heat capacity difference between the liquid and crystal remains constant with undercooling, and  $\Delta G_m$  can be better estimated with Hoffman's equation:

$$\Delta G_m = \frac{\Delta H_f (T - T_m) T}{T_m^2} \quad (2.78)$$

In many multi-oxide glass systems, viscosity tends to increase rapidly with decreasing temperature and undercoolings are large. For this case, Hoffman's equation provides the best approximations. (All of the equations in this section are left in terms of the standard relation (2.77), but equation (2.78) can be substituted when appropriate.)

The nature of the matrix/crystal interface has a strong influence on the kinetics of crystallization. Models used to predict the crystallization process are based on different assumptions regarding interface geometry.

In oxide glasses the velocity of crystallization  $u$  is often estimated with

$$u = \frac{\Delta G_m}{3\pi \lambda^2 \eta} \quad (2.79)$$

where  $\lambda$  is the thickness of the transition layer between liquid and crystal. Equation (2.79) demonstrates the reliance of crystallization on temperature, viscosity and  $\Delta H_f$ . Often, crystallization velocity versus temperature is derived using (2.79), but inaccuracies in calculated values may result from uncertainties in geometrical factors.

One factor that has been used to estimate the suitability of applying (2.79) was formulated by Jackson [Dor94]:

$$\alpha = \Delta H_f / RT_m \quad (2.80)$$

where  $R$  is the gas constant.

If  $\alpha \leq 2.0$ , rough interfaces form and (2.79) is not accurate. Values of  $\alpha \geq 4.0$  also result in discrepancies when using (2.79) for reasons not clear [Dor94].

The growth rate for a typical glass is zero at the melting point, increases with undercooling, rises to a maximum, then decreases as the viscosity increases. This is demonstrated with Avrami's equation [Rah95], which also indicates that the volume fraction of crystals  $v$  with a given thermal history is an exponential function of time ( $t$ )

[Rah95]:

$$v = 1 - \exp \left( \frac{-\pi I u^3 t^4}{3} \right) \approx \frac{\pi I u^3 t^4}{3} \quad (2.81)$$

Crystalline phase formation can be observed as exothermic transformations on DTA or DSC curves, while fusion and melting are endothermic. Activation energy for crystal growth ( $Q$ ) has been determined using DTA measurements and [Pop77]:

$$\ln \left[ C_p \frac{d(\Delta T)}{dt} + K\Delta T \right] = \frac{-Q}{RT} + \text{const.} \quad (2.82)$$

where  $C_p$  is the heat capacity of the sample and sample holder,  $K$  is the heat transfer coefficient and  $\Delta T$  is the temperature difference between the sample and reference at time  $t$ . The heat transfer coefficient can be calculated with

$$\Delta H = KA \quad (2.83)$$

where  $\Delta H$  is the total heat evolved during the reaction and  $A$  is the area under the DTA exothermic peak.

For DSC studies with a constant heating rate, the activation energy can be derived from the temperature at the peak maximum point ( $T_p$ ) [Dor94]:

$$\ln \left( T_p \frac{dT}{dt} \right) = \ln (Q/R) - \ln v + Q/RT_p \quad (2.84)$$

where  $dT/dt$  is the heating or cooling rate,  $v$  is a constant and  $R$  is the gas constant. When  $\ln[T_p(dT/dt)]$  is plotted vs.  $1/T_p$  for various heating rates, the slope of the curve is  $Q$ .

The beginning particle size of a glass frit also has an effect on crystallization. An increase in mean particle diameter raises the starting temperature of crystallization and lowers nucleation and crystallization rates. This is depicted on DSC or DTA with a peak exotherm shift to a higher temperature and a reduction in the maximum exothermic band height. Larger particles lower the specific surface area available for surface nuclei formation [Amo94].

If heating rates are sufficiently low, crystal species will precipitate in some glaze compositions during heating and then partially or totally dissolve at the peak temperature, as demonstrated in Figure 2.24. In the case of ceramic tile processing, where cooling is much faster than heating or critical cooling rates, crystals that do not completely dissolve at the peak temperature are "frozen" in their high-temperature state during cooling.

It is common for multi-oxide glasses to develop anisotropic crystal morphologies and growth rates. Pronounced asymmetry in the crystallization rates of multiple species is observed at and in the vicinity of the melting temperature. For this reason, existing models, including those described in this section, may not be completely accurate in describing crystallization kinetics [Kin76].



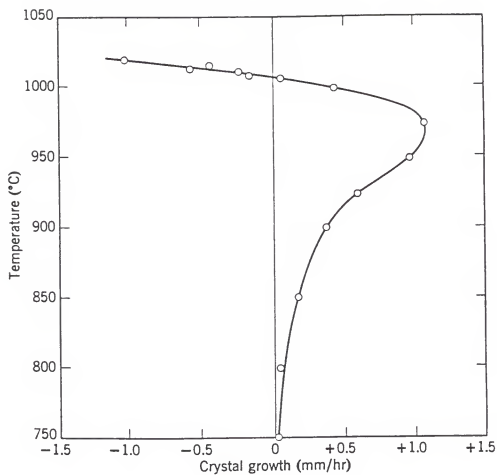


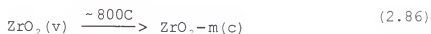
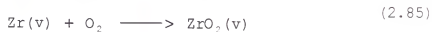
Figure 2.24. Crystal growth rate as a function of temperature in  $\text{Na}_2\text{O-CaO-Al}_2\text{O}_3\text{-SiO}_2$  glass. [Adapted from Kin76]

The equations described in this section help to identify variables which control nucleation and growth during crystallization. Models for accurately estimating crystallization processes for all multi-oxide systems have not been developed. Hypotheses of varying complexity have been proposed, but there is still a great deal of dissention.

#### 2.2.5b Zircon Crystallization and Dissolution

Zircon is an excellent opacifier for glazes due to its high refractive index and ease in forming small crystals that scatter light. Its structure (described in detail in Section 2.2.4d) has good resistance to chemical attack and is relatively stable at high temperature due to its high atomic bonding strength and kinetics of thermodynamic equilibrium. The zircon structure is also widely used as a ceramic colorant due to its thermal stability and ability to accommodate rare-earth metallic ions. Even with its relatively stable properties, dissolution and crystallization of zircon has been found to occur at high temperature in some glazes [Blo94a, Cas97]. This can result in significant variations in optical properties.

Zircon was found to crystallize (c) from  $\text{ZrO}_2$  and  $\text{SiO}_2$  oxides in a vitreous (v) multi-oxide glaze frit during heating, according to sequence [Esc96]:

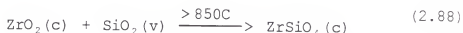


and



where monoclinic (m) and tetragonal (t) zirconia continue to precipitate and can be present up to as high as  $1100^\circ\text{C}$  [Amo94].

Reactions (2.86) and (2.87) are controlled by diffusion of  $\text{ZrO}_2$  structural units to the crystal-glass interface. Finally,



which is a diffusion controlled, first order irreversible reaction. The temperature of maximum crystallization of zircon shifts upward with an increase in heating rate, since the process is time dependent. Normally, crystallization of all species in glazes subjected to rapid heating cycles occurs at  $\geq 900^\circ\text{C}$  [Kin76, Amo94].

Some frits crystallize zircon during the firing process, providing opacity and whiteness. Crystallites formed are

normally  $<10\mu\text{m}$  in size and strongly orient along the crystal c-axis lying in the plane of the glaze surface [Blo93]. Maximum whiteness occurs at a zircon mass fraction of approximately 0.16 [Esc96]. Crystallite size and amount depend on heating time vs. temperature and the frit composition and particle size. Phase diagrams can be used to predict zircon crystallization for simple 2-3 oxide systems.

Nucleation and growth of zircon from frit predominates heterogeneously on the frit particle surfaces. As the specific surface area available for nucleation on particles  $>40\mu\text{m}$  decreases with increasing size, so does the amount of zircon precipitated in a given heating profile. Larger sizes cause crystallization to occur at higher temperatures and at slower rates. Deviations in frit mean particle size between  $>10\mu\text{m}$  and  $<40\mu\text{m}$ , which is the normal range for industrial frits, did not cause variations in crystal growth [Esc96]. Undissolved zircon seeds  $<1.0\%$  by weight in the original frit also had no effect on the results due to the predomination of surface nucleation [Amo94].

Ceramic tiles processed in industry are subjected to nonisothermal firing cycles. At temperatures where nucleation and growth can occur, typical fast-fire cycle heating rates of  $40\text{--}50^\circ\text{C}/\text{min.}$ , peak temperatures of  $1000\text{--}$

1150°C and cooling rates of 100-300°C/min. are utilized. Devitrification of two zircon opacified frits was found to occur during the heating step and hold at the peak temperature, but was not a function of the cooling cycle. Ranges in cooling cycles tested which fell outside of the limits normally employed to manufacture ceramic tile had no effect on the amount or morphology of zircon present in the fired glaze [Esc96].

Dissolution of zircon opacifier and pigment crystals in the glaze melt leads to loss of opacification and color. Dissolution rates increase with higher temperatures, smaller particle sizes and lower viscosities. The solubility limit of zircon in most silicate melts is 3-5% [Kin76, Con97, Par73] but is also dependent on composition and processing conditions.

Zircon by itself dissociates into  $\text{ZrO}_2$  and  $\text{SiO}_2$  at 1720°C  $\pm$  20°C, as shown in the phase diagram in Figure 2.25 [Lev69]. Melting points of the individual oxides are 1713°C for  $\text{SiO}_2$  and 2700°C for  $\text{ZrO}_2$ . Zircon begins to dissolve in a glaze usually below 1100°C, but this varies significantly with the melt composition. No accurate models have been developed for predicting zircon dissolution given the starting glaze or glass frit oxide composition.

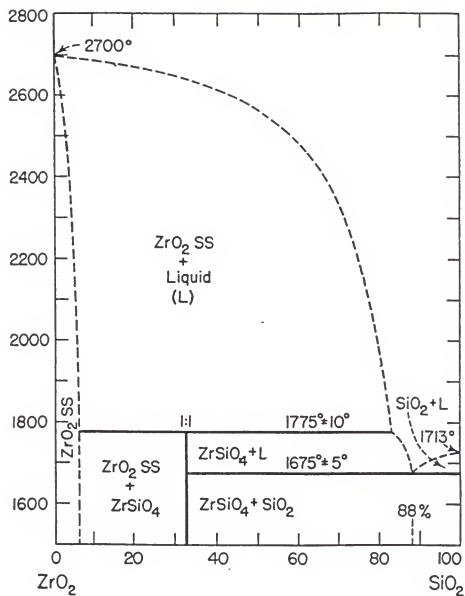


Figure 2.25. Binary phase diagram of  $\text{ZrO}_2$  and  $\text{SiO}_2$  system (temperature in degrees celcius). [Adapted from Lev69]

Castilone et al. (1997) and Concepcion et al. (1977) [Cas97, Con97] found that in one unopacified glaze frit slow-fired to 1100°C, 3% to 5% weight additions of zircon completely dissolved and created  $\text{ZrO}_2$  as a network former. Continuously less zircon dissolved with concentrations increasing from 5% to 13%. From 13% to 23% additions, all of the zircon crystallized and none was present as  $\text{ZrO}_2$  in the final glass structure. They theorized that *complete* dissolution of crystals for satisfying  $\text{ZrO}_2$  requirements in the glass does not occur at high zircon concentrations. Volume is lost from each crystal but the original number of sites remain. The sites function as nuclei seeds for recrystallization during the slow cooling cycle. Recrystallization during the cooling step in fast-fire processes was found not to occur [Esc96].

The effect of particle size on the melting temperature can be related with [DeH93]

$$T(H) = T(H=0) - 2\gamma^s H / \Delta S \quad (2.89)$$

where  $T(H)$  is the melting temperature of a system containing solid particles with a mean curvature  $H$ ,  $T(H=0)$  is the bulk melting temperature (found on most phase diagrams),  $\gamma$  is the specific interfacial free energy (ergs/cm<sup>2</sup>),  $V^s$  is the solid

particle molar volume and  $\Delta S$  is the entropy of fusion.

Equation (2.88) assumes all particles are the same size and spherical. Generally, as a particle size gets smaller, its mean curvature increases, and from (2.89), the melting point is lowered.

The solubility ( $c$ ) of a nonspherical surface is [Chi97]

$$c = c_0 \exp \left[ \frac{\gamma^s}{RT} \left( \frac{1}{r_1} + \frac{1}{r_2} \right) \right] \quad (2.90)$$

where  $r_1$  and  $r_2$  are principal radii of curvature and  $c_0$  is the equilibrium solubility. Again, as the radius of curvature decreases and the interfacial free energy gets larger, the solubility of the solid in the liquid phase increases.

Interfacial free energy is a function of the chemical potential of the solid and liquid phases, temperature and the specific interfacial excess of moles per unit area at the interface.

Blonski [Blo94a] found that the weight % of zircon dissolved in a slow-fire ceramic tile glaze increased exponentially with a decrease in mean particle diameter. He determined that for zircon pigments with an aspect ratio  $>1$ , dissolution was a function of the narrowest cross-sectional dimension.



The sizes of zircon pigments used in industry, usually 1-12 $\mu$ m in mean diameter, provide optimum dispersability in liquid glazes. The sizes of zircon opacifiers utilized varies widely, depending on opacification requirements, firing schedules, glaze compositions and cost.

#### 2.2.5c Liquid-Liquid Phase Separation

Special glaze or glass compositions are formulated so the melt separates into two different liquid phases. More than one amorphous phase remains in the cooled glass and may cause opalescent opacification.

A thermodynamic description of liquid-liquid phase separation is given with  $\Delta G_{\text{mix}}$  vs. composition plots at different temperatures. If the plot is concave upward, a single phase has a lower free energy than any mechanical mixture of two phases with the same average composition and is thus most stable. But a miscibility gap occurs in phases that have a positive excess Gibbs free energy at sufficiently low temperatures. In this case, a single phase is not most energetically favorable, and the plot is concave downward. Spontaneous unmixing of an initially uniform phase, known as uphill diffusion, reduces the difference in chemical potential of the components and lowers the Gibbs free energy

of the system. This thermodynamic process, referred to as spinodal decomposition, is responsible for liquid-liquid phase separation [ DeH93] .

Phase separation in silicate glasses results from a combination of silica network-forming limitations and competition between cations to surround themselves with the lowest energy oxygen configuration [ Kin76] . Nonglass-forming cations with a strong oxygen bond strength can raise the energy of the glass system by breaking up the network. A more energetically favorable system is achieved when two separate phases form; one high-silica network and another favoring the lowest-energy modifier phase. The ionic potential of a cation is used to measure its tendency to cause phase separation in silicates.

Phase separation in ceramic glazes is typically encountered in slow-fire compositions high in  $B_2O_3$ . The resulting two-framework continuous structure consists of one low temperature, boron rich, high alkali  $BO_3$  phase and a  $BO_4$  phase.

In aluminosilicate glasses with high  $B_2O_3$  and low alkali content,  $B^{+3}$  assumes  $BO_4$  tetrahedral and some  $BO_3$  planar coordination. An addition of alkali and alkaline earth oxide modifiers raises the amount of  $BO_4$  formed by increasing

connectivity, with local charge compensation by the alkali. As the alkali oxide concentration is increased beyond approximately 16 mole %, a loss in simple tetrahedral coordination occurs. Less tetrahedral sites are available for  $B^{+3}$  and  $Al^{+3}$ , and they compete for tetrahedral grouping, with  $AlO_4$  favored [Paw96]. Planar  $BO_3$  content increases with higher alkali and  $B_2O_3$ . The amorphous phases associated with  $BO_3$  and  $BO_4$  equilibrium tend to separate from the liquid melt.

Consistent optical properties of ceramic glazes are easier to achieve if phase separation is not a factor. Opacification and color are easier to control with inert particulates suspended in the glassy matrix. The following steps are taken in order to avoid phase separation in fast-fire glazes [Toz86, Par73, Paw96, Tay86, Chi97]:

1.  $B_2O_3$  contents are held  $\leq 10.0$  wt %.
2. Seger's rule #2 is followed (Section 2.22), where the ratio of alkalis to other oxides in the RO group is  $\leq 1:1$ . The overall alkali content is kept at  $\leq 10.0$  wt %.
3. Care is taken to avoid water incorporation in frits during smelting. Introduction of  $OH^-$  groups tends to disrupt the glass network and convert  $BO_4$  to  $BO_3$ . Water can be minimized by using unhydrated batch raw materials

- and smelting with methane fuel which tends to liberate less water during combustion than natural gas.
4.  $\text{Al}_2\text{O}_3$  ( $\geq 2.0$  wt %) and  $\text{ZrO}_2$  additions increase the glass viscosity and have a marked effect on slowing diffusion-driven processes such as immiscibility.
  5. Phase separation is suppressed with rapid cooling from the melt.

#### 2.2.5d Viscosity Relationships

Crystallization and melting conditions are markedly affected by viscosity. Glass viscosity varies enormously with composition and is a strong function of temperature. As demonstrated with equations (2.70), (2.71), (2.79) and Figure 2.23, in previous sections of this dissertation, nucleation rates are a function of  $1/\eta$  and crystallization rates are proportion to  $T/\eta$ . The glass-forming tendency is low and crystallization rates are high in glasses that exhibit a low viscosity increase with decreasing temperature near the liquidus point [Sim93].

Viscosity is related to the internal friction of atoms or groups. Stronger, more complex bonds and low disruption of glass-forming chains results in higher viscosity. Low viscosity enhances diffusion, and related process such as

nucleation and growth, by increasing atomic mobility and chemical changes. The addition of oxides to silica always drops its viscosity. As shown in Figure 2.26, the lowering is least with alumina and alkaline earth oxides and greatest with alkali oxides, ZnO and B<sub>2</sub>O<sub>3</sub>, which tend to break up the silicate lattice [Dor94].

At high temperature, glasses exhibit Arrhenius behavior [Dor94]:

$$\eta = \eta_0 \exp (Q/RT) \quad (2.91)$$

where  $Q$  is the activation energy for viscous flow and  $\eta_0$  is a temperature independent coefficient.

Investigators found that glasses follow Arrhenian behavior at very high temperatures and below the glass transition temperature ( $T_g$ ), but the true viscosity is greater than predicted by (2.91) at intermediate temperatures above  $T_g$  [Sim93].

The Vogel-Fulcher-Tamman equation (VFT) has been applied to calculate  $\eta$  while accounting for the non-Arrhenian stage:

$$\eta = \eta_0 \exp \left( \frac{A}{T - T_0} \right) \quad (2.92)$$

or

$$\log \eta = A + B/(T - T_0) \quad (2.93)$$

where  $T_0$ ,  $A$  and  $B$  are constants.

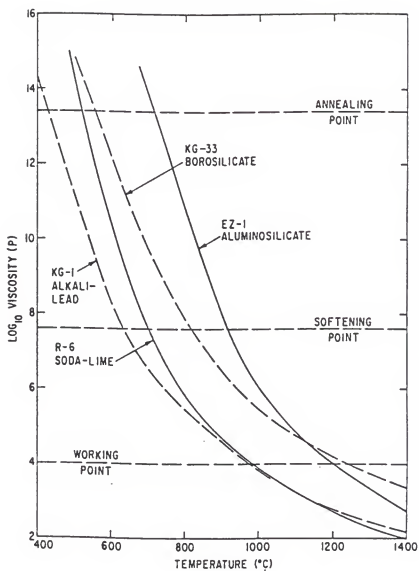


Figure 2.26. Viscosities of some commercial silicate glasses. [Dor94]

Figures obtained from the VFT equation are more accurate than equation (2.91) for a wide temperature range, but calculated values begin to diverge from actual viscosities near  $T_g$ .

Ceramic whitewares manufacturers and researchers in Europe and the U.S. normally calculate the viscosities of glass frits and glazes using the VFT equation 2.93. The constants  $T_0$ , A and B are derived with mathematical models which require parameters that are measured with dilatometry and heating microscopy techniques [Bur96, Con97, Sch62, Pag97] .

The heating microscope measures dimensional changes of a sample as it is heated. The technique, in principle, is based on the relationship between dimensional changes of a sample ( $\Delta L/L_0$ ) and its surface tension ( $\gamma$ ) and viscosity under gravitational force ( $g$ ) during heating. At a fixed temperature, the sintering relationships are

$$\alpha = \frac{\Delta L}{L_0} = \frac{3\gamma}{4\eta r} \quad (2.94)$$

and for nonisothermal conditions are

$$\frac{\partial \alpha}{\partial t} = \frac{(3\gamma) / (4\eta r)}{(\partial T) / (\partial t)} \quad (2.95)$$

where  $r$  is the principal radius of curvature of the material. As viscosity drops with increasing temperature, the sample's

surface tension tends to pull it into a spherical shape and the force of gravity pulls it downward. Considering that viscous flow is not in equilibrium during firing, the dynamic conditions are described with

$$\frac{2\gamma}{b} - \rho gh - \frac{2\gamma}{r} = \eta(\partial v / \partial x) \quad (2.96)$$

where  $b$  is a constant  $\rho$  is sample density,  $g$  is gravitational force,  $h$  is the height of the sample and  $\partial v / \partial x$  is the rate of change of kinematic viscosity with thickness.

VFT equation (2.93) constants  $T_o$ ,  $A$  and  $B$  are calculated for glazes and frits from models which assume the following characteristic points [Bur96, Con97, Sch62]:

$$\eta = 10^{13} \text{ poise at the dilatometric } T_g$$

$$\eta = 10^{10.25} \text{ poise at the dilatometric softening point, } T_s$$

$$\eta = 10^{4.55} \text{ poise at the half-sphere point determined by a heating microscope, } T_{1/2}$$

The models are

$$T_o = \frac{13T_g - 4.55T_{1/2} + (10.25T_s - 13T_g)(T_{1/2} - T_g) / (T_s - T_g)}{8.45 - 2.75(T_{1/2} - T_g) / (T_s - T_g)} \quad (2.97)$$

$$A = \frac{10.25 T_s - 13 T_g + 2.75 T_o}{T_s - T_g} \quad (2.98)$$

$$B = (T_g - T_o)(13 - A) \quad (2.99)$$

where all temperatures are in degrees celsius.



These models yield useful viscosity data for crystallization and dissolution studies involving fast-fire ceramic glazes and frits because

1. The characteristic viscosity data at  $T_g$ ,  $T_s$  and  $T_{1/2}$  are well known for these specific materials.
2. Crystallization and dissolution in fast-fire systems occurs at temperatures exceeding 900°C [Amo94, Toz86, Apa94, Con97]. The  $T_g$ , where accuracy of the VFT equation is reduced, is far below this temperature at  $T_g < 700^\circ\text{C}$ .
3. Glasses with high  $T_s$ , such as silicate fast-fire frits, tend to follow Arrhenian-type behavior over most of the melt-forming temperature range [Dor94], which improves VFT equation accuracy.

Lehmann, Engell and Hellbrugge found a good correlation between the dimensional changes in a glaze during firing and the measured viscosity of bulk glaze in a crucible. James and Norris identified that glaze exhibited Newtonian flow as an ideal fluid at high temperature, even when loaded with 5% inert pigment particles. Glazes behave in accordance with traditional glass viscosity theories and viscosity-temperature curves [Par73].

## CHAPTER 3 EXPERIMENTAL PROCEDURES

### 3.1 Materials and Methods

A total of thirty-two batches were prepared from eight glass frits loaded with four different zircon-vanadium pigment concentrations of 0%, 0.5%, 2.0% and 5.0%. The batches were blended with water and a suspending agent and applied to white opaque ceramic tile substrates using a wet spray method. The green coatings were fired to 1000°C, 1050°C and 1100°C peak temperatures utilizing a typical industrial "fast-fire" ceramic tile firing curve. A total of 96 different fired samples were produced for examination.

#### 3.1.1 Glass Frits and Zr-V Pigment

Compositions of the eight glass frits investigated are listed in Table 3.1. They incorporate the most cost effective and environmentally safe oxides for producing frits. Formulations do not include BaO or PbO which are now designated as hazardous materials by the EPA. The range of oxide contents formulated exceeds the range normally utilized



Table 3.1--continued.

Molar Equivalents (Segey):	A	B	C	D	E	F	G	H
SiO <sub>2</sub>	2.267	1.778	2.459	1.907	1.857	1.494	1.984	1.583
B <sub>2</sub> O <sub>3</sub>	0.214	0.184	0.232	0.198	0.146	0.129	0.156	0.123
Na <sub>2</sub> O	0.08	0.138	0.087	0.148	0.065	0.116	0.07	0.123
K <sub>2</sub> O	0.079	0.136	0.086	0.146	0.065	0.114	0.069	0.121
CaO	0.353	0.305	0.383	0.327	0.47	0.416	0.502	0.441
Al <sub>2</sub> O <sub>3</sub>	0.097	0.084	0.105	0.09	0.159	0.141	0.17	0.149
ZrO <sub>2</sub>	0.161	0.139	0.175	0.149	0	0	0	0
MgO	0.123	0.106	0.133	0.114	0.101	0.089	0.108	0.094
SrO	0	0	0.311	0.266	0	0	0.251	0.22
ZnO	0.365	0.315	0	0	0.299	0.265	0	0
Molecular weight	247.7	213.7	268.7	229.3	202.9	179.6	216.8	190.2
Si:Al	23.37	21.17	23.42	21.19	11.68	10.60	11.67	10.6
RO:RO <sub>2</sub>	0.41	0.52	0.38	0.49	0.54	0.67	0.50	0.63
Alkalis:Other RO	0.19	0.38	0.21	0.42	0.15	0.30	0.16	0.32
Σ R <sub>2</sub> O <sub>3</sub>	0.31	0.27	0.34	0.29	0.30	0.27	0.33	0.29
Σ RO <sub>2</sub>	2.43	1.92	2.63	2.06	1.86	1.49	1.98	1.58
Calculated Expansion Coeff. (Hall) (50-450°C; X 10 <sup>-6</sup> /C	7.3	8.9	7.8	9.4	7.7	9.3	8.2	9.7

for glossy fast-fire glazes, conforms to Seger's empirical rules outlined in Section 2.2.2 and was designed to avoid phase separation by following the steps outlined in Section 2.2.5c. Frits for producing glossy coatings were evaluated because the vast majority of whiteware glazes are glossy. Major variations in compositions between the frits involved  $\text{ZrO}_2$  content (0% and 8%), replacement of  $\text{ZnO}$  with  $\text{SrO}$ , and alkali: $\text{SiO}_2$  ratio. The alkalis ( $\text{K}_2\text{O}$  and  $\text{Na}_2\text{O}$ ),  $\text{SrO}$  and  $\text{ZnO}$  were of special interest because of their extensive use as fluxes and their marked influence on modifying the  $\text{SiO}_2$  glass network. In frits containing no  $\text{ZrO}_2$ ,  $\text{Al}_2\text{O}_3$  and  $\text{CaO}$  were increased to follow industrial practice.

The frits were produced by Ferro Corporation in Cleveland, Ohio, by laboratory smelting raw materials at approximately  $1400^\circ\text{C}$ , water quenching to avoid unwanted crystallization, then ball milling to achieve the desired particle size. Compositions were confirmed using AAS and XRF analyses outlined in Section 3.2.1.

A zircon-vanadium (Zr-V) blue pigment 41715A *dispersible stain* from Ceredec Corporation was the colorant tested. This is the most commonly used Zr-V pigment in the whitewares industry. Its mechanisms for color production are detailed in Sections 2.1.2d and 2.2.4a. Of the three triaxial

pigments, blue was chosen because it has intermediate high temperature stability when compared to Zr-Pr yellow (lowest stability) and Zr-Fe coral (highest stability) [Dec93]. Also, color changes due to precipitated crystal species are more distinguishable when using blue colorants because most devitrified phases tend to scatter light of wavelengths near blue pigment's peak absorption in the red to yellow region.

### 3.1.2 Coatings Preparation and Application

Coatings formulations consisted by dry weight of 0%, 0.5%, 2.0% or 5.0% Zr-V, 2.5% Bentonite B from Milwhite Inc. and frit. The materials were blended with water and applied over a 2"x6" opaque ceramic tile body substrate using a wet spray method.

Bentonite (68.6%  $\text{SiO}_2$ , 18.4%  $\text{Al}_2\text{O}_3$ , 2.4%  $\text{Fe}_2\text{O}_3$ , 1.9%  $\text{MgO}$ , 1.4%  $\text{CaO}$ , 1.1%  $\text{Na}_2\text{O}$ , 6.2% LOI) was necessary for suspension and avoidance of settling prior to spraying. Levels of Zr-V pigment concentrations comprised the range applied in industrial glazes, where 0.5% to 2.0% zircon pigment loading is most common. The substrate was ceramic wall tile body which contained a 0.25 mm thick layer of Florida Tile's white opaque engobe primer. The substrate was prefired before

coatings were applied in order to avoid body volatilization influence on the results.

The thickness of a ceramic coating influences its opacity (equations 2.31 and 2.32 in Section 2.1.2c). An opaque substrate is required for implementation of Kubelka-Munk equations (Section 2.2.4b) for calculation of color strength due to the pigment. For these reasons, careful control was maintained to ensure that a constant volume of coatings solids was applied to each substrate in order to negate this as a color influencing variable.

A volume of 2.70 cm<sup>3</sup> of glaze solids on a 2"x6" substrate represents average industrial specifications. Water was added to provide a 1.75 specific gravity for each wet glaze, and then the application weight which provides 2.70 cm<sup>3</sup> volume of solids was calculated with

$$W = \frac{V_s M}{P} \quad (3.1)$$

and

$$P = \frac{M - MS}{S - MS} \quad (3.2)$$

where

W = coating application weight (grams)

V<sub>s</sub> = volume of solids = 2.70 cm<sup>3</sup>

P = weight % solids

$M$  = density of solids ( $\text{g}/\text{cm}^3$ )

$S$  = specific gravity of coating = 1.75

The procedure used for determining  $M$  is outlined in Section 3.2.2 and the results are discussed in Section 4.1.

### 3.1.3 Firing Curves

Tiles were fired in a relatively small (20 m length) industrial pilot roller kiln at Florida Tile Industries. The high volume of air and gas flow in the kiln ensures uniform temperature distribution and close correspondence between thermocouple readings and actual tile temperatures. Figure 3.1 displays the time-temperature profiles employed, consisting of three different curves with peak temperatures of 1000, 1050 and 1100 degrees celsius. The shapes of the curves (i.e., heating and cooling rates, hold at the peak temperature, etc.) equate to typical industrial fast-fire tile processing. A previous study of fast-fire tile processes concluded that the heating rate above the glaze softening temperature (approximately  $\geq 700^\circ\text{C}$ ) and the hold time at the peak temperature influenced glaze development, but the cooling rate had no effect [Amo94]. Figure 3.1 shows a heating rate above  $700^\circ\text{C}$  of  $43^\circ\text{C}/\text{min.}$  and a 4-minute hold time at the peak temperature.



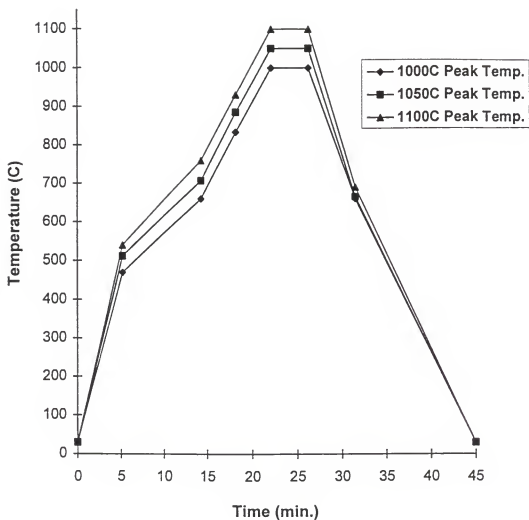


Figure 3.1. Time-temperature profiles used to fire the tiles.

Following the initial firing of samples, preparation and firing of tiles with frits A and E were repeated to verify test method consistency. No visual differences were observed between initial and repeated tests.

### 3.2 Materials Characterization and Analytical Techniques

#### 3.2.1 AAS and XRF

Smelted frit compositions were confirmed using a Perkin Elmer model 2100 atomic absorption spectrometer (AAS) for all oxides except  $B_2O_3$ ,  $ZnO$ ,  $SrO$  and  $ZrO_2$ . The accuracy of the device is approximately  $\pm 0.5\%$  for  $SiO_2$  and  $Al_2O_3$ ,  $\pm 0.1\%$  for alkaline earth oxides and  $\pm 0.05\%$  for alkalis. A Rigaku 3370 wavelength dispersive x-ray fluorescence (XRF) spectrometer confirmed the weight percent of the other oxides to within 0.5% accuracy by implementing an Agel computer program.

#### 3.2.2 Frit Density Determination

Weights of 50, 100 and 150 grams of dried frit were added to 300 cc of water and blended thoroughly. The specific gravity of each mixture was measured and input along with the weight percent solids into equation 3.2. The

equation was solved for M, and the average M for the three weights was taken to be the frit true density. The bentonite density was found using the same method. The results were input into equation 3.1 in order to determine the required coating application thickness.

### 3.2.3 Laser Diffraction Particle Size Analysis

A Coulter LS 100 Fraunhofer laser diffraction device was used to measure frit and pigment particle size distributions. Frits with very close particle size distributions were desired for the experiments.

### 3.2.4 Spectrophotometry and Color Calculations

A Macbeth White-Eye 3000 spectrophotometer was employed to generate reflectance versus wavelength data from 360 nm to 740 nm. The general method applied was previously outlined in Section 2.1.4a. The light source was a pulsed xenon flash lamp which produces light with almost exactly the same wavelength distribution as daylight. When compared to tungsten sources, xenon provides more accurate measurements, and no heating of the sample occurs. Illuminance near  $10^3$  cd/m<sup>2</sup> is furnished, which relates to cone vision described in Section 2.1.3.

The spectrophotometer was configured to exclude the specular reflection component in order to eliminate variations in gloss (from differences in surface roughness due to poor coatings applications) as a variable in color calculations. Specular reflectance was also excluded so that  $R_{\min}$  could be applied in equation 2.64 to calculate color strength.

The diffraction grating, photodetectors and microprocessor were arranged to output results in terms of a D65 noon daylight standard source and a 2-degree angular subtense.

Spectral reflectance curves were converted into CIE  $L^*$ ,  $a^*$  and  $b^*$  values so correlations to human vision could be achieved. For each tile sample, measured reflectance, standard observer weighting functions and light energy values in terms of wavelength were integrated from 400 nm to 700 nm using equations 2.47-2.49 in order to calculate tristimulus values  $X$ ,  $Y$  and  $Z$ . These values as well as  $X_n$  and  $Z_n$  factors shown in Table 2.4 for a 2-degree observer were used to calculate  $L^*$ ,  $a^*$  and  $b^*$  from equations 2.53-2.55.

Equation 2.56 was applied to calculate  $\Delta E^*$  for quantifying color changes resulting from firing tiles to different peak temperatures. A smaller  $\Delta E^*$  indicates that a

color is less sensitive to variations in firing temperature and thus is more stable. A  $\Delta E^*$  of 1.0 is "just noticeable" and ANSI specifications for ceramic tile glazes list a tolerable range of  $\Delta E^* \leq 3.0$ .  $L^*$ ,  $a^*$  and  $b^*$  values at 1050°C and 1100°C were used to calculate  $\Delta E^*$  because this is the peak temperature range typically utilized by ceramic tile manufacturers.

Absorption factors (K/S) were calculated using equation 2.64 and were employed to quantify color strength. Values of K/S were calculated using R-values at the wavelength where maximum absorption of visible light by the pigment occurred.

### 3.2.5 Gloss Measurements

Gloss or specular reflectance was measured separately from color, using a Hunter Lab ProGloss PRO-3 gloss meter. The data were used to supplement the XRD analyses in identifying devitrification and to provide a better description of the visual quality of the fired coatings. Light was directed onto the samples at 60° from perpendicular, which is standard for glazes and corresponds to an index of refraction of  $n = 1.7$  according to Brewster's law (equation 2.27, Section 2.2.1b).

### 3.2.6 Heating Microscopy

Melt viscosity and flow of coatings batched with 2.0% Zr-V pigment were studied using a Misura 2.0 Heating Microscope (HSM). Dry batches were pressed into small samples approximately 1x1x5 mm in dimension. The samples were heated in the microscope's furnace at a rate of 43°C/min. up to 1150°C peak temperature in order to simulate the experimental firing curves. Sample images were acquired during heating with a CCD TV camera and lens digital system, with a resolution of 1  $\mu$ m. Photographs of the samples at various temperatures were generated and their geometries were compared and related to flow behavior. Parameters such as sample height, width, contact angle and their temperature derivatives are automatically measured by the HSM software to as low as 0.1% dimensional change.

Half-sphere temperatures ( $T_{1/2}$ ) established using heating microscopy, and dilatometric  $T_g$  and  $T_s$  data were entered into equations 2.97-2.99 and then 2.93 in order to generate  $\log \eta$  versus temperature plots based on the models described in Section 2.2.5d.

### 3.2.7 Dilatometry

Dry coatings batches were pressed into 25-50 mm long rods and heated with a Netzsch dilatometer at a rate of 43°C/minute to just above the glass softening temperature. Both  $T_g$  and  $T_s$  were identified and coefficients of thermal expansion were calculated.

### 3.2.8 X-Ray Diffraction (XRD)

X-ray diffraction scans were performed on all unfired and fired coatings containing 2.0% Zr-V pigment. This colorant loading level was selected for the analyses because a range of 0.5-2.0% zircon pigment is most commonly used in industry, but the 2.0% level would better conceal the substrate and thus improve the XRD quantitative analysis accuracy.

The XRD scans and JCPDS cards were used to qualitatively identify all crystalline phases that developed during firing. A quantitative analysis of zircon content in the unfired and fired coatings served to measure any pigment dissolution or zircon crystallization in frits containing  $ZrO_2$ . These results were equated to the color strength and stability of the coatings.

A Siemens D500 Diffractometer scanned samples at a  $2\theta$  range of  $10-60^\circ$  with a step size of  $0.02^\circ$   $2\theta$  and a counting time of 2 seconds/step using  $\text{CuK}\alpha$  radiation. In order to achieve maximum diffraction intensity and to ensure X-rays do not detect phases under a coating, the thickness of a coating ( $t$ ) should be [Ale74]

$$t \geq \frac{3.2 \rho \sin \theta}{\mu \rho'} \quad (3.3)$$

where  $\mu/\rho$  is the mass absorption coefficient,  $\rho'$  is the coating density and  $\theta$  is the XRD scan angle. Calculations with (3.3) using the mass absorption coefficients ( $\text{CuK}\alpha$ ) of the elements in the coatings at the minimum application thickness tested revealed that coating densities  $\geq 1.8 \text{ g/cm}^3$  are sufficient for avoiding transmission through to the engobe substrate. Section 4.1 provides the results of the frit density determinations.

Measurement of zircon content first involved scanning unfired coatings with known quantities of zircon from  $50-57^\circ$   $2\theta$  and computing the integrated areas under the  $53.5^\circ$   $2\theta$  reflection peaks. A  $2\theta$  of  $53.5^\circ$  for zircon corresponds to [312] Miller index reflection. A zircon weight % versus integrated intensity baseline curve was established from the unfired standards using regression methods. This



relationship was applied to estimate the quantity of zircon in fired coatings based on their measured integrated [ 312] intensity.

Previous studies found that zircon forming at the glaze surface has a strong orientation along the c-axis lying in the plane of the surface. This causes substantial exaggeration of [ h00] and [ hk0] lines. Therefore, mixed index lines such as [ 312] are less susceptible to surface orientation effects and more accurate for measuring zircon content in ceramic coatings [ Blo93, Blo94a, Cas97] .

#### 3.2.9 Scanning Electron Microscopy (SEM) and Energy Dispersive X-Ray Spectroscopy (EDS)

A JEOL JSM-6400 SEM was used to generate micrographs of crystalline phases present in the fired coatings, at 1000X and 6000X magnification. Crystalline precipitate sizes, distributions and morphologies resulting from different frits and firing temperatures were compared and related to color development.

Crystalline species that were difficult to identify with XRD due to strong preferred orientation were analyzed with a Tracor System II EDS under SEM view. A semi-quantitative analysis of elements present in unidentified crystals

assisted in distinguishing their phase. Samples evaluated with EDS were coated with carbon rather than gold-palladium because carbons peaks overlap less with the peaks of other elements in the frits.

### 3.3 Statistical Methods for Deriving Equations

Rigorous statistical analyses of the results data were conducted for the purpose of quantifying variable relationships. Several linear and nonlinear equations were developed from the experiments:

1.  $L^*$  (perceived lightness) versus  $b^*$  (perceived yellowness-blueness).
2.  $L^*$ ,  $a^*$  (perceived redness-greenness) and  $b^*$  versus K/S (pigment absorption factor) (3 equations).
3. K/S versus frit composition for Zr-V loadings of 0.5%, 2%, 5% and 0-5% (4 equations).
4.  $\Delta E^*$  (color change from 1050°C to 1100°C peak temperature) versus frit composition for Zr-V loadings of 0.5%, 2%, 5% and 0-5% (4 equations).
5. Weight percent zircon versus zircon [312] XRD integrated peak intensity.

6. K/S, L\*, a\* and b\* versus weight percent zircon precipitated from frit loaded with 2% Zr-V pigment (4 equations).
7. Log  $\eta$  versus temperature and frit composition with 2% Zr-V loading.

Equations 1-7 were created using experimental design and analysis computer software [Bow87]. Independent variables with calculated absolute t-values  $\geq 1.9$  were considered to have significant effects (95% confidence level) on the dependent variable and were included in the equation. A t-value is given by [Bow90]

$$t = \frac{b_i}{S(b_i)} \quad (3.4)$$

where  $b_i$  is the regression coefficient for the  $i^{\text{th}}$  variable and  $S(b_i)$  is the standard deviation of the  $i^{\text{th}}$  coefficient.

Equation coefficients were generated with a least squares regression method [Dow83]. The procedure involves minimizing the sum of squares of the residuals by differentiating with respect to each unknown coefficient, setting the equations equal to zero and solving for the coefficients using matrix methods. Linear, nonlinear and interactive relationships were identified using this method.

Other statistics were also applied to confirm equation validity. Coefficients of multiple correlation ( $R^2$ ) were computed to indicate the total variability of the dependent variable explained by an equation.

The  $R^2$  is given by [Bow90]

$$R^2 = 1 - \frac{(n-p-1) (S_{y \cdot x})}{(n-1) (S_{TOT})} \quad (3.5)$$

where  $n$  is the number of experiments,  $p$  is the number of terms in the equation,  $S_{TOT}$  is the standard deviation of dependent variable actual values and  $S_{y \cdot x}$  is the standard deviation of the residuals. The expected accuracy of a statistically derived equation is  $\pm 2S_{y \cdot x}$ , with a 95% confidence level.

Statistics that were evaluated in order to detect outlier experiments, unidentified time effects and model overfitting included externally studentized (E.S.) and standardized (Std.) residuals, Cook values and Durbin Watson (DW) statistics. Absolute values of E.S. or Std. residuals  $> 3.0$  or  $> (1.5X \text{ the next largest residual})$  are considered outliers. For  $DW < 1.0$ , unidentified time-related effects exist, while  $DW > 2.5$  suggests an overfitted equation. Comparisons of Cook values were made to determine the impact of each individual experiment on the overall equation.

## CHAPTER 4 RESULTS

### 4.1 Frit and Pigment Properties

AAS and XRF analyses confirmed the compositions listed in Table 3.1. Trace quantities of  $\text{Fe}_2\text{O}_3$  ( $\leq 0.08\%$ ) were also found in each of the frits.

Densities, mean particle diameters and coatings application weights calculated based on the frit densities are listed in Appendix C. Frit mean particle diameters ranged from 20 to 28 microns with mean/median ratios of 1.50-1.75. These values conform to industrial standards. The pigment particle size distribution was typical, with a mean of 8.9 microns and a  $\pm 2$  standard deviations range of 0.4 to 12.29 $\mu\text{m}$ . Frit densities ranged from 2.70 to 2.91  $\text{g}/\text{cm}^3$ , which were well above the minimum of 1.80  $\text{g}/\text{cm}^3$  (Section 3.2.8) required to avoid x-ray transmission through to the substrate. This assumes the densities are not significantly lowered during fast-fire ceramic tile processing.

#### 4.2 Color of Fired Coatings

Appendix D tabulates the frit composition, Zr-V loading and peak firing temperature versus  $L^*$ ,  $a^*$ ,  $b^*$ ,  $\Delta E^*$ , K/S, gloss and glaze fit (i.e., crazing) observations for all 96 experiments. None of the optical properties were found to correlate to differences in the coatings application weights which were required to supply a constant volume of solids on the substrate.

Normally, the appearance of a colored opaque ceramic tile glaze is uniform throughout the entire surface while translucent coatings are darker at the tile edges. Greenware tile edges have a higher pressed density than the center of the piece. The resulting lower pore volume at the edges causes water to be absorbed from the applied wet coating at a slower rate. The longer drying time allows for fine pigment particles to segregate to the surface above coarse frit particles, due to the pigment's slower settling rate. This segregation at the edges results in a denser color layer and a darker fired appearance only if there is not enough dispersed pigment and/or crystalline phases present to produce a completely opaque coating.

Coatings with frits A-H fired to 1000°C and 1050°C, and frits A, B, C and H fired to 1100°C appeared to be opaque.

Thus, their colors are a function of incident light reflected by the pigment crystal structure and other species that precipitated in the coatings during firing, minus light absorbed by the vanadium metal atoms on the pigment lattice. Effects due to transmission of light through to the engobe substrate were not evident.

Coatings with frits D, E, F and G fired to 1100°C appeared to be *slightly* translucent. Thus, their colors are mainly a function of reflection by the Zr-V pigment and other crystalline phases in the glasses, minus absorption by the vanadium. In addition, a small amount of reflection from the opaque engobe substrate background may have influenced the appearance of these coatings. The engobe was very light and slightly yellow (Figure 4.1), so it would tend to lessen the blue color from the Zr-V.

The crystallization and pigment dissolution which caused differences in the optical properties of the coatings are detailed in Section 4.5 and Chapter 5.

#### 4.2.1 Spectral Reflectance Curves

Figure 4.1 shows the spectral reflectance versus wavelength profiles for the unfired batch materials and the engobe substrate. Maximum absorption by the Zr-V pigment

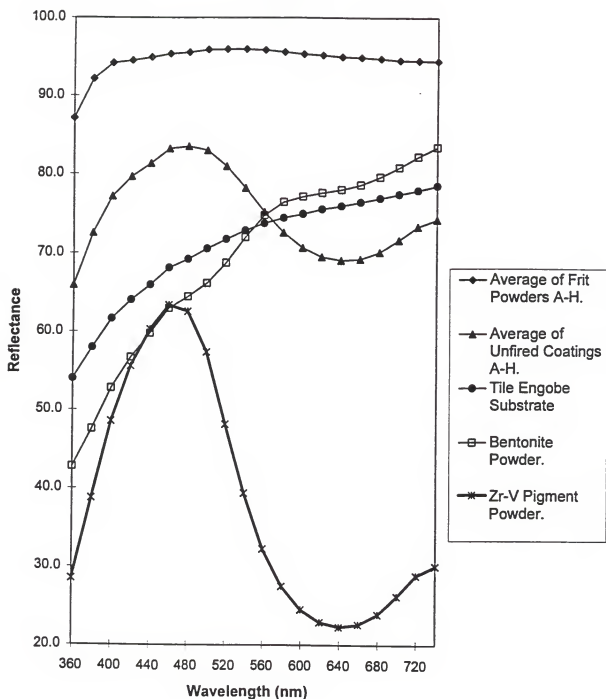


Figure 4.1. Spectral reflectance of unfired raw materials and the engobe substrate backing (coatings contain 2% Zr-V, 2.5% bentonite and 95.5% frit by weight).



occurs at 640 nm. The Zr-V reflectance value of 22 at 640 nm may be artificially high because powders were measured in clear plastic bags that may scatter a small quantity of light. Maximum reflectance from Zr-V within the visible spectrum occurred from 440-480 nm. Thus, Zr-V absorbs yellow to red light and reflects blue to green.

From equation 2.1, Zr-V characteristic peak absorption or  $R_{\min}$  at 640 nm equates to 1.94 electron volts of energy. This is the difference in energy between split d orbitals in  $V^{+4}$  which allows electron transitions from the ground to excited state. Dissolution of the Zr-V pigment into the glass structure during firing would change the coordination about  $V^{+4}$ , resulting in a loss of split orbitals and the energy gap that causes absorption of visible light. Hence, a reduction in the absorption of 640 nm light and a corresponding loss in blue color would occur. Therefore, K/S calculated with equation 2.64 using reflectance values at 640 nm could be applied as an indicator of pigment color strength and dissolution.

In Figure 4.1, the reflectance of unfired coatings is a weighted combination of the frit, bentonite and Zr-V curves. The unfired coatings were opaque; therefore, their reflectance curves were not influenced by the engobe backing.

Frit and bentonite increase the amount of yellow light reflected and thus lower the quantity of 640 nm light absorbed by the pigment. Spectral curves of all unfired coatings were compared, and one trial exhibited a significantly lower reflectance of yellow light, indicating a batching error where the bentonite was missing. This batch was repeated and yielded a reasonable reflectance curve.

Figures 4.2 and 4.3 display changes in reflectance curves of fired coatings due to pigment loading. Increases in pigment content caused the curves to shift towards the Zr-V pigment powder profile in Figure 4.1. Higher Zr-V resulted in a maximum reflectance shift towards lower wavelengths which approach 460 nm (blue light) and reduced reflectance values above 460 nm. Comparisons of Figure 4.2 and 4.3 demonstrate the extreme variation in optical properties resulting from different frits. With 2.0% Zr-V content, frit C fired to 1000°C had the highest absorption at 640 nm ( $R = 15.0$ ) while frit H fired to 1100°C yielded the lowest ( $R = 51.6$ ). Spectral properties of the unglazed engobe substrate were found to be stable over the firing range investigated and thus did not cause color shifts due to changes in peak temperature. Appendix E reveals spectral reflectance curves for all 96 fired coatings.

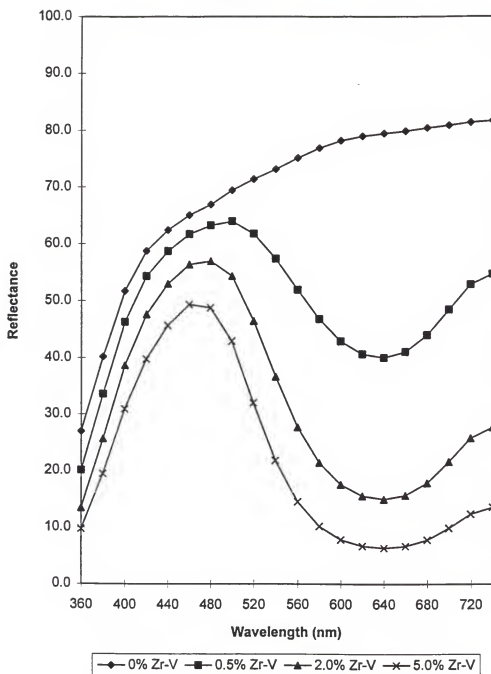


Figure 4.2. Spectral reflectance of coatings batched with frit C, fired to 1000°C.

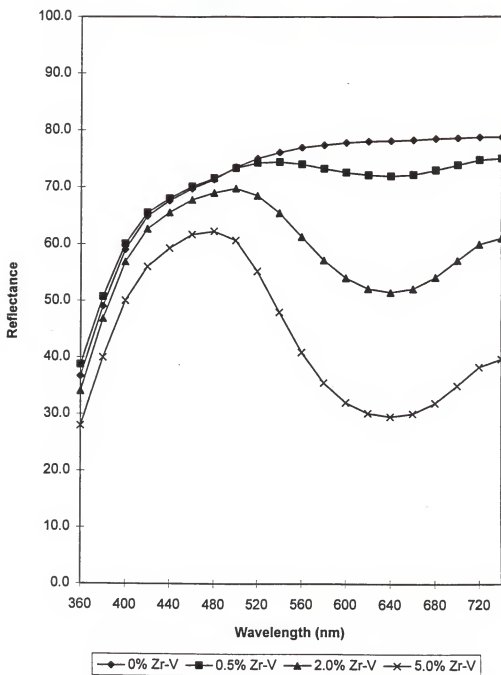


Figure 4.3. Spectral reflectance of coatings batched with frit H, fired to 1100°C.

Figures 4.4, 4.5 and 4.6 illustrate peak firing temperature effects on reflectance from coatings batched with 2.0% Zr-V. At 1000°C, frit A produced the lowest absorption at 640 nm and frit C the highest, while the overall shapes of all the curves are alike. From 1000°C to 1100°C several changes occurred. Peak reflectances from E, F, G and H, the frits containing no  $\text{ZrO}_2$ , shifted to higher wavelengths. From 1000°C to 1100°C, maximum reflectance raised from 460 nm to approximately 490 nm for E and G, and 500 nm for F and H. Reflectance at 640 nm increased slightly with frits A, B, C, D and to a much greater degree with frits E, F, G and H. The data show a strong decrease in the amount of yellow light absorbed from fired coatings batched with frits containing no  $\text{ZrO}_2$  as the peak firing temperature was raised from 1000°C to 1100°C.

#### 4.2.2 Pigment Absorption Factors (K/S)

Absorption factors (K/S) calculated using  $R_{640\text{nm}}$  values are plotted versus weight percent Zr-V in Figure 4.7. Although Figure 4.7 confirms a previous study which found a linear correlation between K/S and pigment concentration [Epp97b], the strong influence of matrix conditions on the slope of the curve is evident. The relationship between K/S

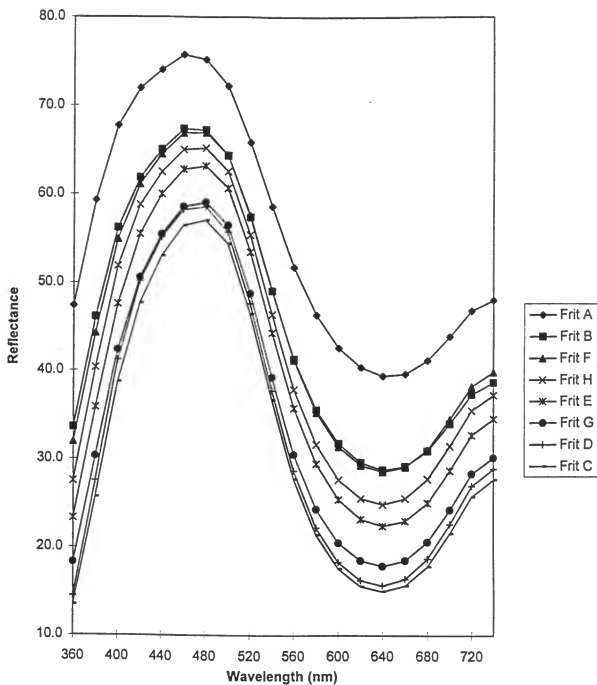


Figure 4.4. Spectral reflectance of coatings batched with 2.0% Zr-V, fired to 1000°C.

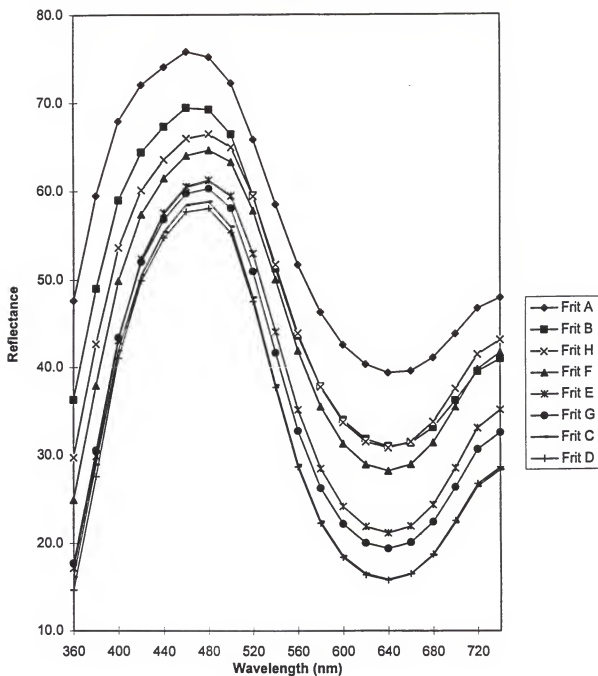


Figure 4.5. Spectral reflectance of coatings batched with 2.0% Zr-V, fired to 1050°C.

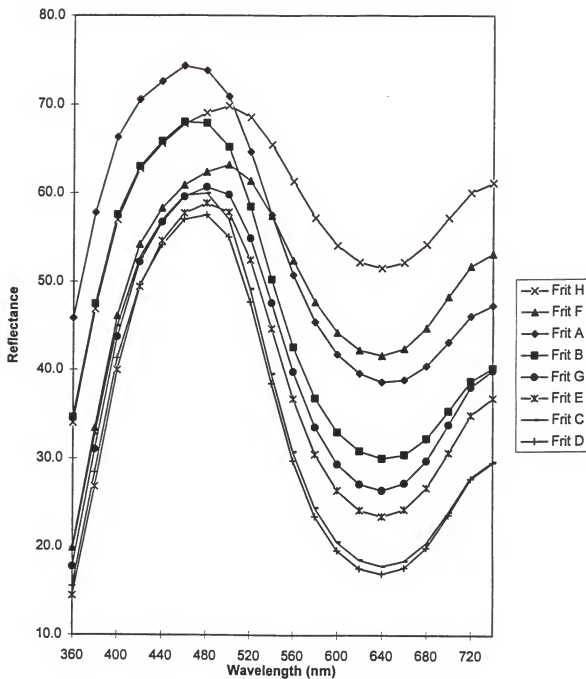


Figure 4.6. Spectral reflectance of coatings batched with 2.0% Zr-V, fired to 1100°C.



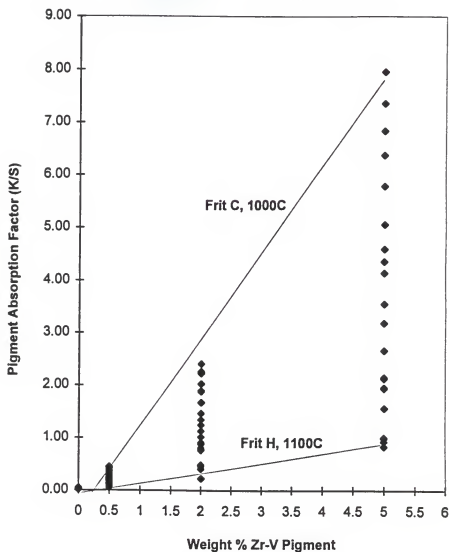


Figure 4.7. Pigment absorption factors versus weight percent Zr-V batched in coatings fired to 1000°C, 1050°C and 1100°C peak temperature. Labeled are data points and linear regression lines that represent frit/peak temperature combinations which yielded the highest (C, 1000°C) and lowest (H, 1100°C) K/S values.

and Zr-V content remains nearly linear for each frit composition/peak firing temperature combination, but the slopes of the curves vary greatly with changes in frit composition and temperature. The temperature and frit composition effects on K/S are quantified with equations derived in Section 4.4.1 of this dissertation.

#### 4.2.3 Color in L\*, a\* and b\* Values

Figures 4.8 and 4.9 compare color values which relate to human vision, for coatings fired to 1050°C and 1100°C, respectively. Good correlation between trends at different pigment loadings confirms test method repeatability. The a\*-value (redness-greenness) plot at 5.0% Zr-V was the only ambiguous data. Otherwise, color progressed darker (lower L\*), greener (lower a\*) and bluer (lower b\*) with increasing Zr-V pigment concentration.

At 1050°C, frits A, B, F and H produced the lightest, least blue color while C and D are the darkest and bluest. At 1100°C, F and H overtake A and B as the lightest colors and C and D remain the darkest and bluest. Also at 1100°C, frits E, F, G and H overtake A and B for generating the least blue. The blue color loss in frits without ZrO<sub>2</sub> (E-H) with

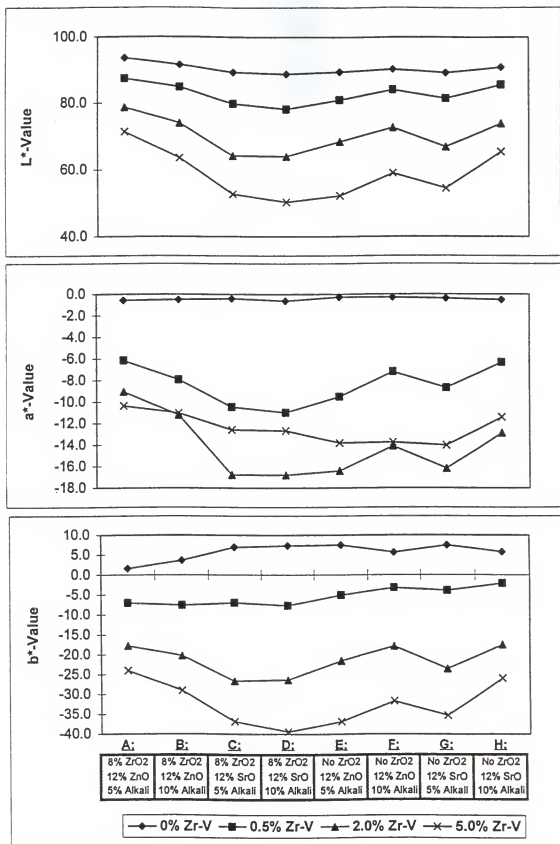


Figure 4.8. Color values of coatings batched with frits (A-H) and Zr-V pigment, and fired to 1050°C.

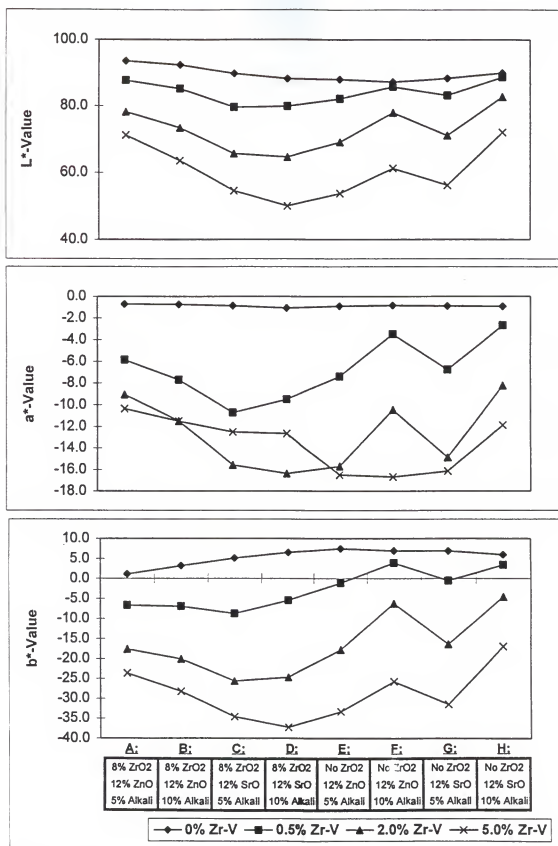


Figure 4.9. Color values of coatings batched with frits (A-H) and Zr-V pigment, and fired to 1100°C.

increasing peak temperature correlates to the shifts in their spectral curves, noted in Section 4.2.1, Figures 4.5-4.6.

From 2% to 5% Zr-V, the observed reverse from increasing green appearance ( $-a^*$ ) with pigment loading to a lessening of green (shown in Figures 4.8 and 4.9) can be explained by comparing the coatings spectral reflection curves, standard observer weighting functions in Figure 2.13, and equations 2.47-2.49 and 2.53-2.55. The  $a^*$ -value magnitude is nonlinearly related to the ratio of  $\bar{x}:\bar{y}$  weighting functions. As Zr-V concentration in the coatings is raised, peak reflectance shifts towards lower wavelengths near 460 nm and reflection of light greater than 460 nm drops. In comparison, the  $\bar{x}$  magnitude drops from 600 nm to 500 nm where a minima is reached, then abruptly increases with decreasing wavelengths to 450 nm. In this wavelength interval, the  $\bar{y}$  magnitude continues to drop and the curves cross at about 475 nm, where  $\frac{d\bar{x}}{d\lambda} > \frac{d\bar{y}}{d\lambda}$ . Therefore, as Zr-V concentrations from 2% to 5% shift a greater portion of reflectance towards wavelengths between 450 nm and 500 nm, at one point the increasing  $\bar{x}$  curve begins to dramatically overtake the  $\bar{y}$  curve, resulting in a redder appearance. This explains the abrupt reverse in  $a^*$ -value trend with increasing pigment levels. Care should be taken to avoid formulations which

create this phenomenon; otherwise, slight batching errors could result in large deviations in the color perceived.

Figures 4.10, 4.11, 4.12 and 4.13 present color values for coatings fired to different peak temperatures with Zr-V concentrations of 0%, 0.5%, 2.0% and 5.0%, respectively. Figures 4.11-4.13 use the same y-axis color scales, but Figure 4.10 required a blown up scale because unpigmented coatings resulted in less color variations.

In Figure 4.10 where no pigment was present, all coatings progressed greener at higher temperatures although the  $a^*$  scale shown represents a very small noticeable difference ( $\Delta E^* = 2.0$ ). With increasing temperature, noticeable lightening of frits without  $ZrO_2$ , E, F, G and H, as well as a lowering of yellow ( $b^*$ ) in all frits except E, F and H was observed.

At 0.5% Zr-V (Figure 4.11), the most significant variations in color occur in the  $b^*$ -value. From 1000°C to 1100°C peak temperature, E, F, G and H (frits without  $ZrO_2$ ) became less blue (higher  $b^*$ ), while the blue color of A-D (frits with  $ZrO_2$ ) was stable. Frits F and H lost all blue color at 1100°C and appear slightly yellow. The yellowing shifts the color towards that of unpigmented coatings. Figure 4.12 shows the same trends for 2.0% Zr-V as

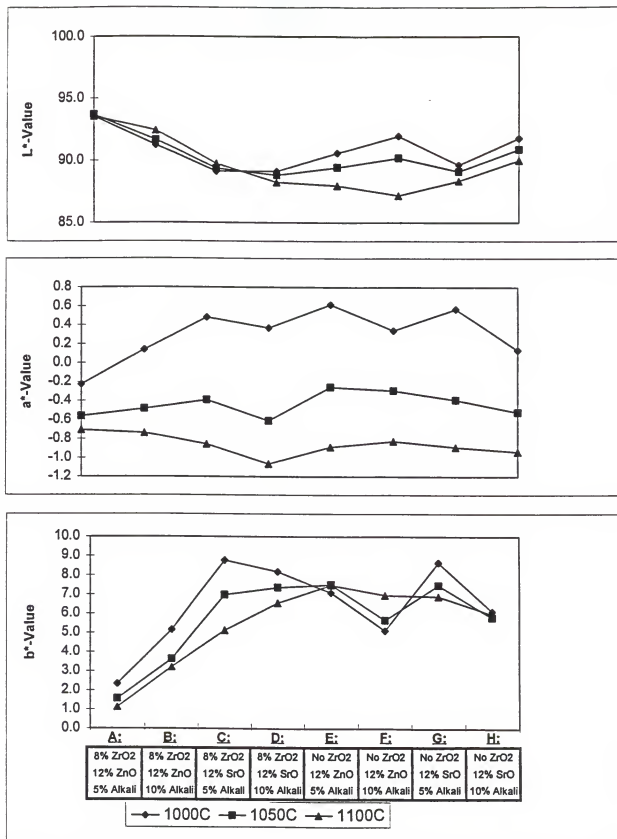


Figure 4.10. Color values of coatings batched with frits (A-H) and no Zr-V, and fired to 1000°C, 1050°C or 1100°C.

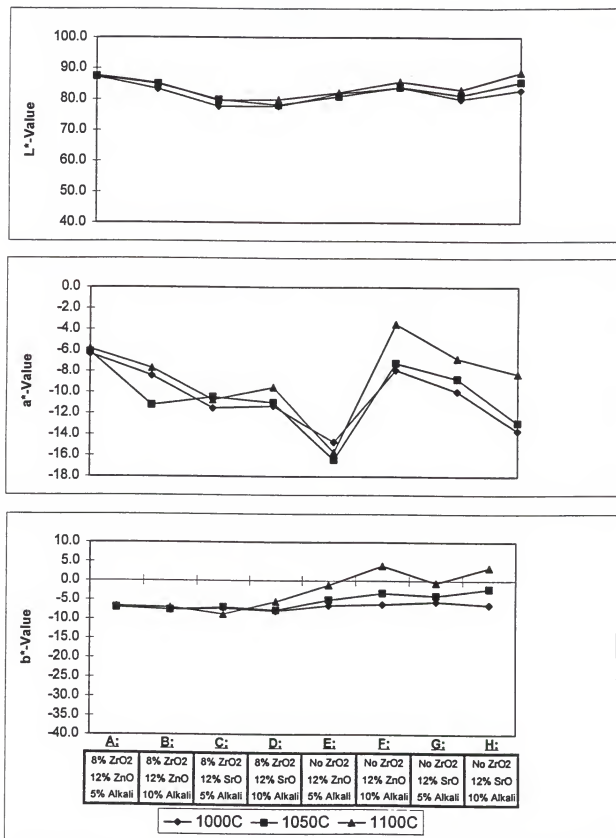


Figure 4.11. Color values of coatings batched with frits (A-H) and 0.5% Zr-V, and fired to 1000°C, 1050°C or 1100°C.



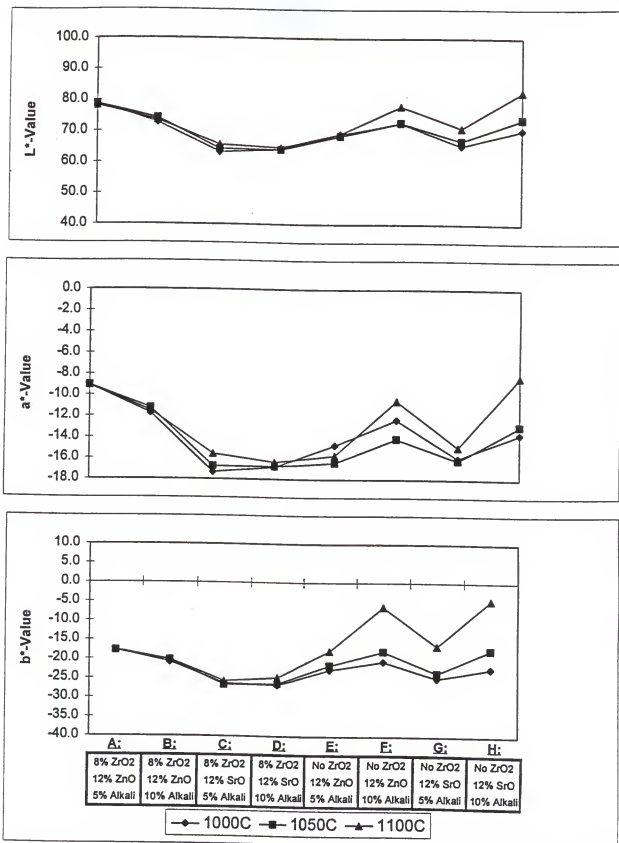


Figure 4.12. Color values of coatings batched with frits (A-H) and 2.0% Zr-V and fired to 1000°C, 1050°C or 1100°C.

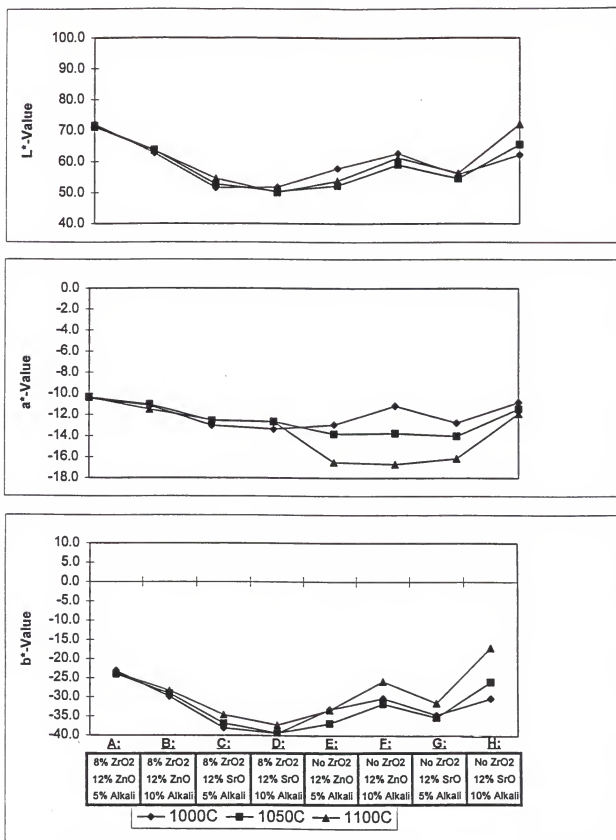


Figure 4.13. Color values of coatings batched with frits (A-H) and 5.0% Zr-V, and fired to 1000°C, 1050°C or 1100°C.

demonstrated with Figure 4.11, but to a greater degree. Color intensity in frits without  $\text{ZrO}_2$  (E-H) was significantly reduced with increasing temperature. Of those frits, compositions with 10% alkalis (F and H) had lower color stability over the range of firing temperatures than frits which contained 5% alkalis (E and G).

Figure 4.13 exhibits color values at each peak temperature with coatings containing 5.0% Zr-V. The  $L^*$  and  $b^*$  changes with temperature for frits E-H are in the same direction but with less magnitude than coatings with 0.5% and 2.0% Zr-V. This indicates that the higher pigment concentration provides less color sensitivity to the glass matrix or pigment dissolution changes due to temperature. However, the effect of temperature on perceived greenness is shown to be greater than with lower pigment concentrations. The increased sensitivity of  $a^*$  to temperature is due to the shifting of a great portion of the spectral curve past the  $\bar{x}$  weighting function minima near 500 nm. From 1000°C to 1100°C peak temperature, color progressed greener in frits E, F, G and H with 5.0% Zr-V.

Figure 4.14 relates the relationship between observed lightness and blueness for all 96 coatings trials. The Zr-V pigment creates color which becomes exponentially darker as

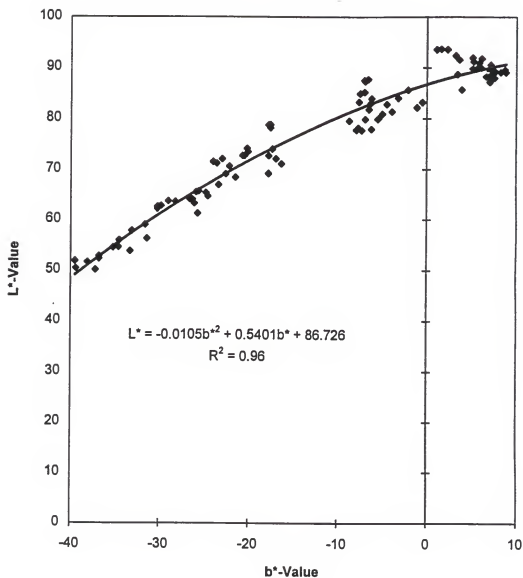


Figure 4.14. Relationship between lightness ( $L^*$ ) and blueness ( $-b^*$ ) of coatings batched with Zr-V pigment and fired to 1000°C, 1050°C and 1100°C peak temperature. Note  $b^* > 0$  in coatings without Zr-V.

blueness increases. A second order polynomial relationship well conforms ( $R^2=.96$ ) to the experimental data. Lower  $L^*$  and  $b^*$  values resulting from higher Zr-V concentrations yielded a better fit to the equation. Points on the graph where  $b^* \leq -16.4$  depict pigment concentrations of 2.0% or 5.0%. Positive  $b^*$  values represent coatings which accommodate no Zr-V. The figure indicates that at a low Zr-V contents, the relationship between  $L^*$  and  $b^*$  is less predictable. The discussion in Section 5.1.2 regarding crystallization and Zr-V dissolution will provide insights into the causes of this observation. Figure 4.14 also substantiates the use of either  $L^*$  or  $b^*$  for evaluating visual blue color saturation with Zr-V pigments.

All three color parameters were found to be logarithmic functions of the Zr-V pigment absorption factor (Figure 4.15). Values of  $R^2$  for the relationships are highest for  $L^*$  and  $b^*$  ( $R^2 = .93$ ). The redness-greenness of Zr-V systems is less predictable from  $R_{640nm}$  ( $R^2 = .87$ ). With the equations in Figure 4.15, statistical models (in Section 4.4 of this dissertation) for predicting K/S can be converted into numbers that are proportional to human vision. The absorption factor was chosen as a primary variable for quantifying color strength due to its direct correlation with

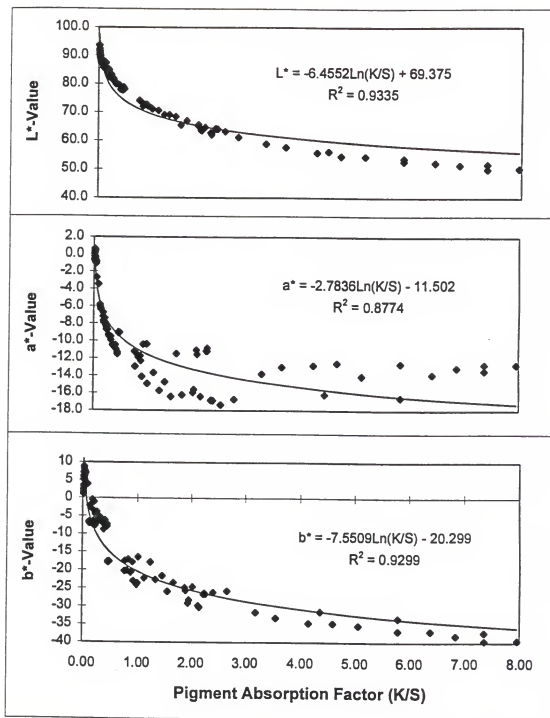


Figure 4.15. Zr-V pigment absorption factor relationships with L\*, a\* and b\* color values of fired coatings.

pigment concentration. Thus, Zr-V dissolution and/or reflection of light from crystalline precipitates which counters the characteristic 640 nm absorption peak are easier to evaluate with K/S values. However, as Figure 4.15 illustrates, changes in K/S are most visible for  $K/S \leq 1.0$  and least observable for  $K/S \geq 2.5$ . Any Zr-V contents  $\leq 2.0\%$  yielded  $K/S \leq 2.4$  for all frits and processing conditions. Thus, changes in K/S and corresponding pigment concentration in frit systems which incorporate Zr-V pigments are most noticeable for  $Zr-V \leq 2.0\%$ .

#### 4.2.4 Color Stability

Color variations resulting from an increase in peak firing temperature from 1050°C to 1100°C are represented with  $\Delta E^*$  values in Figure 4.16. Since previous data showed that K/S never increased with temperature,  $\Delta E^*$  indicates the magnitude of color loss which correlates to human vision. The  $\Delta E^*$  from frits containing  $ZrO_2$  (A-D) at all pigment concentrations, and unpigmented frits with no  $ZrO_2$  (E-H, 0% Zr-V) fell below the ANSI requirement of  $\Delta E^* < 3.0$  for compatible ceramic tile glazes. However, manufacturers prefer to conform to  $\Delta E^* \leq 1.0$  for matching surface appearances. Only frits A and B, which unlike any of the

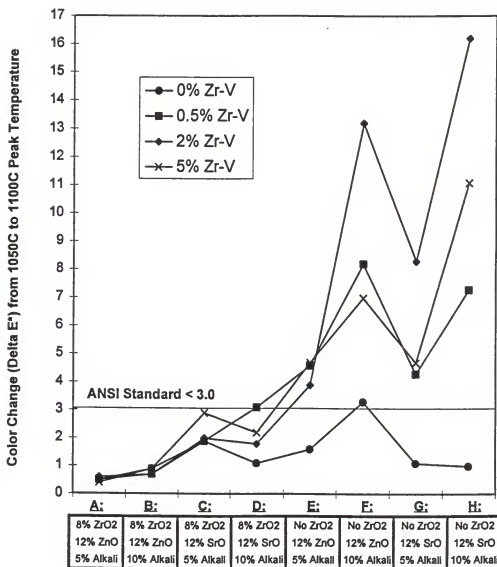


Figure 4.16. Color changes ( $\Delta E^*$ ) due to a variation in peak firing temperature from 1050°C to 1100°C for coatings batched with frits (A-H) and Zr-V pigment.



other frits contained both  $\text{ZrO}_2$  (8%) and  $\text{ZnO}$  (12%), met this standard. Pigmented frits E-H exhibited considerable color changes due to the  $50^\circ\text{C}$  increase in peak firing temperature. These data concur with the figures in Sections 4.2.1 and 4.2.3 in identifying that frits with no  $\text{ZrO}_2$  yield the most temperature sensitive color. Frit composition and temperature influences on  $\Delta E^*$  are quantified with statistical models in Section 4.4.2.

#### 4.2.5 Specular Gloss

Except for coatings with frit B, there was very little influence of pigment concentration on gloss, as shown in Figure 4.17. Also excluding B, frits containing  $\text{ZrO}_2$  had more stable gloss over the  $1000^\circ\text{C}$  to  $1100^\circ\text{C}$  peak temperature range, while frits E, F and G exhibited increased gloss at higher temperatures. Frit H yielded by far the lowest gloss in all cases. Overall except for B, frits with  $\text{ZrO}_2$  produced a higher gloss. The gloss results were used in later sections of this dissertation to collaborate with other evidence of crystallization in some coatings.

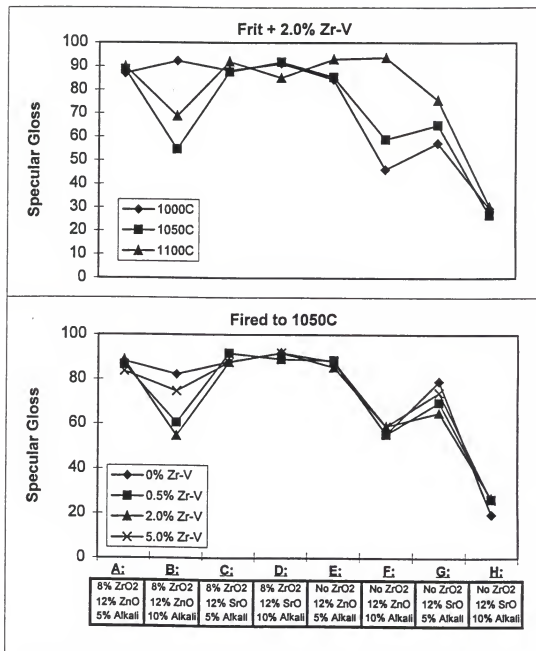


Figure 4.17. Specular gloss of fired coatings at a 60° angle of incidence.

### 4.3 Viscosity of Coatings During Heating

Results in viscosity measurements for coatings batched with 2.0% Zr-V are detailed in this section and are related to crystallization and pigment dissolution data in Section 4.5. In Section 5, these data are further linked to color properties obtained with all three pigment loadings, based on previous correlations found between color and Zr-V concentration. The goal was to determine if the viscosity of a coating at high temperature can be applied as a single indicator of color stability and strength for industrial quality control purposes.

#### 4.3.1 Heating Microscope Images

Several of the images acquired using heating microscopy techniques are pictured in Figures 4.18 and 4.19. The dimensional changes versus temperature shown reveal distinct patterns:

1. Raising the alkalis from 5 to 10% by weight at the expense of silica (frits B, D, F and H) caused the greatest increase in molten flow at all temperatures.
2. Overall, frits with  $\text{ZrO}_2$  (A-D) flowed less at low temperature up to approximately 1000°C and required higher temperatures to reach the "sphere" point (contact

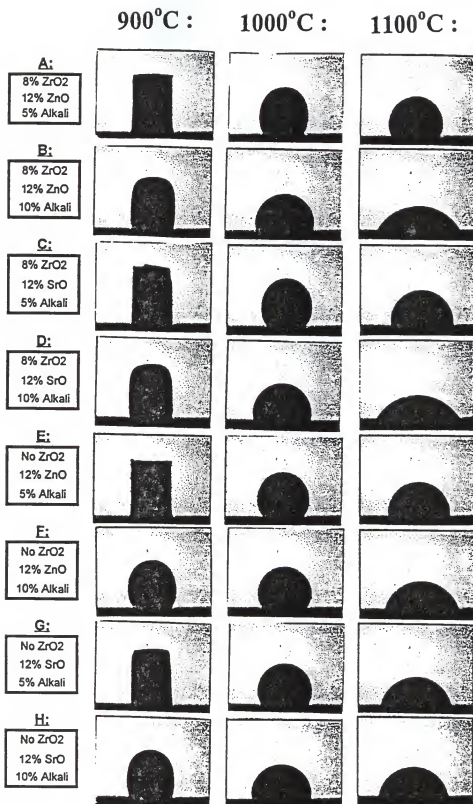


Figure 4.18. Heating microscope images of coatings batched with frits (A-H) and 2.0% Zr-V, at 900°C, 1000°C and 1100°C.

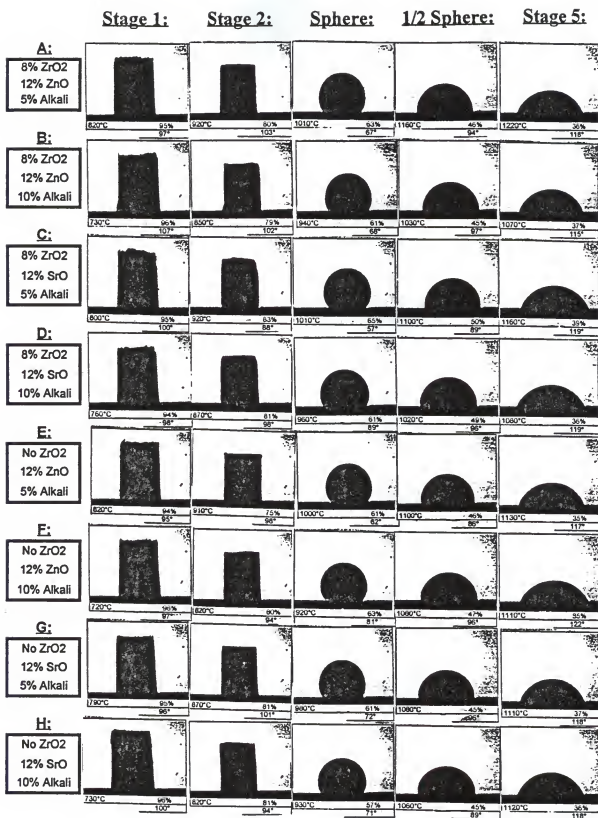


Figure 4.19. Heating microscope images of characteristic stages of flow of coatings batched with frits (A-H) and 2.0% Zr-V. (The temperature, % of original sample height and contact angle are listed under each image.)

angle  $\cong 57-72^\circ$ , % original height/contact angle  $\cong .80-1.14$ ).

3. Frits containing both  $\text{ZrO}_2$  and high alkali content exhibited the greatest flow at high temperatures near  $1100^\circ\text{C}$ .

The temperature at the 1/2 sphere stage ( $T_{1/2}$ ) was combined with dilatometric data to generate  $\log \eta$  versus temperature curves for each coating, as described in Section 2.2.5d.

#### 4.3.2 Dilatometric $T_g$ and $T_s$

Dilatometric curves, including identification of glass transition ( $T_g$ ) and softening ( $T_s$ ) temperatures, and calculated coefficients of thermal expansion (listed as C.o.E. under each graph) are displayed in Figures 4.20 and 4.21 for all 2.0% Zr-V coatings. The crazing observed on tile samples made with frits D, F and H could be attributed to the high thermal expansion of the frits ( $91.8$ ,  $96.9$  and  $105.1 \times 10^{-7} \text{ K}^{-1}$ , respectively, from  $50-450^\circ\text{C}$ ) when compared to the body/engobe substrate ( $65-67 \times 10^{-7} \text{ K}^{-1}$ ). None of the other frits crazed.

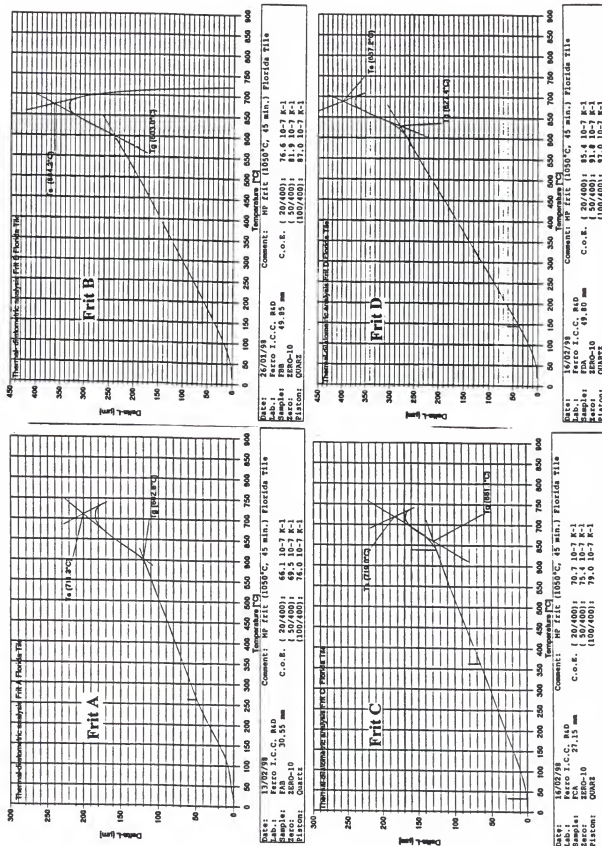


Figure 4.20. Thermal dilatometric analyses of coatings A-D batched with 2.0% Zr-V. (Heating rate of 43°C/min.)

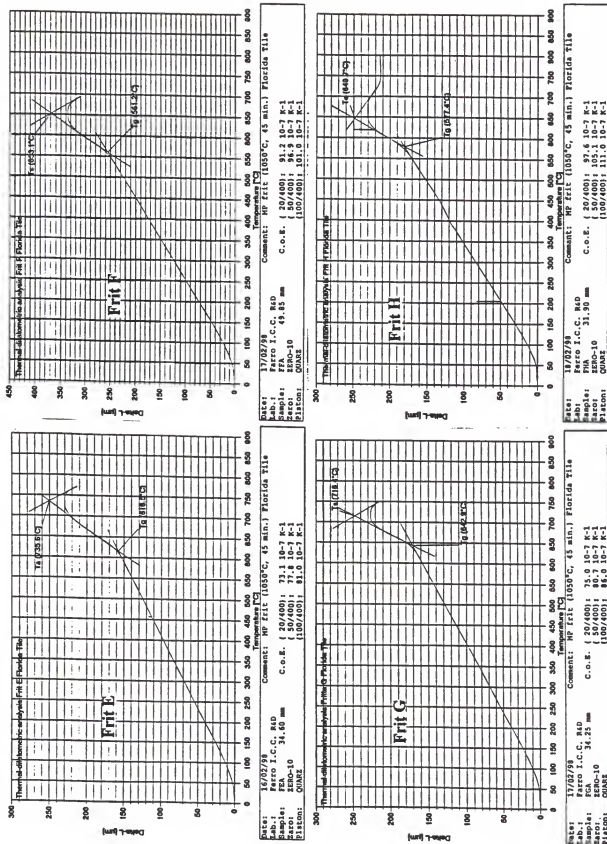


Figure 4.21. Thermal dilatometric analyses of coatings E-H batched with 2.0% Zr-V. (Heating rate of 43°C/min.)



The  $T_g$  and  $T_s$  data disclose the following:

1. Alkali content in the frits had the largest influence on  $T_s$ . The average  $T_s$  with frits containing 5% alkalis was 721°C. When the alkalis were raised to 10% at the expense of  $\text{SiO}_2$ ,  $T_s$  dropped to 688°C.
2. Changes in SrO versus ZnO caused the greatest shift in  $T_g$ . The average  $T_g$  in frits containing SrO was 627°C, and lowered to 596°C when replacing SrO with ZnO.
3. Substituting SrO for ZnO in the glass structure produced a significant increase in the ratio of  $T_g:T_s$ . Less of a temperature rise after  $T_g$  was required to reach  $T_s$  with SrO present.

No other effects of the oxides on  $T_g$  and  $T_s$  were distinguished.

#### 4.3.3 Viscosity vs. Temperature

Data from Sections 4.3.1 and 4.3.2, as well as equations 2.93 and 2.97-2.99 in Section 2.2.5d, were used to generate the  $\log \eta$  vs. temperature curves in Figures 4.22 and 4.23. The temperature range of interest begins near the average softening point of the frits (~700°C) and ends at the highest peak firing temperature tested. This is the temperature range where crystallization and dissolution can occur.

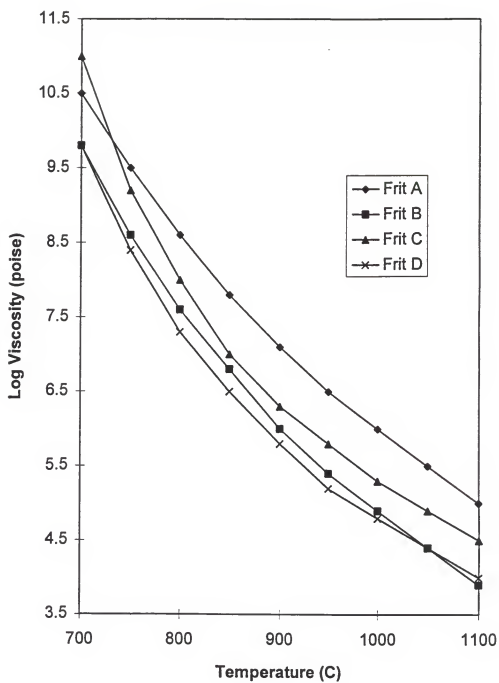


Figure 4.22. Log  $\eta$  versus temperature of coatings batched with 2.0% Zr-V. Frits A-D incorporate 8% ZrO<sub>2</sub>.

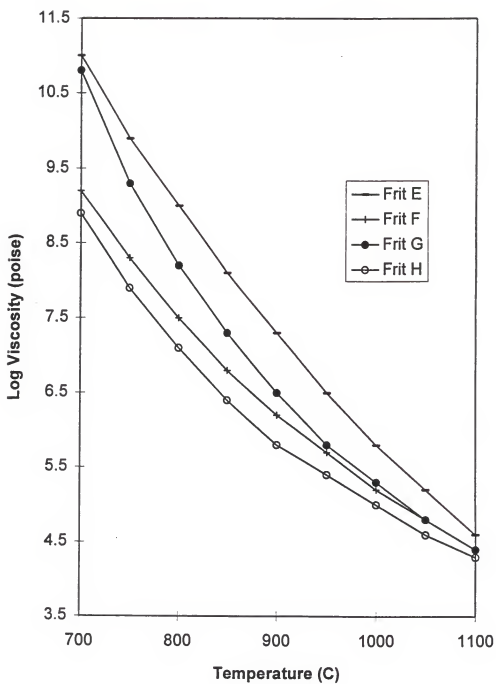


Figure 4.23. Log  $\eta$  versus temperature of coatings batched with 2.0% Zr-V. Frits E-H contain no  $\text{ZrO}_2$ .

In both figures, a drop in viscosity across the whole temperature range is shown for parallel compositions where only the alkalis/SiO<sub>2</sub> ratio is increased (i.e., A→B, C→D, E→F, G→H). The increase in nonbridging alkali ions in the glass has a marked effect on weakening the structure and lowering viscosity. An increase in the slope of the curves near the softening point of 700°C for frits where SrO replaced ZnO is also evident. The influence of other oxides in the frit on viscosity is not obvious from the plots, but a rigorous statistical analysis of the data in Section 4.4.3 identifies significant variables. In the Discussion, Section 5.1.3, viscosity results will be related in detail to other phenomena which affected the optical properties of the coatings.

#### 4.4 Derived Statistical Models

Simultaneous variations of oxide levels between the frits necessitated the implementation of tedious statistical methods in order to quantify the oxide's true effects on the dependent variables. Several equations were derived using the statistical techniques briefed in Section 3.3. Color strength (K/S), color stability (inverse of  $\Delta E^*$ ) and melt viscosity relationships with coating composition and

temperature have been quantified. The equations are useful for identifying the weights of influence of the significant independent variables on color and melt viscosity, and for interpolating predictions within the experimental parameters of this dissertation. However, predictions based on extrapolations beyond the range of conditions tested during this research (i.e., firing curves, coating thicknesses, substrate composition, etc.) will be much less accurate. Scientific interpretations of the physical basis for the results of this section are given in Chapter 5, Discussion.

#### 4.4.1 K/S vs. Coating Composition and Temperature

The following mathematical models were developed using experimental results from each individual pigment loading (4.1-4.3) and for compositions with Zr-V as an independent variable (4.4):

	<u>Variable</u>	<u>Coefficient</u>	<u>t-Value</u>
K/S <sub>0.5% Zr-V</sub> =	+ Y-intercept	1.136	---
	- ZrO <sub>2</sub>	0.191	-1.42 (4.1)
	+ SrO	2.162	1.84
	+ SrO X ZrO <sub>2</sub>	5.227	8.87
	- SrO X T	21.046 X 10 <sup>-4</sup>	-1.88
	- Al <sub>2</sub> O <sub>3</sub> /alkalis	0.654	-5.82
	+ (Al <sub>2</sub> O <sub>3</sub> /alkalis) <sup>2</sup>	0.451	6.65
	- T	71.179 X 10 <sup>-5</sup>	-3.41

	<u>Variable</u>	<u>Coefficient</u>	<u>t-Value</u>
K/S <sub>2.0%</sub> Zr-V =	+ Y-intercept	1.912	---
	- ZrO <sub>2</sub>	1.449	-1.90 (4.2)
	+ SrO	24.224	5.08
	+ SrO X ZrO <sub>2</sub>	30.396	9.08
	- SrO X T	2.272 X 10 <sup>-2</sup>	-5.02
	- Al <sub>2</sub> O <sub>3</sub> /alkalis	3.588	-5.63
	+ (Al <sub>2</sub> O <sub>3</sub> /alkalis) <sup>2</sup>	2.585	6.72

	<u>Variable</u>	<u>Coefficient</u>	<u>t-Value</u>
K/S <sub>5.0%</sub> Zr-V =	+ Y-intercept	8.825	---
	- ZrO <sub>2</sub>	12.725	-3.21 (4.3)
	+ SrO X ZrO <sub>2</sub>	130.854	7.54
	- SrO X T	34.558 X 10 <sup>-4</sup>	-1.70
	- Al <sub>2</sub> O <sub>3</sub> /alkalis	17.861	-5.39
	+ (Al <sub>2</sub> O <sub>3</sub> /alkalis) <sup>2</sup>	12.277	6.14

	<u>Variable</u>	<u>Coefficient</u>	<u>t-Value</u>
K/S <sub>0-5%</sub> Zr-V =	+ Y-intercept	1.254	---
	+ Zr-V/T	799.062	14.76 (4.4)
	- ZrO <sub>2</sub>	3.000	-1.47
	+ SrO X ZrO <sub>2</sub>	36.632	5.84
	- Al <sub>2</sub> O <sub>3</sub> /alkalis	5.480	-2.94
	+ (Al <sub>2</sub> O <sub>3</sub> /alkalis) <sup>2</sup>	3.792	3.38

In equations 4.1-4.4, units for ZrO<sub>2</sub>, SrO, Al<sub>2</sub>O<sub>3</sub> and alkalis (Na<sub>2</sub>O + K<sub>2</sub>O) are molar equivalents of the oxides in the frits, Zr-V is the weight percent pigment added to the batch and T is the peak firing temperature in degrees celsius. Although there was a correlation between molar equivalents of CaO and Al<sub>2</sub>O<sub>3</sub> in the frits, Al<sub>2</sub>O<sub>3</sub> provided for a better equation fit and was thus included in the models. Equation 4.2 for 2.0% Zr-V was developed first, using

variables whose absolute t-values were  $\geq 1.9$ . Then the other models were derived with the same variables if their absolute t-values were  $\geq 1.4$ . Calculated  $R^2$  values of 0.95, 0.95 and 0.88 for equations 4.1-4.3, respectively, verify thorough explanation of K/S variation in terms of the independent variables in the models. Equation 4.4, which includes all Zr-V levels, was less accurate ( $R^2 = .75$ ) than the other models. Evaluation of residuals (E.S. and Std.) and Durbin Watson statistics (all 2.0-2.5) revealed no outlier experiments and validated the models. The precision of an equation is estimated with the standard deviation of the residuals ( $S_{y,x}$ ). Values of  $S_{y,x}$  for equations 4.1-4.4 are 0.030, 0.169, 0.878 and 0.987, respectively.

The magnitudes and signs of coefficients in all four equations corroborate the following conclusions:

1. Higher SrO in the frit tends to raise the color strength (K/S) unless the pigment concentration is high (5%). In this case, SrO boosts K/S only in frits containing  $ZrO_2$ .
2. Increased  $ZrO_2$  lowers K/S, unless SrO is present (in place of ZnO). An interaction between SrO and  $ZrO_2$  boosts K/S at all pigment loadings.
3. The curvilinear ( $X^2-X$ ) effect of the  $Al_2O_3$ /alkalis ratio reveals that (a) at low levels, increasing  $Al_2O_3$ /alkalis

tends to slightly decrease K/S, but (b) at high levels, K/S is significantly raised as  $\text{Al}_2\text{O}_3/\text{alkalis}$  is increased.

4. At a low pigment concentration (0.5%), higher temperatures cause K/S to drop in all of the frits. At 2% and 5% Zr-V, only frits which include SrO experience a decrease in K/S with increasing temperature.

Figure 4.24 relates the good fit between actual data, and equation 4.2 predicted results for all 24 trials with 2.0% Zr-V. Note K/S is predicted to remain constant over all three temperature points for frits which include ZnO (A, B, E and F) rather than SrO (C, D, G and H), indicating superior color stability with ZnO.

The statistically adjusted effects of individual variables from equation 4.2 (2.0% Zr-V) are displayed in Figure 4.25. Data for the plots were generated by inputting the actual range of composition tested of the x-axis variable into equation 4.2, while holding values of all other variables in the equation at their average level. Thus, Figure 4.25 depicts mathematical interpolations based on the statistical model. An increase in  $\text{ZrO}_2$  (from 0 to 0.311 molar equivalents) is shown to raise K/S in the presence of SrO (at average of 0.131 equivalents), but decrease K/S when ZnO (at



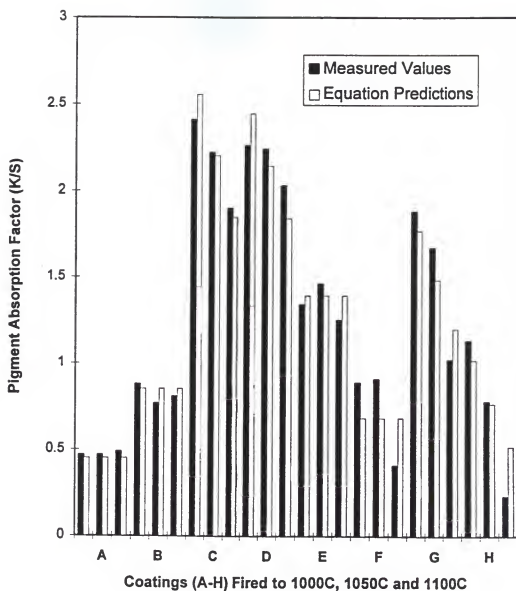


Figure 4.24. Pigment absorption factor actual and equation (4.2) predicted results for fired coatings batched with 2.0% Zr-V.

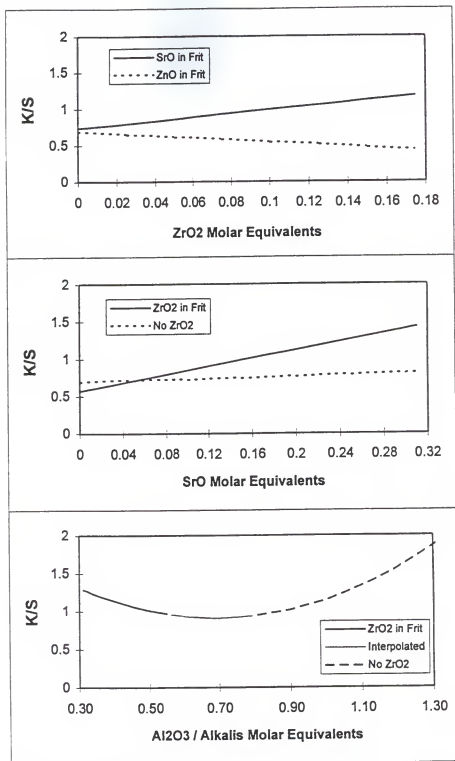


Figure 4.25. Individual effects of frit oxides on K/S based on statistical model (4.2) for 2.0% Zr-V and a peak firing temperature of 1050°C.

average of 0.156 equivalents) replaces SrO. The middle graph illustrates that higher SrO (with ZnO still present at .156 equivalents) raises K/S to a much greater degree when  $\text{ZrO}_2$  (at average of 0.078 equivalents) is in the frit. The bottom plot portrays the curvilinear relationship between K/S and  $\text{Al}_2\text{O}_3$ /alkalis ratio.

Frits manufactured without  $\text{ZrO}_2$  are normally designed with a higher  $\text{Al}_2\text{O}_3$ /alkalis because more  $\text{Al}_2\text{O}_3$  is added to maintain glass strength and durability. With  $\text{ZrO}_2$  in the glass, increasing  $\text{Al}_2\text{O}_3$ /alkalis (<0.5 molar equivalents) caused K/S to lower slightly. As  $\text{Al}_2\text{O}_3$ /alkalis levels were increased (>0.80) when no  $\text{ZrO}_2$  was present, a significant increase in K/S occurred.

The weights of influence of independent variables on K/S, derived with models 4.1-4.3, are disclosed in Figure 4.26. A variable's percent total influence (%I) was calculated by

$$\%I = \frac{K/S_i}{\sum K/S_{i \dots n}} \times 100 \quad (4.5)$$

where

$K/S_i$  = the maximum range of K/S obtained by  
inputting all values tested of independent  
variable (i) into the statistical equation,

while holding other variables at their average level.

$\sum K/S_{i...n}$  = summation of all the  $K/S_i$  ranges calculated.

Figure 4.26 does not consider interactive effects but provides a picture of how Zr-V loading changes the systems. The graphs reveal that with increasing pigment concentration, the impact of  $Al_2O_3$ /alkalis increases, while  $ZrO_2$  and temperature become less of a factor. SrO influence remains similar at all three Zr-V contents.

Cause/effect relationships between the frit oxides and color results are not easily distinguishable without statistically adjusted data. This is because more than one color influencing oxide was varied simultaneously between the experiments. Thus, regression methods were employed to separate the true effects of each individual oxide and generate Figures 4.25 and 4.26.

Figures 4.27-4.30 reveal nonadjusted, actual results for each experiment with 2.0% Zr-V loading. Although less distinct, the plots show trends which correlate to the statistical models.

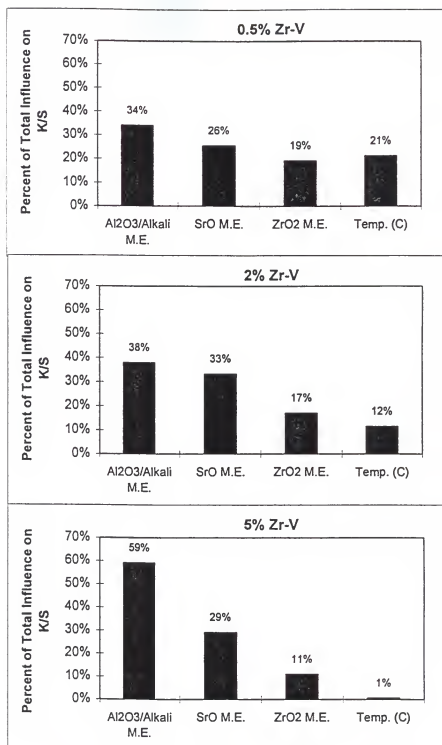


Figure 4.26. Variables weight of influence on K/S, based on statistical models 4.1 (0.5% Zr-V), 4.2 (2% Zr-V) and 4.3 (5% Zr-V).

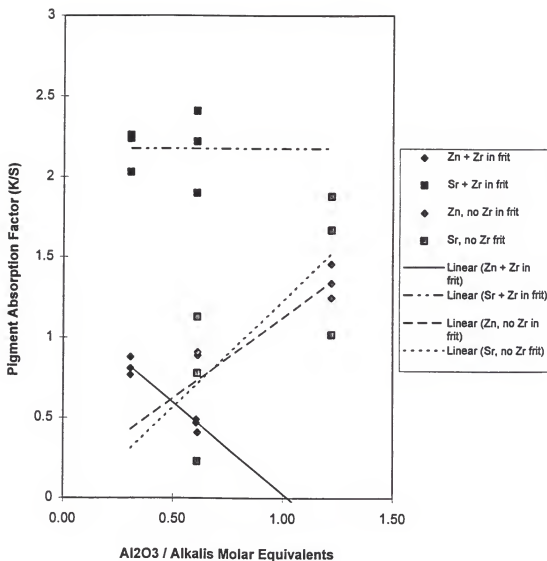


Figure 4.27. Pigment absorption factor trends with frit  $\text{Al}_2\text{O}_3$ :alkalis ratio of coatings batched with 2.0% Zr-V and fired to 1000°C, 1050°C or 1100°C. For each group of three data points at a specific  $\text{Al}_2\text{O}_3$ /alkali, the highest point represents a coating fired to 1000°C peak temperature; the lowest point was fired to 1100°C. Lines shown intersect average K/S values for each group of three data points.

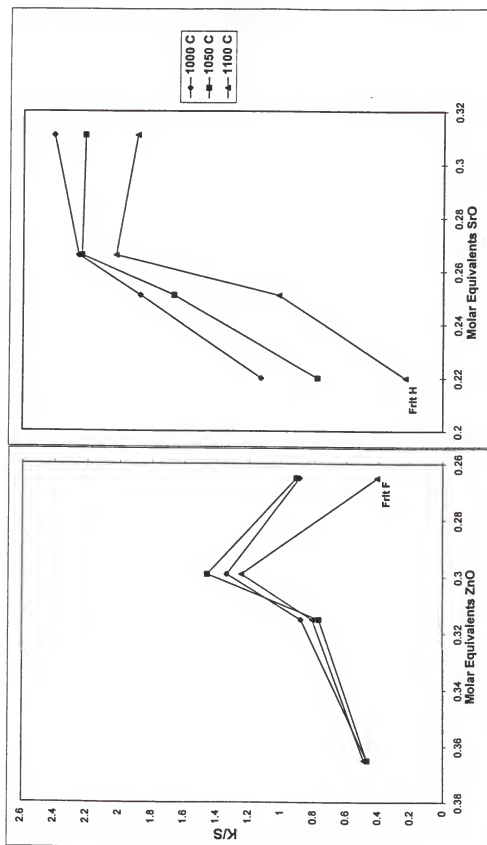


Figure 4.28. Pigment absorption factor versus frit ZnO and SrO molar equivalents of fired coatings batched with 2.0% Zr-V and fired to 1000°C, 1050°C or 1100°C peak temperature.

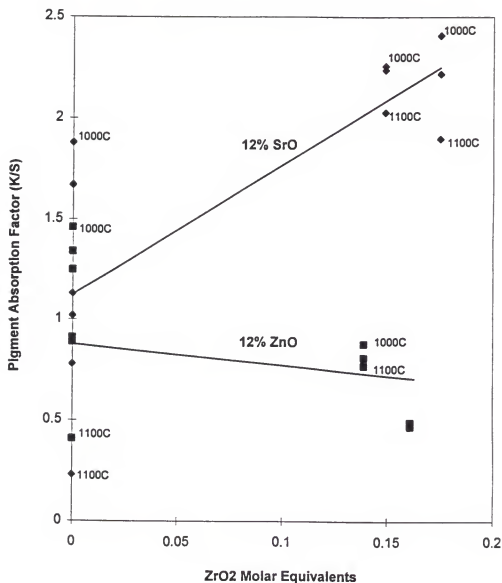


Figure 4.29. Influence of frit  $\text{ZrO}_2$ , in the presence of SrO or ZnO, on K/S of fired coatings batched with 2.0% Zr-V and fired to 1000°C, 1050°C or 1100°C. All data points for 1000°C, 1050°C and 1100°C peak firing temperatures are plotted. Lines shown intersect average K/S values for each  $\text{ZrO}_2$  and SrO or ZnO combination.



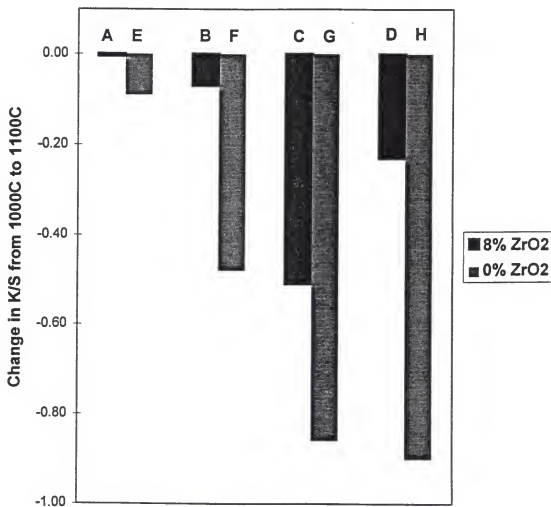


Figure 4.30. Variations in pigment absorption factor (K/S) due to changes in peak firing temperature, for coatings batched with 2.0% Zr-V and frits containing 8% ZrO<sub>2</sub> versus 0% ZrO<sub>2</sub>.

Frits also include the following weight percentages:

A and E: 5% alkalis, 55% SiO<sub>2</sub>, 12% ZnO;

D and F: 10% alkalis, 50% SiO<sub>2</sub>, 12% ZnO;

C and G: 5% alkalis, 55% SiO<sub>2</sub>, 12% SrO;

D and H: 10% alkalis, 50% SiO<sub>2</sub>, 12% SrO.

Figure 4.27 confirms that when  $\text{ZrO}_2$  and  $\text{SrO}$  were present, the highest K/S was achieved and was not dependent upon  $\text{Al}_2\text{O}_3$ /alkalis. Coatings with frits containing  $\text{ZnO}$  and  $\text{ZrO}_2$  exhibited a sharp drop in K/S with increasing  $\text{Al}_2\text{O}_3$ /alkali and produced a weaker color than the  $\text{SrO} + \text{ZrO}_2$  combination. Coatings without  $\text{ZrO}_2$  in the frit showed intermediate color strength, which increased with a higher  $\text{Al}_2\text{O}_3$ /alkalis.

Figure 4.27 also demonstrates color loss with increasing temperature. For each group of three data points at a specific  $\text{Al}_2\text{O}_3$ /alkali, the strongest color (highest K/S) represents a coating fired to  $1000^\circ\text{C}$  while the lowest K/S represents a peak temperature of  $1100^\circ\text{C}$ . The vertical spread in each group of data points, which represents color variation with temperature, is greatest for the coatings without  $\text{ZrO}_2$  and least when both  $\text{ZrO}_2$  and  $\text{ZnO}$  are present.

A comparison of K/S values resulting from frits with  $\text{SrO}$  and  $\text{ZnO}$  at 2.0%  $\text{Zr-V}$  is made in Figure 4.28. An overall pattern of increasing pigment absorption and color strength with a reduction in  $\text{ZnO}$  or higher  $\text{SrO}$  is evident. Color degradation from  $1000^\circ\text{C}$  to  $1100^\circ\text{C}$  was dramatically reduced with frits containing high  $\text{ZnO}$  and no  $\text{SrO}$ . Frits F and H generated data that slightly deviated from the overall

trend. They had in common the lowest  $\text{Al}_2\text{O}_3$ /alkali ratio of the frits with no  $\text{ZrO}_2$  and produced coatings with the lowest gloss due to high devitrification/crystallization in the glass.

Figure 4.29 relates the interaction between  $\text{ZrO}_2$  and  $\text{SrO}$  or  $\text{ZnO}$ . For frits that incorporated  $\text{SrO}$ , K/S increased with  $\text{ZrO}_2$  content. Absorption of light by the pigment was not significantly influenced with higher  $\text{ZrO}_2$  when the frit contained  $\text{ZnO}$  rather than  $\text{SrO}$ . The range of K/S with temperature is again shown to be lower with  $\text{ZnO}$ . Overall K/S variation due to peak firing temperature is lower for both  $\text{ZnO}$  and  $\text{SrO}$  frits when  $\text{ZrO}_2$  is present.

In Figure 4.30, frits with equal weight percentages of silica, alkalis and  $\text{SrO}$  or  $\text{ZnO}$  are grouped together on the x-axis (A and E, B and F, C and G, D and H). In each case, K/S changes less with peak temperature in frits with  $\text{ZrO}_2$ . The largest drops in K/S stability when  $\text{ZrO}_2$  was removed (increased vertical distance between two bars) occurred when shifting to higher alkalis (A-E to B-F and C-G to D-H) and when  $\text{SrO}$  replaced  $\text{ZnO}$  (A-E to C-G and B-F to D-H).

#### 4.4.2 $\Delta E^*$ vs. Coating Composition

Values of  $\Delta E^*$  were calculated as the color difference between coatings fired to 1050°C° versus 1100°C peak temperature. Since K/S never increased with temperature,  $\Delta E^*$  denotes the magnitude of color loss which correlates to human vision, and the degree of instability of the system. The following statistical models were developed using experimental results from each individual pigment loading (4.6-4.9) and for all compositions with Zr-V as an independent variable (4.10):

	<u>Variable</u>	<u>Coefficient</u>	<u>t-Value</u>	
$\Delta E^*_{0.5\% \text{ Zr-V}} =$	Y-intercept	6.49	---	
	- ZrO <sub>2</sub>	47.07	-10.99	(4.6)
	+ SrO X ZrO <sub>2</sub>	49.77	3.79	
	+ Al <sub>2</sub> O <sub>3</sub> /alkalis	5.80	1.48	
	- (Al <sub>2</sub> O <sub>3</sub> /alkalis) <sup>2</sup>	6.10	-2.59	

	<u>Variable</u>	<u>Coefficient</u>	<u>t-Value</u>	
$\Delta E^*_{2.0\% \text{ Zr-V}} =$	Y-intercept	4.98	---	
	- ZrO <sub>2</sub>	76.04	-24.83	(4.7)
	+ SrO	15.70	9.51	
	- SrO X ZrO <sub>2</sub>	49.29	-3.67	
	+ Al <sub>2</sub> O <sub>3</sub> /alkalis	26.84	10.48	
	- (Al <sub>2</sub> O <sub>3</sub> /alkalis) <sup>2</sup>	22.51	-14.59	

	<u>Variable</u>	<u>Coefficient</u>	<u>t-Value</u>	
$\Delta E^*_{5.0\% \text{ Zr-V}}$	Y-intercept	3.90	---	
	- $\text{ZrO}_2$	46.31	-5.92	(4.8)
	+ $\text{SrO}$	8.43	2.42	
	+ $\text{Al}_2\text{O}_3/\text{alkalis}$	14.01	1.66	
	- $(\text{Al}_2\text{O}_3/\text{alkalis})^2$	11.63	-2.29	

	<u>Variable</u>	<u>Coefficient</u>	<u>t-Value</u>	
$\ln \Delta E^*_{0-5\% \text{ Zr-V}}$	Y-intercept	1.89	---	
	- $\text{ZrO}_2$	16.57	-12.99	(4.9)
	+ $\text{SrO}$	1.48	1.94	
	+ $\text{SrO} \times \text{ZrO}_2$	20.88	3.52	
	- $(\text{Al}_2\text{O}_3/\text{alkalis})^2$	0.59	-3.95	
	+ $\text{Zr-V}$	0.37	2.76	
	- $(\text{Zr-V})^2$	$6.13 \times 10^{-2}$	-2.45	

Oxides in equations 4.6-4.9 are in molar equivalents. As previously noted for K/S equations, although  $\text{CaO}$  and  $\text{Al}_2\text{O}_3$  fritted molar equivalents correlate,  $\text{Al}_2\text{O}_3$  in the models provide for better accuracy. Equation 4.7 for 2.0% Zr-V was developed first using variables whose absolute t-values were  $\geq 2.0$ , then other models were derived using the same variables, with absolute  $t \geq 1.4$ . Calculated  $R^2$  values of 0.98, 0.99, 0.94 and 0.92 for equations 4.6-4.9, respectively, validate the models. Values of  $S_{y.x}$  for equations 4.6-4.9 are 0.60, 0.39, 1.29 and 0.37, respectively.

Equation 4.9 for all Zr-V levels required a logarithmic transformation of  $\Delta E^*$  in order to establish a correlation

with the independent variables. The logarithmic dependency found between  $K/S$  and  $L^*$ ,  $a^*$  and  $b^*$  in Figure 4.15, Section 4.23, and the linear relationship between  $K/S$  and pigment concentration (reviewed in Sections 4.2.2 and 2.2.4b) explain this relationship. Small changes in perceived color with pigment absorption are nearly linear around 0.5%, 2.0% and 5.0% Zr-V areas. Large swings in  $L^*$ ,  $a^*$ ,  $b^*$  and corresponding  $\Delta E^*$ , resulting from significant changes in pigment content or glass matrix compositional changes that influence  $K/S$ , require a logarithmic function to describe the whole range.

Formation of equation 4.9 also required the omission of two outlier data; frit H fired to 1100°C at 2.0% and 5.0% Zr-V. Calculated Durbin Watson and residual statistics fell within the acceptable range. Model 4.9 attests that pigment loading has an influence on color stability. The curvilinear relationship between  $\ln \Delta E^*$  and Zr-V content indicates that an intermediate pigment level is least visually stable with temperature. This conforms with Figure 4.16, where  $\Delta E^*$  results were overall greater for 2.0% Zr-V than 0.5% or 5.0%.

Although  $\Delta E^*_{1050-1100^\circ\text{C}}$  and  $K/S_{1050}$  results did not correlate well to each other (linear correlation coefficient  $r=-.33$ ), the same independent variables were found to

significantly affect both, albeit with different magnitude and direction in some cases. Evaluation of the coefficients in 4.6-4.9 reveals

1. Higher  $\text{ZrO}_2$  in the frit improves color stability (lower  $\Delta E^*$ ).
2. Increased  $\text{SrO}$  lowers stability (raises  $\Delta E^*$ ).
3. The  $(X-X^2)$  effect of  $\text{Al}_2\text{O}_3$ /alkalis dictates that at low levels, increasing  $\text{Al}_2\text{O}_3$ /alkalis tends to slightly raise  $\Delta E^*$ , but at high levels, stability is improved.

Figure 4.31 compares measured and equation predicted  $\Delta E^*$  for all eight fired coatings batched within 2.0%  $\text{Zr-V}$ . Displayed is the good fit of the model, and the tendency for increased color sensitivity to temperature when  $\text{ZrO}_2$  is removed (E, F, G, H). Color variation is further increased in E-H when the alkali level is raised (F and H) and when  $\text{SrO}$  replaces  $\text{ZnO}$  (G and H).

Individual effects of oxide compositions on  $\Delta E^*$  at 2.0%  $\text{Zr-V}$ , calculated by inputting the range of composition tested into 4.7 and holding the other oxides at their average level, are displayed in Figure 4.32. Note the y-axis scale of 0 to 18 represents a dramatically noticeable color change. A  $\Delta E^* \geq 1.0$  is noticeable with the human eye. Linear trends of improved color stability with higher  $\text{ZrO}_2$  (0 to .175 molar

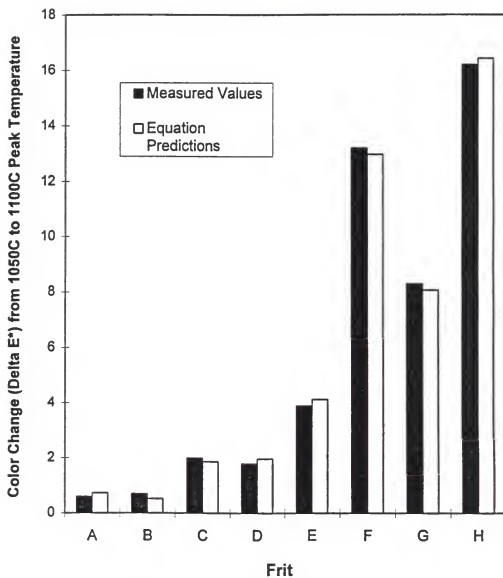


Figure 4.31. Delta E\* actual and equation (4.7) predicted results for fired coatings batched with 2.0% Zr-V.



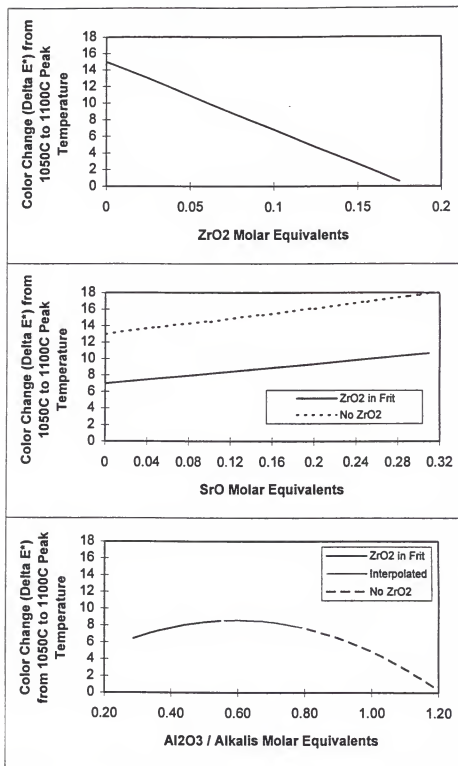


Figure 4.32. Individual effects of frit oxides on  $\Delta E^*$ , based on statistical model 4.7 for 2.0% Zr-V.

equivalents) and lower SrO (.311 to 0 molar equivalents) are shown. The middle graph illustrates that SrO additions increase  $\Delta E^*$ , but the overall color stability is better if  $ZrO_2$  is also present. The bottom plot shows increases in  $Al_2O_3$ /alkalis at high levels (>0.80 molar equivalents) provided great improvements in color stability.

The weights of influence of the oxides on  $\Delta E^*$  for each pigment loading, based on 4.6-4.8 equations coefficients, are disclosed in Figure 4.33. Percentages were calculated using equation 4.5 and the procedure described in Section 4.4.1. The bar graphs reveal that  $ZrO_2$  content in the frit has the greatest overall influence on color stability, followed by  $Al_2O_3$ /alkalis and SrO. As the pigment concentration increased, SrO had a slightly larger influence on color stability.

Experimental, nonstatistically adjusted data which relate the oxide influence on color stability are disclosed in Figure 4.34. There are some discernable patterns shown which appear to substantiate the statistical interpretations. Systems containing  $ZrO_2$  are the most stable. Replacement of SrO with ZnO also improves stability, and to a greater degree when no  $ZrO_2$  is present. Higher  $Al_2O_3$ /alkalis results in a significant increase in stability when no  $ZrO_2$  is in the frit

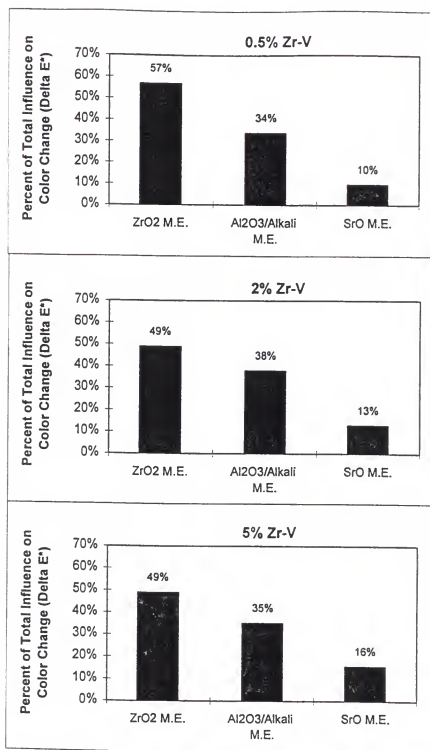


Figure 4.33. Variables weight of influence on Delta E\*, based on statistical models 4.6 (0.5% Zr-V), 4.7 (2.0% Zr-V) and 4.8 (5.0% Zr-V).

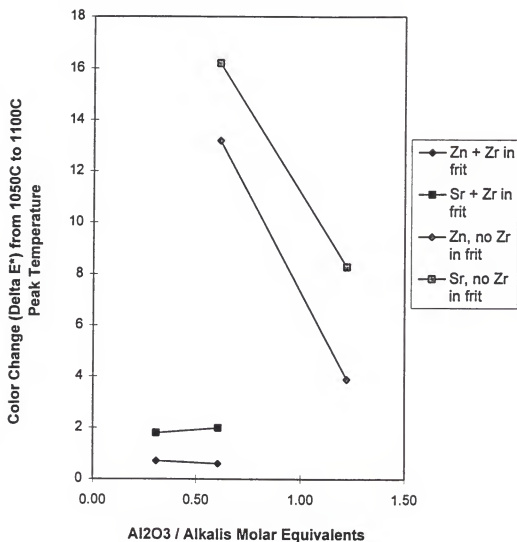


Figure 4.34. Color changes due to variations in peak firing temperature and frit Al<sub>2</sub>O<sub>3</sub>:alkali ratio of coatings batched with 2.0% Zr-V.

but has an insignificant influence at low levels when  $\text{ZrO}_2$  is present.

#### 4.4.3 Log Viscosity vs. Coating Composition and Temperature

For coatings batched with 2.0% Zr-V, their viscosity ( $\eta$ ) during heating from 700°C to 1100°C was thoroughly explained by the model:

	<u>Variable</u>	<u>Coefficient</u>	<u>t-Value</u>
log $\eta$ =	- Y-intercept	7.049	---
	+ $\text{ZrO}_2$	5.278	9.03 (4.10)
	- SrO	1.531	-5.84
	+ $\text{Al}_2\text{O}_3/\text{alkalis}$	1.736	12.73
	+ $1/T$	10,914.600	53.03

where oxides are in molar equivalents in the frit and temperature (T) is in degrees celsius. Equation 4.10 fits the experimental data very well ( $R^2 = 0.98$ ) and no outlier experiments were detected. The standard deviation of the residuals ( $S_{y,x}$ ) was 0.29. Thus, the accuracy of equation 4.10 for predicting log  $\eta$  from 700°C to 1100°C was estimated to be within  $\pm 0.58$  log poise, with a 95% confidence level.

Equation 4.10 is of the form of the Vogel-Fulcher-Tamman (VFT) equation 2.93 in Section 2.2.5d. The A constant in 2.93 can be taken as the temperature-dependent oxide

composition effect of the first four factors in 4.10. The B constant in 2.93 is the coefficient for  $1/T$  in 4.10.

The same frit oxides found to significantly modify  $\Delta E^*$  and K/S also controlled viscosity, but with different magnitudes of influence. Temperature, of course, had the largest effect with its inverse relationship to  $\log \eta$ . The second greatest overall shift in viscosity resulted from the range in frit  $\text{Al}_2\text{O}_3$ /alkali equivalents tested. Unlike relationships with K/S and  $\Delta E^*$ , the  $\text{Al}_2\text{O}_3$ /alkalis molar equivalents in the frit did not produce a curvilinear effect on viscosity.  $\log \eta$  linearly increased with  $\text{Al}_2\text{O}_3$  (from 0.084 to 0.170 molar equivalents) and decreased with alkali content (from 0.130 to 0.294 equivalents). At an average temperature of  $900^\circ\text{C}$  and with other oxides in 4.10 held at their average molar equivalent level ( $\text{ZrO}_2 = 0.078$ ,  $\text{ZnO} = 0.156$ ,  $\text{SrO} = 0.131$ ), the range of  $\text{Al}_2\text{O}_3$ /alkalis tested produced a 1.74 change in  $\log \eta$ . Using the same procedure,  $\text{ZrO}_2$  had the second largest oxide effect, where increasing  $\text{ZrO}_2$  through the range experimented (0 to 0.175 equivalents) caused  $\log \eta$  to raise by 0.92.  $\text{SrO}$  content had the least influence of the significant independent variables, where increasing  $\text{SrO}$  from 0 to 0.311 equivalents resulted in an estimated lowering of  $\log \eta$  by 0.47.

In the Discussion, Section 5.2.2, of this dissertation, the preceding viscosity data are related to color strength and stability results. The potential for applying viscosity data to estimate zircon pigment color stability in new frit compositions is considered.

#### 4.5 Evolved Crystalline Species

X-ray scans of the unfired frits without pigment or bentonite exhibited no crystalline phase peaks.

##### 4.5.1 XRD, SEM and EDS Evaluations

Analyses of crystalline phases present in fired coatings batched with 2.0% Zr-V are detailed in this section. These data are further linked to color properties in the Discussion, Section 5.1.2.

##### 4.5.1a Frits with $ZrO_2$

XRD patterns from fired coatings batched with frits A, B, C and D, all of which contained  $ZrO_2$ , are displayed in Figures 4.35, 4.37, 4.39 and 4.40, respectively. Corresponding SEM micrographs are pictured in Figures 4.36, 4.38 and 4.41 (for C and D).

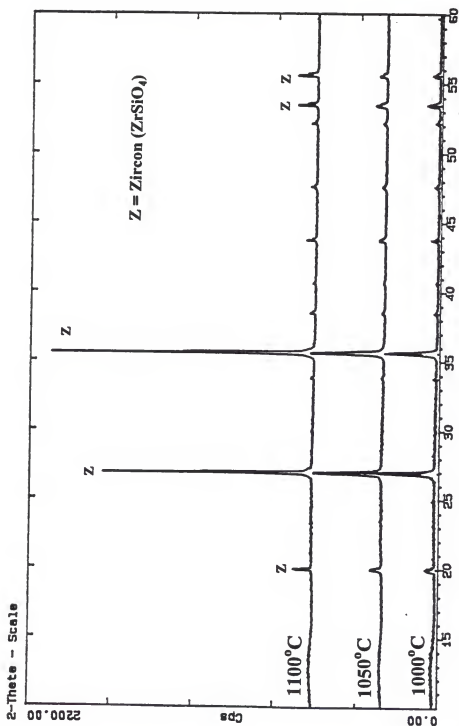


Figure 4.35. XRD patterns from coatings batched with frit A and 2.0% Zr-V, and fired to 1000°C, 1050°C and 1100°C. Frit A includes 8%  $\text{ZrO}_2$ , 12%  $\text{ZnO}$ , 0%  $\text{SrO}$ , 5% alkalis.



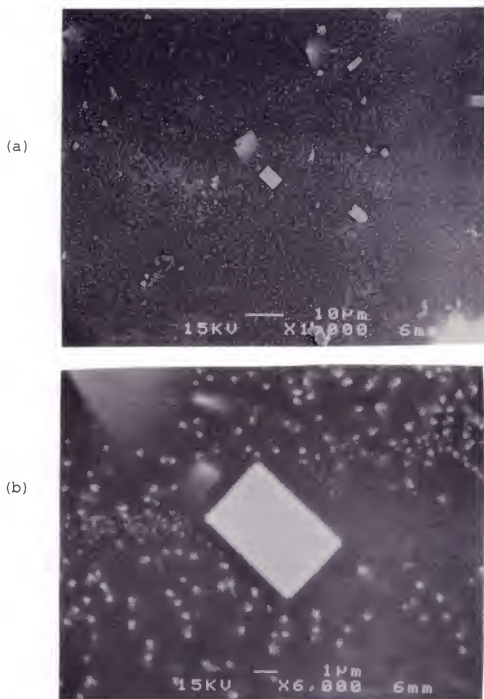


Figure 4.36. SEM micrographs of a coating batched with frit A and 2.0% Zr-V, and fired to 1100°C. Magnification is (a) X 1,000 and (b) X 6,000. Shown are large Zr-V particles surrounded by fine zircon precipitates.

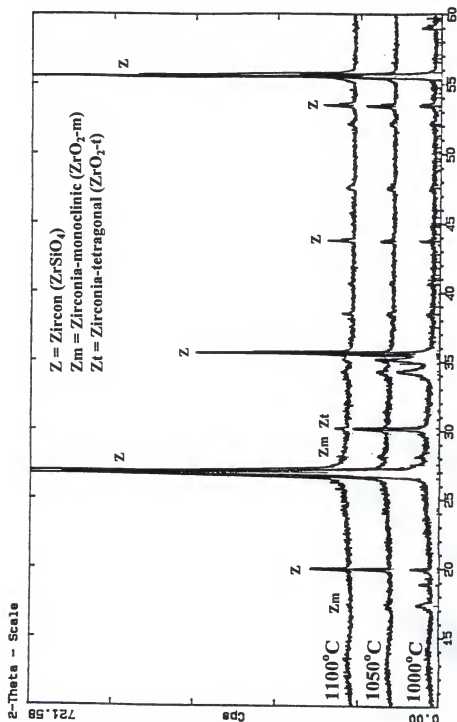
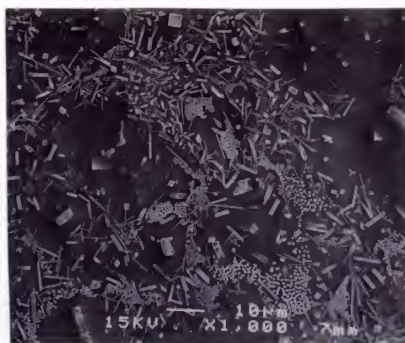


Figure 4.37. XRD patterns from coatings batched with frit B and 2.0% Zr-V, and fired to 1000°C, 1050°C and 1100°C. Frit B includes 8%  $\text{ZrO}_2$ , 12%  $\text{ZnO}$ , 0%  $\text{SrO}$ , 10% alkalis.

(a)



(b)

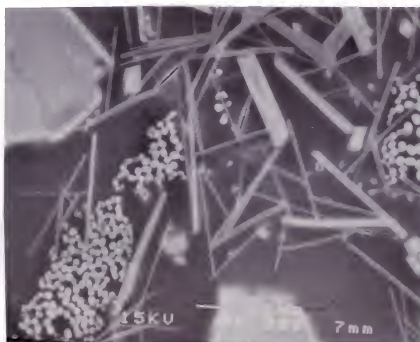


Figure 4.38. SEM micrographs of a coating batched with frit B and 2.0% Zr-V, and fired to 1100°C. Magnification is (a) X 1,000 and (b) X 6,000. Shown are large Zr-V particles, fine zircon precipitates and large zircon fibers.

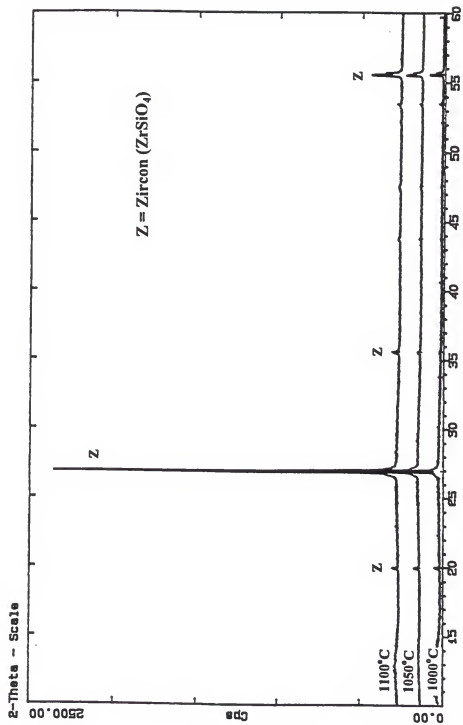


Figure 4.39. XRD patterns from coatings batched with frit C and 2.0% Zr-V, and fired to 1000°C, 1050°C and 1100°C. Frit C includes 8%  $\text{ZrO}_2$ , 0%  $\text{ZnO}$ , 12%  $\text{SrO}$ , 5% alkalis.

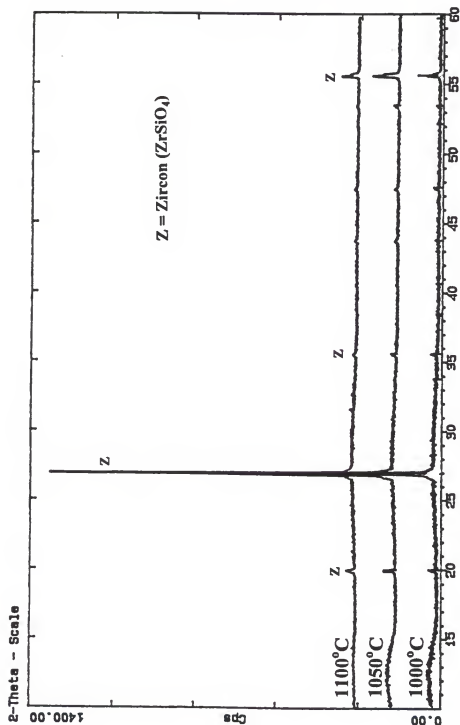
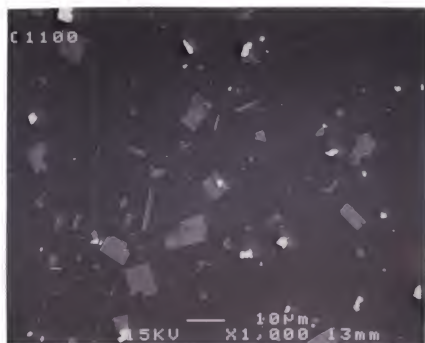


Figure 4.40. XRD patterns from coatings batched with frit D and 2.0% Zr-V, and fired to 1000°C, 1050°C and 1100°C. Frit D includes 8% ZrO<sub>2</sub>, 0% ZnO, 12% SrO, 10% alkalis.

(a)



(b)

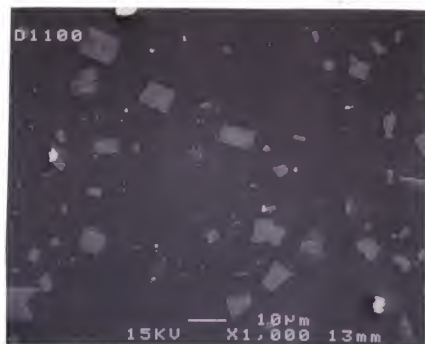


Figure 4.41. SEM micrographs of coatings batched with 2.0% Zr-V, (a) frit C and (b) frit D, and fired to 1100°C. (magnification X 1,000). Particles shown are Zr-V pigment.

Patterns from all four coatings align well with the zircon profile shown in Figure 4.42, where strong peaks exist at reflection planes and  $2\theta$  of [ 101]  $20.20^\circ$ , [ 200]  $26.98^\circ$ , [ 112]  $35.63^\circ$  and [ 312]  $53.48^\circ$ . Zircon was the only phase detected in A,C and D, while additional phases were observed in B. A previous investigation [Blo93] noted that zircon tends to strongly orient along the c-axis in the plane of a coating's surface. With zircon's tetragonal structure ( $a = 6.604 \text{ \AA}$ ,  $c = 5.979 \text{ \AA}$ ), orientation along the c-axis results in enhanced [ h00] lines. Zircon in B, C and D causes exaggerated [ 200] lines, which tend to rise with peak temperature. An increase in temperature lowers the coating viscosity and allows for faster transport of zircon from the bulk melt to the surface.

The zircon profile from frit A (Figure 4.35) has a stronger [ 112] line than B, C or D. SEM micrographs for A in Figure 4.36 reveal numerous small ( $0.2\text{-}0.5\mu\text{m}$ ) zircon precipitates in the glass matrix surrounding a large particle, whose morphology matches that of the Zr-V pigment pictured in Figure 4.43. The small round precipitate clumps are responsible for the [ 112] intensity relative to the exaggerated [ 200] from the pigment. Thus in frit A, both

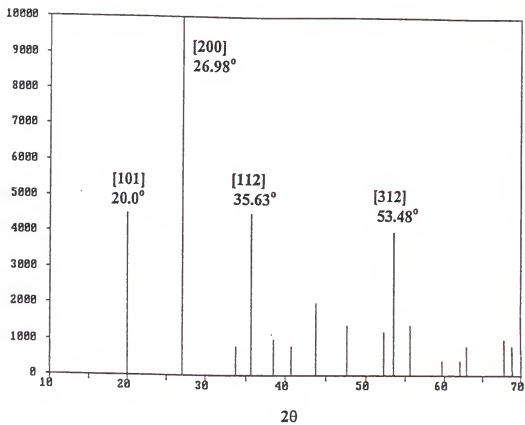


Figure 4.42. X-ray diffraction profile for zircon,  $\text{ZrSiO}_4$ .  
(JCPDS card file data from Ferro Corporation, Cleveland, OH)





Figure 4.43. SEM micrograph of zircon-vanadium (Zr-V) pigment, Ceredec 41715A, X 1,000 magnification.

zircon precipitating from  $\text{ZrO}_2$  in the frit and zircon from the Zr-V pigment structure were identified.

Enlarged XRD patterns from frit B in Figure 4.37 show the presence of not only zircon but also  $\text{ZrO}_2$ -tetragonal ( $a = 5.12 \text{ \AA}$ ,  $c = 5.25 \text{ \AA}$ ) peaks at  $[111] 30.2^\circ 2\theta$ ,  $[002] 34.5^\circ 2\theta$  and  $[200] 35.3^\circ 2\theta$ , again with exaggerated  $[h00]$ .

Intensities of the  $\text{ZrO}_2$ -t lines drop significantly with an increase in firing temperature from  $1000^\circ\text{C}$  to  $1100^\circ\text{C}$ . Very small peaks of  $\text{ZrO}_2$ -monoclinic (baddeleyite) also appear at  $1000^\circ\text{C}$  at exaggerated  $[100] 17.45^\circ 2\theta$  and  $[-111] 28.19^\circ 2\theta$ . The  $\text{ZrO}_2$ -monoclinic completely disappears at  $1100^\circ\text{C}$ . Thus, both zirconia phases crystallized below  $1000^\circ\text{C}$  and dissolved from  $1000^\circ\text{C}$  to  $1100^\circ\text{C}$ . SEM focus on the frit B coating fired to  $1100^\circ\text{C}$  (Figure 4.38) revealed Zr-V pigment, smaller particles which resemble the zircon precipitates in frit A, as well as large fibers of zircon. Overall, SEM showed there was much less fine zircon precipitated from B when compared to A. In addition to strong XRD peaks at  $[200]$  (pigment) and  $[112]$  (spherical zircon precipitates), the fibrous zircon resulted in strong  $[400]$  ( $55.6^\circ 2\theta$ ) intensities.

Small compositional differences between frits A and B produced very different crystallization tendencies. Mainly the  $\text{SiO}_2$ :alkalis ratio varied, where A consisted of 55%  $\text{SiO}_2$

and 5%  $K_2O+Na_2O$ , and B contained 50%  $SiO_2$  and 10%  $K_2O+Na_2O$ .

The 5% increase in alkalis and 5% reduction of silica may deter zircon precipitation and induce formation of lower temperature  $ZrO_2$  phases observed in B for the following reasons:

1. Less  $SiO_2$  is available for formation of  $ZrO_2 \cdot SiO_2$ .
2. An increase in nonbridging alkali ions in the glass results in lower energy requirements for breaking up the network. Figures 4.20 and 4.22 disclose that raising the alkalis from 5% to 10% dropped the softening temperature from 711.3°C to 684.2°C.  $\log \eta$  was also reduced by a factor of 0.75 to 1.0 across the temperature range. More rapid diffusion transport due to a drop in  $\log \eta$  to 6.8-7.6 at the temperatures where  $ZrO_2$  phases have been found to begin precipitating (800-850°C) results in significant  $ZrO_2$  crystallization. Enough  $ZrO_2$  is precipitated at low temperature to where there is still a small amount of undissolved crystals remaining at 1100°C.
3. More energy is required to form zircon from crystalline  $ZrO_2$  and vitreous silica than when both oxides are in the vitreous state. Crystallization data for B and Figure 4.17 indicate that variations in gloss in tiles

produced with frit B could be attributed to the precipitation and dissolution of  $\text{ZrO}_2$  phases.

4. The molar  $\text{Al}_2\text{O}_3$ :alkalis ratio was lower in B, thus less  $\text{Al}^{+3}$  was available to compete with  $\text{Zr}^{+4}$  for glass network sites. More  $\text{Zr}^{+4}$  was required to maintain network connectivity in B and less was freed up to form zircon.

Figures 4.39, 4.40 and 4.41 confirm that Zr-V pigment is the only crystalline phase in frits C and D at all peak firing temperatures. Frits C and D vary from A and B only in that  $\text{ZnO}$  was replaced with  $\text{SrO}$ . Crystallization of zirconium phases did not occur in the presence of  $\text{SrO}$ , thus  $\text{SrO}$  raised the  $\Delta G$  of formation. Sections 4.3.2 and 4.4.3 demonstrated that substituting  $\text{SrO}$  for  $\text{ZnO}$  in the glasses results in higher glass transition temperatures and lower melt viscosities (equation 4.10). Lower viscosities would tend to favor rather than inhibit crystallization, so this does not provide an explanation for the lack of crystallization which resulted in increased color strength with  $\text{SrO}$ . The roles of  $\text{SrO}$  versus  $\text{ZnO}$  in zircon precipitation, dissolution and color development will be further discussed in Section 5.1.1c.

#### 4.5.1b Frits without $\text{ZrO}_2$

XRD patterns from fired coatings batched with frits E, F, G and H are displayed in Figures 4.44, 4.46, 4.48 and 4.50 respectively. Corresponding SEM micrographs are pictured in Figures 4.45, 4.47, 4.49 and 4.51.

Each of the coatings E-H at all three peak firing temperatures still contained some zircon pigment, which is evident by [200] lines which are enhanced due to surface orientation. All of the zircon lines dropped with increased peak temperature, indicating pigment dissolution in the frits without  $\text{ZrO}_2$ . Zircon precipitation and dissolution are detailed with a quantitative analysis in Section 4.5.2.

Dissimilar to coatings A-D, precipitation of non-zirconium species was pronounced in E-H, and the amount of crystal phase increased with higher frit alkali levels. SEM and XRD also indicated that unlike A-D where crystallization was nearly complete by  $1000^\circ\text{C}$ , the total amount of precipitate increased in E-H from  $1000^\circ\text{C}$  to  $1100^\circ\text{C}$ . Enhanced crystallization in the frits without  $\text{ZrO}_2$  could not be explained with changes in viscosity or ionic potentials of the cations. Overall, no significant differences between viscosity curves for A-D (Figure 4.22) versus E-H (Figure

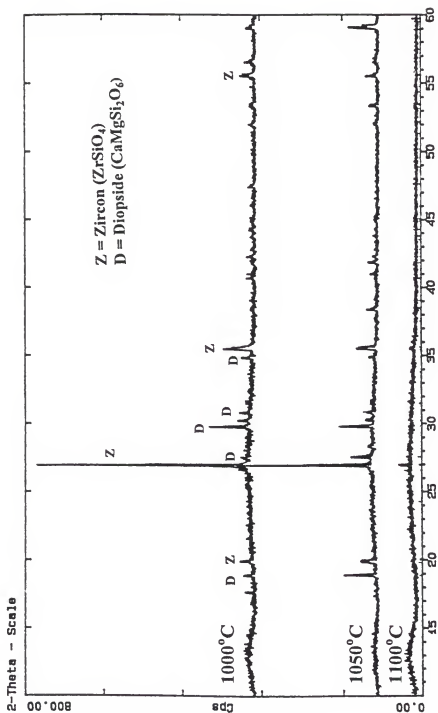


Figure 4.44. XRD patterns from coatings batched with frit E and 2.0% Zr-V, and fired to 1000°C, 1050°C and 1100°C. Frit E includes 0%  $\text{ZrO}_2$ , 12%  $\text{ZnO}$ , 0%  $\text{SrO}$  and 5% alkalis.

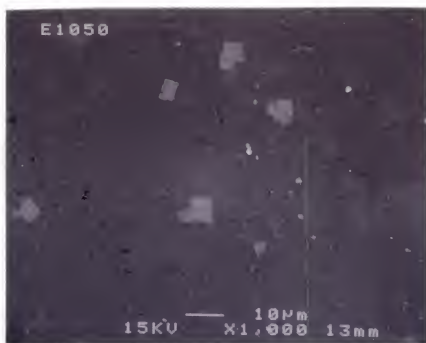


Figure 4.45. SEM micrograph of a coating batched with frit E and 2.0% Zr-V, and fired to 1050°C. Magnification is X 1,000. Shown are large Zr-V particles surrounded by dispersed diopside.

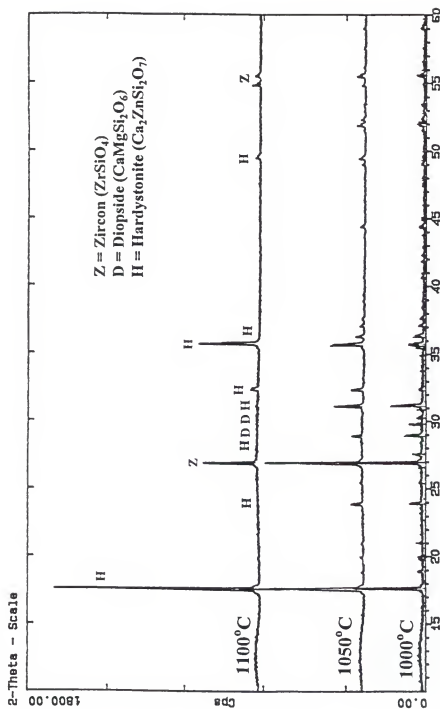
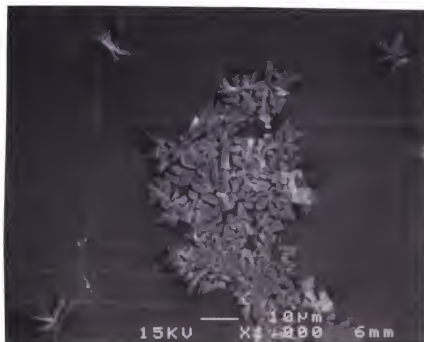


Figure 4.46. XRD patterns from coatings batched with frit F and 2.0% Zr-V, and fired to 1000°C, 1050°C and 1100°C. Frit F includes 0%  $\text{ZrO}_2$ , 12%  $\text{ZnO}$ , 0%  $\text{SrO}$  and 10% alkalis.



(a)



(b)

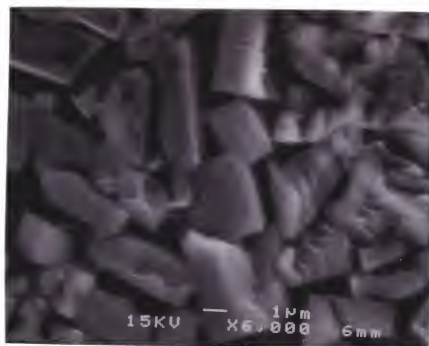


Figure 4.47. SEM micrographs of a coating batched with frit F and 2.0% Zr-V, and fired to 1100°C. Magnification is (a) X 1,000 and (b) 6,000. All particles shown are hardystonite.

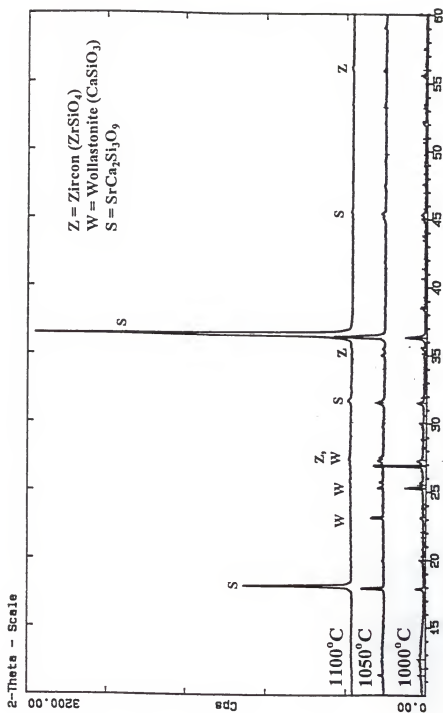


Figure 4.48. XRD patterns from coatings batched with frit G and 2.0% Zr-V, and fired to 1000°C, 1050°C and 1100°C. Frit G includes 0%  $\text{ZrO}_2$ , 0%  $\text{ZnO}$ , 12%  $\text{SrO}$  and 5% alkalis.

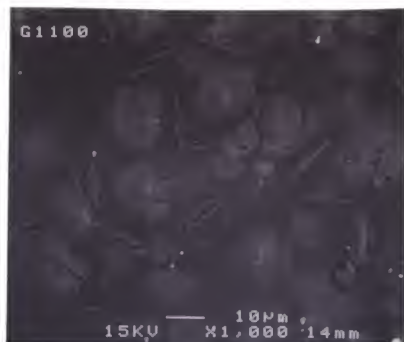


Figure 4.49. SEM micrograph of a coating batched with frit G and 2.0% Zr-V, fired to 1100°C (magnification X 1,000). Shown is crystallized  $\text{SrCa}_2\text{Si}_3\text{O}_9$ .

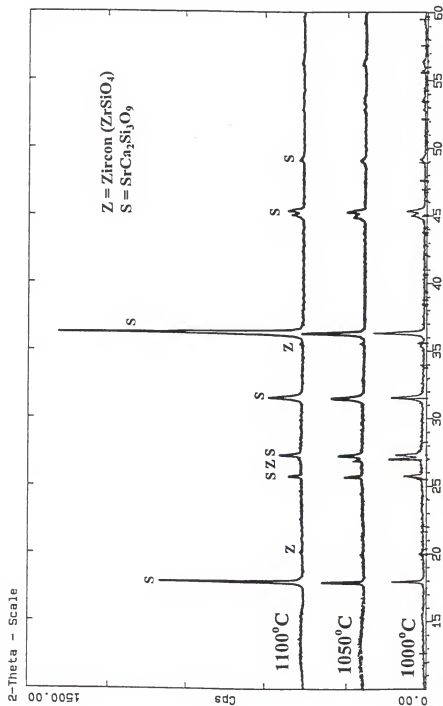


Figure 4.50. XRD patterns from coatings batched with frit H and 2.0% Zr-V, and fired to 1000°C, 1050°C and 1100°C. Frit H includes 0% ZrO<sub>2</sub>, 0% ZnO, 12% SrO and 10% alkalis.

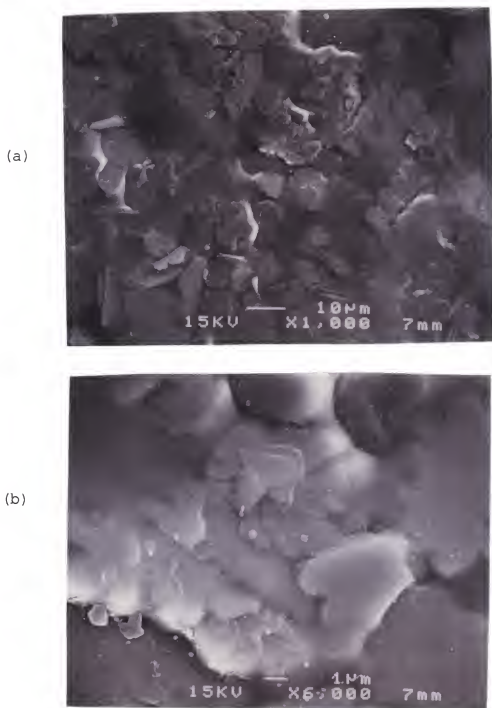


Figure 4.51. SEM micrographs of a coating batched with frit H and 2.0% Zr-V, and fired to 1100°C. Magnification is (a) X 1,000 and (b) X 6,000. Shown is crystallized  $\text{SrCa}_2\text{Si}_3\text{O}_9$ .

4.23) are discernable. Although  $\text{Zr}^{+4}$  has a relatively high ionic potential of 4.6, summations of the moles of each cation multiplied by its ionic potential (from Table 2.5) reveal that the overall bond strengths of E-H (range from 12.54 for H to 13.45 for E) are not significantly different from A-D (range from 12.69 for D to 13.60 for A). The increase in  $\text{Al}_2\text{O}_3$  (ionic potential = 5.3) in E-H makes up for the loss of  $\text{ZrO}_2$

The strong progression of crystallization in E-H caused significant variations in the optical properties of the coatings. This is evident by the large shifts in spectral curves (Figures 4.4-4.6),  $L^*$ ,  $a^*$  and  $b^*$  values (Figures 4.8-4.13) and  $\Delta E^*$  (Figure 4.16) over the range of peak temperatures tested. Overall, lower gloss was also exhibited when no  $\text{ZrO}_2$  was present in the frit (Figure 4.17).

Diopside,  $\text{CaMg}(\text{SiO}_3)_2$  with a monoclinic structure, was identified in E at  $1000^\circ\text{C}$  and  $1050^\circ\text{C}$ , where several XRD lines in Figure 4.44 match the standard pattern. Diopside peaks lowered from  $1000^\circ\text{C}$  to  $1050^\circ\text{C}$ , then disappeared at  $1100^\circ\text{C}$ . A SEM micrograph of the surface of E fired to  $1050^\circ\text{C}$  (Figure 4.45) shows large pigment particles surrounded by a very faint pattern of crystals. The faint crystals appear granular in morphology with particle sizes near 2 to 4  $\mu\text{m}$ .

An EDS of the faint crystals confirmed the presence of diopside by detecting mainly the elements Ca, Mg, Si and O. No faint crystals were viewed under SEM for E fired to 1100°C; only the pigment was present.

Hardystonite,  $\text{Ca}_2\text{ZnSi}_2\text{O}_7$ , with a tetragonal structure, was the predominant crystalline phase in F. Figure 4.46 shows that hardystonite peak intensities at [001]  $17.67^\circ 2\theta$  and [002]  $35.70^\circ 2\theta$  rise dramatically from 1000°C to 1100°C peak temperature. An increase in the number of hardystonite crystals with basal [00k] planes strongly aligned at the surface would account for the exaggerated peaks. Small peaks for diopside are also present at 1000°C but not at 1050°C or 1100°C. Apparently diopside dissolves with temperatures exceeding 1000°C but hardystonite continues to form. Crystals (2-8  $\mu\text{m}$ ) of hardystonite are displayed in the SEM micrographs in Figure 4.47.

An increase in alkalis from 5% in E to 10% in F at the expense of silica resulted in (a) more precipitate in the glass, and (b)  $\text{Zn}^{+2}$  replacing  $\text{Mg}^{+2}$  as the cation bonding with  $\text{Ca}^{+2}$ ,  $\text{Si}^{+4}$  and  $\text{O}^{-2}$  in the crystal structure. Possible explanations for these observations are

1. From E to F, the glass softening temperature dropped significantly from 736°C to 653°C (Figure 4.21). The

increase in alkalis also reduced the melt viscosity by a  $\log \eta$  of 1.8 at 700°C and 0.2 at 1100°C. This increased the slope of the  $\log \eta$  versus temperature curve. Enhanced diffusion transport due to the large viscosity decrease at lower temperatures where nucleation and growth can occur would tend to raise the number and size of crystals formed. Small drops in viscosity at high temperatures may aid in inhibiting dissolution.

2. Additions of higher radius ions ( $\text{Na}^{+1} = 0.97 \text{ \AA}$ ,  $\text{K}^{+1} = 1.33 \text{ \AA}$ ) open up the structure and allow for easier movement of  $\text{Zn}^{+2}$  (radius =  $0.74 \text{ \AA}$ ) to re-arrange and replace smaller Mg (radius =  $0.66 \text{ \AA}$ ) during crystal formation.
3. Because less  $\text{SiO}_2$  was available as a glass former and the addition of nonbridging ions weakens the structure,  $\text{Mg}^{+2}$  is retained in the glass over  $\text{Zn}^{+2}$  because its ionic potential (2.6) is higher than zinc's (2.4).
4. Since both frits contained only 2.0% MgO versus 12.0% ZnO, the reduced viscosity resulting from higher alkali content would enable faster completion of formation of diopside with all of the MgO present. Lower temperature dissolution of diopside could occur, while hardystonite



could form throughout the cycle due to the large amount of ZnO present.

Greater fluctuations in the optical properties of F when compared to E (Figures 4.4-4.6, 4.8-4.13, 4.16) can be attributed to the crystallization differences. Figure 4.17 also shows the large variation in gloss exhibited with F but not E.

For frit G fired to 1000°C and 1050°C, very small peaks for wallastonite,  $\text{CaSiO}_3$  with a triclinic structure, are observed at  $2\theta$  values of 23.2°, 25.3° and 26.9° (overlaps with zircon) in Figure 4.48. The peaks disappear at 1100°C. By far the predominant crystalline species in G, and the only precipitate detected in H, is represented by strong reflections at  $2\theta$  values of 17.95° and 36.38° in Figures 4.48 and 4.50. Although a JCPDS card search initially revealed no matches, the following steps were taken to identify the phase present [B. Blonski, personal communication, engineer at Ferro Corporation, Cleveland Ohio, May 1998]:

1. XRD scans indicated a line phase rather than a solid solution because the patterns did not shift from different firing temperatures or across the surface. The data were input into Jade Text File Browser, Materials Data Inc., computer software, which calculates

- d-spacings for different structures. The d-spacings observed for G and H matched well with a hexagonal system ( $a = b \neq c$ ,  $\alpha = \beta = 90^\circ$ ,  $\gamma = 120^\circ$ ) with  $a = 3.99 \text{ \AA}$ ,  $c = 9.87 \text{ \AA}$  and a cell volume of  $136.36 \text{ \AA}^3$ . Snyder and DeWolf figures of merit based on a statistical comparison of observed versus calculated d-spacings were  $M(10) = 37.3$  and  $F(10) = 16.5$ , respectively. Figures of merit  $\geq 10$  are considered a good match, thus there was significant indexing between actual and calculated patterns.
2. A JCPDS card search of hexagonal silicates showed that the c-lattice constant found was within normal range, but the a-constant gives a smaller cell volume than expected.
  3. A standard procedure of rotating the coordinate system by  $45^\circ$  was performed. The (h0l) cell direction was moved to (hkl). This yielded lattice constants of  $a = 6.91 \text{ \AA}$  and  $c = 9.87 \text{ \AA}$ , which were in a reasonable range and also provided d-spacings that closely matched the XRD scans.
  4. An EDS under SEM detected primarily Sr, Ca and Si in approximate atom ratios of 1:1-2:3-5, respectively. The proportion of Si was probably overestimated due to its

high concentration in the background matrix. Similar hexagonal structures found in the JCPDS card file were  $\text{BaZrSi}_3\text{O}_9$  ( $a = 6.755 \text{ \AA}$ ,  $c = 9.98 \text{ \AA}$ ) and  $\text{ZrK}_2\text{Si}_3\text{O}_9$  ( $a = 6.93 \text{ \AA}$ ,  $c = 10.21 \text{ \AA}$ ). The present structure was compared to these phases in order to surmise the correct stoichiometry of Ca.

5. The estimated cell volume of the present phase is between the two comparable structures. Atomic radii of Ca ( $0.99 \text{ \AA}$ ) and Sr ( $1.12 \text{ \AA}$ ) also fall between Zr ( $0.79 \text{ \AA}$ ) and Ba ( $1.34 \text{ \AA}$ ) or K ( $1.33 \text{ \AA}$ ). The Sr and Ca radii are relatively close and interchangeable in the silicate structure. Using Pauling's rules [Kin76], coordinations of anions about the cations are Ba, K and Sr = 8, Ca = 6-8 and Zr = 6. Thus, based on comparisons of cell volumes and atomic radii, substitutions of Sr and Ca for K or Ba and Zr are all possible. A stoichiometry with two moles of calcium results in  $\text{SrCa}_2\text{Si}_3\text{O}_9$ . The cyclosilicate ( $\text{Si}_3\text{O}_9^{6-}$ ) subclass of silicate minerals consists of three closed rings of tetrahedra, each sharing two oxygens. It provides 4-fold tetrahedral coordination between  $\text{Si}^{+4}$  and  $\text{O}^{2-}$  and  $2.25 \text{ \AA}$  wide interstices between each 3-member ring. The  $\text{Si}_3\text{O}_8^{4-}$  configuration, which results in  $\text{SrCaSi}_3\text{O}_8$ , is not

energetically as favorable and is not a structural classification for silicate linkages [Mas68].

Given these background data, the phase in G and H was identified as  $\text{SrCa}_2\text{Si}_3\text{O}_9$ . This has a similar stoichiometry to hardystonite ( $\text{ZnCa}_2\text{Si}_2\text{O}_7$ ) found in F which contained ZnO rather than SrO. The  $\text{SrCa}_2\text{Si}_3\text{O}_9$  is a new line phase that is not currently in the x-ray JCPDS data file.

Peak intensities for  $\text{SrCa}_2\text{Si}_3\text{O}_9$  in both G and H increase substantially with peak temperatures. Especially noticeable in Figures 4.48 and 4.50 are the  $[002] \ 17.95^\circ \ 2\theta$  and  $[004] \ 36.38 \ 2\theta$  reflections, which are exaggerated due to surface orientation. SEM micrographs in Figures 4.49 and 4.51 display very large (10-30  $\mu\text{m}$ ) crystals of  $\text{SrCa}_2\text{Si}_3\text{O}_9$  in coatings fired to 1100°C peak temperature. Coating H is shown to have more precipitated material at the surface. In accordance with prior evaluations, higher alkalis in H (10%  $\text{K}_2\text{O}+\text{Na}_2\text{O}$ ) resulted in more crystal formation and greater fluctuations in color with temperature than observed with G (5%  $\text{K}_2\text{O}+\text{Na}_2\text{O}$ ).

The following points summarize the results of Sections 4.5.1a and 4.5.1b:

1. Frits with  $\text{ZrO}_2$

- Zircon and a small amount of  $\text{ZrO}_2$  were the only phases that precipitated during firing. Crystallization was complete by  $1000^\circ\text{C}$ .
- Replacement of  $\text{ZnO}$  with  $\text{SrO}$  in the frit prevented zircon crystallization, regardless of the alkali level tested.
- Increasing the alkalis ( $\text{K}_2\text{O}+\text{Na}_2\text{O}$ ) in frits with  $\text{ZnO}$  (without  $\text{SrO}$ ) reduced the quantity of zircon precipitate and caused its morphology to be large and fibrous rather than small and spherical.

2. Frits without  $\text{ZrO}_2$

- Crystallization and zircon pigment dissolution were pronounced and caused large shifts in color from  $1000^\circ\text{C}$  to  $1100^\circ\text{C}$  peak temperature.
- The amount of crystallization and dissolution increased from  $1000^\circ\text{C}$  to  $1100^\circ\text{C}$ .
- In frits with  $\text{ZnO}$ ,  $\text{Ca}_2\text{ZnSi}_2\text{O}_7$  tended to precipitate, while  $\text{SrCa}_2\text{Si}_3\text{O}_9$  crystals formed in frits with  $\text{SrO}$ .

- Higher alkalis ( $K_2O+Na_2O$ ) and/or replacement of ZnO with SrO in the frits increased both crystallization and pigment dissolution.

Proposed mechanisms and their effects on optical properties will be detailed in Chapter 5.

#### 4.5.2 Zircon Quantitative Analysis

Each fired coating batched with 2.0% Zr-V was rescanned with XRD at  $2\theta$  values near  $53.48^\circ$ . Integrated intensities of zircon [312] reflections were determined as described in Section 3.2.8. Several unfired coatings with known amounts of zircon were also scanned in order to establish the relationship between integrated [312] intensity and weight percent zircon in Figure 4.52.

The quantity of zircon in each fired coating, based on XRD rescanning results and Figure 4.52, is plotted in Figure 4.53. The only source of zircon in E, F, G and H is the Zr-V pigment, while A, B, C and D could also precipitate additional zircon from the frit.

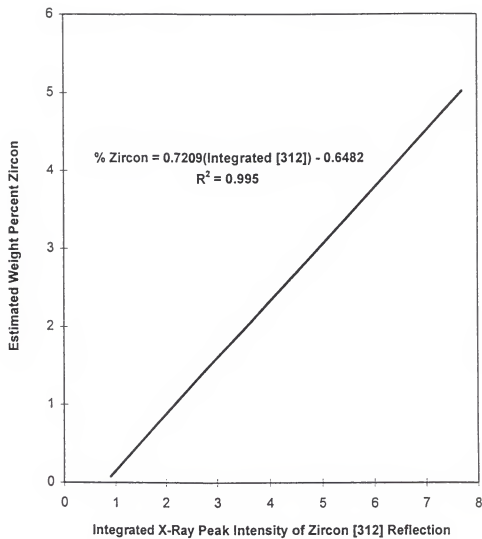


Figure 4.52. Relationship between XRD [312] integrated intensity and weight percent zircon in unfired coatings.

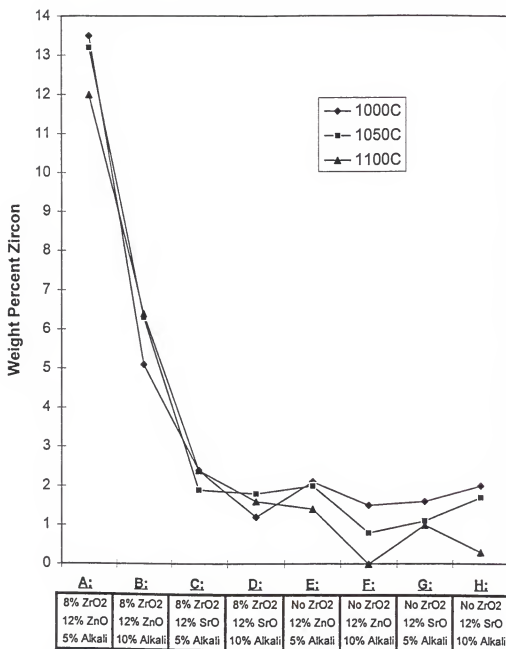


Figure 4.53. Weight percent zircon in fired coatings batched with 2.0% Zr-V.



#### 4.5.2a Frits with $\text{ZrO}_2$ and $\text{ZnO}$

Amounts of zircon much greater than the 2.0% pigment addition were found in A and B.

Zircon in A was found to be between 12.0% and 13.5%. All of the  $\text{ZrO}_2$  in the frit would be required to precipitate 13.4% zircon. It is unlikely that pigment loss occurred in A because zircon crystallization was energetically favorable and the  $\Delta E^*$  from 1050°C-1100°C (Figure 4.16) was extremely low (<1.0).

Zircon content in frit B increased from 8.0% at 1000°C to 9.7% at 1050°C and 1100°C. This is the temperature range where the x-ray scans showed that the small amount of zirconia crystals disappeared and were probably converted to zircon. This may account for the drop in gloss disclosed in Figure 4.17. Since zircon precipitation was energetically favorable and  $\Delta E^*$  was <1.0, no pigment loss was evident in B.

#### 4.5.2b Frits with $\text{ZrO}_2$ and $\text{SrO}$

Zircon pigment was the only crystalline phase found in C and D with XRD and SEM. Frit C yielded Zr-V near 2.0% at all firings with no trend downward with increasing temperature. A slight decrease in zircon content from 1050°C (1.8%) to 1100°C (1.6%) was measured with D. When previous data are

compared, C and D (with SrO) experienced larger  $\Delta E^*$  values (Figure 4.17 and model equation 4.7), shifts in K/S with temperature (Figure 4.28) and energetically unfavorable zircon precipitation when compared to A and B (with ZnO). This provides evidence of slight pigment dissolution in C and D, to within the approximate zircon test measurement accuracy of  $\pm 0.2\%$ .

#### 4.5.2c Frits without $ZrO_2$

Significant dissolution of the Zr-V pigment occurred with increasing temperature in all of the frits without  $ZrO_2$ . Nearly all of the pigment is present at  $1000^\circ C$ , but at  $1100^\circ C$  Zr-V levels for E, F, G and H drop to 1.4, 0.1, 1.0 and 0.3%, respectively. Greater dissolution occurred when alkalis increased from 5% (E and G) to 10% (F and H). No significant difference in pigment loss is evident between frits with ZnO (E and F) or SrO (G and H). Thus, the energetics of the frits without  $ZrO_2$  were favorable for (a) dissolving Zr-V pigment to add  $ZrO_2$  to the glass structure and (b) removing Ca, Zn, Sr and Si to form crystalline species.

## CHAPTER 5 DISCUSSION

### 5.1 Color Strength and Stability Dependency

The previous chapters identified that **color stability** at high temperature in glass frit/zircon-vanadium pigment systems is optimum when both  $ZrO_2$  and ZnO are present in the frit and a relatively high pigment concentration is utilized. In frits without  $ZrO_2$ , increases in the  $Al_2O_3$ /alkalis ratio were found to be beneficial. In all cases, replacement of ZnO with SrO lowered stability.

The highest **color strength** was achieved with frits containing  $ZrO_2$  and SrO, but no ZnO. The weakest colors resulted in frits with no  $ZrO_2$  and low  $Al_2O_3$ /alkalis. In frits without  $ZrO_2$ , increases in the  $Al_2O_3$ /alkalis ratio improved color strength and interchanging SrO and ZnO had no significant effect.

In frits without  $ZrO_2$  (E-H), where crystallization increased with firing temperature, colors not only progressed lighter and less saturated (lower chroma) at higher

temperatures but also shifted in hue. This was evident by changes in the  $L^*:a^*:b^*$  ratios.

Frits containing both  $ZrO_2$  and  $ZnO$  not only yielded excellent color stability but also produced a glossy, highly opacified coating due to the crystallization of fine zircon. The results also revealed that the most stable "transparent" glossy frit, in which no crystallization occurs during firing, incorporates both  $ZrO_2$  and  $SrO$ , but no  $ZnO$ . This combination of oxides provided enough  $ZrO_2$  in the glass structure to preserve the zircon pigment and avoid precipitation of nonzircon species, while  $SrO$  replacement for  $ZnO$  prevented crystallization of opacifying zircon. The optimum transparent frit formula does not conform to the current industry practice of always excluding  $ZrO_2$  from these types of frits.

Chapter 5 proposes explanations for these noted color phenomena. Section 5.2 resolves the validity of applying coating viscosity data, based on heating microscopy and dilatometry measurements, for industrial color quality control purposes.

### 5.1.1 Coating Composition

#### 5.1.1a Zr-V Loading

Color strength due to pigment absorption in terms of K/S was found to increase linearly with pigment content (Figure 4.7), while visual color intensity in terms of  $L^*$ ,  $a^*$  and  $b^*$  values varied logarithmically (Figure 4.15). Higher Zr-V concentrations exhibited less perceivable color changes per weight percent pigment addition. Thus, industrial batching errors are less visible in fired coatings with saturated colors where  $\text{Zr-V} \geq 2.0\%$ . In these coatings, more than enough vanadium atoms are present for contacting nearly all of the incident light and achieving maximum absorption of 640 nm radiation.

Precipitation of typical mineral structures in the glass matrix surrounding the pigment tends to increase reflection at 640 nm and lower reflection at 400 nm, as shown for bentonite in Figure 4.1. The resulting spectral curve redistribution is related in Figure 5.1. Larger shifts in the shapes of the curves occur for 0.5% and 2.0% Zr-V when compared to 5.0%. The 5.0% saturated color tends to be least sensitive to changes in glass matrix conditions due to

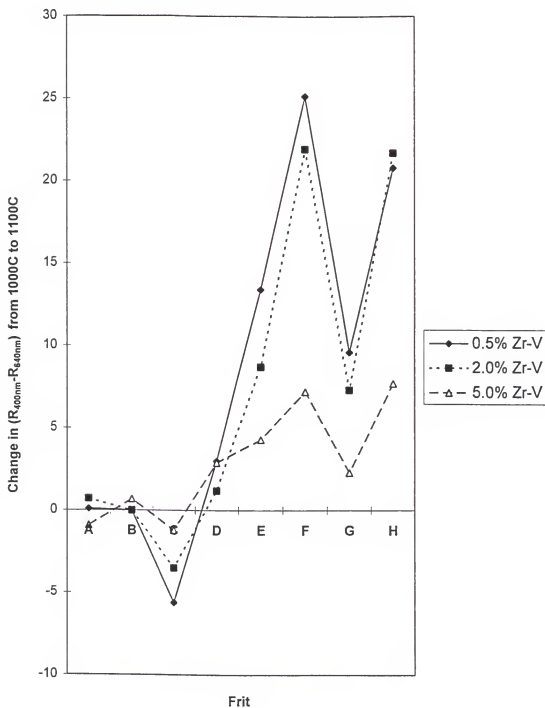


Figure 5.1. Changes in reflectance distributions at 400 nm and 640 nm wavelengths due to increases in peak firing temperature for coatings batched with 0.5%, 2.0% and 5.0% Zr-V.

crystallization in E-H. Thus, higher pigment concentrations are recommended for frits which do not incorporate  $\text{ZrO}_2$ .

Visible color changes due to variations in firing temperature were greatest for an intermediate pigment loading of 2.0% (Figure 4.16, equation 4.9) in frits where pronounced crystallization occurred (E-H). In frits with  $\text{ZrO}_2$  which exhibited little or no crystallization or pigment loss from 1000°C to 1100°C, pigment loading was not a significant variable for color stability. An intermediate Zr-V content exhibited the greatest visible color change due to a shift in peak firing temperature possibly because

1. Very light colors have (a) less pigment and color to lose during processing, and (b) there is a logarithmic relationship between the amount of light reflected and our ability to see it (Figure 2.14), thus, the human eye is less sensitive to changes in light colors.
2. Dark, saturated colors contain more pigment particles than required for maximum absorption of incident light; therefore, pigment dissolution is less noticeable.

#### 5.1.1b $\text{ZrO}_2$

Of all the frit oxides evaluated,  $\text{ZrO}_2$  had the largest influence on improving the color stability of the coatings at

any Zr-V content (Figures 4.16, 4.33 and equations 4.6-4.9). The statistical analysis found an inverse linear relationship between  $\Delta E^*_{1050-1100}$  and  $ZrO_2$  molar equivalents. In frits without  $ZrO_2$ , large precipitates formed during firing and crystallization increased at higher temperatures, causing a reduction in color strength and stability.

Besides  $Si^{+4}$  and  $B^{+3}$  which are strictly glass formers, zirconium has a greater ionic potential and single bond strength with oxygen than any other cation in the frits except  $Al^{+3}$ . Glasses with high  $ZrO_2$  contents tend to have a strong, high melting, viscous and dense structure. Heating microscope images (Figure 4.18), softening temperature ( $T_g$ ) data (Figures 4.20 and 4.21) and viscosity profiles (Figures 4.22 and 4.23) disclose that increases in molten flow and decreases in  $T_g$  and viscosity due to increases in alkali content were of much less magnitude when  $ZrO_2$  was present in the frit. A higher O:Si ratio, due to a reduction in glass forming  $Si^{+4}$  and more nonbridging alkali ions, was partially compensated for by  $Zr^{+4}$  bridging the excess oxygen in the structure. Frit B (10% alkalis) precipitated less zircon than frit A (5% alkalis) because more  $Zr^{+4}$  was retained in the glass structure to bond with the extra  $O^{-2}$  from the higher alkali content. In frits C and D, where SrO replaced ZnO,



all of the  $Zr^{+4}$  remained in the glass structure at both alkali levels tested, for reasons that will be discussed in the next section.

The effect of  $ZrO_2$  on  $\Delta E^*$  is related to the glass density as shown in Figure 5.2. Frits with  $ZrO_2$  are denser and yield improved color stability, while frits without  $ZrO_2$  are shown to be more color sensitive to temperature and alkali level. By comparison, the density of  $ZrO_2$  is 5.5 g/cm<sup>3</sup>, while  $Al_2O_3$  and CaO which replaced  $ZrO_2$  in frits E-H are 3.8 and 3.3, respectively. Higher density glasses contain less permeable structures, smaller rates of removal of latent heat of fusion and lower diffusion coefficients and mass transport rates, resulting in inhibition of devitrification and dissolution reactions.

Fritted  $ZrO_2$  lowered Zr-V color strength (K/S) when ZnO was present (Figure 4.25, equations 4.1-4.4) and raised K/S when SrO replaced ZnO. Zircon precipitation which occurred in frits with ZnO and  $ZrO_2$  increased the overall reflectance from the coating and lightened its color. Zircon formation was complete by 1000°C and resulted in good color stability from 1000°C to 1100°C. When SrO replaced ZnO in frits with  $ZrO_2$ , the solubility of  $ZrO_2$  increased to the point where no zircon crystallized from the frit. Since no zircon

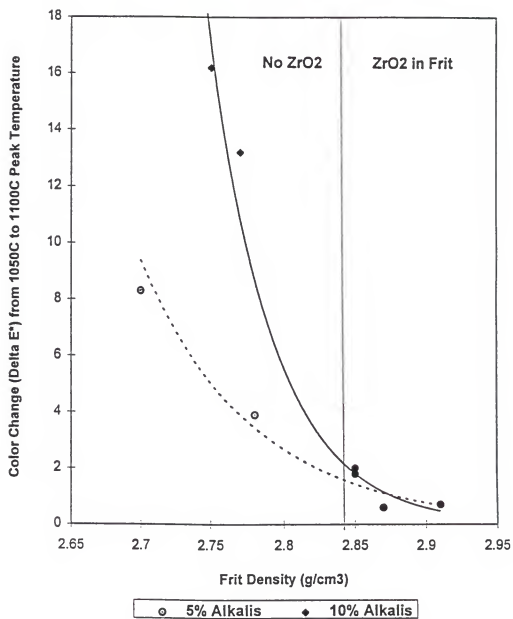


Figure 5.2. Influence of frit density on the color stability of coatings batched with 2.0% Zr-V pigment.

precipitate was present in the coating to reflect light in the wavelength region where pigment absorption occurs, a strong blue color was achieved.

In all cases, regardless of whether ZnO or SrO was in the frit, much less, if any, Zr-V pigment dissolution occurred when  $\text{ZrO}_2$  was present. In the frits tested,  $\text{ZrO}_2 > 0.139$  molar equivalents was sufficient for satisfying most of the zircon solubility requirements and maintaining minimum energy configurations without the necessity of dissolving a significant amount of zircon pigment to acquire more  $\text{ZrO}_2$  for the glass structure.

#### 5.1.1c SrO vs. ZnO

Further evidence that SrO replacement of ZnO raises  $\text{ZrO}_2$  and zircon solubility (and  $\Delta G$  of formation of zircon) is given in Figure 5.3. A graphical method was employed to estimate how much of the zircon present in fired coatings A-D was pigment rather than zircon precipitated from  $\text{ZrO}_2$  in the frit. (The quantitative x-ray analysis of zircon content in Section 4.5.2c identified how much pigment was in E-H, where the frits contained no  $\text{ZrO}_2$  and Zr-V was the only form of zircon in the coatings.) Since  $K/S \rightarrow 0$  as  $\text{Zr-V} \rightarrow 0$ , positive x-axis intercepts estimate quantities of dissolved pigment.

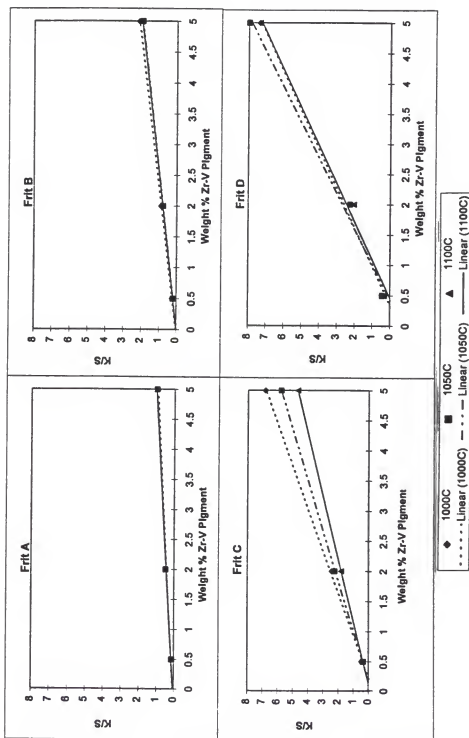


Figure 5.3. Pigment absorption factors (K/S) for coatings batched with Zr-V pigment and frits containing 8% ZrO<sub>2</sub>, and fired to 1000°C, 1050°C or 1100°C peak temperature.

Intercepts for frits A and B are at zero, while frit C varies from 0.1 to 0.3 and D is 0.4 to 0.5. Figure 5.3 indicates that a small amount of pigment dissolution occurs in frits with  $\text{ZrO}_2$  when SrO is present but not when ZnO replaces SrO. The dissolution, however, is still much less than found in frits without  $\text{ZrO}_2$  (E-H). The interaction variable  $-(\text{SrO} \times \text{T})$ , derived in statistical models 4.1-4.4 and illustrated with Figure 4.28, was found to significantly affect K/S. This provides additional proof that SrO increases the dissolution of Zr-V pigment with temperature.

Both SrO and ZnO modify  $\text{SiO}_4$  network interconnectivity by increasing the O:Si ratio, resulting in lower  $T_g$  and viscosity. Similarly,  $\text{Sr}^{+2}$  and  $\text{Zn}^{+2}$  may act as glass modifiers and occupy interstitial sites to provide local charge neutrality near nonbridging oxygen. However, unlike  $\text{Sr}^{+2}$ ,  $\text{Zn}^{+2}$  can also contribute in part to the network structure as an intermediate [Chi97]. The atomic radii ( $\text{Zn}^{+2} = 0.74 \text{ \AA}$ ;  $\text{Zr}^{+4} = 0.79 \text{ \AA}$ ) and oxide densities ( $\text{ZnO} = 5.6 \text{ g/cm}^3$ ;  $\text{ZrO}_2 = 5.5 \text{ g/cm}^3$ ) of zinc and zirconium are comparable. The radius of  $\text{Sr}^{+2}$  is higher ( $1.12 \text{ \AA}$ ) and the density of SrO is lower ( $4.7 \text{ g/cm}^3$ ). Therefore, favorable substitution of  $\text{Zn}^{+2}$  as an intermediate in the glass structure for some  $\text{Zr}^{+4}$  is likely to lower the activation energy and  $\Delta G$  of formation of

zircon from  $\text{ZrO}_2$  in the frit. Because  $\text{Sr}^{+2}$  cannot function as an intermediate and maintain some network interconnectivity,  $\text{Zr}^{+4}$  remains in the structure when SrO replaces ZnO.

Thus, if maximum color stability or opacity due to zircon precipitation is desired, frits containing both ZnO and  $\text{ZrO}_2$  are recommended. If color strength or a relatively stable transparent frit is the highest priority, frits containing  $\text{ZrO}_2$  and SrO but no ZnO are best.

In frits containing no  $\text{ZrO}_2$ , the statistical models substantiate the same decrease in color stability (higher  $\Delta E^*$ ) when SrO replaces ZnO, but no effect on K/S was found. The overall color strength cannot be raised with SrO through a reduction in zircon precipitation because no  $\text{ZrO}_2$  is present in the frit to form zircon. Pigment dissolution, however, and the corresponding high color variation which temperature, still increase when SrO replaces ZnO in frits without  $\text{ZrO}_2$ .

#### 5.1.1d $\text{Al}_2\text{O}_3$ /Alkalies

The data and statistical models revealed that the  $\text{Al}_2\text{O}_3$  : alkalis ratio had a larger influence on  $\Delta E^*$  and K/S than other oxides in frits without  $\text{ZrO}_2$ . When no  $\text{ZrO}_2$  was present, higher ratios resulted in improved color strength and stability at high temperature. Conversely, increases in

$\text{Al}_2\text{O}_3$ /alkalis slightly lowered color strength and stability in frits which incorporated  $\text{ZrO}_2$ . Also, the greatest increases in melt viscosity occurred in frits with or without  $\text{ZrO}_2$  when the  $\text{Al}_2\text{O}_3$ /alkalis was raised.

Although  $\text{Al}^{+3}$  has a large ionic potential (5.6) and increases the softening point, viscosity (and correspondingly lowers mass transport and diffusion rates) and density of a glass, in the present study it was not as effective as  $\text{Zr}^{+4}$  in inhibiting pigment dissolution and crystallization above  $1000^\circ\text{C}$ . Frits with  $\text{ZrO}_2$  yielded much more stable optical properties than frits where  $\text{ZrO}_2$  was replaced with  $\text{Al}_2\text{O}_3$  and  $\text{CaO}$ . When  $\text{Zr}^{+4}$  is missing (frits E-H),  $\text{Al}^{+3}$  takes over as the main glass intermediate but is not as effective in maintaining the structure because it connects with less oxygen and requires adjacent alkalis for charge neutrality. Substitutions for  $\text{Zr}^{+4}$  or  $\text{Si}^{+4}$  require  $\text{Al}^{+3}+\text{Na}^{+1}$  or  $\text{Al}^{+3}+\text{K}^{+1}$ , where  $\text{Al}^{+3}$  occupies the centers of  $\text{AlO}_4$  tetrahedra and converts nonbridging to bridging oxygen. An "equivalency" point is reached when  $\text{Al}_2\text{O}_3$ /alkalis = 1.0. At ratios other than the equivalency point, excess alkalis or  $\text{Al}^{+3}$  behave as a modifier. Network connectivity with small radius  $\text{Al}^{+3}$  (0.51 Å) combined with large radius  $\text{Na}^{+1}$  (0.97 Å) or  $\text{K}^{+1}$  (1.33 Å) occupation of nearby interstitial sites creates a larger

strain on the structure than when  $\text{Zr}^{+4}$  (0.79 Å) is incorporated in the glass network. The increased strain results in lower thermodynamic stability and a greater tendency for devitrification.

In frits where no  $\text{ZrO}_2$  is present, higher  $\text{Al}_2\text{O}_3$ /alkalis ratios reduce crystallization and pigment dissolution by raising the melt viscosity, which inhibits diffusion transport. This provides improved color strength and stability at high temperature. Increases in  $\text{Al}_2\text{O}_3$  help to tie up excess oxygen from the alkalis.

In frits with  $\text{ZrO}_2$ , the  $\text{Al}_2\text{O}_3$ :alkalis ratio has a different effect on the fired color than found in frits without  $\text{ZrO}_2$ . Additions of  $\text{Al}_2\text{O}_3$  allow  $\text{Al}^{+3}$  to compete with  $\text{Zr}^{+4}$  for network sites, and some  $\text{Zr}^{+4}$  is freed up to form zircon crystals. The color strength and stability are slightly lowered due to the increased quantity and variation of zircon crystallization. Although higher alkalis in these frits lower the viscosity, less zircon precipitation results and stronger colors are produced. Zirconium gets tied up in lower temperature  $\text{ZrO}_2$  phases which precipitate and dissolve in the lower viscosity medium. Thus, the statistically derived curvilinear relationships between  $\text{Al}_2\text{O}_3$ /alkalis and



both K/S and  $\Delta E^*$ , as shown in Figures 4.25 and 4.32 and discussed in Chapter 4, are elucidated.

### 5.1.2 Crystalline Species

Crystallization during firing significantly influenced the color strength, stability, gloss and opacity of the coatings. In frits with  $ZrO_2$ , zircon was the only crystalline phase that formed. Most of the quantitative work of the present study was performed on these frits because of their predominant use in industry.

Frits without  $ZrO_2$  tended to precipitate crystals with cations of Ca, Si and either Sr or Zn when present. While precipitation of zircon in frits altered reflectance values but not the wavelengths where peak reflectance and absorption occurred, crystallization of nonzircon species changed the peak reflectance wavelength (Figures 4.4-4.6) and significantly altered the shapes of the spectral curves.

#### 5.1.2a Zircon

The small radius of zirconium provides a high diffusion rate for forming crystals. Figures 4.36 and 4.38 revealed numerous 0.2-0.5  $\mu m$  particles and 2-5  $\mu m$  fibers of zircon

precipitated from  $\text{ZrO}_2$  and  $\text{SiO}_2$  in the frit, surrounding pigment particles 8-10  $\mu\text{m}$  in size.

The particle size and index of refraction of a material determine its ability to scatter light. Zircon's dense tetragonal structure yields a high index of refraction ( $n = 2.05$ ) when compared to the coating matrix ( $n \approx 1.55$ ). Maximum scattering from zircon occurs with particle sizes of 0.60 to 0.75  $\mu\text{m}$  [Blo94b]. The 0.2-0.5  $\mu\text{m}$  zircon precipitate particles in frits A and B are slightly smaller than the optimum size for scattering the most visible light. However, sizes closer to 0.4-0.5  $\mu\text{m}$  (400 nm-500 nm) increase the amount of blue light scattered and lessen the quantity of yellow light reflected because near 450 nm corresponds to the wavelength of blue light. This enhances the blue color produced by the Zr-V pigment, which absorbs yellow light without greatly scattering other visible wavelengths due to its large size.

The small 0.2-0.5  $\mu\text{m}$  zircon precipitates also produced high gloss, where crystallization of larger particles in frits F, G and H (2.0-30.0  $\mu\text{m}$ ) caused a significant increase in diffuse reflectance and lowering of specular reflectance (Figure 4.17). The gloss of frit B was lower than A because some large fibers of zircon (2-5  $\mu\text{m}$ ) had precipitated along

with the smaller particles. The increased alkali content in frit B resulted in a lower viscosity medium which enhanced crystal growth.

Figure 5.4 illustrates how zircon precipitates and blue pigment modified a coating's color. Linear relationships represent fired coatings where the only zircon present is pigment ( $\leq 2.0\%$ ) and nonlinear plots are for coatings containing 2.0% Zr-V plus crystallized zircon. The two curves converge at 2.0% zircon where only pigment is present. Data from all three peak firing temperatures are graphed.

Increases in the quantity of zircon precipitate in the coatings from 2.0% to 13.0% resulted in greater losses in lightness ( $\Delta L^* = 16$ ) than greenness ( $\Delta a^* = 8$ ) or blueness ( $\Delta b^* = 9$ ). The precipitates caused more scattering of all visible wavelengths and less absorption of 640 nm light, which reduced the overall color strength. However, the blue color was partially preserved due to the enhanced scattering of 400-500 nm light from the 0.2-0.5  $\mu\text{m}$  particles. The result is a very light but distinct, high-chroma blue. Frits A and B produced the highest blue ( $-b^*$ ) values of light colors with  $L^*$  values  $> 75.0$  due to this phenomenon. An analysis of the spectral reflectance data also shows that, by comparison, frit A yielded the highest reflectance ( $\approx 75$ ) at

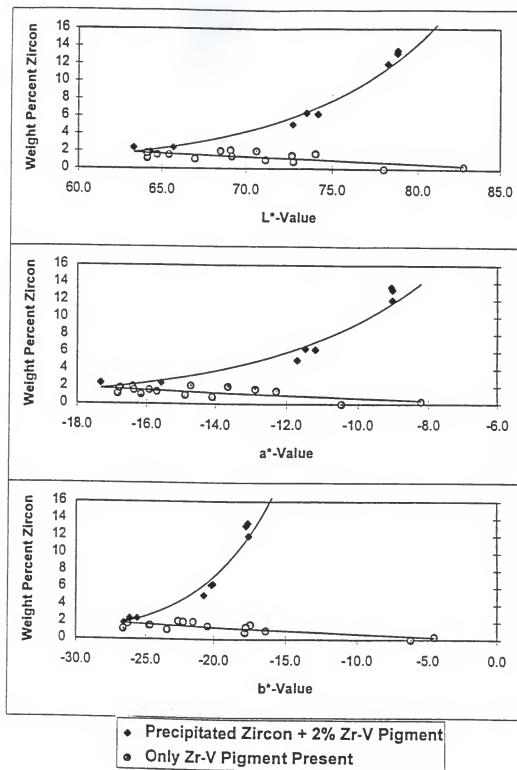


Figure 5.4. Visual lightness ( $L^*$ ), greenness ( $-a^*$ ) and blueness ( $-b^*$ ) as a function of weight percent zircon in the fired coatings batched with 2.0% Zr-V.

460 nm blue wavelengths, when 640 nm reflectance values were near 40. Support of this hypothesis is given in Figure 4.14 of previous Section 4.2.3. Data points for light colors with higher than predicted  $L^*$ -values above the  $L^*$  versus  $b^*$  curve represent frits A and B where zircon precipitated. All of the other coatings appeared to be darker, yellower and greener than A and B.

The relationship between color and weight percent zircon precipitate was found to be logarithmic:

$$L^* = 8.23 \ln (Z) + 57.72 \quad (5.1)$$

$$a^* = 4.45 \ln (Z) - 20.0 \quad (5.2)$$

$$b^* = 4.94 \ln (Z) - 29.8 \quad (5.3)$$

where  $Z$  is the weight percent of zircon precipitate.

These relationships correspond to the phenomenon noted in Background, Section 2.1.3, where perceived lightness has been found to be a logarithmic function of the actual light level reflected from an object [Hun87]. At higher zircon contents and reflectances, a less noticeable color difference is perceivable per unit change in reflectance. Equations 5.1-5.3 also clearly reveal that  $a^*$  and  $b^*$  change less than  $L^*$  with increasing zircon precipitate content. Thus, a method has been quantified for producing very opaque, glossy, light and "clean" blue color by maintaining a low  $b^*$  as  $L^*$

goes up. Similarly, color from other pigments can be enhanced through controlled crystallization of zircon to a particle size that tends to scatter more light of wavelengths corresponding to the desired color and less light where absorption by the pigment occurs. Sections 4.5 and 5.1.1 revealed that zircon crystallization could be controlled by varying the  $\text{SrO}:\text{ZnO}$  and  $\text{Al}_2\text{O}_3:\text{alkali}$  ratios.

Pigment dissolution when no zircon precipitate is present, as denoted with the linear plots in 5.4, yields nearly the same effect on  $L^*$  and  $b^*$ . Adding or subtracting Zr-V at quantities  $\leq 2.0\%$  does not produce unique color. As noted in Section 5.1.1, minimum zircon pigment loss and correspondingly greater color stability is achieved with frits formulated to precipitate zircon.

The relationship between light absorption by the pigment, in terms of K/S values, and weight percent zircon is displayed in Figure 5.5. The curves again converge at 2.0% zircon where only pigment is present. Zircon affected K/S by

$$K/S = 3.975 (Z)^{-0.8283} \quad (5.4)$$

Comparisons of equations 5.1-5.3 and Figure 5.4, with equation 5.4 and Figure 5.5, confirm that the 0.2-0.5  $\mu\text{m}$  zircon precipitate crystals influenced lightness ( $L^*$ ) to a greater degree than the absorption of light near 640 nm which

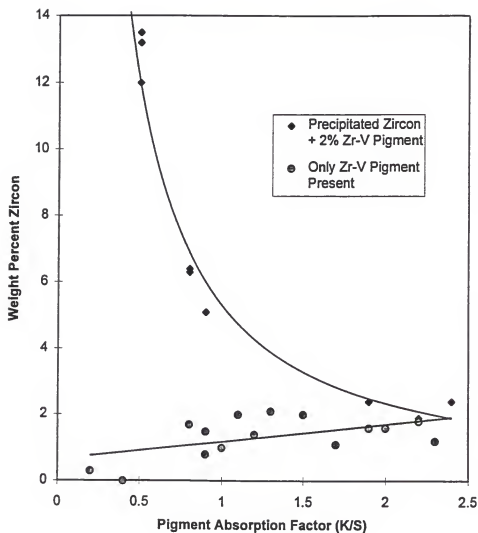


Figure 5.5. Pigment absorption factor (K/S) as a function of Zr-V pigment and zircon contents in coatings batched with 2.0% Zr-V.

causes blueness ( $-b^*$ ). The asymptotic curve in Figure 5.5 reveals that raising the amount of zircon from 5% to 13.5% dropped K/S by only 0.3. Correspondingly, blue color lowered by only  $\Delta b^* = 3.0$  while lightness changes were much more visible, where  $\Delta L^* = 6.0$ . Thus, precipitation of 0.2-0.5  $\mu\text{m}$  zircon from 5% to 13.5% by weight does not significantly alter the blue color strength if the Zr-V pigment is maintained.

The wider spread of data points on color and absorption plots (Figures 5.4 and 5.5) where only pigment is present is indicative of the simultaneous Zr-V dissolution and pronounced crystallization of large nonzircon species in frits E-H. In frits where no zircon precipitated, both pigment dissolution and extensive crystallization were more prevalent and caused significant color variations (Figure 5.6). Precipitation of zircon was complete before 1000°C, and the amount of zircon in systems where its crystallization was energetically favorable stays nearly constant from 1000°C to 1100°C. The energetic preference for crystallizing zircon in these glasses inherently preserves zircon pigments and, consequently, yields good color stability.



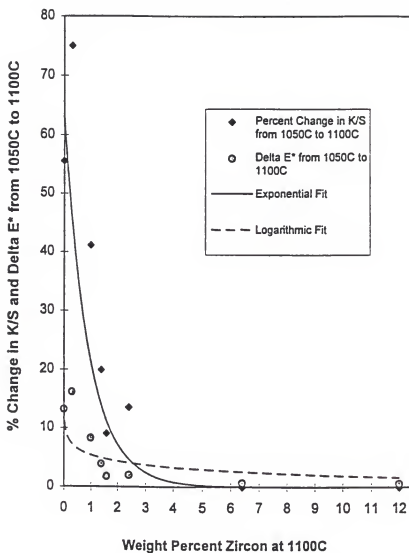


Figure 5.6. Changes in color stability denoted by K/S and Delta E\*, as a function of weight percent zircon in coatings batched with 2.0% Zr-V.

### 5.1.2b Diopside

A small amount of diopside,  $\text{CaMg}(\text{SiO}_3)_2$  with a monoclinic structure was identified in coatings batched with frit E and fired to 1000°C and 1050°C (Figure 4.45), but the diopside was completely dissolved at 1100°C. This progression, combined with Zr-V pigment dissolution, altered the colors of these coatings.

Diopside's density ( $\rho = 3.3\text{--}3.6 \text{ g/cm}^3$ ) index of refraction ( $n = 1.66\text{--}1.76$ , depending on crystal orientation) and corresponding ability to scatter light are less than zircon's. Its particle sizes (2-4  $\mu\text{m}$ ) in the fired coating were too large to cause preferential scattering of visible light wavelengths. Strong x-ray peaks at a  $2\theta$  of 29.85° from  $[-221]$  reflection result from the diopside structure. Figure 5.7 weighs the impact of pigment dissolution and diopside crystallization signified by  $[-221]$  reflection, on color changes. Simultaneous dissolution of diopside and pigment occurred with increasing temperature. The color changes are mainly due to pigment dissolution rather than the small amount of diopside formed, as denoted by the low x-ray peak intensities. Because frit E contained ZnO rather than SrO and a high  $\text{Al}_2\text{O}_3$ :alkali ratio (1.22), it had the most stable glass structure of the frits without  $\text{ZrO}_2$ . These conditions

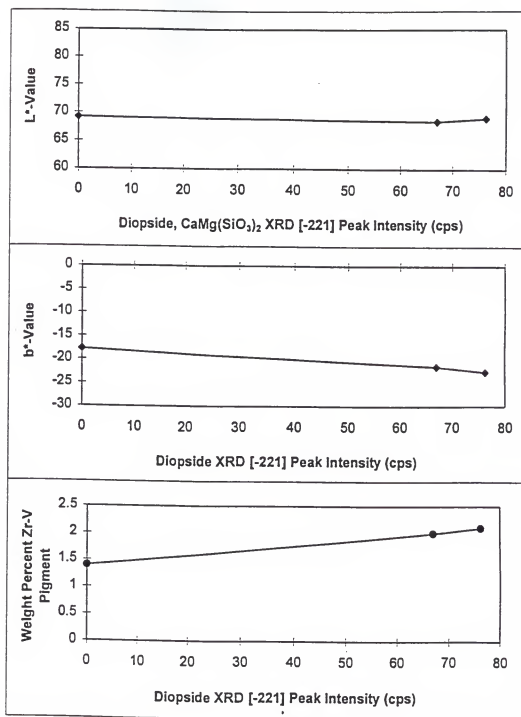


Figure 5.7. Color lightness ( $L^*$ ) and blueness ( $-b^*$ ) progression with diopside crystallization and pigment dissolution in coatings batched with frit E and 2.0% Zr-V.

yielded the least crystallization and Zr-V dissolution, and best color stability and strength when no  $\text{ZrO}_2$  was present in the frit.

#### 5.1.2c Hardystonite

A dramatic increase in the magnitude of crystallization and pigment dissolution occurred when the  $\text{Al}_2\text{O}_3$ /alkali molar ratio was decreased from 1.22 in frit E to 0.61 in frit F. When the ratio falls below the equivalency point of 1.0, excess alkalis serve as modifiers and lower viscosity, enhance devitrification and increase zircon pigment solubility. The drop in gloss exhibited in Figure 4.17 and a reduction in color stability ( $\Delta E^* = 3.9$  for E,  $\Delta E^* = 13.2$  for F at 2.0% Zr-V) were consequences.

Crystallization of hardystonite,  $\text{Ca}_2\text{ZnSi}_3\text{O}_7$  with a tetragonal structure, increased with peak temperature in coatings batched with frit F (Figure 4.47). Its density ( $\rho = 3.4 \text{ g/cm}^3$ ), relatively low index of refraction (no values were found in the literature, but  $n$  is proportional to  $\rho$ ) and large precipitate size (2-8  $\mu\text{m}$ ) produced less scattering of visible light than zircon. Progression of hardystonite crystallization with peak temperature is denoted by the strong x-ray [001] reflection peak intensities shown in

Figure 5.8. Over the range of hardystonite precipitated, Zr-V pigment weight dropped from 1.5% to near 0%. Unlike the case where fine crystals of zircon preserved some of the blue color in frits A and B, simultaneous precipitation of hardystonite and loss of Zr-V in F result in a larger reduction in blue ( $\Delta b^* = 14.3$ ) than increase in lightness ( $\Delta L^* = 5$ ). Thus, a much greater lowering of chroma with increasing lightness occurred.

#### 5.1.2d Strontium Calcium Silicate

The magnitude of crystallization and pigment dissolution in frits without  $ZrO_2$  is further increased when SrO replaces ZnO, as was the case in frits G and H. A reduction in melt viscosity and greater zircon pigment solubility (for reasons detailed in Section 5.1.1c) accompanying the substitution resulted in lower color stability ( $\Delta E^* = 8.3$  for G and 16.3 for H at 2.0% Zr-V) and gloss.

A previously unidentified crystalline phase,  $SrCa_2Si_3O_9$ , crystallized in coatings batched with frits G and H (Figure 4.49 and 4.51). The large, 10-30  $\mu m$  precipitates with a hexagonal structure, relatively low density (approximately 3.0-3.3 g/cm<sup>3</sup> estimated based on comparisons with similar structures) and small index of refraction produce less

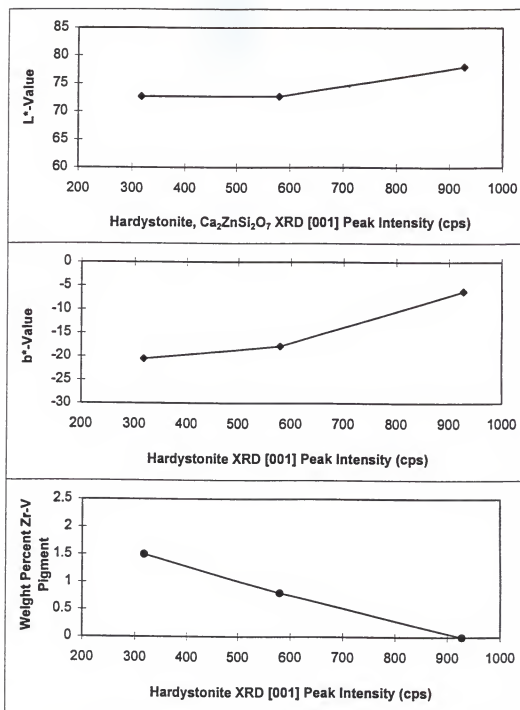


Figure 5.8. Color lightness ( $L^*$ ) and blueness ( $-b^*$ ) progression with hardystonite crystallization and pigment dissolution in coatings batched with frit F and 2.0% Zr-V.

visible light scattering than zircon. The amount of crystalline phase formed in the glass increased with peak temperature while the quantity of zircon pigment decreased. Figure 5.9 illustrates the color changes due to  $\text{SrCa}_2\text{Si}_3\text{O}_9$  crystallization, denoted by x-ray [002] reflection peak intensity, versus pigment loss. The plots show greater Zr-V dissolution in frit H where the  $\text{Al}_2\text{O}_3$ /alkali ratio (0.61), and thus the melt viscosity, are lower. Higher XRD peak intensities result from frit G ( $\text{Al}_2\text{O}_3$ /alkalis = 1.22), perhaps due to preferred orientation at the surface of the coating. The gloss readings (Figure 4.17) and SEM micrographs (Figures 4.49 and 4.51) indicate that more  $\text{SrCa}_2\text{Si}_3\text{O}_9$  is present in fired coatings batched with frit H.

Ultimately, color is weakened more by pigment dissolution than the crystallization of large, low reflecting precipitates. Thermodynamic instability at high firing temperatures in the relatively weak glass structures without  $\text{ZrO}_2$  is a catalyst for both processes. Conversely, inhibition of diffusion transport processes in molten glass with increased  $\text{Al}_2\text{O}_3$ /alkalis helps to preserve color by simultaneously limiting pigment loss and the precipitation of new species.

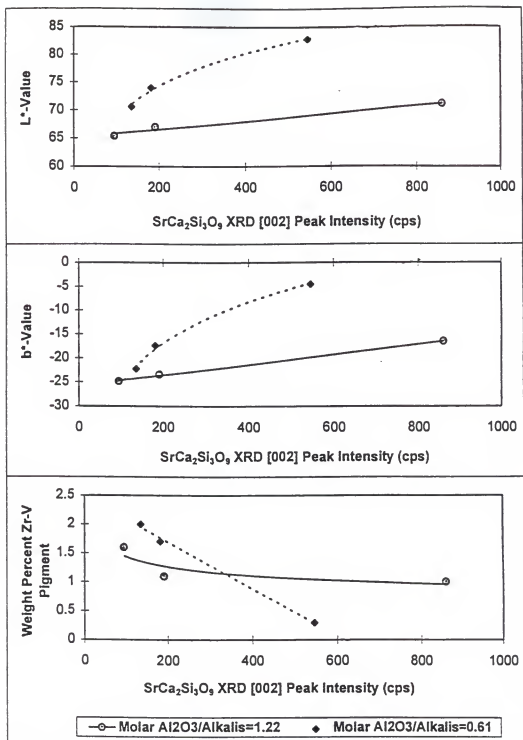


Figure 5.9. Color lightness ( $L^*$ ) and blueness ( $-b^*$ ) progression with  $\text{SrCa}_2\text{Si}_3\text{O}_9$  crystallization and pigment dissolution in coatings batched with 2.0% Zr-V.



## 5.2 Melt Viscosity

Even if a given state is thermodynamically favorable, it may never occur unless adequate kinetics conditions exist. Diffusion transport kinetics in glasses are governed by viscosity. As the viscosity and density of a glass decrease with rising temperature, rates of removal of latent heat of fusion and mass transport increase, and diffusion coefficients get larger. Consequently, the tendency for crystallization and dissolution reactions increases.

### 5.2.1 Influence on Crystallization and Zr-V Dissolution

At a given temperature, differences in viscosities between the coatings were primarily attributed to variations in molar  $\text{Al}_2\text{O}_3$ /alkali ratios in the frits (Figures 4.22 and 4.23, statistical equation 4.10). Modifying  $\text{Na}^+$  and  $\text{K}^+$  alkali cations enhance flow by disrupting bond linkages and breaking up the glass network, while high ionic potential  $\text{Al}^{+3}$  counteracts this effect. To a lesser degree, coating viscosity also correlated directly to  $\text{ZrO}_2$  content and inversely with  $\text{SrO}$ .

Nucleation proceeds at a lower temperature and higher viscosity than crystallization. In frits with  $\text{ZrO}_2$  and  $\text{ZnO}$  where zircon crystallization was most favorable (frits A and

B), a greater number of finely dispersed spherical precipitates resulted from increased viscosity conditions (frit A, Figure 4.36), where the  $\text{Al}_2\text{O}_3/\text{alkalis}$  was higher. In high viscosity mediums with low diffusion rates, internal energy due to interfaces is reduced with spherical particles. Larger precipitates with a fibrous morphology and a smaller number of particles crystallized in the lower viscosity medium (frit B, Figure 4.38) where the growth rate was higher. The demonstrated size and morphology control of zircon precipitation through viscosity regulation can be used to alter color, gloss and opacity in glass coatings.

In frits with  $\text{ZrO}_2$  where zircon did not crystallize (C and D), higher slopes in the  $\log \eta$  versus temperature curves are noted near the softening points of approximately  $700^\circ\text{C}$ . Less crystallization tends to result when there is a high viscosity at the softening point ( $T_s$ ) and a viscosity which increases rapidly below  $T_s$  [Kin76]. Hence, there is less opportunity for nuclei formation, and the subsequent volume of crystals precipitated at high temperature is lower. Replacement of  $\text{ZnO}$  with  $\text{SrO}$  in these frits prompted this outcome.

In frits without  $\text{ZrO}_2$  (E-H), the size and volume of  $\text{ZnO}$ -based (Figure 4.47) or  $\text{SrO}$ -based (Figures 4.49 and 4.51)

precipitates increased with lowering viscosity. This caused severe loss of color and gloss in the coatings. Although replacement of ZnO with SrO in these systems also raised the slope on the  $\log \eta$  curves near  $T_g$ , no corresponding reduction in crystallization was observed. Precipitation of zircon, where most of the nucleation and growth occur below 1000°C, is more influenced by the values and rates of changes of viscosity near  $T_g$ .

Comparisons of frits with and without  $ZrO_2$  suggest that Zr-V pigment dissolution in both systems cannot be directly linked to the same viscosity characteristics. For example, frits B (8%  $ZrO_2$ ) and F (0%  $ZrO_2$ ) had similar viscosity curves, but all of the pigment was still present in B after firing to 1100°C where less than 0.1% was measured in F. However, if the frits without  $ZrO_2$  are evaluated separately, an inverse correlation between viscosity and both Zr-V dissolution and crystallization becomes evident. The melt viscosity of frit systems has less of an influence on dissolving zircon pigments when enough  $ZrO_2$  is present in the frit to cause zircon to be the only energetically favorable crystalline phase. When sufficient  $ZrO_2$  is present in the glass for achieving network connectivity and stability, there

is no driving force for dissolving the zircon pigment in order to free up  $Zr^{+4}$  for the structure.

#### 5.2.2 Value as a Predictor of K/S and $\Delta E^*$

Plots of melt viscosities versus K/S and  $\Delta E^*$  of fired coatings batched with 2.0% Zr-V are given in Figure 5.10. X-axis values were derived for each coating by inputting their frit oxide molar equivalent values into equation 4.10 and then integrating the remaining function of temperature from 700°C to 1100°C. The integrated area provides an overall representation of the magnitude of viscosity during the firing cycle. Excellent correlations exist for frits containing no  $ZrO_2$ , where an increased viscosity throughout the firing cycle results in better color strength and stability. No correlations for frits with  $ZrO_2$  are evident.

Figure 5.10 demonstrates the usefulness of comparing areas under viscosity curves for predicting potential color strength and stability achieved with zircon pigments in frits without  $ZrO_2$ . In this case, where crystallization and pigment dissolution proceed through the whole firing range above  $T_s$ , the overall melt viscosity is a useful indicator. Higher viscosities inhibit both processes in these types of frits. However, in  $ZrO_2$  containing frits, crystallization proceeds

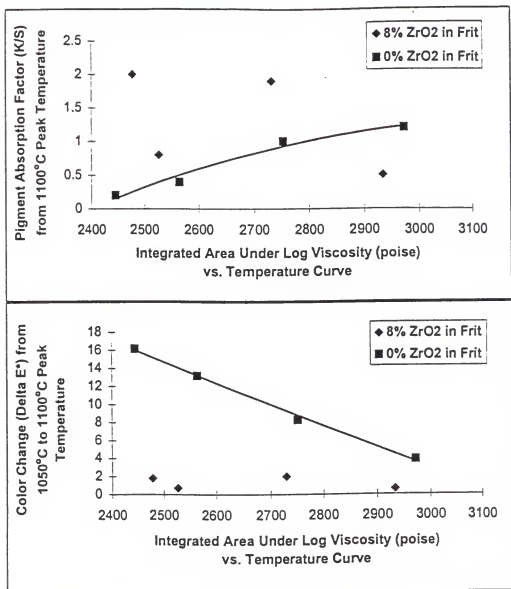


Figure 5.10. Integrated log viscosity from 700°C to 1100°C versus fired color strength (K/S) and stability (Delta E\*) in coatings batched with 2.0% Zr-V.

rapidly to equilibrium soon above  $T_g$ . Thus, viscosity over the whole temperature range is not a significant factor in crystallization and corresponding color alterations.

For frits with  $ZrO_2$ , the slope of the log viscosity curve near the softening point ( $T_g$ ) was found to correlate positively with overall color strength (K/S) but inversely with stability. Figure 5.11 reveals that this relationship can be applied to predict K/S ( $R^2 = .86$ ) and  $\Delta E^*$  ( $R^2 = .84$ ). Low  $R^2$  values for frits without  $ZrO_2$  verify no significant correlations.

For frits with  $ZrO_2$ , color strength is greatly increased with a higher slope due to the corresponding lower crystallization of zircon that tends to lighten color. A very slight, hardly noticeable decrease in stability ( $\Delta E^*$  from 1.0 to 2.0) resulting from a higher slope is due to the increase in Zr-V solubility as a consequence of higher SrO levels. If high color strength is the main objective, tighter control of firing temperatures can be used to compensate for the slight loss of stability.

In summary, Figures 5.10 and 5.11 demonstrate that color strength and stability in glass frit/zircon pigment systems can be controlled by regulating the melt viscosity.

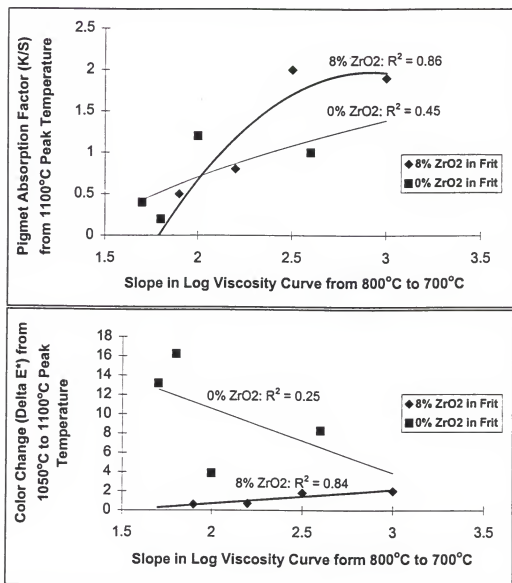


Figure 5.11. Slope in the log viscosity versus temperature near the softening point versus fired color strength (K/S) and stability (Delta E\*) in coatings batched with 2.0% Zr-V.

Increasing the magnitude of the viscosity curve by raising the molar ratio of  $\text{Al}_2\text{O}_3$ /alkalis is effective for improving color strength and stability in frits without  $\text{ZrO}_2$ . In frits with  $\text{ZrO}_2$ , raising the slope of the log viscosity curve near the softening point by increasing  $\text{SrO}$  at the expense of  $\text{ZnO}$  can be applied to increase color strength with a slight lowering of stability. Modest improvements in color stability in frits with  $\text{ZrO}_2$  can be accomplished by reducing the slope, but at the expense of significant color strength losses.



## CHAPTER 6 SUMMARY AND CONCLUSIONS

The present research investigated the development of blue color in glass frit/zircon-vanadium pigment systems for ceramic whitewares coatings. The primary objectives were to (a) determine if cost effective, environmentally safe glass frits could be formulated to improve the fired color strength and high-temperature stability of ceramic coatings and (b) relate the frit composition, pigment content, firing temperature, melt viscosity, crystallization and pigment dissolution to the fired color.

"Fast-fire" ceramic tile manufacturing accounts for a major portion of the whitewares industry and was the chosen processing method for producing fired coatings. Other whitewares industries, including manufacturers of sanitaryware and dinnerware, are currently attempting to convert to the same fast-fire roller kiln firing technology.

Silicate glass frits were of interest for this study because they are the main ingredients in fast-fire glazes. Frit is also the most reactive part of the formula and the

most corrosive to ceramic colorants. Experimental frit compositions were designed to include low cost, nonhazardous oxides, and conform with Seger's rules. The range of oxide contents tested encompassed and exceeded the range normally employed for glossy ceramic tile glazes. Special emphasis was placed on comparing compositions with  $\text{ZrO}_2$  (opacified) versus no  $\text{ZrO}_2$  (unopacified),  $\text{SrO}$  versus  $\text{ZnO}$  and low versus high alkalis ( $\text{K}_2\text{O}$ ,  $\text{Na}_2\text{O}$ ). The  $\text{SrO}$  and  $\text{ZnO}$  were of special interest because of their extensive use as secondary fluxes and their marked influence on modifying the  $\text{SiO}_2$  glass network. Other oxides in the frit formulas were  $\text{Al}_2\text{O}_3$ ,  $\text{CaO}$ ,  $\text{MgO}$  and  $\text{B}_2\text{O}_3$ . The  $\text{B}_2\text{O}_3$  contents were kept low in order to avoid liquid-liquid phase separation. A zircon-vanadium (Zr-V) blue pigment was tested because it belongs to the most common and stable group of colorants used in ceramic glazes, the zircon triaxial pigments.

A coating's fired color strength was quantified by its pigment absorption factor (K/S), calculated with the reflectance value at the Zr-V pigment peak absorption wavelength of 640 nm. Color stability was expressed as the inverse of  $\Delta E^*$ . The  $\Delta E^*$  was calculated as the magnitude of the position vector in  $L^* a^* b^*$  color space, between the colors of two coatings fired to 1050°C and 1100°C peak

temperature, respectively. The  $L^*$   $a^*$  and  $b^*$  values, calculated based on spectral reflectance curves and standard observer tristimulus weighting functions, correlate to lightness ( $L^*$ ), redness-greenness ( $a^*$ ) and yellowness-blueness ( $b^*$ ) color perception by the human eye. Equations were developed from the results that relate pigment absorption of 640 nm light to the color visualized.

Significant improvements in coating color strength and stability through adjustments in frit oxide compositions were demonstrated. Over the range of compositions tested,  $ZrO_2$ ,  $SrO$ ,  $ZnO$ ,  $Al_2O_3$  and alkali contents had varying degrees of influence over a coating's melt viscosity, crystallization, pigment dissolution and corresponding fired color. Equations were derived for predicting color strength and stability, and melt viscosity based on the frit oxide composition, Zr-V loading and firing temperatures. Thus, the results provide information useful to industry where material costs versus desired color properties can be weighed and prioritized.

Optimum **color stability** was achieved with frits which incorporated both  $ZrO_2$  and  $ZnO$ , but no  $SrO$ . These frits also yielded good opacity due to zircon precipitation from  $ZrO_2$  and  $SiO_2$  in the frit. The quantity of zircon that crystallized increased with higher  $ZnO$  and lower alkali molar equivalents.

The greatest **color strength** resulted from frits containing  $\text{ZrO}_2$  and  $\text{SrO}$ , but no  $\text{ZnO}$ . The replacement of  $\text{ZnO}$  with  $\text{SrO}$  prevented zircon crystallization during firing, and thus these glasses can be classified as transparent frits. These frits exhibited better color stability than conventional transparent frits which incorporate no  $\text{ZrO}_2$ . In frits without  $\text{ZrO}_2$ , increases in the  $\text{Al}_2\text{O}_3$ /alkalis improved both color strength and stability.

Crystalline species that developed during firing were related to the color perceived. Unique light blue color was produced from a combination of Zr-V pigment and finely crystallized 0.2-0.5  $\mu\text{m}$  zircon particles in the coating. Zircon precipitates 0.4-0.5  $\mu\text{m}$  in size tend to enhance the scattering of 400-500 nm blue light while increasing the overall lightness. A new, previously unidentified crystalline species ( $\text{SrCa}_2\text{Si}_3\text{O}_9$ ) precipitated in two frit compositions which contained no  $\text{ZrO}_2$  or  $\text{ZnO}$ .

This research also established that melt viscosity data, estimated with models that utilize heating microscopy and dilatometry measurements, can be applied as an industrial quality control tool for predicting a frit's potential for producing strong and stable color. The area under a log viscosity versus temperature curve, from  $T_g$  to the peak

temperature, was proportional to color strength and stability in frits without  $\text{ZrO}_2$ . In these frits, crystallization and pigment dissolution occurred throughout the firing cycle above  $T_g$ . The slope of the curve near  $T_g$  was proportional to color strength and inversely proportional (with a small effect) to color stability in frits with  $\text{ZrO}_2$ , where crystallization was complete below  $1000^\circ\text{C}$ .

Significant results of this research are summarized in the following sections.

#### 6.1 Zr-V Pigment and Color Values

- Maximum absorption of visible light by the zircon-vanadium pigment (Zr-V) occurs at 640 nm wavelength (1.94 eV), in the red-yellow region of the spectrum. This is the difference in energy between split d-orbitals in  $\text{V}^{+4}$  on the zircon lattice.

- Maximum reflectance from Zr-V occurs with 460 nm (2.69 eV) blue-green light.

- There is a linear relationship between the pigment absorption factor (K/S) calculated at 640 nm and Zr-V content. However, the slope of the line varies significantly with frit oxide composition and firing temperature.

- With increasing Zr-V content, the perceived color of a ceramic coating progresses darker (lower  $L^*$ ) and bluer (lower  $b^*$ ). However, the trend of increasing green (lower  $a^*$ ) with pigment content from 0% to 2% Zr-V reverses from 2% to 5%, where the greenish hue appears to shift direction and progress towards red (higher  $a^*$ ). A shift in maximum reflectance to wavelengths below the  $\bar{x}$  standard weighting function minima correlates to the abrupt, nonlinear shift in human perception.

- Variations in crystallization and pigment dissolution have a lesser effect on the perceived color when high pigment loadings  $\geq 5\%$  are utilized.

- Pigment content increases from 0 to 5% have no significant influence on fired gloss.

- At a constant pigment loading, most of the color variation, due to changes in frit composition or firing temperature, occurs in  $L^*$  and  $b^*$ .

- For Zr-V pigments, a second order polynomial function well describes ( $R^2 = .96$ ) the positive correlation between  $L^*$  and  $b^*$ .

- Values for perceived color,  $L^*$ ,  $a^*$  and  $b^*$ , are all logarithmic functions of K/S at 640 nm, where a higher K/S results in lower color values (higher chroma).

## 6.2 Frit Oxide Composition

- The strongest blue color, or highest K/S, is produced with frits containing high  $\text{ZrO}_2$  and  $\text{SrO}$ , and no  $\text{ZnO}$ . The weakest color results in frits with no  $\text{ZrO}_2$  and low  $\text{Al}_2\text{O}_3$ /alkalis.

- In frits with  $\text{ZrO}_2$ , color strength (K/S) is increased to the greatest degree when  $\text{SrO}$  replaces  $\text{ZnO}$ . This inhibits precipitation of zircon from the frit which ultimately lightens color. A relatively stable transparent frit results from glass compositions with  $\text{ZrO}_2$  and  $\text{SrO}$  but no  $\text{ZnO}$ . The statistical models predict a linear relationship between  $\text{SrO}$  and K/S when  $\text{ZnO}$  is also present.

- In frits without  $\text{ZrO}_2$ ,  $\text{SrO}$  versus  $\text{ZnO}$  causes no significant difference in K/S.

- If  $\text{SrO}$  is present in the frit without  $\text{ZnO}$ , an increase in  $\text{ZrO}_2$  molar equivalents in the frit linearly raises K/S by reducing the solubility of the zircon pigment. In frits with  $\text{ZnO}$  where zircon precipitation is favorable, higher  $\text{ZrO}_2$  content linearly lowers K/S.

- Raising the  $\text{Al}_2\text{O}_3$ /alkalis molar equivalents slightly lowers color strength in frits with  $\text{ZrO}_2$  which tend to precipitate zircon. This occurs because  $\text{Al}^{+3}$  replaces some  $\text{Zr}^{+4}$  in the glass network, which releases more  $\text{Zr}^{+4}$  to form

zircon and lighten the color. When no  $\text{ZrO}_2$  is present, higher  $\text{Al}_2\text{O}_3$ /alkalis ratios significantly increase K/S and color stability at high temperature by inhibiting crystallization and Zr-V dissolution due to an increased melt viscosity.

- The effects of  $\text{ZrO}_2$  and temperature on color strength are progressively reduced with increasing Zr-V content. The same quantity of pigment dissolution is less noticeable in saturated colors.

- The least noticeable color changes in fired coatings due to variations in peak firing temperature are achieved with high  $\text{ZrO}_2$  and  $\text{ZnO}$ , and no  $\text{SrO}$  ( $\Delta E^*$  was  $\leq 0.9$ ). The lowest color stability results from frits without  $\text{ZrO}_2$  and low in  $\text{Al}_2\text{O}_3$ /alkalis ( $\Delta E^*$  ranged from 7.0-16.3).

- Color stability is increased to the greatest degree by raising the  $\text{ZrO}_2$  content, which inhibits both crystallization near the peak firing temperature and zircon pigment dissolution. There is an inverse linear relationship between  $\text{ZrO}_2$  molar equivalents and  $\Delta E^*$ .

- Raising the  $\text{SrO}$  molar equivalents in frits with or without  $\text{ZrO}_2$  linearly reduces high temperature color stability due to an increase in zircon pigment solubility.

- In frits with  $\text{ZrO}_2$ , color stability lowers very slightly with higher  $\text{Al}_2\text{O}_3$ /alkalis. When no  $\text{ZrO}_2$  is present,



significant improvements in color stability are accomplished by raising the  $\text{Al}_2\text{O}_3$ /alkalis, which increases viscosity and thus inhibits crystallization and Zr-V dissolution.

### 6.3 Viscosity, Crystallization and Zr-V Dissolution

- Data obtained with dilatometry and heating microscopy analyses of frits can be correlated to melt viscosity, crystallization and color development with zircon pigments.

- The melt viscosity of frits can be described with a model of the form of the VFT equation, where the A constant can be taken as the temperature independent oxide composition effect.

- An increase in the molar equivalents ratio of  $\text{Al}_2\text{O}_3$ /alkalis has the largest influence of the frit oxides on raising the glass softening point and melt viscosity.

- To a lesser degree, higher  $\text{ZrO}_2$  and lower  $\text{SrO}$  results in increased viscosity.

- Replacing  $\text{ZnO}$  with  $\text{SrO}$  has the largest effect on increasing  $T_g$  and the ratio  $T_g:T_s$ .

- In frits with  $\text{ZrO}_2$  and  $\text{ZnO}$ , a greater number of fine (0.2-0.5  $\mu\text{m}$ ) spherical particles of zircon precipitate when the viscosity is increased by raising the  $\text{Al}_2\text{O}_3$ /alkalis ratio.

A more elongated, fibrous morphology predominates from lower viscosity conditions.

- Precipitation of zircon from  $\text{ZrO}_2$  in the frit is inhibited when the slope of the  $\log \eta$  versus temperature curve near the softening point is increased by replacing  $\text{ZnO}$  with  $\text{SrO}$ .

- In frits without  $\text{ZrO}_2$ , the size and volume of precipitate increases with lowering viscosity, resulting in weaker color and lower gloss.

- In frits without  $\text{ZrO}_2$ , there is no correlation between crystallization and the slope of the  $\log \eta$  curve near the softening point.

- In frits without  $\text{ZrO}_2$ , a lower viscosity causes more pigment to dissolve, resulting in a weaker color. Viscosity is not a dominant factor in Zr-V dissolution in frits containing  $\text{ZrO}_2$ .

- A higher integrated area under the  $\log \eta$  versus temperature curve from  $T_s$  to the peak firing temperature correlates well with increased color strength (K/S) and stability (lower  $\Delta E^*$ ) in frits without  $\text{ZrO}_2$ . A greater overall viscosity inhibits crystallization of nonzirconium species in these frits. In frits containing  $\text{ZrO}_2$ , where

zircon precipitation is complete by 1000°C, no such correlation exists.

- A higher slope in the  $\log \eta$  versus temperature curve near the softening point correlates well with increased color strength and a slight decrease in stability ( $\Delta E^* \leq 2.0$ ) in frits with  $\text{ZrO}_2$  because zircon nucleation and growth is inhibited. No such correlation exists for frits without  $\text{ZrO}_2$ , where crystallization occurs through the range of firing temperatures.

- In frits with  $\text{ZrO}_2$ , zircon is the only energetically favorable precipitate present at normal peak temperatures of 1050°C and 1100°C.

- Zircon crystals near 0.4-0.5  $\mu\text{m}$  in size in the glass with Zr-V allow for blue color with a very high lightness ( $L^*$ ), due to enhanced scattering of blue light.

- Values for the color perceived;  $L^*$ ,  $a^*$  and  $b^*$  are all logarithmic functions of the weight percent zircon precipitated in the glass. Higher zircon causes more lightening (higher  $L^*$ ) than losses of green (higher  $a^*$ ) and blue (higher  $b^*$ ).

- The pigment absorption factor ( $K/S$ ) increases exponentially with a decrease in the amount of zircon precipitate.

- Perceptible color alterations due to variations in firing temperatures are reduced in systems that crystallize zircon from  $\text{ZrO}_2$  in the frit. Crystallization is complete before  $1000^\circ\text{C}$  and the amount of zircon left in coatings fired to  $1000^\circ\text{C}$ ,  $1050^\circ\text{C}$  and  $1100^\circ\text{C}$  remains nearly the same.

- In frits where zircon does not crystallize, Zr-V pigment dissolution tends to occur, with the greatest loss resulting in frits without  $\text{ZrO}_2$  and a low  $\text{Al}_2\text{O}_3/\text{alkalis}$  ratio. In frits with  $\text{ZrO}_2$ , zircon crystallization does not occur when SrO replaces ZnO.

- $L^*$ ,  $a^*$  and  $b^*$  increase and K/S decreases linearly with the weight percentage of Zr-V pigment dissolved (from 0 to 2%) in the glass.

- In the frits tested without  $\text{ZrO}_2$ , the main phases that crystallized were diopside and hardystonite when ZnO was present and  $\text{SrCa}_2\text{Si}_3\text{O}_9$  when SrO replaced ZnO. The  $\text{SrCa}_2\text{Si}_3\text{O}_9$  is a new line phase unidentified on the standard x-ray JCPDS card file.

- The quantity of hardystonite or  $\text{SrCa}_2\text{Si}_3\text{O}_9$  precipitate increases with temperature from  $1000^\circ\text{C}$  to  $1100^\circ\text{C}$ , resulting in poor color strength and stability. Crystallization of the two species causes a shift in the maximum reflectance from 460 nm at  $1000^\circ\text{C}$  to near 500 nm at  $1100^\circ\text{C}$ . This results in

higher  $L^*$  and  $b^*$  values and greatly perceptible changes in color (high  $\Delta E^*$ ). A greater amount of either material precipitates when the  $Al_2O_3$ / alkali content is low.

In conclusion, the research of this dissertation quantified methods for improving the color strength and stability of glass frits colored with zircon-vanadium pigment for whitewares coatings applications. Glossy opaque and transparent frit compositions which yield excellent color strength and stability over a range of firing temperatures were formulated. In addition, a technique for producing uniquely light but high chroma color with zircon pigments through control of zircon precipitate particle size was illustrated. The results also apply qualitatively to other ceramic pigments which use the same zircon structure to incorporate colorant metal ions.

The color, crystallization and dissolution data presented, as well as the mathematical models derived during this study, will be of interest to materials scientists and industries that manufacture ceramics coatings, glass frits and ceramic colorants. The applications established for using melt viscosity data as an industrial color quality control tool will also be of use to the ceramics industry.

## CHAPTER 7 FUTURE WORK

The present dissertation uncovered several potential research topics which are of interest for both basic science and industrial purposes. Possible future investigations include

- Expand the mathematical models established in this study for predicting  $K/S$ ,  $\Delta E^*$ ,  $L^*$ ,  $a^*$ ,  $b^*$  and  $\log \eta$  by adding as independent variables

- (a) the other two zircon triaxial pigments; zircon-praseodymium yellow and zircon-iron coral,

- (b) complete time versus temperature firing profiles, rather than the peak temperature of a specific cycle, and

- (c) a wider range of glass oxide compositions.

- Derive statistical models to describe the influences of frit oxide composition and crystallization on gloss.

- Develop matte whitewares coatings (gloss  $\leq 20.0$ ) at  $60^\circ$  incidence) with improved color strength and stability. Investigate whether batches containing fritted  $ZrO_2$  and high

mineral additions of relatively coarse  $\text{Al}_2\text{O}_3$  are optimum. Based on the findings of this research, fritted  $\text{ZrO}_2$  would tend to inhibit crystallization and pigment dissolution that cause color variation while  $\text{Al}_2\text{O}_3$  minerals may provide for an "underfired" matte crystalline texture.

- Control the quantity, size and morphology of zircon precipitating from  $\text{ZrO}_2$  in the glass frit by varying ratios of  $\text{SrO}:\text{ZnO}$  and  $\text{Al}_2\text{O}_3$ :alkalis. Explore the range of colors and opacification that can be achieved with zircon pigments through selective scattering of light by the zircon precipitates.

- Study the influence of zircon pigment particle size on the color of a fired coating. Investigate if 450 nm Zr-V blue, 580 nm Zr-Pr yellow and 650 nm Zr-Fe coral pigment sizes provide optimum color strength and opacity by enhancing the reflection of the desired color of light. Develop surfactants that allow for easy dispersion of such fine particles in an industrial coating base. Devise methods for avoiding dissolution of the small zircon particles.

- Compare the effects of batch additions of zircon minerals versus fritted  $\text{ZrO}_2$  on the melt viscosity, crystallization and color development of ceramic coatings. Determine what maximum zircon mineral particle size preserves

the color by dissolving into the melt before the zircon pigment is attacked.

- Determine whether other intermediate or glass former oxides tend to stimulate or inhibit zircon precipitation from  $\text{ZrO}_2$  in the frit. In the present study,  $\text{ZnO}$  enhanced zircon crystallization and  $\text{SrO}$  prevented it. For example, investigate  $\text{BaO}$ , which has a density ( $4.7\text{--}5.5\text{ g/cm}^3$ ), cation radius ( $1.34\text{ \AA}$ ) and cation charge (+2) that are comparable to  $\text{SrO}$  ( $4.7\text{ g/cm}^3$ ,  $1.12\text{ \AA}$ , +2 charge).

- Perform quantitative thermodynamic and kinetic studies of crystallization and zircon pigment dissolution in frits without  $\text{ZrO}_2$ . Determine the  $\Delta G$  of formation of each crystalline species.

- Synthesize the new  $\text{SrCa}_2\text{Si}_3\text{O}_9$  crystalline phase and thoroughly study its structure and properties. Add the new information to the existing x-ray JCPDS card file.

- Compare microwave versus conventional heating methods for firing colored ceramic coatings. Evaluate if melting behavior, crystallization, zircon pigment dissolution and the corresponding color stability and strength are altered due to possible changes in diffusion transport processes.

- Synthesize zircon pigments using alternative methods such as microwave processing. Determine if a greater number



of dopant color ions can be incorporated on the zircon lattice than currently achieved with conventional techniques.

APPENDIX A  
UNITS FOR DESCRIBING LIGHT AND COLOR [Nas83]

A1.1 Units Related to Energy

Color	Wavelength ( $\lambda$ ) in Nanometers (nm)	Frequency $\nu$ (Hz) ( $\times 10^{14}$ )	Wave _ Number $\nu$ ( $\text{cm}^{-1}$ )	*Energy in eV	*Energy in cal mol <sup>-1</sup> ( $\times 10^3$ )
Infrared, far	30,000	0.10	333	0.041	0.95
Infrared, near	1,000	3.00	10,000	1.24	28.6
Red	650	4.62	15,400	1.91	44.0
Orange	600	5.00	16,700	2.06	47.7
Yellow	580	5.17	17,240	2.14	49.3
Green	500	6.00	20,000	2.48	57.2
Blue	450	6.66	22,200	2.75	63.4
Violet	400	7.50	25,000	3.10	71.4
Ultra- violet, long wave	366	8.19	27,300	3.39	78.0
Ultra- violet, short wave	254	11.82	39,400	4.89	112.6

$$\text{Wave Number (cm}^{-1}\text{)} = \bar{\nu} = 1/\lambda \quad (\text{A1})$$

$$\text{Frequency (Hz)} = \nu = \bar{\nu} \times c \quad (\text{A2})$$

where  $c$  = the speed of light =  $2.998 \times 10^{10}$  cm/sec.

$$\text{*Energy (eV)} = E = \bar{\nu} \times 1.2399 \times 10^{-4} \quad (\text{A3})$$

$$\text{*Energy (cal mol}^{-1}\text{)} = E = \bar{\nu} \times 2.8573 \quad (\text{A4})$$

$$\text{*Wavelength (nm)} \times \text{Energy (eV)} = 1239.9 \quad (\text{A5})$$

### A1.2 Photometric Units

Candela (cd): SI unit for luminous intensity.

One square meter of blackbody at 2042K emits 600,000 cd.

One candela produces one lumen of flux per steradian of solid angle measured from the source.

Lumen (lm): unit of luminous flux or light intensity emitted by a point source of 1 cd through a unit solid angle (steradian).

Luminance (L): unit of brightness in (cd m<sup>-2</sup>).

The sun has  $L = 1.6 \times 10^9$  cd m<sup>-2</sup> and a fluorescent lamp approximately 10,000 cd m<sup>-2</sup>.

Illuminance in lux (lx): One lm/m<sup>2</sup>.

One lux = 10.76 foot candles.

---

\*Units apply to a single electron.

APPENDIX B  
THE 15 CAUSES OF COLOR [ Nas83]

*Transitions Involving Ligand Field Effects*

1. *Transition Metal Compounds:* Many pigments, some fluorescence, lasers, phosphors and turquoise.
2. *Transition Metal Impurities:* Ruby, emerald, red iron ore, some fluorescence and lasers.

*Transitions Involving Energy Bands*

3. *Metals:* Copper, silver, gold, iron, brass, "ruby" glass
4. *Pure Semiconductors:* Silicon, galena, cinnabar, diamond
5. *Doped or Activated Semiconductors:* Blue and yellow diamond, light-emitting diodes, some lasers and phosphors
6. *Color Centers:* Amethyst, smoky quartz, desert "amethyst" glass, some fluorescence and lasers

*Transitions between Molecular Orbitals*

7. *Organic Compounds:* Most dyes, most biological colorations, some fluorescence and lasers
8. *Charge Transfer:* Blue sapphire, magnetite, lapis lazuli, many pigments, graphite

*Vibrations and Simple Excitations*

9. *Incandescence:* Flames, lamps, carbon arc, limelight
10. *Gas Excitations:* Vapor lamps, lightning, auroras, some lasers.
11. *Vibrations and Rotations:* Water, ice, iodine, blue gas flame.

*Geometrical and Physical Optics*

12. *Dispersive Refraction, Polarization, etc.:* Rainbow, halos, sun dogs, green flash of sun, "fire" in gemstones.
13. *Scattering:* Blue sky, red sunset, blue moon, moonstone, Raman scattering, blue eyes and some other biological colors.
14. *Interference:* Oil slick on water, soap bubbles, coating on camera lenses, some biological colors.
15. *Diffraction:* Aureole, glory, diffraction gratings, opal, some biological colors, most liquid crystals.

APPENDIX C  
DENSITY, PARTICLE SIZE AND APPLICATION WEIGHT DATA

C1.1 Density and Particle Size Based on Volume %

FRIT:									41715A
									Zr-V
	A	B	C	D	E	F	G	H	Pigment
Density (g/cm <sup>3</sup> )	2.87	2.91	2.85	2.85	2.78	2.77	2.70	2.75	---
Mean Particle Diameter ( $\mu$ m)	23.4	19.7	19.4	24.4	23.9	22.9	27.5	24.4	8.9

C1.2 Coatings Application Weights (grams) at 1.75 Sp.Gr.

FRIT:									
	A	B	C	D	E	F	G	H	
0% Zr-V	11.7	12.0	11.6	11.6	11.2	11.2	10.7	11.0	
0.5% Zr-V	11.8	12.0	11.7	11.7	11.2	11.2	10.7	11.0	
2.0% Zr-V	11.8	12.1	11.7	11.7	11.3	11.3	10.8	11.2	
5.0% Zr-V	12.1	12.3	12.0	12.0	11.5	11.5	11.0	11.3	

APPENDIX D  
DATA FROM COATINGS BATCHED WITH FRIT, 2.5% BENTONITE AND  
Zr-V PIGMENT, AND FIRED USING A 45-MINUTE  
CERAMIC TILE CYCLE

DATA FROM COATINGS BATCHED WITH FRIT, 2.5% BENTONITE AND Zr-V PIGMENT, AND FIRED USING A 45 MINUTE CERAMIC TILE CYCLE.

* Frit Composition (Weight %):												
SiO2	B2O3	Na2O	K2O	CaO	Al2O3	ZrO2	MgO	SiO2	ZnO	** Wt-% Zr-V Pigment	Peak Firing Temp.(C)	C.I.E.
1	55	6	2	3	8	4	8	2	0	12	1000	L*
2	55	6	2	3	8	4	8	2	0	12	1000	93.6 -0.2 2.3
3	55	6	2	3	8	4	8	2	0	12	1000	87.3 -6.3 -8.9
4	55	6	2	3	8	4	8	2	0	12	1000	78.8 -9.1 -17.8
5	55	6	2	3	8	4	8	2	0	12	1000	72.1 -10.4 -23
6	55	6	2	3	8	4	8	2	0	12	1050	93.7 -0.6 1.6
7	55	6	2	3	8	4	8	2	0	12	1050	87.5 -6.1 -7
8	55	6	2	3	8	4	8	2	0	12	1050	78.8 -9 -17.8
9	55	6	2	3	8	4	8	2	0	12	1050	71.5 -10.4 -24
10	55	6	2	3	8	4	8	2	0	12	1100	93.6 -0.7 1.1
11	55	6	2	3	8	4	8	2	0	12	1100	87.7 -5.8 -8.6
12	55	6	2	3	8	4	8	2	0	12	1100	78.2 -9 -17.8
13	55	6	2	3	8	4	8	2	0	12	1100	71.2 -10.4 -23.6
14	50	6	4	6	8	4	8	2	0	12	1000	91.2 0.1 5.2
15	50	6	4	6	8	4	8	2	0	12	1000	83.3 -8.4 -7.6
16	50	6	4	6	8	4	8	2	0	12	1000	72.7 -11.7 -20.7
17	50	6	4	6	8	4	8	2	0	12	1000	62.8 -11.1 -29.8
18	50	6	4	6	8	4	8	2	0	12	1050	91.6 -0.5 3.6
19	50	6	4	6	8	4	8	2	0	12	1050	84.9 -7.9 -7.5
20	50	6	4	6	8	4	8	2	0	12	1050	74.1 -11.2 -20.2
21	50	6	4	6	8	4	8	2	0	12	1050	63.7 -11 -29
22	50	6	4	6	8	4	8	2	0	12	1100	92.4 -0.7 3.2
23	50	6	4	6	8	4	8	2	0	12	1100	85.2 -7.7 -7
24	50	6	4	6	8	4	8	2	0	12	1100	73.5 -11.5 -28.2
25	50	6	4	6	8	4	8	2	0	12	1100	63.6 -11.5 -28.2
26	55	6	2	3	8	4	8	2	12	0	1000	89.1 0.5 8.8
27	55	6	2	3	8	4	8	2	12	0	1000	77.7 -11.5 -7.3
28	55	6	2	3	8	4	8	2	12	0	1000	63.3 -17.3 -26.1
29	55	6	2	3	8	4	8	2	12	0	1000	51.6 -13 -38.1
30	55	6	2	3	8	4	8	2	12	0	1050	89.4 -0.4 7
31	55	6	2	3	8	4	8	2	12	0	1050	76.9 -10.5 -6.8
32	55	6	2	3	8	4	8	2	12	0	1050	64.3 -18.8 -28.8
33	55	6	2	3	8	4	8	2	12	0	1050	52.8 -12.8 -36.8
34	55	6	2	3	8	4	8	2	12	0	1100	89.8 -0.9 5.1
35	55	6	2	3	8	4	8	2	12	0	1100	79.6 -10.7 -8.7
36	55	6	2	3	8	4	8	2	12	0	1100	65.7 -15.6 -25.6
												54.6 -12.5 -34.8

Delta E*	60-Degree Angle Gloss	K/S at 640nm	** Glaze
1050-1100C			Fit
---	86.6	0.01	O.K.
---	82.9	0.13	O.K.
---	87	0.47	O.K.
---	81.6	0.93	O.K.
---	88.1	0.01	O.K.
---	86.6	0.13	O.K.
---	88.7	0.47	O.K.
---	83.6	0.89	O.K.
---	91.2	0.02	O.K.
---	88	0.12	O.K.
---	90	0.49	O.K.
---	88.1	1.01	O.K.
---	98.1	0.02	O.K.
---	92.4	0.24	O.K.
---	92.3	0.88	O.K.
---	88.2	2.13	O.K.
---	82.3	0.02	O.K.
---	40.6	0.19	O.K.
---	54.8	0.77	O.K.
---	74.8	1.94	O.K.
---	27.7	0.02	O.K.
---	33.6	0.18	O.K.
---	68.9	0.81	O.K.
---	76.9	1.96	O.K.
---	93.1	0.03	O.K.
---	85.3	0.45	O.K.
---	88.3	2.41	O.K.
---	86.9	6.84	O.K.
---	87.8	0.03	O.K.
---	91.7	0.35	O.K.
---	87.7	2.22	O.K.
---	87.7	5.79	O.K.
---	94	0.38	O.K.
---	92	1.90	O.K.
---	90	4.80	O.K.



* Frit Composition (Weight %):										** Wt.% Zn-V Pigment		Peak Firing Temp.(C)		C.I.E.		Delta E* 1050-1100C		60-Degree Angle/Gloss		K/S at 640nm		*** Glaze El	
SiO2	B2O3	Na2O	K2O	CaO	Al2O3	ZrO2	MgO	SiO2	ZnO	Pigment	0	1000	L*	a*	b*	1050-1100C	60-Degree Angle/Gloss	K/S at 640nm	*** Glaze El				
37	50	6	4	8	8	4	2	12	0	0	1000	89.1	0.4	8.2	---	---	93.4	0.03	Crazed				
38	50	8	4	8	8	4	2	12	0	0.5	1000	77.8	-11.3	-7.9	---	---	92.1	0.45	Crazed				
39	50	8	4	6	8	4	2	12	0	2	1000	64.1	-16.8	-28.8	---	---	91.2	2.28	Crazed				
40	50	8	4	6	8	4	2	12	0	5	1000	51.8	-13.4	-39.5	---	---	95	7.36	Crazed				
41	50	8	4	8	8	4	2	12	0	0	1050	88.8	-0.8	7.4	---	---	91.9	0.03	Crazed				
42	50	8	4	6	8	4	2	12	0	0.5	1050	78.2	-11	-7.7	---	---	89	0.42	Crazed				
43	50	6	4	8	8	4	2	12	0	2	1050	64.1	-18.8	-28.3	---	---	91.8	2.24	Crazed				
44	50	8	4	6	8	4	2	12	0	5	1050	50.4	-12.7	-39.4	---	---	91.8	7.98	Crazed				
45	50	8	4	6	8	4	2	12	0	0	1100	88.3	-1.1	6.6	1.1	---	90.1	0.04	Crazed				
46	50	8	4	8	8	4	2	12	0	0.5	1100	79.9	-9.5	-5.5	3.1	---	94.6	0.32	Crazed				
47	50	8	4	8	8	4	2	12	0	2	1100	64.7	-16.4	-24.8	1.8	---	85.2	2.03	Crazed				
48	50	5	2	3	13	8	0	2	12	5	1100	50.1	-12.7	-37.2	2.2	---	85	7.38	Crazed				
49	55	5	2	3	13	8	0	2	12	0	1000	90.8	0.8	7.1	---	---	85.5	0.02	O.K.				
50	55	5	2	3	13	8	0	2	12	0.5	1000	81.8	-9.3	-6.5	---	---	83.1	0.28	O.K.				
51	55	5	2	3	13	8	0	2	12	2	1000	69.1	-14.7	-22.8	---	---	84.5	1.34	O.K.				
52	55	5	2	3	13	8	0	2	12	5	1000	57.8	-12.9	-33.1	---	---	84.1	3.58	O.K.				
53	55	5	2	3	13	8	0	2	12	0	1050	89.4	-0.3	7.5	---	---	87.8	0.03	O.K.				
54	55	5	2	3	13	8	0	2	12	0.5	1050	80.9	-9.5	-5	---	---	86.5	0.28	O.K.				
55	55	5	2	3	13	8	0	2	12	2	1050	68.5	-18.4	-21.5	---	---	85.5	1.46	O.K.				
56	55	5	2	3	13	8	0	2	12	5	1050	52.3	-13.8	-38.8	---	---	87.9	6.39	O.K.				
57	55	5	2	3	13	8	0	2	12	0	1100	88	-0.9	7.5	1.6	---	95.8	0.04	O.K.				
58	55	5	2	3	13	8	0	2	12	0.5	1100	82.2	-7.4	-1.1	4.6	---	92.9	0.21	O.K.				
59	55	5	2	3	13	8	0	2	12	2	1100	69.2	-15.7	-17.8	3.9	---	93	1.25	O.K.				
60	55	5	2	3	13	8	0	2	12	5	1100	53.8	-18.5	-33.3	4.7	---	93.2	5.79	O.K.				
61	50	5	4	8	13	8	0	2	12	0	1000	92	0.3	5.1	---	---	54.3	0.02	Crazed				
62	50	5	4	6	13	8	0	2	12	0.5	1000	83.9	-7.8	-6.2	---	---	45.9	0.21	Crazed				
63	50	5	4	8	13	8	0	2	12	2	1000	72.7	-12.3	-20.5	---	---	48.2	0.89	Crazed				
64	50	5	4	6	13	8	0	2	12	5	1000	62.6	-11.1	-30.2	---	---	42	2.15	Crazed				
65	50	5	4	6	13	8	0	2	12	0	1050	90.2	-0.3	5.7	---	---	55.5	0.03	Crazed				
66	50	5	4	6	13	8	0	2	12	0.5	1050	84	-7.2	-3.2	---	---	55.4	0.18	Crazed				
67	50	5	4	6	13	8	0	2	12	2	1050	72.7	-14.1	-17.8	---	---	59	0.91	Crazed				
68	50	5	4	6	13	8	0	2	12	5	1050	59	-13.7	-31.8	---	---	59	3.19	Crazed				
69	50	5	4	8	13	8	0	2	12	0	1100	87.2	-0.8	7	3.3	---	77.5	0.05	Crazed				
70	50	5	4	8	13	8	0	2	12	0.5	1100	85.7	-3.5	3.9	8.2	---	86.4	0.09	Crazed				
71	50	5	4	8	13	8	0	2	12	2	1100	78	-10.5	-6.2	13.2	---	93.7	0.41	Crazed				
72	50	5	4	6	13	8	0	2	12	5	1100	81.3	-18.7	-25.7	7	---	91.8	2.67	Crazed				

SiO <sub>2</sub>	* Frit Composition (Weight %):										** Wt-% Zr-V Pigment		Peak Firing Temp.(C)	C.I.E.			Delta E* 1050-1100C	60-Degree Angle Gloss	K/S at 640nm	*** Glaze Fit
	B <sub>2</sub> O <sub>3</sub>	Na <sub>2</sub> O	K <sub>2</sub> O	CaO	Al <sub>2</sub> O <sub>3</sub>	ZrO <sub>2</sub>	MgO	SiO <sub>2</sub>	ZnO	L*	a*	b*								
73	55	5	2	3	13	8	0	2	12	0	0	1000	89.6	0.6	8.7	-----	75.6	0.02	O.K.	
74	55	5	2	3	13	8	0	2	12	0	0.5	1000	80.1	-9.8	-5.4	-----	60.2	0.32	O.K.	
75	55	5	2	3	13	8	0	2	12	0	2	1000	65.4	-15.9	-24.8	-----	57.5	1.88	O.K.	
76	55	5	2	3	13	8	0	2	12	0	5	1000	55.9	-12.7	-34.5	-----	54.9	4.15	O.K.	
77	55	5	2	3	13	8	0	2	12	0	0	1050	89.1	-0.4	7.5	-----	78.1	0.03	O.K.	
78	55	5	2	3	13	8	0	2	12	0	0.5	1050	81.4	-8.7	-3.9	-----	69.7	0.26	O.K.	
79	55	5	2	3	13	8	0	2	12	0	2	1050	67	-18.2	-----	-----	65.1	1.67	O.K.	
80	55	5	2	3	13	8	0	2	12	0	5	1050	54.5	-14	-35.2	-----	74.1	5.07	O.K.	
81	55	5	2	3	13	8	0	2	12	0	0	1100	88.4	-0.9	6.9	1.1	79.3	0.04	O.K.	
82	55	5	2	3	13	8	0	2	12	0	0.5	1100	83.2	-6.7	-0.5	4.3	81.4	0.16	O.K.	
83	55	5	2	3	13	8	0	2	12	0	2	1100	71.1	-14.9	-16.4	8.3	75.7	1.02	O.K.	
84	55	5	2	3	13	8	0	2	12	0	5	1100	56.3	-16.1	-31.4	4.7	78.3	4.37	O.K.	
85	50	5	4	6	13	8	0	2	12	0	0	1000	91.8	0.1	6.1	-----	15.4	0.02	Crazed	
86	50	5	4	6	13	8	0	2	12	0	0.5	1000	83	-8.7	-6.3	-----	26.5	0.24	Crazed	
87	50	5	4	6	13	8	0	2	12	0	2	1000	70.6	-13.6	-22.2	-----	29.8	1.13	Crazed	
88	50	5	4	6	13	8	0	2	12	0	5	1000	62.2	-10.8	-30.2	-----	32.5	2.15	Crazed	
89	50	5	4	6	13	8	0	2	12	0	0	1050	90.9	-0.5	5.8	-----	19.5	0.02	Crazed	
90	50	5	4	6	13	8	0	2	12	0	0.5	1050	85.6	-6.3	-2.1	-----	28.3	0.14	Crazed	
91	50	5	4	6	13	8	0	2	12	0	2	1050	74	-12.9	-17.4	-----	27	0.78	Crazed	
92	50	5	4	6	13	8	0	2	12	0	5	1050	65.5	-11.4	-25.8	-----	26	1.56	Crazed	
93	50	5	4	6	13	8	0	2	12	0	0	1100	90	-0.9	6	1	27	0.03	Crazed	
94	50	5	4	6	13	8	0	2	12	0	0.5	1100	86.7	-2.7	3.4	7.3	25.4	0.05	Crazed	
95	50	5	4	6	13	8	0	2	12	0	2	1100	82.8	-8.2	-4.5	16.3	30.7	0.23	Crazed	
96	50	5	4	6	13	8	0	2	12	0	5	1100	72.1	-11.9	-17	11.1	27.6	0.84	Crazed	

\* Coatings were applied at 2.70 cm<sup>3</sup> volume per 2" X 6" tile.  
( average wet application weight of 11.5 grams at a 1.75 specific gravity)

\*\* Pigment was Ceredec 41715A turquoise-blue dispersible stain.

\*\*\* Thermal expansion of the wall tile body/engobe substrate was 65 - 67 X 10e-7/C.

APPENDIX E  
FRIT SPECTRAL REFLECTANCE DATA AND CURVES  
AT EACH TEMPERATURE AND PIGMENT LOADING

Table E.1. Engobe and Frits A and B Reflectance Data  
(+ percentages are wt.% Zr-V pigment added to frit)

Wavelength	1000C PEAK TEMPERATURE:									
(nm)	Engobe	A	A + 0.5%	A + 2.0%	A + 5.0%	B	B + 0.5%	B + 2.0%	B + 5.0%	
360		48.5	58.8	55.3	47.4	37.9	46.9	43.1	33.6	23.3
380		56.7	69.7	66.3	59.3	49.7	57.9	55.2	46.1	35.2
400		64.2	76.4	73.6	67.7	58.7	65.5	63.9	56.2	45.8
420		69.3	79.2	77.0	72.0	63.9	69.3	68.2	61.8	52.6
440		72.0	80.3	78.5	74.0	66.9	71.3	70.5	65.0	56.7
460		73.7	81.7	80.0	75.7	69.0	73.2	72.5	67.3	59.3
480		74.8	82.2	80.2	75.2	68.1	74.3	73.1	67.2	58.4
500		76.7	83.1	79.8	72.2	64.0	76.0	73.1	64.4	53.1
520		78.2	83.6	77.5	65.9	56.1	77.2	70.8	57.4	43.6
540		79.6	84.0	73.9	58.8	47.8	78.3	66.8	49.1	34.4
560		81.4	84.5	69.7	51.8	40.4	79.5	61.9	41.3	27.0
580		83.1	84.7	65.8	46.4	34.8	80.4	57.3	35.8	21.9
600		84.4	85.1	62.9	42.6	31.0	81.2	53.8	31.8	18.8
620		85.1	85.3	61.0	40.4	28.8	81.7	51.8	29.6	17.0
640		85.5	85.3	60.2	39.4	27.9	82.0	51.0	28.8	16.4
660		85.9	85.4	60.4	39.7	28.0	82.2	51.6	29.2	16.7
680		86.4	85.7	61.7	41.2	29.4	82.5	53.6	30.9	18.1
700		86.9	85.9	64.0	43.9	32.0	82.8	56.9	34.0	20.5
720		87.4	86.1	66.4	46.9	34.7	83.1	60.2	37.3	23.2
740		87.9	86.3	67.4	48.1	35.8	83.2	61.8	38.7	24.4
	1050C PEAK TEMPERATURE:									
	Engobe	A	A + 0.5%	A + 2.0%	A + 5.0%	B	B + 0.5%	B + 2.0%	B + 5.0%	
360		44.4	59.6	55.8	47.6	38.1	50.5	47.7	36.3	24.5
380		52.6	70.9	67.3	59.5	49.8	61.9	59.9	49.0	36.5
400		61.0	78.0	74.7	67.9	58.9	69.3	68.1	59.0	47.1
420		67.1	80.8	77.9	72.1	64.0	72.7	72.1	64.4	53.7
440		70.3	81.8	79.2	74.1	66.8	74.2	74.1	67.3	57.5
460		72.0	83.0	80.5	75.8	68.8	75.9	75.8	69.5	60.0
480		73.2	83.4	80.5	75.2	67.8	76.8	76.4	69.3	59.1
500		75.3	84.1	80.1	72.3	63.4	78.2	76.2	66.4	54.0
520		76.9	84.4	77.8	65.9	55.3	79.1	73.9	59.5	44.7
540		78.1	84.6	74.3	58.5	46.8	79.8	69.9	51.3	35.6
560		79.5	84.8	70.2	51.7	39.3	80.3	65.0	43.6	28.2
580		80.7	84.7	66.3	46.3	33.7	80.6	60.4	37.8	23.1
600		81.7	84.8	63.4	42.8	30.0	81.0	57.1	34.0	19.9
620		82.4	84.8	61.5	40.4	27.8	81.2	55.0	31.8	18.1
640		82.8	84.8	60.7	39.4	26.9	81.4	54.3	31.0	17.5
660		80.8	84.8	61.0	39.6	27.1	81.5	54.8	31.4	17.8
680		83.7	84.9	62.4	41.1	28.6	81.8	56.8	33.1	19.2
700		84.2	85.0	64.7	43.8	31.2	81.9	60.0	36.2	21.7
720		84.8	85.2	67.2	46.7	34.1	82.2	63.2	39.6	24.5
740		85.2	85.3	68.2	47.9	35.3	82.3	64.5	41.0	25.6
	1100C PEAK TEMPERATURE:									
	Engobe	A	A + 0.5%	A + 2.0%	A + 5.0%	B	B + 0.5%	B + 2.0%	B + 5.0%	
360		43.1	60.2	56.4	45.9	37.8	53.2	47.5	34.6	23.9
380		51.3	71.6	67.9	57.8	49.4	64.8	59.7	47.5	35.7
400		59.5	78.6	75.1	66.3	58.4	72.1	66.0	57.5	46.1
420		65.8	81.3	78.2	70.5	63.2	75.3	72.0	63.0	52.6
440		69.0	82.1	79.3	72.6	65.9	76.6	73.8	65.9	56.4
460		70.6	83.2	80.4	74.4	67.7	78.3	75.5	68.0	58.9
480		71.8	83.5	80.5	73.8	66.8	79.2	76.1	67.9	58.2
500		74.1	84.2	80.0	70.9	62.6	80.5	76.1	65.2	53.5
520		75.6	84.4	77.9	64.7	54.7	81.4	74.0	58.5	44.6
540		76.7	84.4	74.7	57.5	46.4	81.9	70.3	50.3	35.6
560		77.7	84.5	70.8	50.8	39.0	82.3	65.6	42.7	28.1
580		78.5	84.2	67.0	45.5	33.4	82.4	61.2	36.9	23.0
600		79.3	84.1	64.2	41.8	29.7	82.5	57.9	33.0	19.8
620		79.8	84.1	62.4	39.7	27.6	82.7	55.9	30.9	18.1
640		80.2	84.0	61.6	38.7	26.7	82.8	55.1	30.1	17.4
660		80.6	83.9	61.8	39.0	26.9	82.9	55.7	30.5	17.7
680		81.1	84.0	63.1	40.5	28.4	83.1	57.7	32.3	19.2
700		81.5	84.0	65.3	43.2	31.1	83.2	60.8	35.4	21.7
720		82.0	84.2	67.7	46.2	34.0	83.4	63.8	38.8	24.6
740		82.4	84.2	68.6	47.4	35.1	83.5	65.1	40.3	25.8

Table E.2. Frits C and D Reflectance Data  
(+ percentages are wt.% Zr-V pigment added to frit)

Wavelength (nm)	1000C PEAK TEMPERATURE:						
	C	C + 0.5%	C + 2.0%	C + 5.0%	D	D + 0.5%	D + 2.0%
360	27.0	20.1	13.5	9.8	26.4	21.2	14.5
380	40.2	33.6	25.7	19.5	41.8	35.0	27.8
400	51.7	46.3	36.7	31.0	53.2	47.9	41.2
420	56.6	54.4	47.7	39.8	59.9	55.7	50.1
440	62.5	58.7	53.0	45.7	63.2	59.8	55.1
460	65.1	61.7	56.4	49.4	65.7	62.5	56.2
480	67.0	63.3	57.0	48.8	67.4	63.9	56.5
500	69.5	64.0	54.4	43.0	69.6	64.4	55.7
520	71.5	61.8	46.5	32.0	71.7	62.1	47.7
540	73.2	57.4	36.7	21.6	73.3	57.5	37.7
560	75.2	51.9	27.7	14.5	75.2	52.0	26.7
580	76.9	46.8	21.4	10.2	76.7	46.8	22.2
600	78.2	43.0	17.6	7.9	77.9	43.0	16.3
620	79.0	40.7	15.6	6.6	78.6	40.7	16.2
640	79.5	40.1	15.0	6.4	79.0	40.1	15.7
660	79.9	41.1	15.7	6.7	79.4	41.1	16.4
680	80.5	44.0	17.6	7.6	79.9	44.0	16.7
700	80.9	48.4	21.6	9.9	80.4	48.4	22.6
720	81.4	52.9	25.6	12.4	80.6	52.7	27.0
740	81.7	54.7	27.7	13.6	81.1	54.5	28.9
	1050C PEAK TEMPERATURE:						
	C	C + 0.5%	C + 2.0%	C + 5.0%	D	D + 0.5%	D + 2.0%
360	29.3	24.4	16.1	11.5	27.6	22.0	14.6
380	43.2	38.6	28.9	21.6	41.4	35.7	27.6
400	54.6	51.1	41.9	32.9	53.3	46.5	41.0
420	61.6	58.8	50.5	41.2	60.3	56.4	49.9
440	65.2	62.6	55.4	46.6	63.6	60.3	54.7
460	67.5	65.1	58.4	49.6	65.9	62.9	57.7
480	69.2	66.4	58.8	49.2	67.6	64.2	58.0
500	71.5	67.1	56.0	43.5	70.2	64.7	55.3
520	73.2	65.1	47.9	32.9	72.0	62.6	47.5
540	74.4	61.0	36.0	23.0	73.4	56.2	37.7
560	75.6	55.7	28.9	15.6	74.6	52.7	26.7
580	76.5	50.7	22.5	11.4	75.3	47.6	22.3
600	77.3	47.0	16.5	9.0	76.1	43.8	16.4
620	77.9	44.8	16.5	7.6	76.6	41.7	16.4
640	78.2	44.1	15.9	7.4	76.9	41.1	15.6
660	78.5	45.1	16.5	7.7	77.2	42.1	16.5
680	79.0	47.9	16.7	8.9	77.6	44.9	16.7
700	79.4	52.0	22.4	11.0	78.2	49.0	22.6
720	79.9	56.0	26.5	13.4	78.6	53.0	26.6
740	80.1	57.7	28.4	14.6	78.9	54.7	26.7
	1100C PEAK TEMPERATURE:						
	C	C + 0.5%	C + 2.0%	C + 5.0%	D	D + 0.5%	D + 2.0%
360	35.7	28.4	19.6	13.5	29.3	24.5	15.5
380	49.9	42.9	32.7	23.9	43.1	38.5	26.5
400	60.2	54.5	45.0	34.6	54.3	50.5	41.3
420	65.8	61.2	52.7	42.6	60.6	57.7	49.6
440	68.3	64.3	57.0	47.4	63.4	61.1	54.1
460	70.2	66.6	59.7	50.4	65.7	63.6	57.0
480	71.7	67.6	60.0	49.6	67.4	64.9	57.5
500	73.5	67.6	57.0	44.5	69.7	65.6	55.0
520	74.8	65.3	49.2	34.5	71.4	64.2	47.6
540	75.7	60.7	39.6	25.0	72.5	60.7	36.5
560	76.4	55.0	30.6	17.6	73.4	56.1	29.6
580	76.7	49.6	24.5	13.3	73.7	51.5	23.5
600	77.1	45.7	20.6	10.7	74.1	46.2	19.6
620	77.3	43.4	18.5	9.4	74.5	46.2	17.6
640	77.5	42.7	17.8	9.0	74.7	45.7	17.0
660	77.6	43.5	18.4	9.3	75.0	46.6	17.7
680	78.0	46.1	20.5	10.5	75.5	49.2	19.9
700	78.3	50.1	24.0	12.7	75.9	52.8	23.7
720	78.6	53.9	27.9	15.3	76.3	56.4	27.8
740	78.8	55.6	29.7	16.4	76.5	57.9	29.6

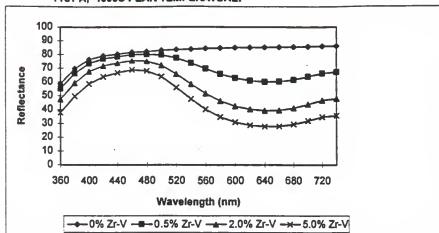
Table E.3. Frits E and F Reflectance Data  
(+ percentages are wt.% Zr-V pigment added to frit)

Wavelength (nm)	1000C PEAK TEMPERATURE:							
	E	E+0.5%	E+2.0%	E+5.0%	F	F+0.5%	F+2.0%	F+5.0%
360	35.1	31.4	23.3	16.1	51.3	42.7	32.0	22.5
380	48.1	44.6	35.8	26.7	60.3	54.0	44.3	34.2
400	58.6	55.8	47.8	37.8	67.5	62.9	54.9	45.2
420	64.8	62.8	55.5	45.8	71.2	67.7	61.1	52.4
440	67.7	66.2	60.0	51.2	73.0	70.0	64.5	56.7
460	89.7	88.4	82.8	54.5	74.8	71.9	66.9	59.4
480	71.1	69.5	63.2	54.0	75.8	72.7	66.9	58.5
500	73.2	69.9	60.7	48.7	77.4	72.9	64.4	53.3
520	75.0	68.1	53.5	38.5	78.7	71.1	57.6	43.8
540	76.5	64.3	44.4	28.6	79.8	67.6	49.2	34.1
560	78.2	59.4	35.8	20.9	81.1	63.2	41.2	26.5
580	79.7	54.7	29.5	16.1	82.1	59.0	35.3	21.5
600	80.9	51.1	25.4	13.2	83.0	55.7	31.4	18.5
620	81.7	48.9	23.2	11.7	83.5	53.7	29.3	16.8
640	82.2	48.2	22.4	11.1	83.8	53.1	28.6	18.3
660	82.6	49.1	23.0	11.5	84.1	53.9	29.1	16.6
680	83.1	51.7	25.1	12.7	84.5	56.2	31.1	18.0
700	83.6	55.7	28.7	15.1	84.8	59.8	34.5	20.6
720	84.1	59.7	32.7	17.8	85.2	63.3	38.2	23.4
740	84.5	61.4	34.5	19.0	85.4	64.9	39.9	24.6
	1050C PEAK TEMPERATURE:							
	E	E+0.5%	E+2.0%	E+5.0%	F	F+0.5%	F+2.0%	F+5.0%
360	25.2	22.5	17.2	9.9	40.6	33.5	25.0	15.7
380	39.2	36.3	29.9	19.4	51.4	46.1	37.9	28.8
400	52.2	49.4	43.0	30.8	60.7	56.9	49.9	38.6
420	60.7	58.2	52.4	39.7	68.0	63.3	57.4	48.8
440	64.8	62.8	57.8	45.6	68.6	66.5	61.5	51.7
460	87.1	85.1	80.5	49.2	70.5	68.7	64.0	54.7
480	88.8	88.5	81.2	48.8	71.9	69.9	64.6	54.4
500	71.3	67.5	59.5	43.4	73.8	70.8	63.3	49.9
520	73.1	68.0	52.9	32.8	75.2	69.9	57.8	40.3
540	74.4	62.5	44.0	22.7	76.3	67.4	50.0	30.2
560	75.8	57.9	35.2	15.2	77.3	63.8	41.9	22.2
580	78.8	53.4	28.5	10.8	78.0	60.2	35.5	17.1
600	77.8	50.0	24.2	8.4	78.7	57.5	31.3	14.1
620	78.4	47.9	21.9	7.2	79.2	55.8	29.0	12.8
640	78.8	47.3	21.2	6.8	79.4	55.2	28.2	12.1
660	79.2	48.2	22.0	7.1	79.7	56.0	29.0	12.5
680	79.7	50.8	24.4	8.2	80.1	58.2	31.4	14.0
700	80.1	54.7	28.8	10.4	80.3	61.3	35.5	16.6
720	80.6	58.5	33.1	13.0	80.6	64.3	39.8	19.6
740	81.0	60.2	35.2	14.2	80.7	65.6	41.7	21.0
	1100C PEAK TEMPERATURE:							
	E	E+0.5%	E+2.0%	E+5.0%	F	F+0.5%	F+2.0%	F+5.0%
360	23.0	20.7	14.5	8.4	25.5	24.3	19.9	11.8
380	38.5	34.2	26.9	18.0	38.6	37.9	33.5	23.2
400	49.3	47.2	40.0	29.8	50.4	50.3	46.1	35.6
420	57.9	56.1	49.4	38.8	57.7	58.0	54.2	44.3
440	61.9	60.5	54.6	44.8	61.0	61.6	58.3	49.4
460	64.3	63.1	57.7	48.1	63.2	64.0	60.9	52.4
480	66.2	64.8	58.8	48.3	64.9	65.7	62.4	53.0
500	68.7	66.3	57.8	44.2	67.3	67.7	63.2	50.5
520	70.5	65.8	52.5	34.8	69.0	68.7	61.4	43.0
540	71.7	63.7	44.7	24.9	70.1	68.7	57.5	33.8
560	72.8	60.7	36.8	17.0	71.1	68.0	52.5	25.8
580	73.5	57.4	30.5	12.0	71.7	67.0	47.8	19.8
600	74.1	54.9	26.4	9.2	72.3	66.2	44.3	18.3
620	74.6	53.4	24.2	7.9	72.7	65.7	42.3	14.5
640	74.9	53.0	23.5	7.4	73.0	65.6	41.7	13.9
660	75.2	53.8	24.3	7.9	73.3	66.1	42.5	14.5
680	75.7	55.9	28.7	9.3	73.7	67.3	44.8	16.4
700	76.0	58.9	30.7	11.9	73.9	68.7	48.4	19.8
720	76.3	61.7	35.0	15.0	74.2	70.0	51.8	23.4
740	76.4	62.9	36.9	16.5	74.3	70.5	53.2	25.1

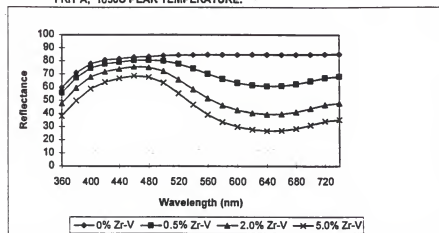
Table E.4. Frits G and H Reflectance Data  
(+ percentages are wt.% Zr-V pigment added to frit)

Wavelength (nm)	1000C PEAK TEMPERATURE:						
	G	G + 0.5%	G + 2.0%	G + 5.0%	H	H + 0.5%	H + 2.0%
360	29.3	25.1	18.3	14.1	42.5	37.8	27.5
380	42.0	38.1	30.3	24.4	54.1	49.8	40.4
400	53.0	49.6	42.4	35.5	63.4	59.6	51.9
420	80.1	57.4	50.8	43.8	68.7	65.3	58.8
440	83.7	81.3	55.4	49.2	71.2	68.2	62.5
460	66.2	64.0	58.5	52.6	73.3	70.4	65.0
480	68.0	85.5	59.1	52.1	74.7	71.4	65.2
500	70.5	86.4	56.5	46.7	78.7	71.8	62.8
520	72.5	64.8	48.8	36.3	78.1	69.9	55.4
540	74.2	81.1	39.2	28.3	79.4	66.1	46.4
560	78.3	56.4	30.5	18.7	80.8	61.4	37.9
580	78.0	51.8	24.3	14.1	82.1	56.9	31.8
600	79.4	48.3	20.5	11.5	83.0	53.5	27.7
620	60.2	46.2	18.5	10.2	83.4	51.4	25.8
640	80.7	45.6	17.9	9.8	83.6	50.7	24.9
660	61.1	46.6	16.5	10.1	83.7	51.6	25.8
680	61.6	49.4	20.6	11.3	83.9	54.1	27.6
700	82.1	53.7	24.3	13.8	84.0	57.8	31.5
720	82.6	57.6	28.3	18.2	84.2	61.4	35.5
740	62.9	59.5	30.2	17.4	84.2	62.6	37.3
	1050C PEAK TEMPERATURE:						
	G	G + 0.5%	G + 2.0%	G + 5.0%	H	H + 0.5%	H + 2.0%
360	27.1	24.4	17.7	11.8	40.3	38.4	29.8
380	40.6	37.9	30.8	21.8	51.9	50.2	42.7
400	52.6	50.1	43.3	33.5	61.4	60.0	53.6
420	80.4	58.1	52.0	42.3	67.1	65.7	60.1
440	84.1	82.1	56.8	47.7	69.7	68.5	63.8
460	66.4	64.8	59.8	51.0	71.8	70.8	66.0
480	88.2	66.0	60.3	50.6	73.3	71.8	66.5
500	70.7	87.2	58.1	45.6	75.3	72.9	65.0
520	72.5	66.0	50.9	35.3	76.6	72.3	59.4
540	73.8	82.9	41.6	25.1	77.8	70.2	51.7
560	75.1	58.8	32.8	17.4	78.8	67.2	43.9
580	78.1	54.7	28.3	12.6	79.5	84.1	37.8
600	77.0	51.8	22.2	10.0	80.1	61.6	33.7
620	77.5	49.8	20.1	8.7	80.5	60.0	31.5
640	77.8	49.3	19.4	8.3	80.8	59.5	30.8
660	78.1	50.2	20.1	8.7	80.6	60.2	31.5
680	78.8	52.7	22.5	10.0	81.0	62.1	33.8
700	79.0	56.4	26.4	12.4	81.1	64.6	37.6
720	79.3	59.6	30.7	15.2	81.3	67.3	41.5
740	79.5	61.3	32.6	16.5	81.3	68.3	43.1
	1100C PEAK TEMPERATURE:						
	G	G + 0.5%	G + 2.0%	G + 5.0%	H	H + 0.5%	H + 2.0%
360	27.1	23.9	17.8	10.4	36.7	38.8	34.1
380	40.9	37.8	31.0	20.9	49.1	50.7	48.9
400	52.6	50.1	43.7	32.8	59.1	60.1	56.9
420	59.9	57.9	52.2	41.5	65.0	65.5	62.7
440	83.3	81.8	56.7	46.8	67.8	68.0	65.8
460	65.6	64.2	59.6	50.1	69.8	70.1	67.8
480	87.4	85.8	60.7	50.3	71.4	71.6	69.1
500	69.7	67.4	59.6	46.5	73.6	73.4	69.9
520	71.4	67.1	54.9	37.4	75.1	74.3	68.8
540	72.6	65.4	47.7	27.8	76.1	74.5	65.5
560	73.5	62.8	39.9	19.5	77.0	74.1	61.3
580	74.1	59.6	33.6	14.3	77.4	73.3	57.2
600	74.7	57.3	29.4	11.4	77.9	72.8	54.1
620	75.1	55.9	27.2	9.9	78.1	72.2	52.2
640	75.3	55.5	28.5	9.4	78.2	72.0	51.6
660	75.6	56.3	27.3	9.9	78.3	72.3	52.2
680	76.0	56.3	29.8	11.5	78.8	73.1	54.3
700	76.2	81.0	33.9	14.3	78.7	74.0	57.2
720	76.5	83.5	38.2	17.5	78.9	74.6	60.1
740	76.6	84.5	40.0	19.1	78.9	75.1	61.2

FRIT A: 1000C PEAK TEMPERATURE:



FRIT A: 1050C PEAK TEMPERATURE:



FRIT A: 1100C PEAK TEMPERATURE:

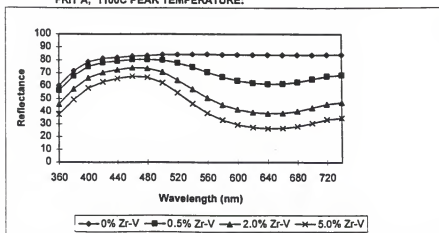
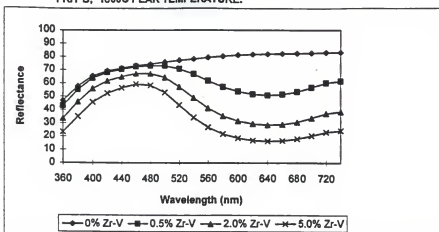


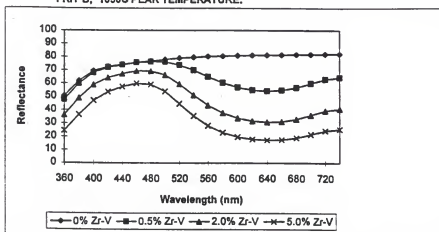
Figure E.1. Frit A spectral reflectance curves.



FRIT B; 1000C PEAK TEMPERATURE:



FRIT B; 1050C PEAK TEMPERATURE:



FRIT B; 1100C PEAK TEMPERATURE:

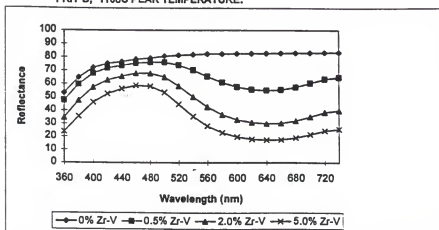


Figure E.2. Frit B spectral reflectance curves.

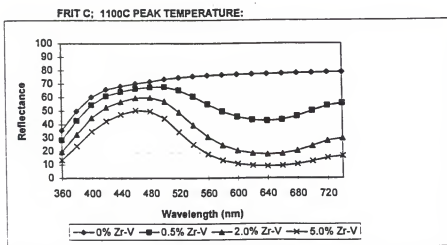
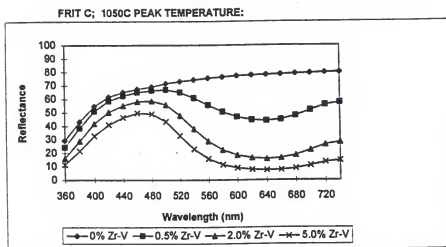
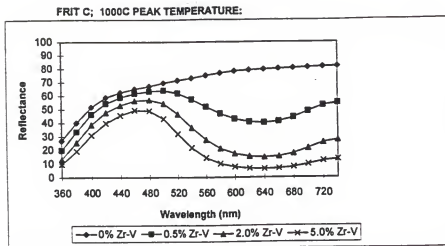
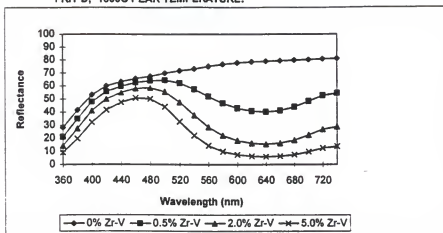
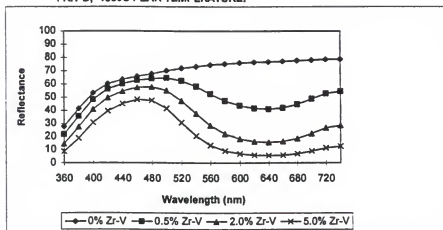


Figure E.3. Frit C spectral reflectance curves.

FRIT D; 1000C PEAK TEMPERATURE:



FRIT D; 1050C PEAK TEMPERATURE:



FRIT D; 1100C PEAK TEMPERATURE:

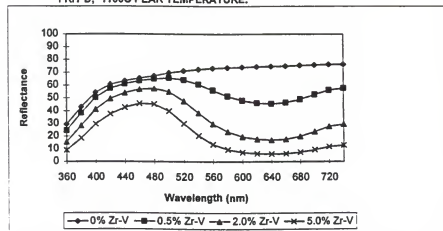
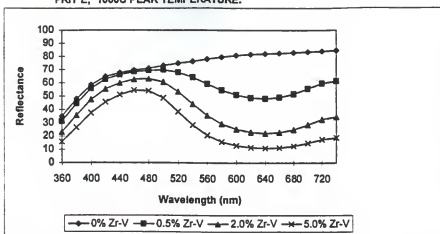
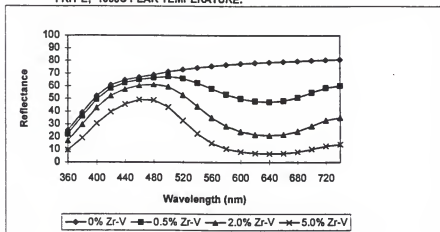


Figure E.4. Frit D spectral reflectance curves.

FRIT E; 1000C PEAK TEMPERATURE:



FRIT E; 1050C PEAK TEMPERATURE:



FRIT E; 1100C PEAK TEMPERATURE:

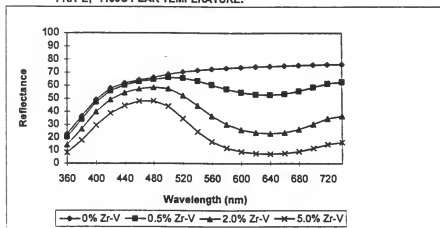


Figure E.5. Frit E spectral reflectance curves.

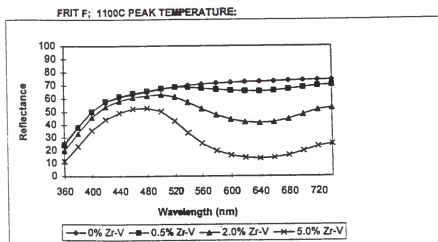
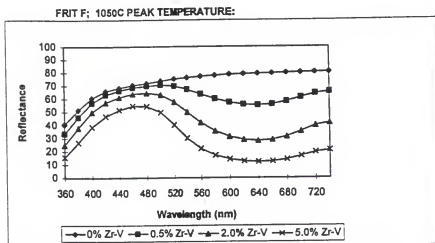
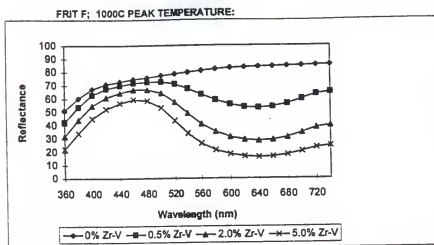
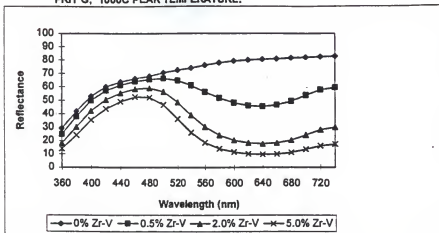
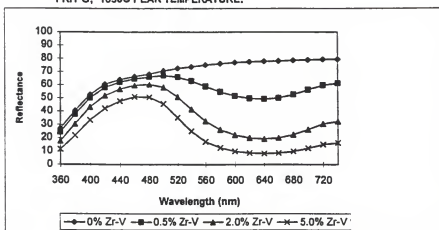


Figure E.6. Frit F spectral reflectance curves.

FRIT G: 1000C PEAK TEMPERATURE:



FRIT G: 1050C PEAK TEMPERATURE:



FRIT G: 1100C PEAK TEMPERATURE:

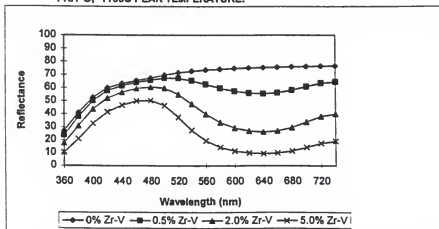
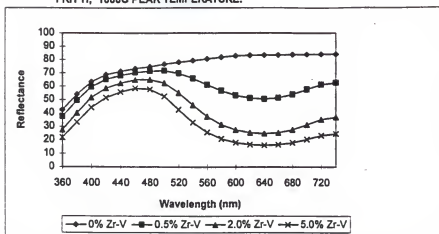
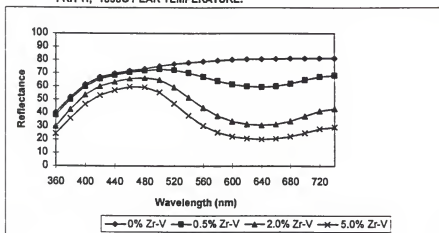


Figure E.7. Frit G spectral reflectance curves.

FRIT H; 1000C PEAK TEMPERATURE:



FRIT H; 1050C PEAK TEMPERATURE:



FRIT H; 1100C PEAK TEMPERATURE:

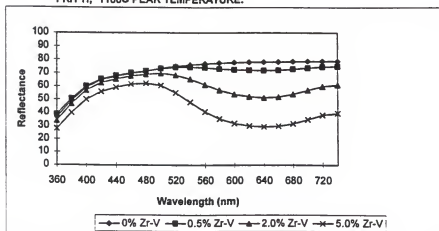


Figure E.8. Frit H spectral reflectance curves.

## REFERENCES

- Ale74 L. Alexander and H. Klug, X-ray Diffraction Procedures, 2nd Ed., John Wiley and Sons, New York (1974).
- Amo94 J. Amoros, British Ceramic Transactions, 93 (6), 224-228 (1994).
- Apa94 J. Aparici, A. Moreno, A. Escardino, S. Mestre, Qualicer 94, 2, 35-45 (1994).
- Ask94 D. Askeland, The Science and Engineering of Materials, 3rd Ed., PWS Publishing Co., Boston MA (1994).
- Aza97 J. Aza, N. Baldini, E. Barszczewski, L. Bernhardt, E. Gutman, J. Kramer and C. Leinweber, Annual Book of ASTM Standards, 15.02 (15) (1997).
- Ban86 N. Bansal and R. Doremus, Handbook of Glass Properties, Academic Press, Orlando, FL (1986).
- Bar96 L. Barbieri, C. Leonelli and T. Manfredini, Ceramic Engineering and Science Proceedings, 17 (1), 11-22 (1996).
- Bar97 T. Barson, Ceramic Engineering and Science Proceedings, 18 (2), 28-36 (1997).
- Bil67 F. Billmeyer and M. Saltzman, Principles of Color Technology, John Wiley and Sons, New York (1967).
- Blo93 R. Blonski, Ceramic Engineering and Science Proceedings, 14 (1-2), 176-189 (1993).
- Blo94a R. Blonski, Ceramic Engineering and Science Proceedings, 15 (1), 249-265 (1994).



- Blo94b R. Blonski, Ceramic Engineering and Science Proceedings, 15 (1), 266-280 (1994).
- Boa83 M. Boas, Mathematical Methods in the Physical Sciences, 2nd Ed., John Wiley and Sons, New York (1983).
- Bow87 R. Bowles and S. Haller, Multiple Correlation, Computer software, SSI Management Consultants, Inc., Cleveland, OH (1987).
- Bow90 R. Bowles and S. Haller, Problem Solving with Experimental Design, Multiple Correlation, Multiple Property Optimization and Partitioning Variability, SSI Management Consultants, Inc., Cleveland, OH (1990).
- Bra86 G. Brady and H. Clauser, Material Handbook, 12th Ed., McGraw Hill, New York, NY (1986).
- Bur79 A. Burgyan, Interceram, 28 (1) 1979.
- Bur96 B. Burzacchini, M. Paganelli and H. Christ, Ceramic Engineering and Science Proceedings, 17 (1), 60-66 (1996).
- Byr94 C. Byrne, S. Kutney and R. Pipoly, Ceramic Engineering and Science Proceedings, 15 (1), 206-223 (1994).
- Cas97 R. Castilone and W. Carty, Ceramic Engineering and Science Proceedings, 18 (2), 83-84 (1997).
- Che83 H. Chen, Theory of Electromagnetic Waves, McGraw Hill, Inc., Fairfax, VA (1983).
- Chi97 Y. Chiang, D. Birnie and W. Kingery, Physical Ceramics, John Wiley and Sons, New York, NY (1997).
- Con97 C. Concepcion, J. Oteo, E. Ocana, J. Rubio and M. Velaso, Ceramic Engineering and Science Proceedings, 18 (2), 96-113 (1997).
- Dec90 C. Decker, Ceramic Engineering and Science Proceedings, 11 (3-4), 307-313 (1990).

- Dec93 C. Decker, Ceramic Engineering and Science Proceedings, 14 (1-2), 155-162 (1993).
- DeH93 R. DeHoff, Thermodynamics in Materials Science, McGraw-Hill, New York (1993).
- Din96 R. Dinger and C. Villa, American Ceramic Society Bulletin, 75 (4), 93-95 (1996).
- Din96a R. Dinger and C. Villa, American Ceramic Society Bulletin, 75 (5), 80-83 (1996).
- Dod94 A. Dodd and D. Murfin, Dictionary of Ceramics, 3rd Ed., University Press, Cambridge, London (1994).
- Dor94 R. Dormeu, Glass Science, 2nd Ed., John Wiley and sons, New York (1994).
- Dow83 S. Dowdy and S. Weardon, Statistics for Research, John Wiley and Sons, New York (1983).
- Dry82 Dry Color Manufacturers Association Classification of Mixed Metal Oxide Inorganic Colored Pigments, 2nd Ed., Published by DCMA, Arlington, VA (1982).
- Dun49 R. Duncan, Journal of Oil and Color Chemists' Association, 32, 296 (1949).
- Ear94 D. Earl, M.S. Thesis, University of Florida (1994).
- Eld94 S. Eldefrawi, Second International Ceramics Congress, 1, 196-205 (1994).
- Enr96 J. Enrique, J. Amoros and A. Moreno, in The Science of Whitewares, American Ceramic Society, Westerville, OH, 357-370 (1996).
- Epp87 R. Eppler, Ceramic Bulletin, 66 (11), 1600 (1987).
- Epp96 D. Eppler and R. Eppler, Ceramic Engineering and Science Proceedings, 17 (1), 77-87 (1996).
- Epp97a D. Eppler and R. Eppler, Ceramic Engineering and Science Proceedings, 18 (2), 141-142 (1997).

- Epp97b R. Eppler and D. Eppler, Ceramic Engineering and Science Proceedings, 18 (2), 150-158 (1997).
- Esc96 A. Escardino, Qualicer 96, 1, 169-184 (1996).
- Fer96 "The U.S. Tile Industry," Pamphlet distributed by Ferro Corporation, Cleveland, OH (1996).
- Fle93 J. Fleming, Experimental Techniques in Glass Science, (C. Simmons and O. El-Bayoumi, eds.), American Ceramic Society, Westerville, OH, 1-29 (1993).
- Gre82 S. Gregorio, M. Greenblatt, J. Pifer and M. Sturge, Journal of Chemistry and Physics, 76 (6), 2931-2937 (1982).
- Gru78 O. Grum-Grzhimailo, Glass Ceramic, 35 (1), 41 (1978).
- Hal86 D. Halliday and R. Resnick, Fundamental of Physics, 2nd Ed., John Wiley and Sons, New York (1986).
- Hum93 R. Hummel, Electronic Properties of Materials, 2nd Ed., Springer-Verlag, New York (1993).
- Hun87 R. Hunter and R. Harold, The Measurement of Appearance, 2nd Ed., John Wiley and Sons, New York (1987).
- Jac96 P. Jackson, Science of Whitewares, American Ceramic Society, Westerville, OH, 395 (1996).
- Jam85 P. James, Journal of Noncrystalline Solids, 73, 517 (1985).
- Jud65 D. Judd and G. Wyszecski, Color in Business, Science and Industry, 2nd Ed., John Wiley and Sons, New York (1965).
- Kim59 K. Kim and F. Hummel, Journal of the American Ceramic Society, 46 (6), 286-291 (1959).
- Kin40 B. King, Journal of the American Ceramic Society, 23 (8), 221-225 (1940).

- Kin76 W. Kingery, H. Bowen and D. Uhlmann, Introduction to Ceramics, 2nd Ed., John Wiley and sons, New York (1976).
- Klu74 H. Klug and L. Alexander, X-Ray Diffraction Procedures, 2nd Ed., John Wiley and Sons, New York (1974).
- LaC97 W. LaCourse and W. Mason, Ceramic Engineering and Science Proceedings, 18 (2), 237-245 (1997).
- Lev69 E. Levin, C. Robbins and H. McMurdie, Phase Diagrams for Ceramists, 2nd Ed., American Ceramic Society, Westerville, OH (1969).
- Mac91a Macbeth Optimatch Color Matching System Reference Guide, Macbeth Corp., Newburgh, New York (1991).
- Mac91b Macbeth White-Eye 3000 Spectrophotometer User's Reference Guide, Macbeth Corp., Newburgh, New York (1991).
- Mac96 Macbeth ProPalette Computer Color Matching System Version 1.6, Computer Index, Macbeth Corp., Newburgh, New York (1996).
- MacA35 D. MacAdam, Journal of Optical Society of America, 25, 361-367 (1935).
- MacA42 D. MacAdam, Journal of Optical Society of America, 32, 247-274 (1942).
- Mal96 R. Malmgren, Ceramic Industry, 146 (10), 31-36 (1996).
- Mas68 B. Mason and L. Berry, Elements of Mineralogy, W. H. Freeman Co., San Francisco (1968).
- Mei97 K. Meinssen, Ceramic Engineering and Science Proceedings, 18 (2), 308-319 (1997).
- Mue83 D. Mueller, "Ceramic Raw Materials," Class Notes from CES314, Alfred University, Alfred, NY (1983).

- Mur89 J. Murray, American National Standard Specifications for Ceramic Tile, A137.1, Tile Council of America, Princeton, NJ (1989).
- Mur90 S. Murdock, T. Wise and D. Eppler, American Ceramic Society Bulletin, 69 (2), 228-230 (1990).
- Nas83 K. Nassau, The Physics and Chemistry of Color, John Wiley and sons, New York (1983).
- Pag97 Mariano Paganelli, Ceramic World, Editore Tile Italia, S.r.l., Sassuolo, MO, Italy, 148-151 (1997).
- Par73 C. Parmelee and C. Harman, Ceramic Glazes, 3rd Ed., CBLS, Marietta, OH (1973).
- Pat67 D. Patterson, Pigments, Elsevier Publishing Co., New York (1967).
- Paw96 E. Pawlicki and D. Fu, Ceramic Engineering and Science Proceedings, 17 (1), 173-179 (1996).
- Pet72 R. Petrucci, General Chemistry, MacMillan Company, New York (1972).
- Pop77 M. Pope and M Judd, Differential Thermal Analysis, Heyden and Son Ltd., Bellmawr, NJ (1977).
- Rah95 R. Rahaman, Ceramic Processing and Sintering, Marcel Dekker, Inc., New York (1995).
- Ree83 J. Reed, "Optical Properties of Ceramic Materials," Class Notes from CES305 Ceramic Lab., Alfred University, Alfred, NY (1983).
- Ree95 J. Reed, Principles of Ceramic Processing, 2nd Ed., John Wiley and Sons, New York (1995).
- Ric92 D. Richerson, Modern Ceramic Engineering, 2nd Ed., Marcel Dekker, Inc., New York (1992).
- Sac86 Sacmi Labs, From Technology Through Machinery to Kilns for Sacmi Tile, 2, Sacmi R&D Lab Notes, Imola, Italy (1986).

- Sac96 M. Sacks, EMA 4645 Ceramic Processing Class Notes, University of Florida (1996).
- San57 C. Sanders and G. Wyszecski, Journal of Optical Society of America, 47, 398-404 (1957).
- Sch62 H. Scholze, Glastech. Ber., 39, 63-68 (1962).
- Sel47 H. Selling, Journal of the Society of Dyers Colorists, 63, 619 (1947).
- Sez98 G. Sezzi, Tile Italia, 1, 46-50 (1998).
- Sha92 J. Shackelford and W. Alexander, CRC Materials Science and Engineering Handbook, CRC Press, Boca Raton, FL (1992).
- She97 L. Sheppard, Ceramic Industry, 147 (1), 41-174 (1997).
- Sim93 J. Simmons, Experimental Techniques in Glass Science (C. Simmons and O. El-Bayoumi, Eds.), American Ceramic Society, Westerville, OH, 383-427 (1993).
- Tay86 J. Taylor and A. Bull, Ceramics Glaze Technology, Pergamon Press, Elmsford, NY (1986).
- Teu95 K. Teuchert, R. Thomas and A. Muller-Zell, Interceram, 44 (4), 230-233 (1995).
- Tip80 P. Tipler, Physics, Worth Publishers, Inc., New York (1980).
- Toz86 R. Tozzi, Glazes for Fast-Firing, Italian Ceramic Society, Rimini, Italy (1986).
- Vic97 W. Vickery, Ceramic Engineering and Science Proceedings, 18 (2), 409 (1997).
- Wea79 R. Weast and M. Astle, CRC Handbook of Chemistry and Physics, 60th Ed., CRC Press, Boca Raton, FL (1979).
- Wor82 W. Worrall, Ceramic Raw Materials, 2nd Ed., Pergamon Press, Elmsford, NY (1982).

- Wyc65 R. Wyckoff, Crystal Structures, 3rd Ed., John Wiley and Sons, New York (1965).
- Yoo97 C. Toon, W. LaCourse and W. Mason, Ceramic Engineering and Science Proceedings, 18 (2), 439-454 (1997).

## BIOGRAPHICAL SKETCH


David Earl was born in Buffalo, New York, on December 28, 1961. He graduated with a B.S. degree in ceramic engineering from the New York State College of Ceramics at Alfred University in 1984. In 1985 he moved to Parkersburg, West Virginia, and worked as a quality control engineer for A.B. Chance Co., a manufacturer of porcelain high voltage insulators. In May of 1986 he joined Florida Tile Industries in Lakeland, Florida, as quality assurance supervisor and was eventually promoted to the positions of corporate statistics consultant and senior engineer. In 1994, David earned an M.S. degree in materials science and engineering from the University of Florida in Gainesville. In July of 1994, he joined Huntington/Pacific Ceramics, Inc., a ceramic tile manufacturer, as plant manager of the Mount Vernon, Texas, facility. David returned to Florida Tile Industries in August of 1995 and has since held the positions of plant manager and director of research and development. He was




admitted to doctoral candidacy at the University of Florida in December of 1996.

His professional affiliations include memberships in the American Ceramic Society (ACerS), National Institute for Ceramic Engineers (NICE), Phi Kappa Phi international academic honor society, Ceramic Manufacturing Council (CMC), Ceramic Educational Council (CEC) and Keramos. He is also a Distinguished Mentor for ACerS.

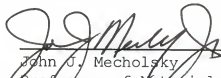
I certify that I have read this study and that in my opinion it conforms to acceptable standards of scholarly presentation and is fully adequate, in scope and quality, as a dissertation for the degree of Doctor of Philosophy.

  
David E. Clark, Chairman  
Professor of Materials Science  
and Engineering


I certify that I have read this study and that in my opinion it conforms to acceptable standards of scholarly presentation and is fully adequate, in scope and quality, as a dissertation for the degree of Doctor of Philosophy.

  
E. Dow Whitney  
Professor of Materials Science  
and Engineering

I certify that I have read this study and that in my opinion it conforms to acceptable standards of scholarly presentation and is fully adequate, in scope and quality, as a dissertation for the degree of Doctor of Philosophy.

  
John C. Mecholsky  
Professor of Materials Science  
and Engineering

I certify that I have read this study and that in my opinion it conforms to acceptable standards of scholarly presentation and is fully adequate, in scope and quality, as a dissertation for the degree of Doctor of Philosophy.

  
Joseph H. Simmons  
Professor of Materials Science  
and Engineering

I certify that I have read this study and that in my opinion it conforms to acceptable standards of scholarly presentation and is fully adequate, in scope and quality, as a dissertation for the degree of Doctor of Philosophy.

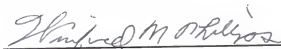


---

Dinesh O. Shah  
Charles A. Stokes Professor  
of Chemical Engineering

This dissertation was submitted to the Graduate Faculty of the College of Engineering and to the Graduate School and was accepted as partial fulfillment of the requirements for the degree of Doctor of Philosophy.

December 1998



Winfred M. Phillips  
Dean, College of Engineering

---

M. J. Ohanian  
Dean, Graduate School

LD  
1780  
199\_

1E12

UNIVERSITY OF FLORIDA



3 1262 08555 1017